

DECELERATION AND ELECTROSTATIC TRAPPING OF OH RADICALS

Deceleration and Electrostatic Trapping of OH Radicals

S.Y.T. van de Meerakker

Thesis Radboud Universiteit Nijmegen - Illustrated

With references - With summary in Dutch

ISBN-10: 90-9019874-1

ISBN-13: 9789090198743

NUR 926

Subject headings: Low Temperatures / Electric Fields / Molecular Beams / Phase-space Dynamics

Cover design: Louise Thomas.

DECELERATION AND ELECTROSTATIC TRAPPING OF OH RADICALS

EEN WETENSCHAPPELIJKE PROEVE OP HET GEBIED VAN DE
NATUURWETENSCHAPPEN, WISKUNDE EN INFORMATICA

PROEFSCHRIFT

TER VERKRIJGING VAN DE GRAAD VAN DOCTOR
AAN DE RADBOUD UNIVERSITEIT NIJMEGEN
OP GEZAG VAN DE RECTOR MAGNIFICUS PROF. DR. C.W.P.M. BLOM
VOLGENS BESLUIT VAN HET COLLEGE VAN DECANEN
IN HET OPENBAAR TE VERDEDIGEN
OP VRIJDAG 6 JANUARI 2006,
DES NAMIDDAGS OM 1.30 UUR PRECIES

DOOR

SEBASTIAAN YVONNE THEODORUS VAN DE MEERAKKER

GEBOREN OP 30 MEI 1977
TE EINDHOVEN

PROMOTOR : PROF. DR. G.J.M. MEIJER

MANUSCRIPTCOMMISSIE : PROF. DR. J.J. TER MEULEN

: DR. H.L. BETHLEM
VRIJE UNIVERSITEIT AMSTERDAM, THE NETHERLANDS

: PROF. DR. J. YE
JILA, NIST, UNIVERSITY OF COLORADO, BOULDER, COLORADO, USA

The work described in this thesis is performed as part of the research program of the “Stichting voor Fundamenteel Onderzoek der Materie” (FOM), which is financially supported by the “Nederlandse organisatie voor Wetenschappelijk Onderzoek” (NWO), and is performed at the FOM-Institute for plasmaphysics ‘Rijnhuizen’ in Nieuwegein, the Netherlands, and at the Fritz-Haber-Institut der Max-Planck-Gesellschaft in Berlin, Germany.

Voorwoord

Het begon allemaal op het toilet. Een damestoilet nog wel. Want daar bevond zich de opstelling van Rick Bethlem, mijn voorganger. Samen met Giel Berden en Gerard Meijer had hij in de tot klein lab omgebouwde toiletruimte aan de (toen nog genaamd) KUN een methode ontwikkeld om een bundel neutrale moleculen af te remmen. Door een serie elektroden op uitgekiende tijden op hoogspanning te zetten, waren ze er in geslaagd een klein deel van een bundel CO moleculen naar een veel lagere snelheid te brengen. Voorbereidingen voor de volgende stap, afremmen naar volledige stilstand en de moleculen vervolgens opsluiten in een val, waren in volle gang. Rond die tijd bood Gerard mij een promotieplaats aan. Ik zou de experimenten van Rick moeten gaan herhalen, maar nu met een machine die in staat zou zijn om een flink groter deel van de bundel af te remmen. De machine opschalen, was dus het devies. Met een dergelijke machine zouden de veelbelovende toepassingen van de geproduceerde pakketjes koude moleculen binnen handbereik komen. Bovendien zouden de experimenten gedaan moeten worden met het chemisch zeer relevante OH radicaal. Moet te doen zijn, dacht ik. Wat die Rick kan, kan ik natuurlijk ook.

Ik begon in april 2000 aan het FOM-instituut "Rijnhuizen" in Nieuwegein. Gerard was daar net benoemd als nieuwe directeur, en vooruitlopend op de verhuizing van zijn groep van Nijmegen naar Nieuwegein, was Rienk Jongma als projectleider druk in de weer om het nieuwe lab in Nieuwegein de juiste vorm te geven. Een laser-hal werd gebouwd, en de volledige infrastructuur werd naar onze wensen opnieuw geïnstalleerd. Samen met Rienk kwamen in deze tijd ook de eerste ideeën voor de nieuwe opgeschaalde machine op papier. Het was een spannende tijd, waarin nagedacht moest worden over elk klein detail van een dergelijke machine. In de zomer van 2000 was eindelijk ons nieuwe lab in Nieuwegein klaar, en werd met vereende kracht de apparatuur van Nijmegen naar Nieuwegein versleept. Toen pas werd duidelijk hoeveel werk zo'n verhuizing eigenlijk is, en we waren het er allemaal over eens dat we dit niet nog eens wilden doen.

Na een jaartje begonnen de eerste onderdelen van de opstelling binnen te komen. De bouten van de eerste vacuumkamers waren nog maar net aangedraaid, toen het grote nieuws kwam. Voor Gerard was het directeurschap van Rijnhuizen niet voldoende, en hij kondigde aan dat hem een positie was aangeboden als directeur van het Fritz-Haber-Instituut van het Max-Planck-Gezelschap in Berlijn. Een nieuwe verhuizing? Vinex-wijk Nieuwegein wilde ik best inruilen voor wereldstad Berlijn, al zou ik het lab en de gezelligheid van de Rijnhuizenaren met het jaarlijkse cabaret en de Rijnhuizencafés in de kelder van het kasteel natuurlijk wel gaan missen. Gelukkig hadden we de dozen van de vorige verhuizing nog staan, sommige nog niet eens uitgepakt.

De resterende anderhalf jaar voor de geplande verhuizing naar Berlijn was intensief. Rienk had inmiddels besloten zijn carrière elders voort te zetten, en verliet kort daarop de groep. Met Gerard al met één been in Berlijn, bleef ik voor de opbouw van de opstelling alleen achter met Paul Smeets, de technicus die al vanaf het begin bij ontwerp en opbouw van de opstelling betrokken was. Het opschalen van een al functionerend prototype bleek veel weerbarstiger dan verondersteld. Designfouten in de keramische isolatoren werden genadeloos door de hoogspanning afgestraft, en het netjes

positioneren van de serie elektroden bleek een bijna onmogelijke taak. En eenmaal netjes op een rijtje gemonteerd, waren doorslagen aan de orde van de dag. Tot overmaat van ramp bleken de hoogspanningsschakelaars niet bestand tegen de zware taak die ze moesten uitvoeren. Maar samen met Pauls strijd lust en de hulp van zo'n beetje het hele lab werd het gevecht uiteindelijk gewonnen. Slechts drie weken voordat de verhuishagens voor de deur stonden, waren alle technische problemen opgelost, en werden de eerste pakketjes OH radicalen afgeremd. Het was inmiddels november 2003. We hadden nog net tijd voor een feestje, voordat de boel definitief naar ons nieuwe lab in Berlijn werd verplaatst.

In Berlijn werd het team versterkt met Nicolas Vanhaecke, een Franse postdoc. Samen met Paul, die tijdelijk meeging naar Berlijn, en de nieuwe Berlijnse collega's is de hele machine in record-tijd weer opnieuw opgebouwd. En met Gerard's inspirerende "We moeten het aan de gang zien te krijgen" werden de eerste OH bundels na een aantal maanden alweer afgeremd. Samen met Nicolas kon nu het laatste stukje aan de opstelling toegevoegd worden: de electrostatische val, met als doel de OH moleculen stil te zetten en op te sluiten. Na wat aanloopproblemen, was het op 28 mei 2004 dan eindelijk zover: de moleculen stonden stil. De overwinning was zoet...

Het relaas hierboven vertelt in het kort de hoogte- en dieptepunten van de vijf jaar werk die het gekost heeft om de machine te ontwerpen, te bouwen, en de experimenten te doen die in dit proefschrift beschreven staan. Een proces dat ik nooit alleen had kunnen volbrengen. Ik wil hier dan ook graag iedereen bedanken die heeft bijgedragen aan dit proefschrift. Het aantal mensen dat betrokken was bij het project, in Nijmegen, Nieuwegein, en Berlijn, is werkelijk enorm. Met name de tekenkamer, instrumentmakerij, ict en de electronica-afdeling van Rijnhuizen hebben ondanks de soms beperkte middelen veel werk verzet. Een aantal mensen wil ik graag in het bijzonder bedanken.

Op de eerste plaats mijn promotor Gerard Meijer. Gerard, ik dank je voor de kansen die je me hebt geboden, en het vertrouwen dat je in me gesteld hebt. Je onaflatende energie en enthousiasme voor molecuulfysica waren erg belangrijk om mijn motivatie op peil te houden, met name op die momenten dat het allemaal erg tegen zat. Je geloof in het project en de durf om daarvoor mankracht en geld niet te sparen, waren essentieel voor een succesvolle afloop. Ook Rienk Jongma heeft veel bijgedragen aan dit proefschrift. Helaas ben je niet meer betrokken geweest bij de experimenten met de afremmer, maar de beslissingen die je in de beginfase van het project genomen hebt betalen zich nog dagelijks uit. Veel dank ben ik ook verschuldigd aan Paul Smeets. Paul, ik zou hier eigenlijk niet eens precies weten waarvoor ik je nu allemaal moet bedanken. Is het je inzet, je kunde, je doorzettingsvermogen, je relativerende humor of de zak drop die ik altijd jatte? Zonder jou was het in ieder geval nooit gelukt. Ik wil je graag bedanken voor alles wat je voor mij en de rest van de groep gedaan hebt. In de laatste fase van het werk dat in Berlijn plaatsvond was Nicolas Vanhaecke mijn steun en toeverlaat. Nicolas, together we had great fun in the lab the last two years, playing very successfully with beams of OH. I thank you for your enormous contributions to this thesis. Both your experimental work (including your 'magic screwdriver') and simulation skills were essential to almost all experiments described in this thesis. I look back with pleasure to our nocturnal trapping experiments, and the very exciting lifetime measurement. I wish you all the best with your new position at the CNRS and in Zürich, and I hope we will continue our cooperation in the future.

Een grote rol heeft ook Rick Bethlem gespeeld. Zijn soms wat speciale kijk op dingen dwingt je

ertoe net wat dieper over een probleem na te denken, zodat er uiteindelijk meer inzicht uitrolt. Rick, we verschillen in heel veel dingen, maar het enthousiasme in het manipuleren van molekulen hebben we gemeen. Ik heb heel veel van je geleerd, en onze vele discussies over fase stabiliteit hebben twee prachtige artikelen opgeleverd. Mede-oio's van het eerste uur Floris en Jacqueline, en alle andere collega's in het lab, bedankt voor alle kleine en grote hulp. Mark van der Loo en Gerrit Groenenboom, bedankt voor de berekening van de levensduur van vibrationeel geëxciteerd OH, en de samenwerking bij het schrijven van de PRL hierover. I thank Irena Labazan for our cooperation on the production of pulsed beams of metastable NH, and Boris Sartakov for the many calculations of transitions in OH and NH. Jochen, thanks for synthesizing HN_3 molecules, for solving many of my computer problems, and for lots of general support. Een korte tijd heeft Allard Mosk me begeleid. Allard, bedankt voor de samenwerking, en voor het weer tot leven brengen van een bijna gestorven ring-dye-laser. Jürgen, vielen Dank für deine Hilfe beim Aufbau der Maschine in Nieuwegein und später beim Wiederaufbau in Berlin. Lou, bedankt voor het ontwerp van de omslag. En zonder de met prijzen omhangen Joost Bakker zijn het lab en de Berlijnse Biergärten een stuk minder kleurrijk en gezellig. Familie en vrienden, bedankt voor de steun en de vele gezellige weekendjes.

Ik ben enorm trots dat ik een bijdrage heb kunnen leveren aan de ontwikkeling van ons lab van een klein damestoilet in Nijmegen tot ons hypermoderne nieuwe lab vol glimmende afremmers in Berlijn. En met opvolgers als Joop Gilijamse en Steven Hoekstra ben ik ervan overtuigd dat die ontwikkeling alleen nog maar sneller zal gaan.

Bas van de Meerakker
Berlijn, oktober 2005

Contents

1	General introduction	1
1.1	Ultimate control over the velocity of gas-phase molecules	1
1.2	Applications of cold molecules	2
1.3	Production of cold molecules	4
1.3.1	Buffer-gas cooling	4
1.3.2	Association of cold atoms	4
1.3.3	Other techniques	5
1.4	Stark deceleration of a molecular beam	5
1.4.1	Previous work using Stark decelerators	6
1.4.2	This thesis	8
1.5	Outline	9
2	The OH radical and the molecular Stark effect	11
2.1	The energy level structure of OH	11
2.1.1	The electronic ground state	11
2.1.2	The first electronic excited state	13
2.1.3	The $A \leftrightarrow X$ transition	13
2.2	Production of a molecular beam of OH radicals	14
2.3	The molecular Stark effect	16
2.3.1	General formalism	16
2.3.2	Matrix elements of H_{Stark}	17
2.3.3	Diatomic molecules; the Stark effect of OH	19
2.3.4	Hyperfine structure of OH	20
2.3.5	Symmetric and asymmetric tops	20
2.4	Candidate molecules for Stark deceleration	21
3	A new generation Stark decelerator	25
3.1	Introduction	26
3.2	Longitudinal motion	26
3.2.1	Phase stability	26
3.2.2	Equation of motion	27
3.3	Experimental set-up	29
3.4	Experimental results	35
3.4.1	Guiding a molecular beam of OH radicals	35
3.4.2	Deceleration of a molecular beam of OH radicals	38
3.4.3	Evolution of the beam through the Stark decelerator	40
3.4.4	Simultaneous deceleration of both $M_J\Omega$ components	43
3.5	Conclusions	46

4	Higher-order resonances in a Stark decelerator	47
4.1	Introduction	48
4.2	Theory	48
4.2.1	Phase stability	48
4.2.2	First order resonances, $n = 1$	50
4.2.3	First-order resonances, $n > 1$	51
4.2.4	Numerical simulations	53
4.2.5	Second-order resonances	56
4.2.6	Summary	60
4.3	Experiment	61
4.3.1	Experimental set-up	61
4.3.2	First-order resonances	61
4.3.3	Second-order resonances	65
4.3.4	Molecular beam modulation	66
4.4	Conclusions	69
5	Transverse stability in a Stark decelerator	71
5.1	Introduction	72
5.2	Longitudinal phase stability	72
5.3	Transverse stability	73
5.3.1	Transverse motion	73
5.3.2	Longitudinal phase stability; 3D versus 1D	76
5.3.3	Effective phase angle	79
5.3.4	Transverse stability	80
5.3.5	Transverse equation of motion, $\phi_0 = 0^\circ$	82
5.3.6	Higher-order resonances	86
5.4	Experiment	89
5.4.1	High phase angles; $\phi_0 = 90^\circ$	89
5.4.2	Low phase angles; $\phi_0 = 0^\circ$	90
5.5	Conclusions	94
6	Electrostatic trapping of OH radicals	97
6.1	Introduction	98
6.2	Experiment	98
6.2.1	The experimental set-up	98
6.2.2	Deceleration and trapping experiments	98
6.2.3	Trap-loading characterization	103
6.3	Conclusions and outlook	105
7	Direct measurement of the radiative lifetime of vibrationally excited OH radicals	107
7.1	Introduction	108
7.2	Experiment	109
7.3	Conclusions	112

8	Accumulating NH radicals in a magnetic trap	113
8.1	Introduction	114
8.2	Accumulation scheme	115
8.3	Optical pumping of NH ($a^1\Delta$) radicals into the $X^3\Sigma^-$ state	118
8.3.1	Experiment	118
8.3.2	Characterization of the molecular beam	119
8.3.3	The $A^3\Pi \leftarrow a^1\Delta$ transition	120
8.3.4	The strength of the $A^3\Pi \leftarrow a^1\Delta$ transition	125
8.4	A slow pulsed molecular beam of NH ($a^1\Delta$) radicals	126
8.5	Deceleration of a molecular beam of NH ($a^1\Delta$) radicals	128
8.6	Conclusions	129
	Summary and outlook	131
	Bibliography	133
	Samenvatting	145
	Curriculum Vitae	151
	List of publications	152

CHAPTER 1

GENERAL INTRODUCTION

During the last three centuries, it has been gradually realized that molecules are the building blocks of our environment. Since the 19th century, it is generally accepted that molecules are built up out of atoms. Since then, molecular physics has rapidly developed into a seminal field of physics. Detailed knowledge of molecules and their interactions is a prerequisite for understanding many chemical and biological processes. It is the goal of the experimental molecular physicist to study the inherent properties of molecules and their interactions in the most detail, and under well controlled (and sometimes exotic) conditions. Gas-phase molecules are ideally suited for that as the interaction of the molecules with their environment is absent. In addition, these isolated samples allow the study of chemically unstable species like radicals. This thesis describes a method to obtain ultimate kinematic control over the chemically very relevant OH radical.

1.1 Ultimate control over the velocity of gas-phase molecules

Getting ever better control over both the internal and external degrees of freedom of gas-phase molecules has been an important theme in molecular physics during the last decades. Molecular beams, both continuous and pulsed, are used throughout to produce large densities of molecules in selected quantum states [1]. In these beams, the longitudinal temperature of the molecules is typically 1 K. State selection of a beam of polar molecules, and control over the orientation of the molecules in space, can be achieved by actively manipulating the transverse motion of the molecules using electrostatic or magnetic multipole fields as well as with the help of laser radiation [1–3]. Sophisticated and powerful detection schemes have been developed to experimentally study (half-) collisions [4, 5] and reactions [6, 7] of the thus prepared molecules in the required detail. Molecular beams have therefore been indispensable in a number of research areas such as molecular (reactive) scattering studies, high resolution spectroscopy, surface science, as well as, for instance, for the production and investigation of transient species. Until recently, it was difficult to obtain full control over the longitudinal motion of molecules in a molecular beam. The mean velocity of the beam can be varied by adjusting the temperature of the source or by using different seed gases, allowing to produce beams in the 250 – 3000 m/s range. However, more precise control over the longitudinal motion, i.e., the ability to vary the velocity(distribution) of the beam to any desired value was not possible until the development of the so-called Stark deceleration technique. The Stark decelerator for neutral polar molecules

is the equivalent of a linear accelerator (LINAC) for charged particles. In a Stark decelerator, the quantum-state specific force that a polar molecule experiences in an electric field is exploited. This force is rather weak, typically some eight to ten orders of magnitude weaker than the force that the corresponding molecular ion experiences in the same electric field. This force nevertheless suffices to achieve complete control over the motion of polar molecules, using techniques akin to those used for the control of charged particles. This has been explicitly demonstrated by the construction of two types of linear accelerators [8, 9], a buncher [10], two types of traps [11, 12] and a storage ring [13] for neutral polar molecules.

With the Stark decelerator, a part of a molecular beam can be selected and transferred to an arbitrary velocity, producing bunches of state-selected molecules with a computer-controlled velocity and with longitudinal temperatures as low as a few mK [14, 15]. When the Stark decelerator is combined with an electrostatic trap, bunches of state-selected polar molecules with a temperature on the order of 10 mK can be confined up to seconds. These experiments are of particular interest to the field of cold molecules, as the Stark deceleration technique is one of the few techniques that offers the possibility to confine ground-state molecules in a trap. In this thesis, a new generation Stark decelerator and electrostatic trap is presented, that allows the deceleration and electrostatic trapping of OH radicals.

1.2 Applications of cold molecules

Interest in the field of cold molecules is triggered by various potential applications and by the promise of the occurrence of interesting new physics (and chemistry!) at the low temperatures and high densities that can ultimately be achieved. Recently, extensive reviews of the applications of (polar) cold molecules, and their production techniques, have been given [15–17]. Only a brief summary of a selection of these applications is given in this section. In section 1.3, the currently available cold molecule production techniques are briefly discussed.

The resolution in a spectroscopic experiment can greatly benefit from the improved interaction time that trapped molecules offer. Cooling and confinement of molecules in the mK range improves the attainable resolution by orders of magnitude compared to thermal molecules. This is generally important to study the molecules in the most detail, but this also holds great promise for the use of cold molecules in metrology, and, for instance, in experiments aimed at testing fundamental symmetries. For instance, it is expected that the most sensitive measurement of a possible electric dipole moment (EDM) of the electron will be performed on a polar molecule, because of the large enhancement of electric fields inside the molecule. The existence of an EDM would have profound consequences for the evolution of the Universe, and would put the Standard Model to test [18]. The molecules YbF and PbO are of particular interest for this [19, 20]. The improved resolution can also be used to study the difference in the spectra between two enantiomers of a chiral molecule, that could be a manifestation of the weak interaction in molecules [21, 22]. This could explain the imbalance between 'left-handed' and 'right-handed' amino-acids in biochemical systems. Precise measurements of ro-vibrational transitions in molecules that have a strong dependence on the proton-electron mass ratio (m_p/m_e), could be used to measure a possible time dependence of fundamental constants, which would be a consequence of the expansion of the Universe [23]. Apart from the obvious benefits in

high-resolution spectroscopy, the long interaction times allow the direct measurement of the lifetime of an electronically or vibrationally excited state. With conventional molecular beam techniques, the determination of these lifetimes is limited to a few milliseconds. By measuring the temporal decay of the population of vibrationally excited OH radicals in an electrostatic trap, we recently obtained an accurate value for the Einstein A -coefficient of the fundamental $1 - 0$ band of OH [24]. This measurement benchmarks the infrared radiative properties in the Meinel system of OH, that is of particular atmospheric and astrophysical importance [25–28]. This experiment is described in detail in chapter 7 of this thesis.

When particles are brought to (ultra)-low temperatures, the de Broglie wavelength that is associated with the wave character of the particles can become comparable to, or even larger than, the inter-particle separation. In this exotic regime, interesting phenomena can be expected that are governed by quantum physics, and that are foreign to processes that take place at higher temperatures. In this respect, the ability to cool and slow *atoms* with light for subsequent trapping has led to exciting and sometimes unforeseen results, and the payoffs have included atom interferometry, precision spectroscopy, Bose-Einstein condensation, and the formation of atom lasers [29–32]. Laser-cooling and the techniques to cool the atoms further have revolutionized atomic physics over the last two decades. Methods to cool and trap molecules have the potential to do the same for molecular physics. Molecules would add extra dimensions to these experiments as they can be prepared in a wide variety of selected rotational and vibrational quantum states and as they can be spatially oriented. Arguably one of the most interesting properties of molecules that are foreign to atoms is that a molecule can possess a permanent electric dipole moment. Ultra-cold polar molecules are therefore currently at the center of theoretical and experimental interest. The anisotropic dipole-dipole interaction in a molecular Bose-Einstein Condensate (BEC) is predicted to give the molecular condensate new and intriguing properties. If the dipoles are oriented head-to-tail, the long-range dipole-dipole interaction is attractive, while this interaction is repulsive for oriented dipoles in lateral geometry. In a polarized bosonic gas, the stability of the BEC therefore depends on the geometry of the trap [33]. By changing the geometry of the trap, one has the possibility to tune the interactions in the gas, offering new possibilities to engineer macroscopic quantum states [34]. Further, the use of trapped dipolar molecules in an optical lattice has been proposed to study exotic quantum phase transitions [35], as well as for quantum computation [36].

The study of chemistry at ultra low temperatures is another exciting avenue. Cooling molecules to (ultra)-low temperatures gives access to an exotic regime for chemical reactivity, governed by quantum tunnelling and resonances [37, 38]. Interesting effects are predicted to occur for collisions at small collision energies. The elastic and in-elastic cross sections show sharp resonances at these energies [39]. Unusual resonant states can be formed when the colliding molecules begin to rotate, leaving them with insufficient translational energy to overcome their van der Waals attraction, effectively binding the molecules transiently together. The slow (or trapped) molecules produced by a Stark decelerator are particularly amenable to these kind of experiments. In a molecular (reactive) scattering experiment using crossed Stark-decelerated molecular beams of identical or different species, for instance, the scattering process can be studied as a function of the collision energy, probing the potential energy surface with unprecedented detail. These new kinds of experiments are complementary to conventional spectroscopy of collision complexes, and to molecular beam scattering experiments

which are commonly performed at relatively high collision energies.

1.3 Production of cold molecules

Unfortunately, the complex structure of molecules has thus far prohibited the type of laser manipulation that has been so crucial for the success in the field of cold atoms. Therefore, cooling and trapping of molecules has proven to be a daunting experimental task. Only in 1998 the first trapping of molecules has been demonstrated, almost 15 years later than the first trapping of atoms. To date, various techniques have been explored to cool molecules, of which a few have been successful in the trapping of molecules. In the next sections, a brief review of (most) of these methods is given. The technique that is used in this thesis to trap OH radicals, the method of Stark deceleration of a molecular beam, will be discussed in more detail in section 1.4.

1.3.1 Buffer-gas cooling

With cryogenic techniques using He, temperatures well below 1 K can be reached. At temperatures of a few hundred mK, He still has a reasonable vapor pressure, high enough to be used as a buffer gas. When high-temperature atoms or molecules are introduced in the cryogenic cell, the atoms or molecules can thermalize via collisions with the buffer gas. If paramagnetic atoms or molecules are used, they can be trapped at the center of a super-conducting magnetic trap that is super imposed with the cryogenic cell. This method has been developed by Doyle at Harvard (Cambridge, USA) [40, 41], and the buffer-gas cooling and magnetic trapping of various atoms has been demonstrated. In 1998, the technique was used to achieve the first trapping of neutral molecules. A plume of gaseous CaH molecules was produced via laser-ablation from a solid target inside the cell, and about 10^8 CaH molecules in the ro-vibrational ground state could be trapped at a density of around 10^8 molecules/cm³ and at a temperature of 400 mK [42]. In principle, buffer-gas cooling and magnetic trapping can be applied to any paramagnetic molecule, provided that the ratio between the elastic and inelastic cross sections of the molecule of interest with He is favorable to allow thermalization. In view of this, the technique can most likely not be applied to OH radicals [43], although OH possesses a significant magnetic dipole moment. The buffer-gas cooling technique has been combined with atomic and molecular beam techniques, to take full advantage of the superior number densities that are available in these beams [44]. Recently, a molecular beam of NH ($X^3\Sigma^-$) radicals was loaded into the buffer gas. Although the trapping has not been achieved yet, up to 10^{12} molecules from the beam could be buffer-gas cooled to temperatures below 6 K [45].

1.3.2 Association of cold atoms

The difficulty associated with the cooling of molecules can be circumvented if molecules are associated from its atomic constituents that are (ultra)cold. This can be done either with the help of a photon (photo-association), with the help of a scattering resonance that is tuned with a magnetic field (Feschbach-resonance association), or by three-body recombination of cold atoms. Spectacular progress has been made in these fields in recent years. Photo-association has been used to produce various ultra-cold alkali-dimers, of which in some cases the molecules could be trapped [46, 47]. Most recently, the heteronuclear polar alkali-diatomics RbCs [48, 49], NaCs [50] and KRb [51, 52]

have been produced. These molecules can be translationally as cold as the atoms, but they are usually produced in highly-excited vibrational levels of an excited electronic state, although in some cases schemes have been developed to produce molecules in lower vibrational levels of the electronic ground state [53]. Molecules can be photo-associated in an atomic Bose-Einstein Condensate as well, providing the possibility to convert an atomic condensate into a molecular condensate. The conversion of a quantum degenerate gas of ultra-cold fermionic atoms into a gas of ultra-cold bosonic molecules by scanning an external magnetic field over a Feshbach resonance has allowed for the first observation of a molecular Bose-Einstein condensate [54–57]. However, Feshbach-resonance association is thus far limited to produce homonuclear alkali-dimers, although Feshbach resonances have been found in Li-Na [58] and in K-Rb [59] collisions. These could potentially be used to produce ultra-cold, or quantum degenerate, polar molecules.

1.3.3 Other techniques

In addition to the techniques described in the previous sections, cold molecules can be produced in a number of other ways. Among these are billiard-like collisions in crossed molecular beams [60], cooling of a beam by mechanical means using a counter-rotating nozzle [61], or velocity filtering of a thermal effusive molecular beam [62, 63]. However, these techniques have not resulted yet in the three-dimensional trapping of cold molecules.

1.4 Stark deceleration of a molecular beam

Analogous to the transverse focussing of a molecular beam using transversally inhomogeneous electric fields, the longitudinal velocity of a beam of polar molecules can be changed using longitudinally inhomogeneous electric fields. The longitudinal velocity of a molecular beam is typically too large, however, to enable a significant change of the velocity in experimentally attainable electric fields. In addition, as the molecule leaves the region of high field, the velocity change is cancelled. If, however, *time-varying* inhomogeneous electric fields are used, this situation can be avoided. When the electric field is reduced before the molecule has left the region of high electric field, the velocity of the molecule will not return to its original value, and can therefore be permanently changed. When this process is repeated using multiple electric field stages, the longitudinal velocity of the beam can be changed to any desired value. This idea was already considered in the late 1950's and 1960's [64–68]. Although even large-scale efforts were then undertaken, the deceleration or acceleration of polar molecules could not be demonstrated [69–71], mainly due to lack of flexibility of the constructed machines. In recent years our group has successfully developed the so-called Stark deceleration technique. For the first time, the deceleration of neutral polar molecules using time-varying inhomogeneous electric fields could be demonstrated [8]. The development of fast semiconductor high-voltage switches allows the use of an array of high-voltage electrodes that are equally spaced, greatly improving the flexibility of the device. In addition, the advent of pulsed supersonic molecular beams provides a source of high densities of molecules distributed over only a small number of internal quantum states and with a narrow velocity distribution, that is ideal to be injected in the decelerator. By employing a properly chosen sequence of switch times, the final velocity of the beam can be selected. Pulsed molecular beams with a computer-controlled velocity and with a narrow velocity distribution can thus be produced. This will be of advantage in any molecular beam experiment where the velocity, or

velocity distribution, of the molecules is an important parameter.

1.4.1 Previous work using Stark decelerators

The possibility to decelerate a beam of neutral polar molecules with an array of time-varying inhomogeneous electric fields was first demonstrated by Bethlem, Berden and Meijer in 1999 [8]. In this work, a small part of a pulsed beam of CO molecules in their metastable $a^3\Pi$ state was slowed down from 225 m/s to 98 m/s using a 35 cm long Stark decelerator that consisted of 63 electric field stages. The similarity of the Stark decelerator for neutral molecules with a LINAC for charged particles, and in particular the demonstration that molecular motion through the Stark-decelerator is also governed by the concept of phase-stability, was demonstrated one year later, again using a beam of metastable CO molecules [72]. This is important as it clearly demonstrates the potential of the Stark decelerator for transferring the high initial phase-space density of molecules in the appropriate quantum state that is present in a molecular beam to any desired laboratory velocity, without loss. In the year 2000, the same decelerator that was used in the CO experiments was then used to decelerate ground-state ND₃ molecules to a standstill, and to subsequently trap these molecules in a quadrupole electrostatic trap [11]. A more detailed description of the Stark decelerator and the trap loading process was published two years later [14]. Meanwhile, an electrostatic storage ring, that allows the confinement of a slow molecular packet in two dimensions, was designed and constructed. In this prototype storage ring, packages of ammonia molecules, travelling with a velocity of about 100 m/s, could be observed up to six round trips [13]. A buncher, an element that allows to longitudinally focus a molecular beam (either spatially or in velocity space) was developed, and was used to spatially focus a decelerated beam of deuterated ammonia, as well as to create a molecular beam with a record-low longitudinal temperature of 250 μ K [10]. Recently, this buncher has been installed between the Stark decelerator and the storage ring to enable the injection of colder packages in the ring; the number of observable round trips could be increased to more than 50 [73]. A second Stark decelerator that is identical to the initial design but with an increased number of 95 deceleration stages, was constructed to demonstrate the improved spectroscopic resolution that can be obtained when using Stark decelerated molecular beams [74]. After deceleration of a beam of ND₃ to about 50 m/s, the spectral width of individual hyperfine transitions, determined by transit-time broadening in the 6.5 cm long microwave interaction zone, could be reduced to about 1 kHz. The hyperfine structure on the inversion doubling transition in the $|J, K\rangle = |1, 1\rangle$ state of ¹⁵ND₃ could be completely resolved and analyzed. This method has also been used to produce slow ¹⁵ND₃ molecules in the high-field seeking $|J, K\rangle = |1, 1\rangle$ state that could subsequently be trapped in an AC electric field trap [12]. This is the first trap of its kind for molecules in their absolute ground state. The strong dipole-dipole interaction between polar molecules is predicted to lead to high trap loss rates if the molecules are electrostatically trapped in a low-field seeking state [75], and the development of the AC trap is therefore expected to be essential for the demonstration of evaporative cooling. The manipulation of polar molecules using miniaturized electrode geometries and only modest voltages has been investigated as well. In a proof-of-principle experiment, a beam of ammonia molecules was retro-reflected from a planar array of 20 μ m wide gold electrodes, spaced 20 μ m apart, on a sapphire substrate [76]. With a voltage difference of only 350 V between adjacent electrodes, the microstructure acts as a flat mirror for ND₃ molecules with a velocity as high as 30 m/s.

All molecular beam deceleration experiments described above, have been performed with molecules in so-called low-field seeking states, i.e., molecules that experience an appreciable positive

Stark shift in experimentally attainable electric fields. Although this covers a relatively large class of polar molecules, many interesting molecules, in particular large or massive polar molecules, exclusively exhibit high-field seeking states. In addition, the absolute ground-state of any polar molecule is high-field seeking. Deceleration of molecules in a high-field seeking state in the Stark decelerator is in principle straightforward, but the molecules are attracted to the region where the fields are the highest. Therefore, high-field seeking molecules have the tendency to crash into the electrodes. An electrode geometry that produces a maximum of electric field in three dimensions, required to solve this fundamental problem, is not possible (Earnshaw's theorem). A scheme that is well known from charged particle accelerator physics, where the same principle difficulty exists, can be used to advantage, however. By alternately focussing and defocussing molecules in each transverse direction, a net overall focussing of a beam of molecules in a high-field seeking state can be obtained. A prototype of an alternating gradient (AG) decelerator with only 12 electric field stages has been constructed to demonstrate focussing and deceleration of metastable CO molecules in a high-field seeking state [9] in 2002. A mechanically improved version of this decelerator has subsequently been used to decelerate a beam of YbF molecules [77]. As mentioned earlier, YbF is of particular interest because it offers one of the most sensitive ways to search for elementary particle physics beyond the Standard Model through a measurement of the electric dipole moment of the electron [19]. By using a decelerated molecular beam, the precision with which this quantity can be measured can be greatly enhanced. When sufficient electric field stages are employed in these decelerators, in principle the molecules can be decelerated to rest. In combination with the AC electric trap discussed before [12], potentially *any* polar molecule, including bio-molecules, could then be decelerated and trapped.

Since the introduction of the Stark-decelerator in 1999, various research groups have followed this experimental approach with the aim to produce samples of cold molecules. Of these, the group of Jun Ye at JILA in Boulder, USA, has successfully implemented the method in recent years. Using a design that is identical to the original design of the decelerator, the possibility to manipulate the phase-space distribution of OH radicals in a Stark decelerator was demonstrated [78]. Although electrostatic trapping was not reported, the deceleration of part of a beam of OH radicals from 385 m/s to 58 m/s was shown [79]. The decelerator has also been used to decelerate a beam of H₂CO molecules. The group of Tiemann and Lisdat in Hannover, Germany, are constructing a (long) Stark decelerator with the aim to decelerate a beam of SO₂ molecules, to subsequently produce slow SO radicals via photodissociation [80]. Another Stark decelerator is currently under construction in the group of Softley in Oxford, UK. A long decelerator of the AG type with the aim to decelerate YbF molecules to rest has just been completed in the group of Hinds and Tarbutt at Imperial College in London, UK, and has been used to decelerate CaF and YbF molecules.

Inspired by the manipulation of polar molecules in a Stark decelerator, studies on the manipulation of atoms and molecules in high Rydberg states with electric fields were recently performed. Compared to the polar molecules used in a Stark decelerator, atoms or molecules in a Rydberg state offer a much larger electric dipole moment. Hence, these particles can be efficiently manipulated using only modest electric field strengths in a single, or a few electric field stages. These methods have been pioneered using H₂ molecules [81] and Ar atoms [82]. Sophisticated schemes in which the electric field continuously follows the motion of the particles, and hence allow phase-stable deceleration, have been proposed as well [83]. The disadvantages of these decelerators are that the atoms or molecules

need to be prepared in the Rydberg states using sophisticated laser systems, and that the lifetime of the Rydberg states severely limits the time that is available to bring the molecules to rest and to store them in a trap.

The interaction of polar molecules with an electric field has also been exploited in schemes to filter out the slow molecules from a thermal gas. Using a linear electrostatic quadrupole guide with a curved section, samples of slow H_2CO and ND_3 molecules, in a large number of quantum states, have been selected from the low-velocity tail of a Maxwellian distribution of a room-temperature effusive source [62]; a successful reincarnation of the Zacharias fountain [84]. More recently, AC voltages have been applied to the guide to (in principle) select ND_3 molecules in both low-field seeking and high-field seeking states [63].

An optical analogue of the Stark decelerator has been developed as well [85, 86]. In this scheme, the interaction of polarizable molecules with a high-intensity pulsed optical lattice, produced by two counter-propagating laser beams, is utilized. By chirping one of the beams, the lattice velocity can be reduced from the mean velocity of a molecular beam to any desired final velocity. In a recent proof-of-principle experiment, a single stage optical Stark decelerator has been used to reduce the velocity of a beam of benzene molecules from 320 m/s to 295 m/s [87].

1.4.2 This thesis

In principle, the technique of Stark deceleration can be applied to any polar molecule that experiences a positive Stark shift in an applied electric field. Thus far, in their low-field seeking state, beams of metastable CO molecules [8], various isotopomers of NH_3 [14], H_2CO molecules and ground-state OH radicals [78, 79] have been decelerated. These experiments are performed using Stark decelerators that can only select and decelerate a relatively small fraction of a molecular beam. To be able to exploit the possibilities that these slow molecular beams offer, the fraction of the pulsed molecular beam that is decelerated and/or trapped needs to come closer to unity, i.e., the 6-dimensional phase space acceptance of the various elements needs to be increased to better match to the typical emittance of a molecular beam. In addition, for collision and reactive scattering experiments, the deceleration and trapping needs to be performed on those molecules that are chemically most relevant; thus far, the electrostatic trapping after Stark deceleration has only been demonstrated for ND_3 molecules [11, 14]. In this thesis, progress is reported in both fields. A molecular beam of ground state OH ($X^2\Pi_{3/2}, J = 3/2$) radicals is decelerated and electrostatically trapped, using a new generation molecular beam deceleration and trapping machine, that is designed such that a large fraction of the molecular beam pulse can be slowed down and trapped [88]. The trapped OH radicals are subsequently used to directly measure the radiative lifetime of the first vibrationally excited state [24].

The role of the omnipresent OH radical as intermediate in many chemical reactions, and in particular its major importance to astrophysical [89], atmospheric [25] and combustion [90] processes, has made this a benchmark molecule in collision and reactive scattering studies [91]. The ability to decelerate and/or to confine OH radicals in a trap offers the possibility to study these processes with unprecedented detail. Therefore, the interaction between OH radicals at (ultra)low temperatures and its implications for (ultra)low temperature chemistry is currently at the center of theoretical interest [92]. Indeed, theoretical investigations predict fascinating processes to occur that are foreign

to collisions at higher temperatures. In particular, in the presence of an electric field, the long-range dipole-dipole interaction between two OH radicals generates a shallow potential that supports bound states of the excited $[\text{OH}]_2$ dimer [93, 94]. The existence of these so-called field-linked states depends very critically on the value of the field strength, offering the unique possibility to control the collision process by varying the electric field strength. As the OH radical possesses a relatively large magnetic dipole moment, it can in principle be magnetically trapped as well [95]. This leaves the electric field strength as a free parameter to control the collision process [78]. The Stark deceleration and electrostatic trapping technique can also be used to confine fermionic OD radicals, in which case inelastic collisions between the trapped molecules that lead to trap loss are suppressed [96]. The samples of electrostatically trapped OH radicals reported in this thesis are ideally suited to investigate cold collisions between OH radicals and the processes mentioned above.

In addition, the new generation Stark decelerator developed in this work allows the motion of the molecules through the Stark decelerator to be studied with unprecedented detail. In particular, hitherto unobserved or uncharacterized features in the observed time-of-flight profiles of molecules exiting the decelerator have revealed the complex phase-space evolution of the beam as it progresses through the decelerator. By a careful comparison of these time-of-flight profiles with numerical simulations, a more complete description of the phase stability in a Stark decelerator has been obtained. Apart from contributing significantly to the understanding of a Stark decelerator, these new insights will beyond doubt contribute to the efficiency of future Stark decelerators.

1.5 Outline

This thesis is organized as follows. In chapter 2 the spectroscopy of the OH radicals, the production methods of OH in a molecular beam and the interaction of OH with an externally applied electric field is discussed. The new generation Stark decelerator is described in chapter 3, and the deceleration of a molecular beam of OH radicals is demonstrated. In addition, a detailed discussion of the evolution of the beam as it progresses through the Stark decelerator is given. In chapter 4, the model for phase stability (the operation principle of a Stark decelerator) is refined using different levels of approximation. The extended model for phase stability predicts a wide variety of additional phase stable regions in a decelerator, that are experimentally verified. A second extension of the model for phase stability is presented in chapter 5. In this chapter, the influence of the transverse motion of the molecules on phase stability is studied. In the experiments described in chapter 6, the Stark decelerator is extended with an electrostatic quadrupole trap. A beam of OH radicals is decelerated and subsequently confined in the trap and stored for times up to seconds. The long interaction time that the trap offers is exploited in the experiments described in chapter 7. After optical preparation of the OH radicals in the $X^2\Pi_{3/2}, v = 1, J = 3/2$ level prior to deceleration and trapping, the radiative lifetime of this state is measured by monitoring the temporal decay of the population in the trap. Finally, in chapter 8, a novel scheme is presented that allows the accumulation of successive pulses of molecules in a trap in order to increase the phase-space density of the trapped gas. This scheme specifically works for the NH radical, and all prerequisites for this proposed accumulation scheme are experimentally demonstrated.

CHAPTER 2

THE OH RADICAL AND THE MOLECULAR STARK EFFECT

For the manipulation of OH radicals with electric fields, a good understanding of the energy level structure and the interaction of OH with an external electric field is required. In this chapter a detailed discussion of the spectroscopy and the Stark effect of OH is given.

2.1 The energy level structure of OH

2.1.1 The electronic ground state

The OH molecule possesses 9 electrons. In the united atom picture this leads to an electron configuration for the electronic ground state of $(1s\sigma)^2(2s\sigma)^2(2p\sigma)^2(2p\pi)^3$. The $(2p\pi)$ shell has one electron short to fill the shell completely. This open shell structure results in a nonzero total electronic orbital (\vec{L}) and spin (\vec{S}) angular momentum. The projections of \vec{L} and \vec{S} on the internuclear axis are $\Lambda = \pm 1$ and $\Sigma = \pm 1$ respectively, with the corresponding term symbol $X^2\Pi$ for the electronic ground state. For low rotational states, the OH molecule is best described by the Hund's case (a) coupling scheme [97]. In this scheme, Λ and Σ couple to form the total electronic angular momentum along the internuclear axis Ω : $\Omega = \pm 1/2$ and $\Omega = \pm 3/2$. The $^2\Pi$ electronic ground state consists of two spin-orbit manifolds: the $^2\Pi_{1/2}$ manifold with $|\Omega = 1/2|$ and the $^2\Pi_{3/2}$ manifold with $|\Omega = 3/2|$. The $^2\Pi_{3/2}$ and the $^2\Pi_{1/2}$ manifolds are also designated as the F_1 and F_2 manifolds, respectively. The angular momentum vector \vec{R} of the end-over-end rotation of the nuclei couples to $\vec{\Omega}$ to give the rotational angular momentum vector \vec{J} :

$$\vec{J} = \vec{L} + \vec{S} + \vec{R}. \quad (2.1)$$

By definition, the projection of \vec{R} onto the internuclear axis is zero, and hence the projection of \vec{J} onto the internuclear axis is given by Ω . The total orbital rotational quantum number \vec{N} is defined as $\vec{N} = \vec{R} + \vec{L}$. The rotational structure and wavefunctions can be obtained from the rotational Hamiltonian [98]

$$H_{rot} = B_v(\vec{J} - \vec{L} - \vec{S})^2 + A_v\vec{L} \cdot \vec{S}. \quad (2.2)$$

The first term of H_{rot} represents the rotational part of the Hamiltonian, and the second part represents the spin-orbit coupling. The rotational constant B_v and the spin-orbit constant A_v depend on

the vibrational quantum number v . For the vibrational ground state these constants take the values 18.515 cm^{-1} and -139.73 cm^{-1} [99], respectively. As the spin-orbit coupling constant is negative, the ${}^2\Pi_{3/2}$ state is lower in energy than the ${}^2\Pi_{1/2}$ state. For diatomics the Hamiltonian can be evaluated on the rigid body rotational basis wavefunctions [98]

$$|J\Omega M_J\rangle = \sqrt{\frac{2J+1}{8\pi^2}} \mathcal{D}_{\Omega, M_J}^{J*}(\phi, \theta, 0), \quad (2.3)$$

where $\mathcal{D}_{\Omega, M_J}^{J*}(\phi, \theta, 0)$ is the Wigner function, describing the molecular rotation in terms of the Euler angles ϕ and θ . The projection of \vec{J} on an external quantization axis (for instance given by the direction of an electric field) is called M_J , which can take the values $-J, -J+1, \dots, J$. When no external quantization axis is present, each rotational level is degenerate in M_J . It is convenient to use a basis set of symmetrized wavefunctions with definite parity that can be written as linear combinations of the wavefunctions $|J\Omega M_J\rangle$:

$$|J\Omega M_J \epsilon\rangle = \frac{1}{\sqrt{2}} (|J\Omega M_J\rangle + \epsilon |J - \Omega M_J\rangle), \quad (2.4)$$

with $\epsilon = \pm 1$. The relation between the parity p and symmetry ϵ of the wavefunction is given by [98]

$$p = \epsilon(-1)^{J-S}. \quad (2.5)$$

The spin-orbit term in the hamiltonian H_{rot} mixes basis wavefunctions with different values of Ω . The resulting eigenfunctions of H_{rot} are given by [100]

$$\begin{aligned} |{}^2\Pi_{3/2}, JM_J \epsilon\rangle &= C_1(J) |J, \Omega = 1/2, M_J \epsilon\rangle + C_2(J) |J, \Omega = 3/2, M_J \epsilon\rangle \\ |{}^2\Pi_{1/2}, JM_J \epsilon\rangle &= -C_2(J) |J, \Omega = 1/2, M_J \epsilon\rangle + C_1(J) |J, \Omega = 3/2, M_J \epsilon\rangle. \end{aligned} \quad (2.6)$$

The mixing coefficients $C_1(J)$ and $C_2(J)$ are given by

$$\begin{aligned} C_1(J) &= \sqrt{\frac{X+Y-2}{2X}} \\ C_2(J) &= \sqrt{\frac{X-Y+2}{2X}} \end{aligned} \quad (2.7)$$

with X and Y given by

$$\begin{aligned} X &= \sqrt{4\left(J + \frac{1}{2}\right)^2 + Y(Y-4)} \\ Y &= \frac{A_v}{B_v}. \end{aligned} \quad (2.8)$$

From these expressions it follows that, for low values of J , the degree of mixing is low, and Ω is almost a good quantum number. The energies $E({}^2\Pi_{\Omega}, J\epsilon)$ of the rotational levels in the ${}^2\Pi_{\Omega}$ manifolds, when no external fields are present, are

$$\begin{aligned} E({}^2\Pi_{3/2}, JM_J \epsilon) &= B_v \left[\left(J + \frac{1}{2}\right)^2 - 1 - \frac{1}{2}X \right] \\ E({}^2\Pi_{1/2}, JM_J \epsilon) &= B_v \left[\left(J + \frac{1}{2}\right)^2 - 1 + \frac{1}{2}X \right]. \end{aligned} \quad (2.9)$$

Up to this point, the rotational levels for which $\epsilon = +1$ and $\epsilon = -1$ within each rotational level labelled by J are degenerate. This degeneracy is lifted if second order effects in the Hamiltonian are taken into account. These effects originate from the gyroscopic effect of \vec{J} on \vec{S} and \vec{L} [101]. These additional terms in the Hamiltonian result in non-zero matrix elements off-diagonal in Λ , introducing a mixing between the electronic ground state ${}^2\Pi$ and the first electronically excited state ${}^2\Sigma^+$. Consequently, within each manifold, the rotational levels corresponding to $|{}^2\Pi_\Omega, JM_J\epsilon = +1\rangle$ and $|{}^2\Pi_\Omega, JM_J\epsilon = -1\rangle$ split into two components to form a so-called Λ -doublet. The Λ -doublet splitting is very small compared to the rotational spacing; for the ${}^2\Pi_{3/2}, J = 3/2$ state that is most relevant to the experiments described in this thesis, the splitting is only 0.05 cm^{-1} [102, 103]. For low values of J , the components with $\epsilon = +1$ are lower in energy than components with $\epsilon = -1$ [104].

Following the convention used in modern spectroscopic literature, the levels with $\epsilon = +1$ and $\epsilon = -1$ are designated with the spectroscopic symmetry labels e and f , respectively. The e/f only refers to the total parity, exclusive of rotation. A nomenclature that accounts for the reflection symmetry of the electronic wavefunctions in the plane of rotation was proposed by Alexander *et al.* [105], labelling the states by A' (if the wavefunction at high- J is symmetric with respect to reflection of the spatial coordinates of the electrons in the plane of rotation) and A'' (anti-symmetric), respectively. For the OH radical, levels in the ${}^2\Pi_{3/2}$ manifold with the parity label e (f) have A' (A'') symmetry. In the ${}^2\Pi_{1/2}$ manifold, this situation is reversed.

2.1.2 The first electronic excited state

In the first electronic excited state, a $(2p\sigma)$ electron is promoted to the $(2p\pi)$ shell. In the united atom picture this leads to the electron configuration $(1s\sigma)^2(2s\sigma)^2(2p\sigma)(2p\pi)^4$ with the corresponding term-symbol $A^2\Sigma^+$. In this state $\Lambda = 0$, and this state is best described using the Hund's case (b) coupling scheme. There are two degenerate wavefunctions for each rotational level, corresponding to $\Omega = 1/2$ and $\Omega = -1/2$. This degeneracy is lifted when the coupling between the nuclear rotation \vec{N} and the electron spin \vec{S} is taken into account. This interaction leads to the additional term $\gamma_v \vec{N} \cdot \vec{S}$ in the Hamiltonian, and results in a splitting of each rotational level, which is referred to as ρ -doubling. For the vibrational ground state of OH (${}^2\Sigma^+$), γ_0 and the rotational constant B_0 take the values 0.226 cm^{-1} [106, 107] and 16.961 cm^{-1} [99], respectively. The parity p of the rotational levels is given by $p = (-1)^N$. A rotational energy level diagram of the vibrational ground state in the electronic ground state $X^2\Pi$ and the first excited state $A^2\Sigma^+$ of OH is presented in Figure 2.1.

2.1.3 The $A \leftrightarrow X$ transition

Detection of OH radicals is conveniently performed by Laser Induced Fluorescence (LIF) on the $A^2\Sigma^+ \leftarrow X^2\Pi$ transition in the UV. Usually, either resonant fluorescence after excitation of the $v' = 0 \leftarrow v'' = 0$ band around 308 nm, or the off-resonant fluorescence around 313 nm after excitation of the $v' = 1 \leftarrow v'' = 0$ band around 282 nm is used to detect OH radicals in the $X^2\Pi, v'' = 0$ vibrational state. The advantage of using the latter scheme is that it is possible to reduce the background radiation that results from scattered laser light by optical filters. This is particularly important when LIF is employed in the proximity of the highly-polished electrodes of, for instance, a Stark decelerator or an electrostatic trap. An alternative technique to sensitively detect OH radicals is Resonance Enhanced Multi-Photon Ionization (REMPI) via the $D^2\Sigma^-$ or the $3^2\Sigma^-$ state in the 225 -

246 nm spectral region [108–111]. Compared to LIF detection, REMPI offers a better sensitivity, a higher collection efficiency and the elimination of stray light problems. The low transition probabilities involved and the tightly focussed UV radiation that is required to drive the multi-photon transitions, however, diminish these advantages. In all experiments that are performed on OH radicals described in this thesis, LIF detection after excitation via the $A^2\Sigma^+, v' = 1 \leftarrow X^2\Pi, v'' = 0$ transition is employed.

The most extensive measurements and analysis of the $A^2\Sigma^+ \leftarrow X^2\Pi$ transition have been performed by Dieke and Crosswhite in 1962 [99]. The selection rules for electric dipole allowed transitions are

$$\Delta J = 0, \pm 1 \quad (2.10)$$

and

$$\Delta N = 0, \pm 1, \pm 2. \quad (2.11)$$

In addition, only parity changing $+ \leftrightarrow -$ transitions are allowed. The transitions are labelled using the nomenclature of Dieke and Crosswhite [99]

$$\Delta N_{F'F''}(N''), \quad (2.12)$$

where O, P, Q, R and S are used to label transitions with $\Delta N = -2, -1, 0, +1$ and $+2$, respectively. The value of the quantum number N in the $X^2\Pi$ state is indicated by N'' , and the subscripts F' and F'' are used to denote the component of the ρ -doublet in the $A^2\Sigma^+$ state, and the Ω manifold in the $X^2\Pi$ state, respectively. For transitions where $F' = F''$ only one subscript is used for convenience. Some electric dipole allowed transitions with their spectroscopic notations are indicated in Figure 2.1.

2.2 Production of a molecular beam of OH radicals

Although the OH radical is a highly reactive species, and laboratory studies of OH radicals require a well controlled source, the OH radical has been frequently used in molecular beam experiments. The first intense continuous molecular beam of OH radicals was produced by ter Meulen *et al.* and was based on the chemical reaction $\text{H} + \text{NO}_2 \rightarrow \text{OH} + \text{NO}$ [112, 113]. In other production techniques radiofrequency discharges [114], DC discharges [100, 115, 116] or photodissociation of different precursors (mostly HNO_3 or H_2O_2) using UV laser radiation are employed to produce the OH radicals. Van Beek *et al.* developed an intense pulsed electrical discharge source for OH radicals, and peak densities close to the nozzle as high as 3×10^{12} molecules/cm³ were measured using cavity ring down spectroscopy [117]. Similar peak densities are reported using a pulsed slit nozzle discharge source [118]. Lewandowski *et al.* slightly modified the DC discharge production technique with the aim to produce an intense beam of OH radicals that can be used in combination with a Stark decelerator [119]. By limiting the time duration of the discharge, the heating from the violent discharge process is greatly reduced, and the initial velocity of the OH radical beam is close to what can be expected for a room temperature expansion. In the experiments described in this work, however, photodissociation of HNO_3 at 193 nm is used throughout. The main advantage of this is that the beam is produced at a well-defined time and at a well-defined position, which is ideal for coupling the molecular beam into the decelerator, and which greatly simplifies the interpretation of observed time of flight profiles.

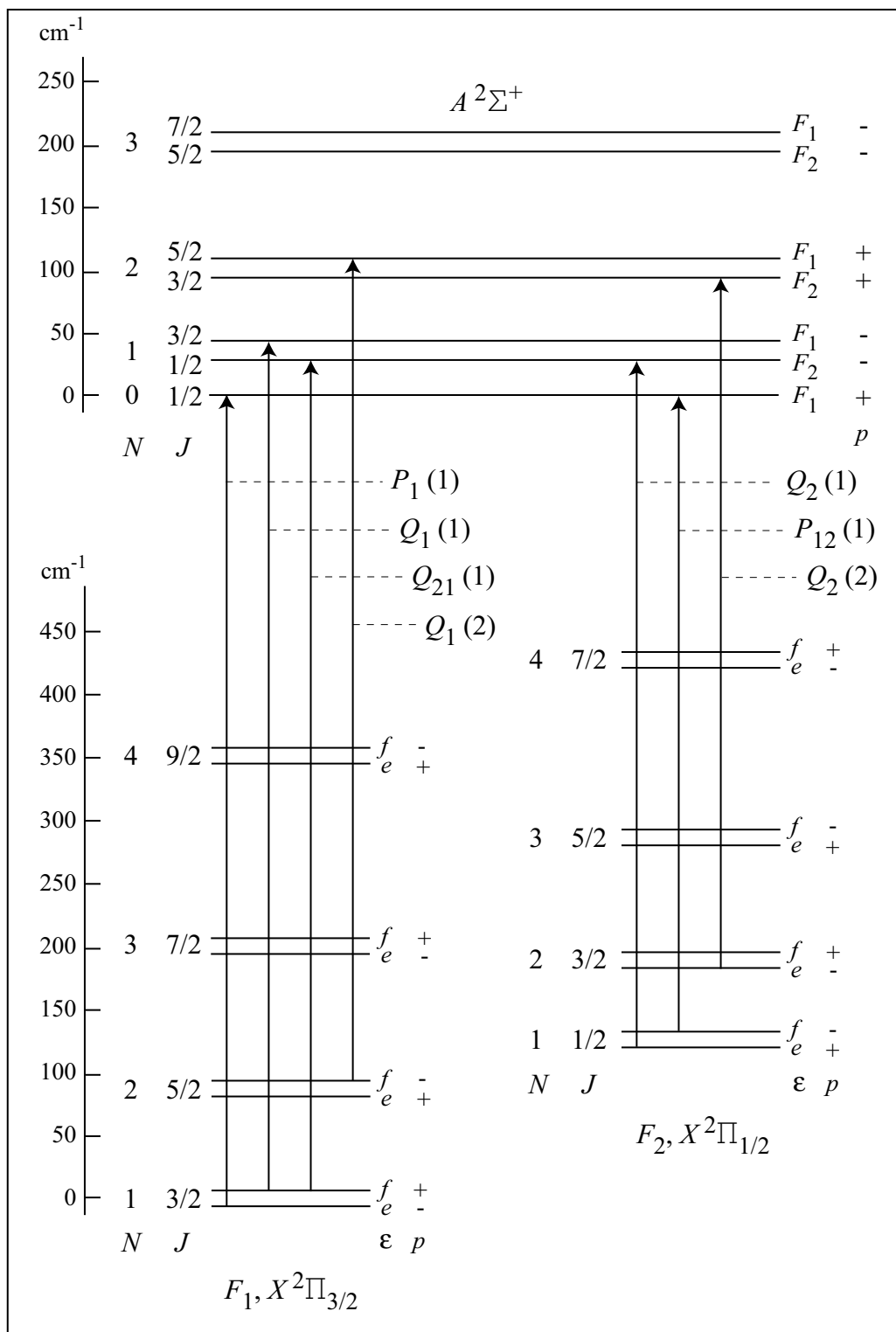


Figure 2.1: Energy level diagram of the vibrational ground states of the electronic ground state $X^2\Pi$ and the first excited state $A^2\Sigma^+$ of OH. The Λ -doublet splitting of the energy levels in the $X^2\Pi$ state and the ρ -doublet splitting of the energy levels in the $A^2\Sigma^+$ state are largely exaggerated for reasons of clarity. Some electric dipole allowed transitions with their spectroscopic notations are indicated.

From successive experiments using a discharge source similar to the one used in ref. [117] and the photodissociation source, it is concluded that the peak intensity of the beam is very similar for both sources.

The photolysis of HNO_3 in the UV was first studied by Bércecs and Förgeteg [120] and later by Johnston *et al.* [121, 122]. The UV absorption spectrum of HNO_3 exhibits a strong absorption ($\sigma \sim 10^{-17} \text{ cm}^2$) band centered at 185 nm and a second, less strong, absorption band around 270 nm with an absorption cross section on the order of 10^{-20} cm^2 . Therefore, the excimer laser wavelengths 193 nm and 248 nm are frequently used for the photolysis of HNO_3 . There has been considerable debate in the literature about the absolute OH quantum yields from HNO_3 at these wavelengths [123]. The quantum yield is approximately 0.3 when 193 nm radiation is used [124, 125] and close to unity at 248 nm [123, 124]. Higher quantum yields between 1.6 and 2.0 or between 1.2 and 1.5 can be obtained when H_2O_2 is photodissociated using 193 nm or 248 nm photons, respectively [124, 126]. However, the absorption cross section of H_2O_2 at 193 nm is about an order of magnitude lower than for HNO_3 [127]. In addition, hydrogen peroxide decomposes on contact with metal surfaces.

The OH radical source used in the present experiments consists of a room-temperature pulsed solenoid valve (General valve, series 9) with a nozzle diameter of 1 mm. A 6 mm long quartz (Suprasil I) capillary with an inner diameter of 1 mm and outer diameter of 3 mm is mounted on the nozzle orifice [104, 128]. The 193 nm UV pulse of a compact ArF excimer laser (Neweks, PSX-501) is focussed onto the capillary by a cylindrical lens with a focal length of 50 cm. It is found experimentally that the most efficient production of OH takes place close to the end of the capillary, as also reported by others [128]. The excimer laser typically produces 5 mJ of radiation in a 5 ns pulse and a $2.5 \times 3 \text{ mm}^2$ rectangular spot. Either Kr or Xe is used as a inert seed gas, with a typical stagnation pressure of 2.5-3 bars. Gaseous HNO_3 is brought in the beam by flowing the seed gas through liquid HNO_3 in a bubbler. The mean velocity of the beam is around 450 m/s when Kr is used, or 365 m/s when Xe is used. In both cases the longitudinal velocity spread (FWHM) is about 15 %. In the supersonic expansion, the beam is rotationally and vibrationally cooled and after the expansion most of the OH radicals ($\sim 90\%$) reside in the lowest rotational ($J = 3/2$) and vibrational state of the electronic ground state $X^2\Pi_{3/2}$.

2.3 The molecular Stark effect

2.3.1 General formalism

The interactions in a molecule are described by the molecular Hamiltonian H , and in general the molecular energy levels can be derived by diagonalizing the Hamiltonian matrix using a complete set of basis wave functions. The interaction of a polar molecule with an applied electric field is represented by adding the appropriate Stark Hamiltonian H_{Stark} to H . Diagonalization of this new matrix yields the energy levels of the molecule in an electric field. In this section, the required matrix elements of the type $\langle JKM | H_{Stark} | J'K'M' \rangle$ will be generally derived. These matrix elements can also be found in several text books (see for instance [129]), however, they are usually written using analytical expressions. Recently, based on the derivation given in ref. [129], the methods to calculate the Stark effect in (a)symmetric tops were summarized by Hain *et al.* [130]. Unfortunately, the matrix elements given in that paper contain a few errors. The compact form of the matrix elements given

in this section is very useful for the calculation of the Stark effect in a wide variety of molecules. A brief description of the application of the formalism to diatomic molecules and (a)symmetric tops is given. Based on the calculation of the Stark effect of a variety of molecules, the suitability of these molecules for Stark deceleration (and electrostatic trapping experiments) is discussed. The interaction of OH radicals with electric fields will be discussed in section 2.3.3.

2.3.2 Matrix elements of H_{Stark}

The interaction that a dipole $\vec{\mu}$ experiences in a homogeneous electric field \vec{E} can be expressed as $-\vec{\mu} \cdot \vec{E}$. However, the dipole moment vector $\vec{\mu}$ has a well defined orientation in the (rotating) body-fixed frame of the molecule, while the electric field vector \vec{E} is usually defined in the (static) laboratory frame of reference, complicating the calculation of the product $\vec{\mu} \cdot \vec{E}$. We define the space-fixed frame of coordinates as $(\hat{X}, \hat{Y}, \hat{Z})$, while the molecular coordinate frame is given by $(\hat{x}, \hat{y}, \hat{z})$. It is convenient to represent the dipole moment and electric field vectors as irreducible spherical tensor operators [98] of rank 1:

$$H_{\text{Stark}} = -\vec{\mu} \cdot \vec{E} = - \sum_{p=-1}^1 (-1)^p T_{\mu}(1, p) T_E(1, p) \quad (2.13)$$

where T_{μ} and T_E are defined in the space fixed frame and take the form

$$\begin{aligned} T_{\mu,E}(1, -1) &= \frac{1}{\sqrt{2}}(\mu, E_X - i\mu, E_Y) \\ T_{\mu,E}(1, 0) &= \mu(E)_Z \\ T_{\mu,E}(1, 1) &= -\frac{1}{\sqrt{2}}(\mu, E_X + i\mu, E_Y) \end{aligned} \quad (2.14)$$

Suppose the space-fixed coordinate system is chosen such that the electric field vector is directed along the \hat{Z} -axis:

$$\vec{E} = T_E(1, 0)\hat{Z} \equiv E\hat{Z} \quad (2.15)$$

Then $p = 0$ and the Hamiltonian reduces to

$$H_{\text{Stark}} = -T_{\mu}(1, 0) \cdot E \quad (2.16)$$

with $T_{\mu}(1, 0)$ the projection of the dipole moment on the space-fixed \hat{Z} -axis (see eqn. (2.14)). The molecular dipole moment $\vec{\mu}$ is defined in the molecular coordinate system and therefore rotates along with the molecule. A transformation from the space-fixed frame to the rotating molecular frame can be made with the help of the Wigner rotation matrices [98]:

$$T_{\mu}(1, 0) = \sum_{q=-1}^1 \mathcal{D}_{0q}^{(1)*}(\phi, \theta, \chi) \tilde{T}_{\mu}(1, q) \quad (2.17)$$

The Euler angles ϕ , θ , and χ define the orientation of the \hat{X} , \hat{Y} and \hat{Z} -axis with respect to the \hat{x} , \hat{y} and \hat{z} -axis, and $\tilde{T}_{\mu}(1, q)$ are the components of $\vec{\mu}$ on the molecule-fixed reference frame. It is essential to use the Euler angles consistently throughout the calculation. Here, the convention of Zare [98] is used throughout.

The calculation of the Stark effect requires the evaluation of matrix elements of the type *

$$\langle JKM|H_{Stark}|J'K'M'\rangle \quad (2.18)$$

where $|JKM\rangle$ are the rigid rotor functions:

$$|JKM\rangle = \sqrt{\frac{2J+1}{8\pi^2}} \mathcal{D}_{MK}^{(J)*}(\phi, \theta, \chi), \quad (2.19)$$

where K and M are the projections of J on the molecule-fixed \hat{z} -axis and the space-fixed \hat{Z} -axis respectively and run from $-J$ to J . With the help of equations (2.16), (2.17) and (2.19) and the properties of the Wigner rotation matrices [98], the Stark matrix elements are easily evaluated:

$$\begin{aligned} & \langle JKM|H_{Stark}|J'K'M'\rangle \\ &= \frac{E}{8\pi^2} \sqrt{(2J+1)(2J'+1)} \sum_q \tilde{T}_{\mu(1,q)} \int \mathcal{D}_{MK}^{(J)*} \mathcal{D}_{0q}^{(1)*} \mathcal{D}_{M'K'}^{(J')} d^3\tau \\ &= -\frac{E}{8\pi^2} \sqrt{(2J+1)(2J'+1)} \sum_q (-1)^{-q} \tilde{T}_{\mu}(1,q) (-1)^{M'-K'} \\ & \quad \times \int \mathcal{D}_{-M'-K'}^{(J)} \mathcal{D}_{0-q}^{(1)} \mathcal{D}_{M'K'}^{(J')} d^3\tau \\ &= -E \sqrt{(2J+1)(2J'+1)} \sum_q (-1)^{M'-K'-q} \tilde{T}_{\mu}(1,q) \\ & \quad \times \begin{pmatrix} J' & 1 & J \\ -M' & 0 & M \end{pmatrix} \begin{pmatrix} J' & 1 & J \\ -K' & -q & K \end{pmatrix} \\ &= -\delta(M, M') E \sqrt{(2J+1)(2J'+1)} \sum_q (-1)^{M-K} \tilde{T}_{\mu}(1,q) \\ & \quad \times \begin{pmatrix} J & 1 & J' \\ M & 0 & -M \end{pmatrix} \begin{pmatrix} J & 1 & J' \\ K & -q & -K' \end{pmatrix}, \end{aligned} \quad (2.20)$$

where in the last step the selection rules

$$J = J' \quad \text{or} \quad J = J' \pm 1, \quad M = M', \quad K = K' + q \quad (2.21)$$

that follow from the 3- J symbols were used.

It is often advantageous to calculate the rotational energy levels of a molecule on the basis of the symmetrized wavefunctions of definite parity $|JKM\epsilon\rangle$ (eqn. (2.4) instead of the pure rigid rotor functions $|JKM\rangle$). From eqn. (2.20) it follows that on this basis the matrix elements of the Stark Hamiltonian are given by

$$\begin{aligned} \langle J = J', KM \pm |H_{Stark}|J'K'M'\mp\rangle &= \langle J = J', KM|H_{Stark}|J'K'M'\rangle \\ \langle J = J' \pm 1, KM \pm |H_{Stark}|J'K'M'\pm\rangle &= \langle J = J' \pm 1, KM|H_{Stark}|J'K'M'\rangle \end{aligned} \quad (2.22)$$

Notice that since the molecular dipole moment has odd parity, it connects rotational wave functions with different parity if $\Delta J = 0$, and wave functions with the same parity if $\Delta J = \pm 1$.

*In the case of diatomics like the OH radical, K is usually referred to as Ω .

2.3.3 Diatomic molecules; the Stark effect of OH

In the case of diatomic molecules an important simplification to the discussion given above can be made: the dipole moment of a diatomic molecule is always directed along the internuclear axis. The vector \vec{K} is by definition also directed along this axis, and $q = 0$ in eqn. (2.17). In many situations, however, fine structure effects like Λ -doubling complicates the calculation of the wavefunctions of the rotational levels involved. In the case of the OH radical, the Λ -doubling is very small compared to the rotational spacing, and to a good approximation the rotational wavefunctions are given by the equations (2.6). From the selection rules eqn. (2.21) it follows that the Stark interaction only couples states with $\Omega' = \Omega$, $M'_J = M_J$, and states with $J' = J$ or $J' = J \pm 1$. Due to the relatively large rotational spacing in OH, the coupling between states with $J' = J \pm 1$ is very weak. For the electric field strengths that are typically used in a Stark decelerator, the mixing between rotational levels with different J can be neglected. For each possible value of M_J , the Stark shifts of both Λ -doublet components of the $^2\Pi_{3/2}$, $J = 3/2$ rotational ground state of OH are given to first order by the eigenvalues of the matrix

$$\begin{pmatrix} E_\Lambda & Q \\ Q & 0 \end{pmatrix}, \quad (2.23)$$

where E_Λ is the zero-field Λ -doublet splitting. Using eqn. (2.20), the off-diagonal elements Q are given by

$$\begin{aligned} Q &= \langle ^2\Pi_{3/2}, J, M_J, f | H_{Stark} | ^2\Pi_{3/2}, J, M_J, e \rangle \\ &= -\mu |\vec{E}| \frac{M_J \Omega_{eff}}{J(J+1)}, \end{aligned} \quad (2.24)$$

where Ω_{eff} represents the 'effective' value of Ω :

$$\Omega_{eff} = \left(\frac{1}{2} C_1(J)^2 + \frac{3}{2} C_2(J)^2 \right). \quad (2.25)$$

For the $^2\Pi_{3/2}$, $J = 3/2$ rotational ground state, the values of the mixing coefficients C_1 and C_2 are 0.17 and 0.98, respectively, resulting in $\Omega_{eff} = 1.46$. The eigenvalues of the matrix (2.23), and hence the Stark-shifted energy levels are then given by

$$E_{Stark} = \frac{E_\Lambda}{2} \pm \sqrt{\left(\frac{E_\Lambda}{2}\right)^2 + Q^2}, \quad (2.26)$$

where the plus and the minus sign are used for the low-field-seeking upper Λ -doublet component and the high-field-seeking lower Λ -doublet component, respectively. The dipole moment of the OH radical is 1.67 D [131, 132], and the Stark shift of the $^2\Pi_{3/2}$, $J = 3/2$ state for fields up to 150 kV/cm is presented in the left panel of Figure 2.2. In an electric field, both Λ -doublet components split into a $|M_J\Omega| = 3/4$ and a $|M_J\Omega| = 9/4$ component. The shift is quadratic for low values of the electric field strength. For higher electric fields, the wavefunctions of the two Λ -doublet states become completely mixed, and the Stark shift becomes linear. The low-field-seeking $^2\Pi_{3/2}$, $J = 3/2$, $f, M_J\Omega = -9/4$ component is used in the deceleration and trapping experiments described in this thesis. This component experiences a Stark shift of 1.8 cm^{-1} in an electric field of 100 kV/cm.

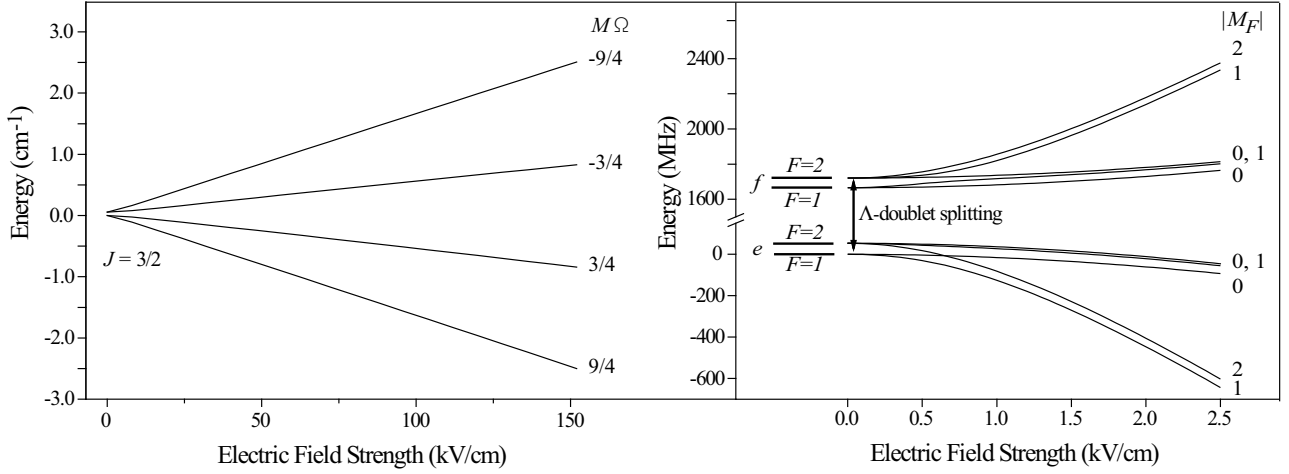


Figure 2.2: Stark shift of the ${}^2\Pi_{3/2}$, $J = 3/2$ state of OH as a function of the electric field strength without (left panel) and with (right panel) hyperfine structure. Note the different energy units used in both panels.

2.3.4 Hyperfine structure of OH

So far, the hyperfine structure of a molecule was neglected in the description of the molecular Stark effect in section 2.3. Although in the deceleration and trapping experiments described in this thesis the hyperfine structure of the OH molecule can be neglected, the hyperfine structure of the OH radical in the presence of an electric field is briefly discussed. The theory of magnetic hyperfine structure in diatomic molecules has been treated by Frosch and Foley [133]. The first measurements of the Λ -doubling spectra of OH were reported by Dousmanis *et al.* [102], and later by ter Meulen *et al.* [112], and Meerts *et al.* [103, 134]. The hyperfine interaction couples the spin \vec{I} of the hydrogen nucleus to the rotational angular momentum vector \vec{J} to form \vec{F} : $\vec{F} = \vec{J} + \vec{I}$. Each Λ -doublet component of the ${}^2\Pi_{3/2}$, $J = 3/2$ rotational ground state is split in the two hyperfine levels $F = 1$ and $F = 2$. The basic hyperfine wavefunctions take the form $|{}^2\Pi_{|\Omega\rangle} JIFM_F\epsilon\rangle$. The matrix elements of the Stark contribution to the Hamiltonian can be derived similar to the description given in section 2.3 and are given by [131]

$$\begin{aligned}
& \langle {}^2\Pi_{|\Omega\rangle} JIFM_F\epsilon | H_{Stark} | {}^2\Pi_{|\Omega'\rangle} J'IF'M'_F\epsilon' \rangle \\
&= \alpha \delta(|\Omega|, |\Omega'|) \delta(M_F, M'_F) \mu |\vec{E}| (-1)^{2J+I+F+F'-M_F-|\Omega|} \\
&\quad \times \sqrt{(2J+1)(2J'+1)(2F+1)(2F'+1)} \\
&\quad \times \begin{Bmatrix} J & F & I \\ F' & J' & 1 \end{Bmatrix} \begin{pmatrix} F & 1 & F' \\ -M_F & 0 & M'_F \end{pmatrix} \begin{pmatrix} J & 1 & J' \\ \Omega & 0 & \Omega' \end{pmatrix},
\end{aligned} \tag{2.27}$$

where the factor α is zero if $|J - J'| = 0$ and $\epsilon = \epsilon'$ or if $|J - J'| = 1$ and $\epsilon \neq \epsilon'$. The Stark shift of the ${}^2\Pi_{3/2}$, $J = 3/2$ state including hyperfine structure for fields up to 2.5 kV/cm is presented in the right panel of Figure 2.2.

2.3.5 Symmetric and asymmetric tops

In absence of an applied field the rotational Hamiltonian for a free rigid rotor is given by [98, 129]

$$H_R = AJ_a^2 + BJ_b^2 + CJ_c^2 \tag{2.28}$$

where J_a, J_b and J_c are the projections of \vec{J} on the three principal axis of inertia (a, b, c) of the molecule, and A, B and C are the rotational constants that are inversely proportional to the principal moments of inertia (with the common convention that $A > B > C$). In the special case of a symmetric top at least two of the moments of inertia are equal. The Hamiltonian H_R is defined with respect to the principle axes of inertia of the molecule, whereas the functions $|JKM\rangle$ are defined in the molecule-fixed ($\hat{x}, \hat{y}, \hat{z}$) coordinate system. It is therefore convenient to choose the natural coordinate system of the molecule ($\hat{a}, \hat{b}, \hat{c}$) as the molecule-fixed reference frame ($\hat{x}, \hat{y}, \hat{z}$). There are now three different ways in which we can identify ($\hat{a}, \hat{b}, \hat{c}$) to ($\hat{x}, \hat{y}, \hat{z}$) [98, 129]. A proper choice of representation is very useful when calculating the rotational energies since it can simplify the energy matrix considerably. When the Stark effect is incorporated in the calculation, the situation is different. In many cases, the dipole moment of a (a)symmetric top is directed along one of the principle axes of inertia. It is very convenient to choose a representation that identifies the \hat{z} -axis with the direction of the dipole moment. It then follows that $q = 0$ in eqn. (2.17), simplifying the matrix elements of H_{Stark} . It is clear that the best choice for calculating the rotational energy levels and for the Stark effect can in principle be conflicting, and the best choice depends on the symmetry of the top and the direction of its dipole moment *. The matrix elements for H_R in all three representations are found in ref. [98, 130]. Note that since the quantum number K in $|JKM\rangle$ is defined as the projection of J on the molecule-fixed \hat{z} -axis, the physical meaning of K is different in the three representations. Using this formalism, the Stark effect of the (for Stark deceleration relevant) asymmetric tops H_2CO (with its dipole moment along the a -axis of the molecule), H_2O (dipole along b -axis), and ND_3 (c -axis) are easily calculated. If the dipole moment of the molecule is not directed along one of the principle axes of the molecule, the full sum over q in eqn. (2.17) needs to be evaluated. The molecule HDO is an example of this situation.

2.4 Candidate molecules for Stark deceleration †

To date, the molecules CO ($a^3\Pi_1$) [8], NH ($a^1\Delta$), various isotopomers of NH_3 [11, 14], H_2CO , and OH [78, 79, 88] have been decelerated in a low-field seeking state. With a Stark decelerator, however, any polar molecule can be decelerated to rest provided that it has a sufficiently large positive Stark effect in experimentally obtainable electric fields. A selection of polar molecules suited for deceleration, and ultimately trapping, is given in Table 2.1. Most of the molecules that are listed have been used extensively in hexapole focusing experiments, in which case a reference to these experiments is given. The deceleration experienced by the molecules in the decelerator depends on the ratio of their (positive) Stark-shift to their mass. The Stark shifts are calculated using the formalism outlined in section 2.3. The Stark shift to mass ratio of the molecule is given as a 'figure of merit' in Table 2.1, scaled relative to the Stark shift to mass ratio of OH ($J = 3/2, M_J\Omega = -9/4$). Unless stated otherwise, the Stark shift in an electric field of 200 kV/cm is used. When the Stark shift reaches a maximum at lower values of the electric field, this maximum shift is given, together with the value of the electric field (in brackets). It is noted that for molecules with a second order Stark effect, the value

*It is remarked here that a further simplification of the matrix can be obtained exploiting group theory. The asymmetric rotor belongs to the D_2 point group, and the matrix can in principle be divided into four blocks. The Stark effect operator can then only couple different blocks of specific symmetry [129].

†Partially adapted from: H.L. Bethlem, F.M.H. Crompvoets, R.T. Jongma, S.Y.T. van de Meerakker, and G. Meijer, Phys. Rev. A. **65** 053416 (2002).

of the Stark shift/mass ratio can change considerably for the better if higher values of the electric field are used in the decelerator. In Figure 2.3 the Stark shift of a selection of molecules listed in Table 2.1 is shown; in this figure, the rotational level that is of most relevance to Stark deceleration experiments is shown. The number of electric field stages that would be required to bring the molecules to a standstill in the present set-up (see chapter 3), i.e. with the decelerator operating at a phase angle of 70° and with identical electric field strengths in a deceleration stage, is given. For this, the beam of interest is assumed to have an initial velocity determined by the Xe carrier gas at a temperature determined by the vapor pressure of the molecules. For stable molecules, the temperature at which the vapor pressure is 0.1 atm. is taken; for radicals a room-temperature expansion is assumed. Both the production in a molecular beam and the detection methods of the molecules listed in Table 2.1 are well known, although the production of an intense beam with a sufficiently low initial velocity constitutes a formidable experimental challenge for some molecules. In addition to OH radicals, the deceleration and subsequent trapping of a molecular beam of (isotopomers of) SH, CH, CO ($a^3\Pi$), H₂CO, LiH, NH ($a^1\Delta$) and NH₃ are considered most realistic. Of these, NH is of special interest, as for this radical it is possible to increase the number of trapped molecules by accumulating molecules from successive loading cycles in a magnetic trap [135, 136]. This trap re-loading scheme, and a preliminary deceleration experiment with a beam of NH ($a^1\Delta$, $J = 2$) molecules, is discussed in chapter 8. In view of its low mass and its large electric dipole moment of almost 6 D, and hence its prospects for the study of dipole-dipole interactions in cold polar gases, LiH is an interesting candidate as well.

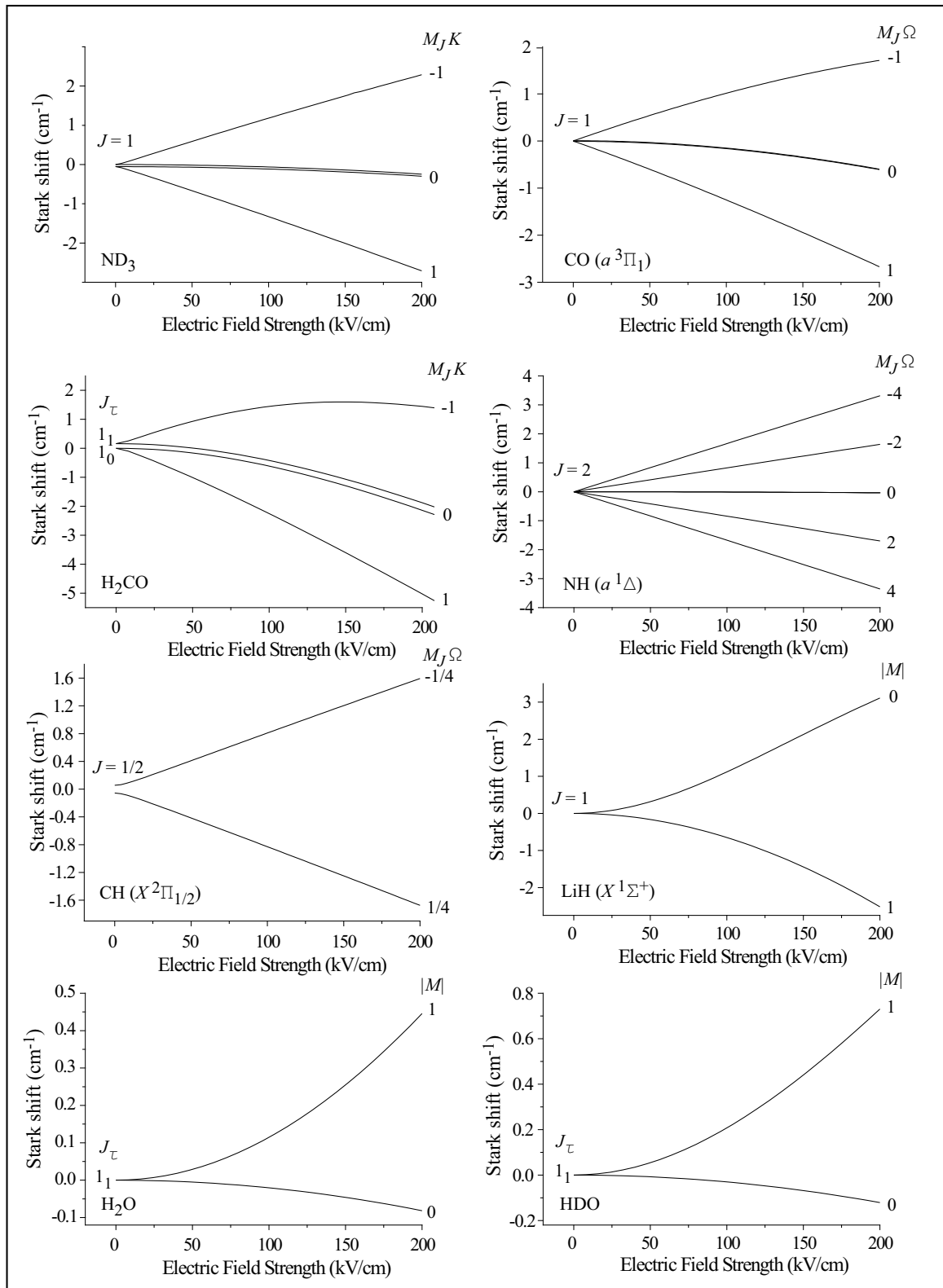


Figure 2.3: Stark shift of the rotational level that is of most relevance to Stark deceleration experiments of the molecules ND_3 , $\text{CO} (a^3\Pi_1)$, H_2CO , $\text{NH} (a^1\Delta)$, $\text{CH} (X^2\Pi_{1/2})$, $\text{LiH} (X^1\Sigma^+)$, H_2O and HDO . Note the different energy scale for each molecule.

Table 2.1: A selection of polar molecules suited for deceleration and trapping experiments, with their relevant properties.

Molecule	State	Multi- plicity of hyperfine levels	Stark shift at 200 kV/cm (cm^{-1})	Shift/mass (relative to OH)	# stages required in present setup	Dipole moment (D)
CH [137, 138]	$ X^2\Pi_{1/2}, J = 1/2, M\Omega = -1/4\rangle$	4	1.54	0.62	90	$\mu_a = 1.46$
	$ X^2\Pi_{3/2}, J = 3/2, M\Omega = -9/4\rangle$	4	1.88	0.90	71	
CF [139]	$ X^2\Pi_{1/2}, J = 1/2, M\Omega = -1/4\rangle$	4	0.44	0.08	533	$\mu_a = 0.65$
	$ X^2\Pi_{1/2}, J = 3/2, M\Omega = -3/4\rangle$	4	0.32	0.05	845	
CH ₂ F ₂ [130]	$ J_\tau M\rangle = 2_{-2}0\rangle$		1.52 (184 kV/cm)	0.15	168	$\mu_b = 1.96$
CH ₃ F [140, 141]	$ JKM\rangle = 100\rangle$		0.54 (128 kV/cm)	0.08	217	$\mu_a = 1.86$
	$ JKM\rangle = 1 \pm 1 \mp 1\rangle$		1.05 (118 kV/cm)	0.16	99	
CO [142, 143]	$ a^3\Pi_{\Omega=1}, J = 1, M\Omega = -1\rangle$	2	1.71	0.32	89	$\mu_a = 1.37$
	$ a^3\Pi_{\Omega=2}, J = 2, M\Omega = -4\rangle$	2	2.87	0.54	63	
H ₂ CO [130, 144–146]	$ J_\tau M\rangle = 1_1 1\rangle$	6	1.44 (144 kV/cm)	0.25	130	$\mu_a = 2.34$
D ₂ CO [147]	$ J_\tau M\rangle = 1_1 1\rangle$	6	1.11 (112 kV/cm)	0.18	155	$\mu_a = 2.34$
H ₂ O	$ J_\tau M\rangle = 1_1 1\rangle$	6	0.45	0.13	1081	$\mu_b = 1.82$
D ₂ O	$ J_\tau M\rangle = 1_1 1\rangle$	6	0.72	0.19	667	$\mu_b = 1.85$
HDO	$ J_\tau M\rangle = 1_1 1\rangle$	12	0.73	0.22	558	$\mu_a = 0.66$ $\mu_b = 1.73$
HCN	$ (v_1, v_2^l, v_3), J, M\rangle = (0, 0^0, 0), 1, 0\rangle$	6	0.92 (144 kV/cm)	0.17	177	$\mu_a = 3.01$
	$ (v_1, v_2^l, v_3), J, M\rangle = (0, 1^1, 0), 1, -1\rangle$	12	1.80 (136 kV/cm)	0.36	79	
	$ (v_1, v_2^l, v_3), J, M\rangle = (0, 1^1, 0), 2, -1\rangle$	12	2.58	0.50	150	
	$ (v_1, v_2^l, v_3), J, M\rangle = (0, 1^1, 0), 2, -2\rangle$	12	1.66 (200 kV/cm)	0.32	109	
LiH [148]	$ X^1\Sigma^+, J = 1, M = 0\rangle$	8	3.11	2.06	45	$\mu_a = 5.88$
LiD	$ X^1\Sigma^+, J = 1, M = 0\rangle$	12	2.67	1.58	34	
NH	$ a^1\Delta, J = 2, M = 2\rangle$	12	3.34	1.17	48	$\mu_a = 1.49$
¹⁴ NH ₃ [149–151]	$ JKM\rangle = 1 \pm 1 \mp 1\rangle$		2.11	0.66	79	$\mu_c = 1.47$
¹⁵ NH ₃	$ JKM\rangle = 1 \pm 1 \mp 1\rangle$		2.11	0.62	84	$\mu_c = 1.47$
¹⁴ ND ₃ [151]	$ JKM\rangle = 1 \pm 1 \mp 1\rangle$	48	2.29	0.60	65	$\mu_c = 1.50$
¹⁵ ND ₃	$ JKM\rangle = 1 \pm 1 \mp 1\rangle$	32	2.29	0.57	68	$\mu_c = 1.50$
NO [140, 152]	$ X^2\Pi_{1/2}, J = 1/2, M\Omega = -1/4\rangle$	6	0.17	0.03	1179	$\mu_a = 0.16$
N ₂ O [140, 153]	$ (v_1, v_2^l, v_3), J, M\rangle = (0, 1^1, 0), 1, -1\rangle$	18	0.26	0.03	1041	$\mu_a = 0.17$
OCS [150, 154]	$ (v_1, v_2^l, v_3), J, M\rangle = (0, 0^0, 0), 1, 0\rangle$	1	0.13 (82 kV/cm)	0.01	1172	$\mu_a = 0.72$
	$ (v_1, v_2^l, v_3), J, M\rangle = (0, 0^0, 0), 2, 0\rangle$	1	0.43	0.04	1407	
	$ (v_1, v_2^l, v_3), J, M\rangle = (0, 1^1, 0), 1, -1\rangle$	2	0.25 (84 kV/cm)	0.02	647	
	$ (v_1, v_2^l, v_3), J, M\rangle = (0, 1^1, 0), 2, -1\rangle$	2	0.56	0.05	759	
	$ (v_1, v_2^l, v_3), J, M\rangle = (0, 1^1, 0), 2, -2\rangle$	2	0.24 (120 kV/cm)	0.02	779	
OH [100, 116, 155, 156]	$ X^2\Pi_{3/2}, J = 3/2, M\Omega = -9/4\rangle$	4	3.22	1.00	56	$\mu_a = 1.67$
OD [100, 157]	$ X^2\Pi_{3/2}, J = 3/2, M\Omega = -9/4\rangle$	6	3.22	0.95	58	$\mu_a = 1.65$
SH [137, 158]	$ X^2\Pi_{3/2}, J = 3/2, M\Omega = -9/4\rangle$	4	1.51	0.24	227	$\mu_a = 0.76$
SD	$ X^2\Pi_{3/2}, J = 3/2, M\Omega = -9/4\rangle$	6	1.49	0.23	235	$\mu_a = 0.76$
SO ₂ [144, 151]	$ J_\tau M\rangle = 1_0 0\rangle$	1	1.47	0.13	343	$\mu_b = 1.59$

CHAPTER 3

A NEW GENERATION STARK DECELERATOR

In a Stark decelerator polar molecules can be decelerated, exploiting the interaction of these molecules with time-varying inhomogeneous electric fields. We here report the deceleration of a molecular beam of ground state OH ($X^2\Pi_{3/2}$, $J = 3/2$) radicals. The experiments are performed in a new generation molecular beam deceleration machine, designed such that a large fraction of the molecular beam pulse can be slowed down. The evolution of the phase space distribution of the beam as it progresses through the Stark decelerator is studied in detail.

Based on:

Stark deceleration and trapping of OH radicals

Sebastiaan Y.T. van de Meerakker, Nicolas Vanhaecke, and Gerard Meijer

Ann. Rev. of Phys. Chem. 57 (2006) (in press).

3.1 Introduction

In this chapter, a detailed description is given of the new generation Stark decelerator, that is used in many experiments described in this thesis. The phase-stable guiding and deceleration of a beam of OH radicals is demonstrated, and a detailed discussion of the evolution of the beam as it progresses through the Stark decelerator is given.

3.2 Longitudinal motion

3.2.1 Phase stability

The operation principle of a Stark decelerator and a description of phase stability are given in detail in ref. [8, 14, 72]. The description is only briefly repeated here. Extensions to this description and the influence of the transverse motion on phase stability will follow in the chapters 4 and 5. The decelerator consists of an array of electric field stages centered a distance L apart, as schematically represented in Fig. 3.1. Opposing rods are connected to a switchable power supply with different polarity. Alternating electric field stages are electrically connected to each other. When the odd electrodes are switched to high voltage, the even electrodes are switched to ground and vice versa. At a given time t , the potential energy of a polar molecule as a function of its position z has periodicity $2L$. It is therefore convenient to describe the motion of a molecule in terms of its reduced position $z\pi/L$, which has periodicity 2π . The energy a molecule loses per stage depends on its position at the time the fields are switched. This position is indicated by the 'phase angle' ϕ [8, 14, 72]. We define the position $\phi = 0$ at the position in between two adjacent pairs of electrodes such that the electrodes at $\phi = \pi/2$ are grounded just after the fields are switched.

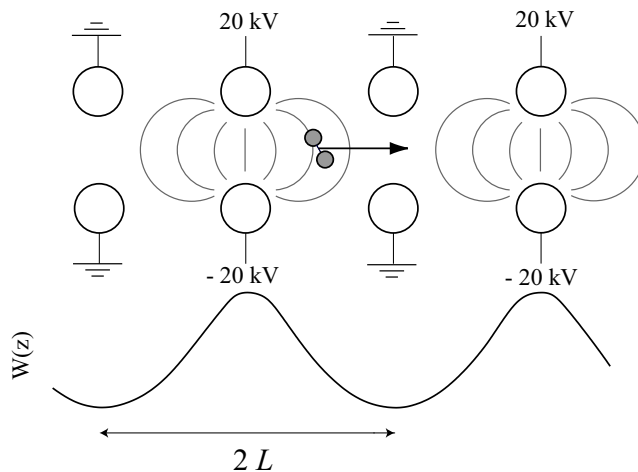


Figure 3.1: Scheme of the Stark decelerator, together with the Stark energy of a molecule as a function of position z along the molecular beam axis. Adjacent electric field stages are spaced a distance $L = 11$ mm apart. Each electric field stage consists of two parallel 6 mm diameter cylindrical rods with a center to center distance of 10 mm. A maximum voltage difference of 40 kV is applied to opposing rods in an electric field stage.

By definition, a molecule with velocity v_0 is called *synchronous* if its phase ϕ_0 on the potential is

always the same at the time the fields are switched, i.e., ϕ_0 remains constant and the molecule will lose a constant amount of kinetic energy $\Delta K(\phi_0)$ per stage. The synchronous molecule achieves this by travelling exactly a distance L in the time ΔT between two successive switch times. This means that the synchronous molecule is always 'in phase' with the switching of the decelerator. A molecule that has a slightly different phase ϕ and/or velocity v than the synchronous molecule will experience an automatic correction towards the equilibrium values ϕ_0 and v_0 . For instance, a molecule that has a phase that is slightly higher than ϕ_0 at a certain switch time, will lose more kinetic energy than the synchronous molecule, and the molecule will slow down with respect to the synchronous molecule. Its phase will get smaller, until it lags behind, after which the process reverses. Molecules within a certain region in phase-space, bounded by the so-called separatrix, will undergo stable phase-space oscillations around the synchronous molecule. This mechanism is called phase stability, and ensures that a package of molecules is kept together in the Stark decelerator throughout the deceleration process. In the next section, a more quantitative description of phase stability will be given.

3.2.2 Equation of motion

To derive the longitudinal equation of motion of molecules through the Stark decelerator, we will consider molecules that move along the molecular beam axis of the decelerator. The Stark energy of a molecule $W(z\pi/L)$ is symmetric around the position of a pair of electrodes and can be conveniently written as a Fourier series:

$$\begin{aligned} W(z\pi/L) &= \frac{a_0}{2} + \sum_{n=1}^{\infty} a_n \cos(n(z\pi/L + \pi/2)) \\ &= \frac{a_0}{2} - a_1 \sin \frac{z\pi}{L} - a_2 \cos 2\frac{z\pi}{L} + a_3 \sin 3\frac{z\pi}{L} + \dots \end{aligned} \quad (3.1)$$

By definition, the synchronous molecule travels a distance L in the time ΔT between two successive switch times. The change in kinetic energy per stage $\Delta K(\phi_0) = -\Delta W(\phi_0)$ for a synchronous molecule with phase ϕ_0 and velocity v_0 at a certain switch time is then given by the difference in potential energy at the positions $z\pi/L = \phi_0$ and $z\pi/L = \phi_0 + \pi$:

$$\Delta W(\phi_0) = W(\phi_0 + \pi) - W(\phi_0) = 2a_1 \sin \phi_0. \quad (3.2)$$

In the Stark decelerator, one repeatedly switches between two *static* situations. This is represented by the variable ϕ that is only defined when the fields are switched, and $z\pi/L$ whose origin jumps by π every time the fields are switched. However, to derive the equation of motion, continuous variables are required. If the deceleration rate is small compared to the kinetic energy of the molecule, we can regard the lost kinetic energy of the synchronous molecule between two successive switch times as the result of a continuously acting *average* force $\bar{F} = -\Delta K/L$. This approximation is equivalent to assuming that the phase of the synchronous molecule ϕ_0 is not only constant (and defined) at a switch time, but is also constant for the time in between two successive switch times. In this picture, the repeated switching of the potential between two *static* situations after a time interval ΔT is replaced by a *travelling* potential well that moves with velocity $L/\Delta T$. An equation of motion can then be derived that describes the motion of molecules through the Stark decelerator.

Within these approximations the average force \bar{F} that acts on the synchronous molecule is simply:

$$\bar{F}(\phi_0) = \frac{-\Delta W(\phi_0)}{L} = -\frac{2a_1}{L} \sin \phi_0 \quad (3.3)$$

if we only take the leading terms up to $n = 2$ in eq. 1 into account. The average force acting on a non-synchronous molecule with phase $\phi = \phi_0 + \Delta\phi$, but with velocity v_0 , is given by $-\frac{2a_1}{L} \sin(\phi_0 + \Delta\phi)$, and in a good approximation the equation of motion with respect to the synchronous molecule is

$$\frac{mL}{\pi} \frac{d^2 \Delta\phi}{dt^2} + \frac{2a_1}{L} (\sin(\phi_0 + \Delta\phi) - \sin(\phi_0)) = 0 \quad (3.4)$$

where m is the mass of the molecule. In the phase stability diagrams of Fig 3.2, lines of constant

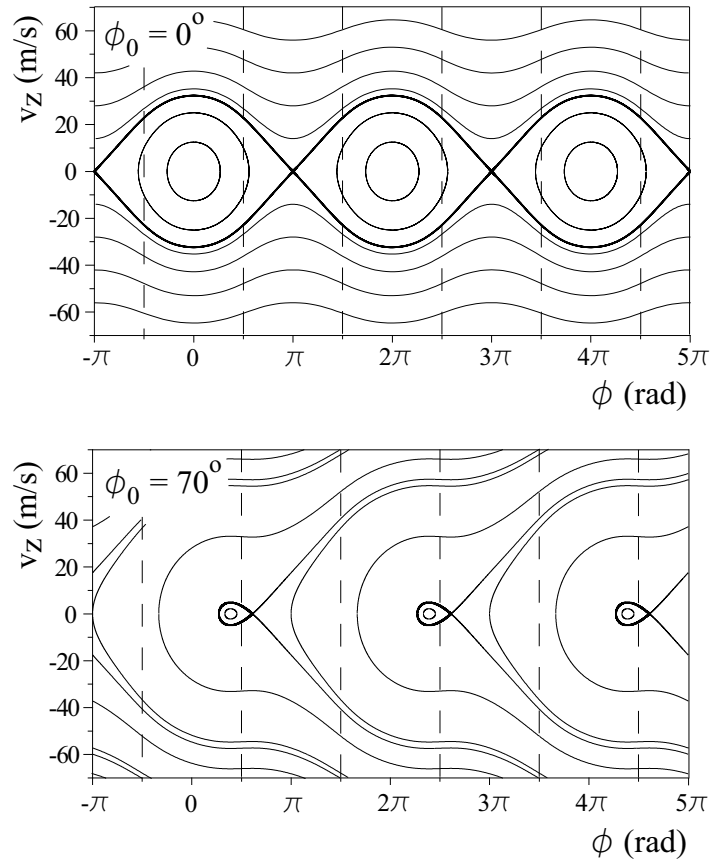


Figure 3.2: Phase stability diagram for OH ($J = 3/2$, $M\Omega = -9/4$) radicals when the decelerator is operated at a phase angle of $\phi_0 = 0^\circ$ or $\phi_0 = 70^\circ$. The positions of the electrodes of the decelerator are indicated by the dashed lines; a phase difference of 2π corresponds to a distance of 22 mm.

energy are shown that result from a numerical integration of eqn. 3.4 for OH radicals in the $J = 3/2$, $M\Omega = -9/4$ state and for the decelerator used in the present experiments. The equilibrium phase angles $\phi_0 = 0^\circ$ and $\phi_0 = 70^\circ$ for the synchronous molecule are used. The solid lines indicate the trajectories in phase space that molecules will follow. The positions of the electrodes of the decelerator are indicated by the dashed lines. In the present decelerator a phase difference of 2π corresponds to a distance of 22 mm, a factor of 2 larger than the corresponding distance in Stark decelerators of earlier designs. Closed curves in the phase space diagram correspond to bound orbits; molecules within the 'bucket' bound by the thick contour (called 'separatrix') will oscillate in phase space around the phase and velocity of the synchronous molecule. Close to the synchronous molecule

the potential is (almost) harmonic, and the oscillation frequency is given by

$$\omega_z/2\pi = \sqrt{\frac{a_1 \cos \phi_0}{2m\pi L^2}}. \quad (3.5)$$

Further outward, the oscillation frequency is lowered, approaching zero on the separatrix. It is noted that operation of the decelerator at $\phi_0 = 0^\circ$ corresponds to transporting (part of) the beam through the decelerator without deceleration, while acceleration or deceleration of the beam occurs for $-90^\circ < \phi_0 < 0$ and $0 < \phi_0 < 90^\circ$, respectively.

The separatrix defines the region in phase space where molecules are phase stable and gives the longitudinal acceptance of the decelerator. In Fig. 3.3 the acceptance is depicted for different phase angles ϕ_0 . The depth of the travelling potential well rapidly decreases for higher phase angles, reaching zero for $\phi_0 = 90^\circ$. It is therefore in principle advantageous to operate the decelerator at a phase angle that is as low as possible, although more deceleration stages are required to compensate for the reduced deceleration rate. In addition to the larger spatial acceptance of the Stark decelerator described in this thesis, an increased number of electric field stages is employed (108 in the present design) that enables the use of a relatively low phase angle, increasing the phase space acceptance even further. Alternatively, molecular beams with a relatively high initial velocity can be decelerated to a standstill, which is required for beams where it is not favorable to use Xe as a carrier gas, or to cool the beam source. In the chapters 4 and 5, extensions to the model of phase stability presented above are made. These extensions, however, do not significantly influence the discussions of phase stability and the phase-space evolution of the beam in the Stark decelerator that are given in this chapter.

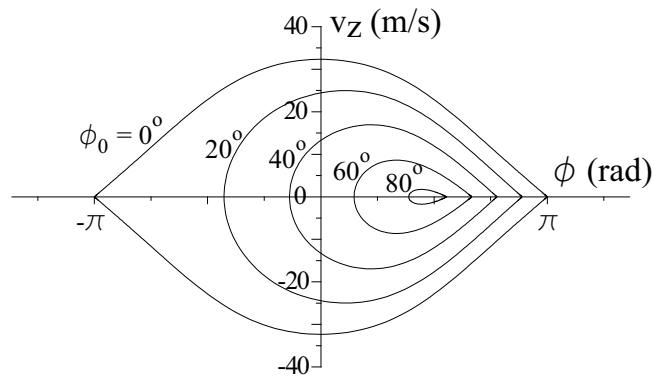


Figure 3.3: Longitudinal acceptance of the decelerator for different values of the phase angle ϕ_0 . The velocity $v_z = 0$ corresponds to the velocity of the synchronous molecule.

3.3 Experimental set-up

The experiments described in this chapter are performed in a molecular beam machine, schematically shown in Fig. 3.4, that consists of three differentially pumped vacuum chambers. The source, deceleration and detection chamber are pumped by a 1400 l s^{-1} (Pfeiffer Vacuum TMU 1600M), $2 \times 400 \text{ l s}^{-1}$ (TMU 400M), and a 400 l s^{-1} turbo molecular drag pump, respectively. The oil-free turbo

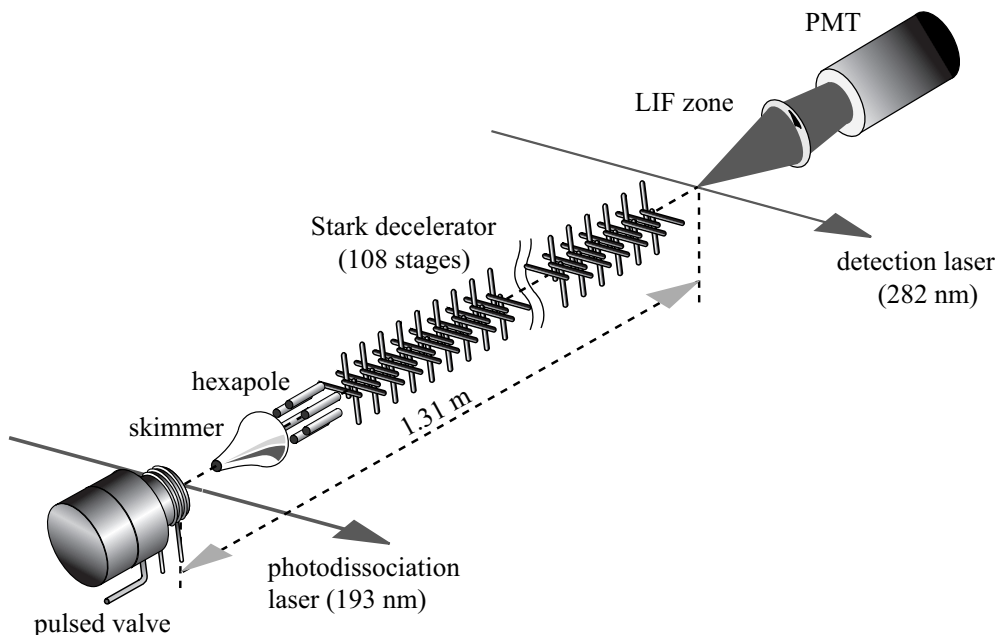


Figure 3.4: Scheme of the experimental set-up. A pulsed beam of OH with a mean velocity of 450 m/s is produced via ArF-laser photodissociation of HNO₃ seeded in Kr. The molecular beam passes through a skimmer, hexapole and Stark decelerator into the detection region. State-selective LIF detection is used to measure the arrival time distribution of the OH ($J = 3/2$) radicals in the detection zone.

pumps are equipped with magnetic bearings to make the vacuum system compatible with radical production methods that rely on the use of corrosive gases as a precursor. A pulsed beam of OH radicals is produced by photodissociation of HNO₃ molecules that are co-expanded with a rare gas through a room-temperature pulsed solenoid valve (General valve, series 9), as described in detail in chapter 2. In the experiments described in this chapter, Kr is used as a seed gas. The mean velocity of the beam is around 450 m/s with a velocity spread (FWHM) of about 15 %. In the supersonic expansion, the beam is rotationally and vibrationally cooled and after the expansion most of the OH radicals reside in the lowest rotational ($J = 3/2$) and vibrational state of the electronic ground state $X^2\Pi_{3/2}$. As was discussed in chapter 2, this state has a Λ -doublet splitting of 0.055 cm^{-1} and each Λ -doublet component is split into a $|M_J| = 1/2$ and a $|M_J| = 3/2$ component when applying an electric field. The $|M_J| = 3/2$ component offers a three times larger Stark shift than the $|M_J| = 1/2$ component. In the experiments described here, only the $M_J\Omega = -3/4$ and $M_J\Omega = -9/4$ components of the low-field seeking upper Λ -doublet component of f parity are of interest. The molecular beam passes a skimmer placed 21 mm from the capillary, and enters the second vacuum chamber. In the experiments described in this thesis, either a skimmer with a 1.5 mm or a 2.0 mm diameter is used. To increase the pumping capacity in the source chamber, the skimmer and the wall that separates the source and decelerator chamber, can be cooled down to liquid nitrogen temperatures. In most experiments however, this possibility is not used. The experiment runs at a repetition rate of 10 Hz, and during operating conditions the pressure in the source and decelerator chambers are typically 2×10^{-5} and 4×10^{-7} Torr, respectively.

In the decelerator chamber, the beam of OH radicals enters a 37 mm long hexapole 23.5 mm from

the skimmer. The hexapole consists of 6 stainless steel rods with 3 mm diameter, placed equidistantly on the outside of a circle with a diameter of 6 mm. Alternating rods are electrically connected to each other. One set of rods is actively grounded, while the other set can be switched to high voltage, using a high voltage power supply (Spellman SL150) in combination with a fast high voltage switch (Behlke Elektronik HTS 151-03-GSM). When a high voltage pulse is applied to the hexapole, the electric field inside the hexapole is zero on the molecular beam axis, and increases quadratically with radial distance r from the beam axis [1, 159]. Molecules in a low field seeking state therefore experience a restoring force towards the molecular beam axis. For these states, a hexapole acts as a positive lens, and the divergence of the molecular beam can be reduced. Using hexapoles of sufficient length, the beam can even be focussed, as is applied to beams of OH radicals by many groups [100, 155, 156]. The Stark effect of the $^2\Pi_{3/2}, J = 3/2, f$ state of OH is (nearly) linear, resulting in a nearly linear restoring force. For low electric fields close to the beam axis, however, the Stark effect is quadratic, causing aberrations of the hexapole lens [143]. In the experiments reported here, the hexapole is used to optimize the (transversal) in-coupling of the beam of OH radicals into the Stark decelerator. The importance of this phase-space matching is explained in detail in ref. [14]. The hexapole is switched on (off) when the beam enters (exits) the hexapole. The voltage on the hexapole is set to maximize the signal of the selected package of OH radicals that exits the decelerator. In most experiments, the hexapole is operated between 10 and 14 kV, resulting in approximately a factor three increase in signal intensity, relative to when the hexapole is not used.

To minimize the longitudinal spreading out of the beam, the Stark decelerator is placed only 16.8 mm from the exit of the hexapole, limiting the total distance from the nozzle orifice to the Stark decelerator to less than 10 cm. The 1188 mm long Stark decelerator consists of an array of 108 equidistant electric field stages, with a center to center distance L of adjacent stages of 11 mm. Each stage consists of 2 parallel 6 mm diameter polished hardened steel rods that are centered 10 mm symmetrically around the beam axis. Alternating stages are rotated by 90° with respect to each other, providing a $4 \times 4 \text{ mm}^2$ spatial transverse acceptance area. It is important to note that the geometry of this new generation Stark decelerator is scaled up by a factor of 2 compared to earlier designs, increasing the spatial acceptance of the decelerator by a factor 2^3 . This up-scaling has been performed while keeping the electric fields in the decelerator the same (*vide infra*). The electrodes of the decelerator are positioned relative to the molecular beam axis within a specified precision of 0.05 mm. A picture of the decelerator, with a close-up of the $4 \times 4 \text{ mm}^2$ opening area between the electrodes, is shown in Fig. 3.5.

Obviously, an electric field strength as high as possible is desired to increase the deceleration rate that can be obtained in the decelerator. The maximum electric field strength that can be reached critically depends on the surface roughness and material of the electrodes, and on the quality of the design of the overall structure. Special care was taken in the design to eliminate any sharp edges in the construction, and to shield the triple junctions (boundary between insulator, metal and vacuum) of the ceramic insulators that support the decelerator [160]. To reduce the risk of electrical breakdown further, the decelerator is exposed to a substantially higher DC voltage before operating the decelerator with switched high voltage pulses. Typically, a maximum voltage up to 130 % of the operation voltage is applied to the electrodes in a high voltage conditioning procedure. During this procedure, the high voltage is applied while the current is limited by $0.5 \text{ G}\Omega$ damping resistors. If the current has been less than 100 nA during at least 10 minutes, the high voltage is increased by 1.0 or 0.5 kV.

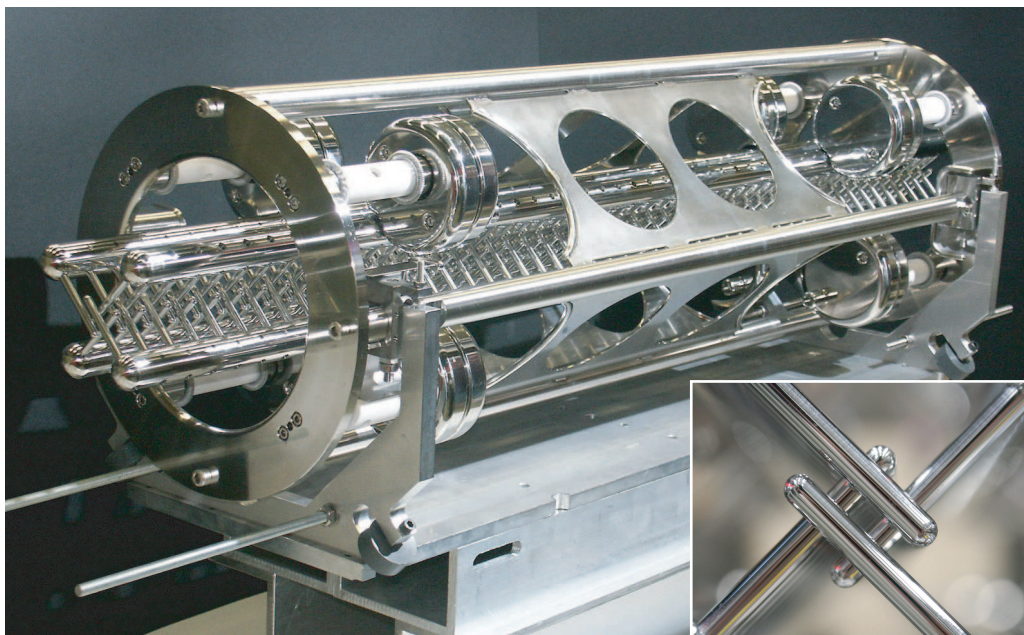


Figure 3.5: Picture of the Stark decelerator. The electric field stages are spaced 11 mm from each other. The length of the device is 1111 mm. The molecular beam passes through the $4 \times 4 \text{ mm}^2$ opening area between the electrodes, that is shown enlarged in the inset. The molecules are decelerated by switching at the appropriate times a voltage difference of 40 kV between opposing electrodes.

This procedure is repeated until the final required voltage is reached, and is applied every time the machine has been exposed to air. In an experiment to investigate the maximum attainable electric fields, the insulators and a small number of electric field stages have been successfully conditioned to $\pm 39 \text{ kV}$, corresponding to a maximum field strength between the electrodes exceeding 220 kV/cm . Operating the decelerator at $\pm 30 \text{ kV}$ or higher should therefore be realistic. However, when all electric field stages are mounted, obtaining these field strengths is considerably more difficult. To date, the decelerator has been successfully conditioned to a maximum DC voltage of $\pm 32.5 \text{ kV}$ between opposing rods, and was tested with switched voltages up to $\pm 25 \text{ kV}$. In the experiments described in this thesis, however, the decelerator was routinely operated using a voltage of $\pm 20 \text{ kV}$ between opposing electrodes in a field stage, creating a maximum electric field strength near the electrodes of 115 kV/cm . This electric field strength is identical to the field strengths used in earlier versions of the Stark decelerator.

The high voltage pulses can be applied to the electrodes using fast high voltage switches (Behlke Elektronik HTS 651-03-GSM), that were specifically developed for the decelerator described here. The individual electrodes of alternating stages are electrically connected to a single high voltage switch, requiring a total number of four independent switches for the decelerator. The switches that are used at the same polarity share a high voltage power supply (Spellman SL1200). In Fig. 3.6 the high-voltage circuitry that is used for the decelerator is schematically depicted. During a single time sequence, the high voltage is delivered by a 300 nF capacitor bank, limiting the voltage drop during a burst to only 3%. Depending on the experiment, the duration of a high voltage burst is typically 2-6 ms. In the remaining time before the next burst starts, the capacitor is charged by a 1.2 kW high voltage power supply that is connected in series with a $26 \text{ k}\Omega$ loading resistor to the

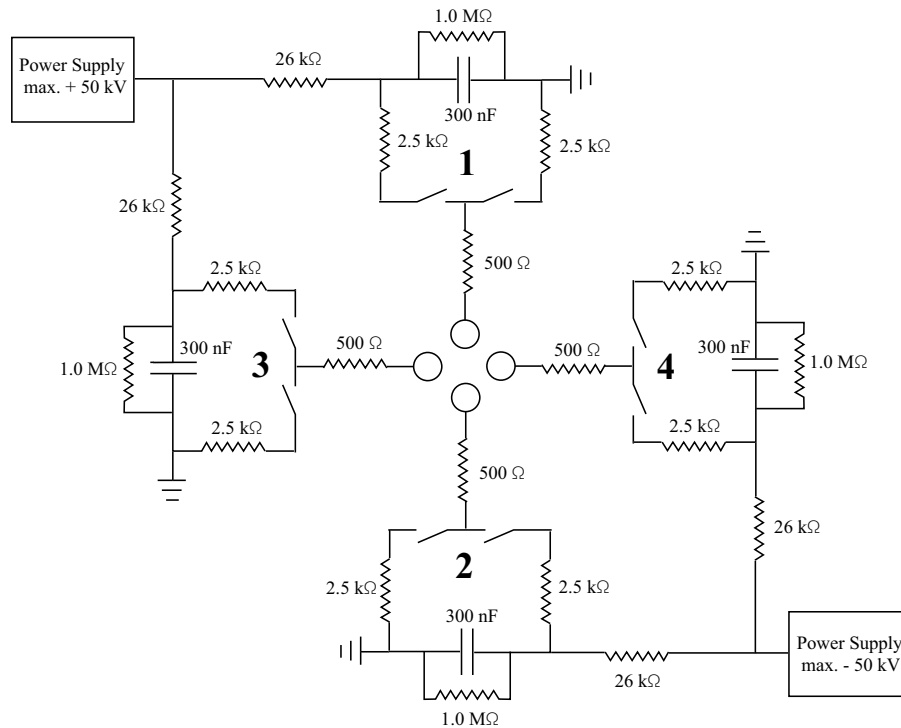


Figure 3.6: The high voltage circuitry that is used to operate the decelerator. Each of the four independent rods of the decelerator is connected to a fast high voltage push-pull switch that is connected to a 300 nF high voltage capacitor bank. Switches of the same polarity share a 50 kV power supply.

capacitor bank. The high voltage push-pull switches switch between both voltage input ports upon application of a TTL trigger pulse. The two voltage inputs are, in series with a 2.5 kΩ resistor, connected to ground and the high voltage capacitor bank, respectively. The decelerator represents a capacitance of approximately 120 pF. With in total a resistance of 3 kΩ between the voltage supply and the decelerator, the voltage can be switched with a $1/e$ time of about 450 ns. During switching, a maximum current of approximately 13 A flows through the switch and the high voltage circuitry. Each of the 4 switch units is placed in a metal box that shields the generated radiation. The molecular beam machine runs at a repetition rate of 10 Hz. Every unit switches about 1000 times per second, and the total power that is dissipated in a unit is on the order of 150 W. Therefore, the resistors are cooled by small fans, and the switches are cooled by a 3 l/min oil (Galden ht 200) flow. The current is monitored by magnetic current probes placed around the high voltage feedthroughs. The total high voltage circuitry described above, allows a maximum number of 120 switch times in a time sequence, with a minimum duration of 20 μs between successive switch times. An interrupt system protects the decelerator and switches against discharges with a current exceeding 15 A, a vacuum in the chambers that is higher than 5×10^{-5} Torr, an insufficient oil flow, or a temperature of the oil exceeding 30°C. In those situations, the switches are interrupted and the high voltage power supplies are disabled. The charged capacitors will then slowly discharge via the 1 MΩ leak resistors. It is emphasized that the increased high voltage required in this decelerator to obtain identical electric field strengths compared to the earlier designs of the Stark decelerator, constitutes a disproportional higher strain on the electrodes, insulators and the high voltage switches and circuitry.

The last 7 stages of the decelerator are electrically and mechanically decoupled from the first

101 stages, and are operated with a separate set of high voltage switches and power supplies. The advantage of this is that maximum flexibility can be obtained, as these last stages are easily replaced or modified leaving the main decelerator intact. The limited number of electric field stages enables a compact design, which is advantageous when the decelerator is to be used in combination with an electrostatic trap, as will be discussed in chapter 6. In addition, the operation voltage of these last stages can be selected independently from the first 101 stages to reduce the risk of electrical breakdown between the decelerator and the electrostatic trap. A maximum voltage of ± 15 kV is applied to these last stages, using a high voltage circuitry similar to Fig. 3.6. The switches (Behlke Elektronik HTS 301-03-GSM) and power supplies (Spellman SL150) are connected to the interrupt system discussed before. For these switch units, no oil or air cooling is required. Unless stated otherwise, the last 7 stages of the decelerator were not used in the experiments described in this chapter, and were grounded. The trigger pulses for the switches are generated by a programmable pulse generator, with a resolution of 100 ns. In total 8 independent channels are available, where each channel can trigger a maximum of two switch units. The valve, lasers and pulse generator are synchronized by a master clock (Stanford research DG535) running at a repetition rate of 10 Hz.

The OH radicals are state selectively detected 21 mm downstream from the last electric field stage (1.307 m from the nozzle) using an off-resonant Laser Induced Fluorescence (LIF) detection scheme. All high voltages of the decelerator and hexapole are switched off 3 μ s prior to detection. The 282 nm radiation of a pulsed dye laser (Spectra Physics INDI Nd:YAG laser/PDL3 dye laser combination) crosses the molecular beam at right angles. The population of the low-field seeking $J = 3/2$ component of f parity is probed by inducing both the $Q_{21}(1)$ and the $Q_1(1)$ transitions of the $A^2\Sigma^+, v = 1 \leftarrow X^2\Pi_{3/2}, v = 0$ band. The population in both $M_J\Omega$ components of this state is probed simultaneously. Typically, 1.5 mJ of radiation in a 5 ns pulse with a 0.08 cm^{-1} bandwidth is used in a 5 mm laser beam diameter to saturate the transitions. The $A^2\Sigma^+, v = 1$ state has a radiative lifetime of 760 ns [161], and fluorescence occurs mainly via the $A^2\Sigma^+, v = 1 \rightarrow X^2\Pi_{3/2}, v = 1$ band around 313 nm. The emitted photons are imaged onto a photomultiplier tube (PMT)(Electron Tubes B2/RFI, 9813 QB) using a lens with a focal length of 50 mm, and displayed on a digital oscilloscope (Yokogawa DL4100). Stray light from the laser is reduced by passing the laser beam through light baffles between the entrance and the exit windows. Stray light is further suppressed by optical filtering in front of the PMT. The fluorescence signal is averaged in a time window of approximately 3 μ s, placed about 300 ns after the laser scatter peak. A background signal obtained from a time window placed before the laser scatter peak is subtracted from the fluorescence signal, and stored in a personal computer using home-built data acquisition software.

In most experiments described in this chapter, the performance of the Stark decelerator is studied by recording the time-of-flight (TOF) profile of the OH radicals exiting the decelerator, by scanning the timing of the excitation laser relative to the dissociation laser. For a set time delay between the two lasers, typically between 8 and 32 shots are averaged, before the time delay is increased. It is emphasized that using photodissociation as the production method for the OH radicals, the beam is prepared at a well defined position and time, which is ideal for an accurate interpretation of the observed TOF profiles.

3.4 Experimental results

3.4.1 Guiding a molecular beam of OH radicals

In Fig. 3.7, the TOF profiles are shown that are observed when the decelerator is operated at a phase angle of $\phi_0 = 0^\circ$, but when the time-sequence is calculated for different initial velocities of the synchronous molecule. Operation of the decelerator at $\phi_0 = 0^\circ$ corresponds to a travelling potential well, moving with the (constant) velocity of the synchronous molecule. The first pair of electrodes of the decelerator is switched to high voltage when the synchronous molecule is exactly in between the first and second set of electrodes, thereby coupling in the beam in the center of the longitudinal acceptance region of the decelerator. The velocity distribution of the initial molecular beam can be determined, by choosing a velocity of the well that has no overlap with the velocity distribution of the molecular beam. The molecules in the beam are sometimes accelerated and decelerated, and their velocity will, on average, not change as they move through the decelerator, leaving the (longitudinal) velocity distribution of the initial molecular beam unchanged. The electric fields in the decelerator do exert a net focussing force on the beam though, resulting in a much improved signal to noise ratio, compared to an experiment where the decelerator is not switched. This situation is depicted in curve *a* of Figure 3.7, where the TOF profile is shown that is observed if a velocity of the well of 350 m/s was chosen. From the observed profile, a mean beam velocity of 455 m/s with a velocity spread (full width at half maximum, FWHM) of 15 % is deduced. Curves *b*, *c*, *d*, and *e* show the observed TOF profile when the decelerator is operated with a velocity of the well of 400 m/s, 440 m/s, 455 m/s and 470 m/s, respectively. This series of experiments clearly demonstrates that a significant fraction of the molecular beam, centered around the velocity of the potential well, is selected by the decelerator and transported through the machine as a compact package. The molecules in the beam that are not trapped by the travelling potential well, experience the switched electric fields as well, resulting in rich phase space dynamics that manifests itself by the features in the wings of the TOF profiles. A more detailed description of these untrapped dynamics of the OH molecules in the decelerator is given in section 3.4.3. From a calculation of the (time-dependent) electric field distribution inside the decelerator, and the known Stark effect of OH, the trajectories of the OH molecules through the Stark decelerator can be simulated. The arrival time distributions that result from three dimensional trajectory calculations of the experiment, are shown underneath the observed profiles in Fig. 3.7. In the simulations both $M_J\Omega$ components of the OH ($J = 3/2$) state are taken into account, and it is assumed that directly after production both $M_J\Omega$ components are equally populated in the beam. It is seen that the simulations quantitatively reproduce the observations.

From the calculations, the contributions of the individual $M_J\Omega$ components to the TOF profiles can be identified. In Fig. 3.8 (*a*) the observed TOF profile is shown that is obtained when operating the decelerator at a phase angle $\phi_0 = 0^\circ$ for a velocity of the synchronous molecule of 450 m/s. It is noted that the higher fluorescence collection efficiency of the LIF zone that was used in this experiment results in a significantly improved signal to noise ratio compared to the measurements presented in Fig. 3.7, and the features in the wings of the TOF profiles are more pronounced. Curve *b* shows the TOF profile that results from a three dimensional trajectory simulation, taking both $M_J\Omega$ components into account. A quantitative agreement with the observations is obtained. Curves *c* and *d* show the individual contributions of the $M_J\Omega = -9/4$ and the $M_J\Omega = -3/4$ components to the TOF profile, respectively. The $M_J\Omega = -9/4$ contributes mainly to the main peak, reflecting the larger phase space acceptance of the decelerator, and the more ideal focussing properties of the

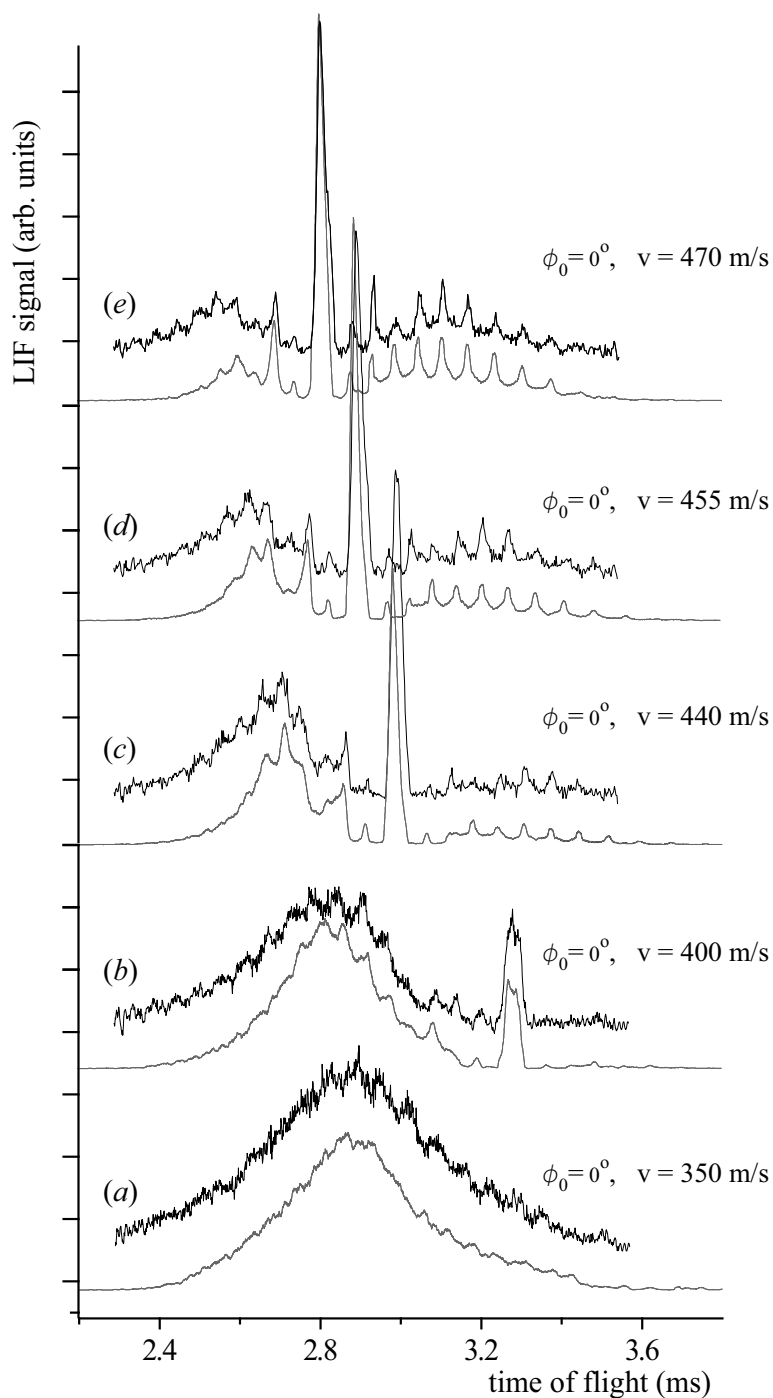


Figure 3.7: Series of observed TOF profiles for a beam of OH radicals with a mean velocity of 450 m/s, when the decelerator is operated at phase angle $\phi_0 = 0^\circ$ for a synchronous molecule with a velocity of 350 m/s (curve a), 400 m/s (curve b), 440 m/s (curve c), 455 m/s (curve d), and 470 m/s (curve e), respectively. The TOF profiles that are obtained from a three dimensional trajectory simulation of the experiment are shown underneath the experimental profiles.

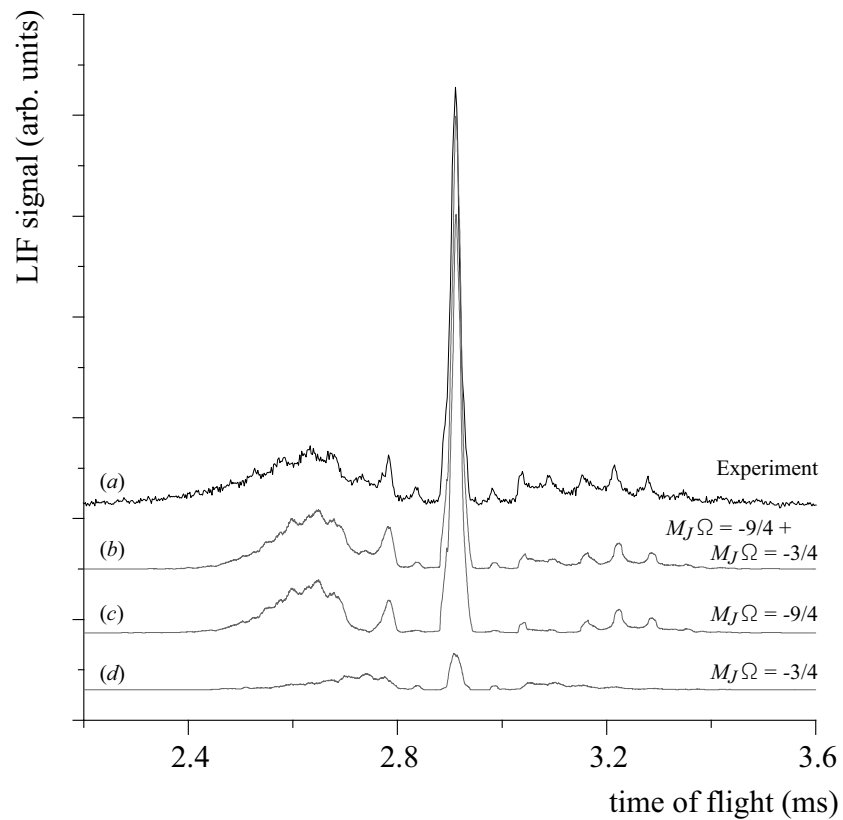


Figure 3.8: Observed TOF profile when the decelerator is operated at a phase angle $\phi_0 = 0^\circ$ for a synchronous molecule with a velocity of 450 m/s. The TOF profile that is obtained from a three dimensional trajectory simulation of the experiment is shown underneath the experimental profile. The individual contributions of both $M_J\Omega$ components of the OH ($^2\Pi_{3/2}$, $J = 3/2$) state to the profile are indicated.

hexapole for this component. Interestingly, the smaller peaks in the wings of the distributions show a mixed $M_J\Omega$ character with a different degree of mixing for each peak. It is evident from Fig. 3.8 that both $M_J\Omega$ components need to be taken into account to obtain a quantitative agreement between trajectory simulations and experimental data.

3.4.2 Deceleration of a molecular beam of OH radicals

A part of the molecular beam can be decelerated when operating the decelerator at a phase angle $0^\circ < \phi_0 < 90^\circ$, decreasing gradually the velocity of the travelling potential well. In Fig. 3.9(a) the observed TOF profile is shown when the decelerator is operated with a time sequence that was calculated for a phase angle of $\phi_0 = 70^\circ$ and for a synchronous molecule with an initial velocity of 470 m/s. With these settings, the decelerator extracts 1.1 cm^{-1} of kinetic energy from the synchronous

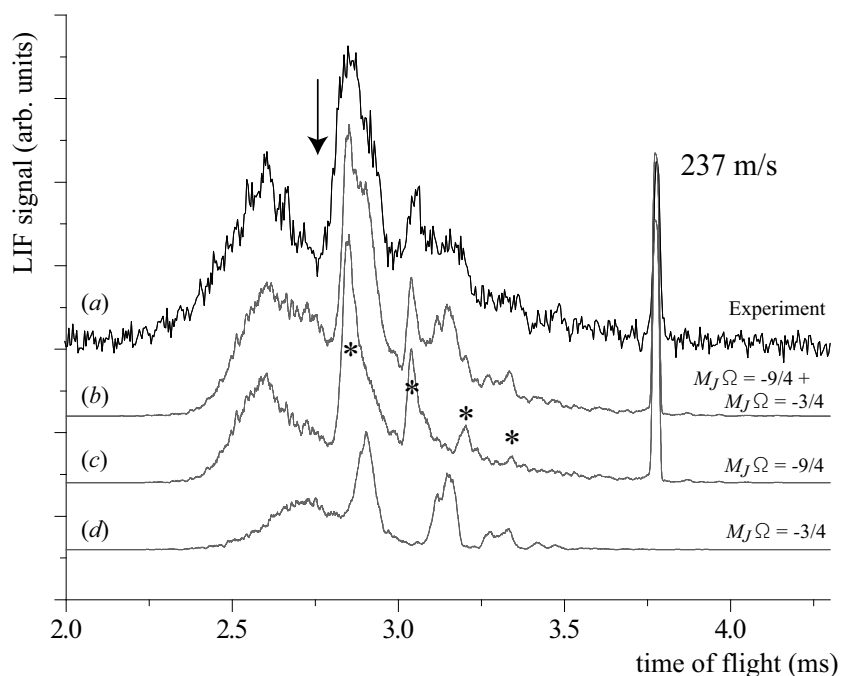


Figure 3.9: LIF signal of OH ($J = 3/2$) radicals exiting the decelerator as a function of time after OH production. The decelerator is operated at a phase angle of $\phi_0 = 70^\circ$ for a synchronous molecule with an initial velocity of 470 m/s. A significant fraction of the molecular beam is decelerated to 237 m/s. The TOF profile that results from a simulation of the experiment, together with the individual contributions of both $M_J\Omega$ components to the profile, is shown underneath the experimental curve.

molecule in every electric field stage. A selected fraction of the molecular beam is decelerated from 470 m/s (kinetic energy of 157 cm^{-1}) to a final velocity of 237 m/s (40 cm^{-1}), and is split off from the remaining part of the beam that is not decelerated. The decelerated bunch of molecules arrives in the LIF zone about 3.8 ms after production. The hole in the TOF profile of the fast beam due to the disappearance of OH radicals that are decelerated is indicated by an arrow. The improved spatial acceptance of this new generation Stark decelerator results in a peak intensity of the decelerated package that is similar to the peak intensity of the non-decelerated beam. The TOF profile that is obtained from a three dimensional trajectory simulation of the experiment is shown in curve (b),

together with the individual contributions of both $M_J\Omega$ components to the profile (curves (c) and (d), respectively). The simulations quantitatively reproduce the observed TOF profile. As expected, the decelerated package purely consists of molecules in the $J = 3/2$, $M_J\Omega = -9/4$ state, but molecules in the $J = 3/2$, $M_J\Omega = -3/4$ state significantly contribute to the signal of the non-decelerated beam. The $M_J\Omega$ composition of the structured TOF profile of the non-decelerated beam is easily identified from the simulations. In addition, these calculations reveal the origin of the interesting structure of the non-decelerated beam, which manifests itself for instance by the series of peaks indicated with a star in Fig. 3.9(c). A detailed discussion of these features will be given in section 3.4.3.

The molecular beam can be decelerated to lower final velocities by operating the decelerator at a higher phase angle, and/or by selecting a lower initial velocity of the synchronous molecule. The depth of the travelling potential well rapidly decreases for increasing values of ϕ_0 . It is therefore advantageous to use a lower initial velocity instead. In Fig. 3.10 a series of TOF profiles is shown

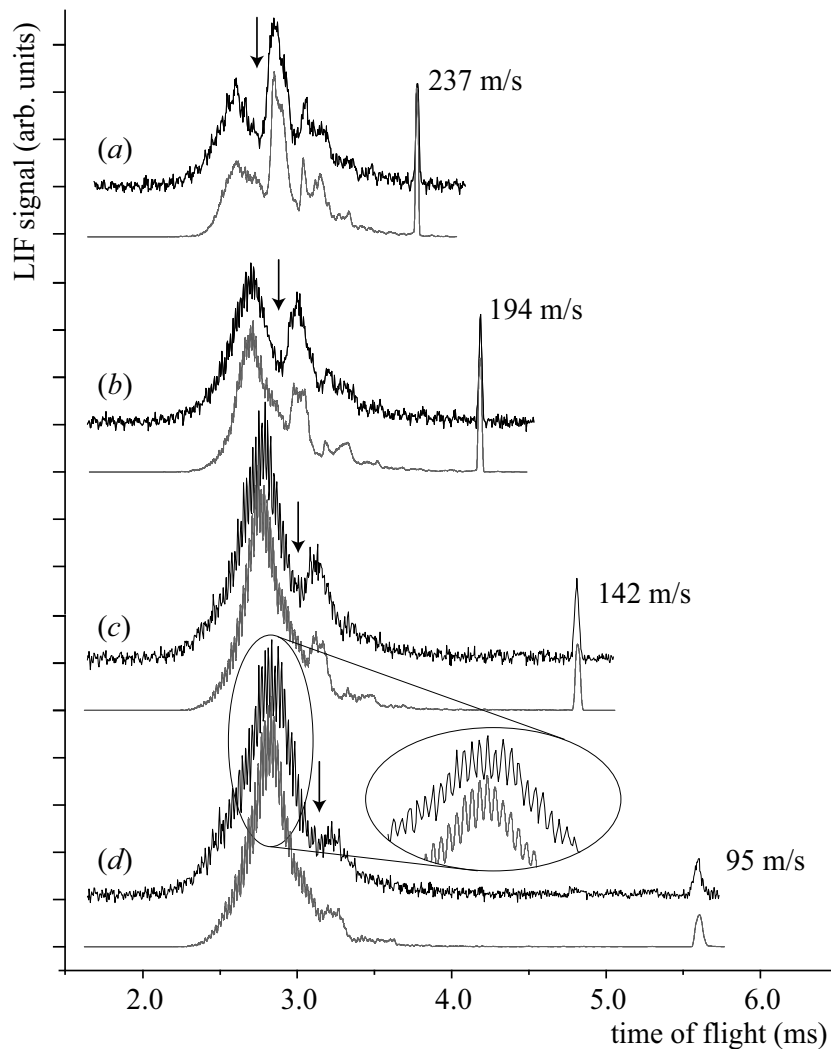


Figure 3.10: Observed and simulated TOF profiles of a molecular beam of OH radicals exiting the Stark decelerator when the decelerator is operated at a phase angle of 70° for a synchronous molecule with an initial velocity of 470 m/s (a), 450 m/s (b), 430 m/s (c) and 417 m/s (d). The molecules that are captured by the decelerator are split off from the molecular beam and arrive at later times in the detection region.

that is obtained when the Stark decelerator is operated at a phase angle of $\phi_0 = 70^\circ$ and an initial velocity of the synchronous molecule of 470 m/s (curve *a*), 450 m/s (*b*), 430 m/s (*c*), and 417 m/s (*d*). With these settings, the decelerated bunch of molecules exits the decelerator with a final velocity of 237 m/s, 194 m/s, 142 m/s and 95 m/s, respectively. These measurements are complementary to the TOF profile shown in Fig. 3.9, which is identical to curve *a*. Again, the holes in the profiles of the non-decelerated beam that results from the removal of the bunch of OH radicals that is decelerated, is indicated by the vertical arrows. The width of the arrival time distribution of the decelerated package becomes larger for lower values of the final velocity. This is due to the spreading out of the beam while flying from the exit of the decelerator to the LIF zone, and the spatial extent of the detection laser beam. Both effects are incorporated in the trajectory simulations of the experiments, shown underneath the observed profiles. In curves (*c*) and (*d*) a rich oscillatory structure on the TOF profile of the fast beam is observed as shown enlarged in the figure. This structure results from a modulation of the phase space distribution of the beam in the decelerator, and will be discussed in more detail in chapter 4. In general, an excellent agreement between the trajectory simulations and the observed TOF profiles is obtained. The relative signal intensities of the different experimental TOF profiles, as well as the relative peak intensity of the decelerated beam and the fast beam within each profile, are quantitatively reproduced. This verifies that indeed the decelerator transports the selected package of molecules to lower velocities without loss. To date, no indications have been found for the occurrence of losses due to, for instance, Majorana transitions [141], or the re-projection of the $M_J\Omega = -9/4$ component onto the $M_J\Omega = -3/4$ component when the fields are switched in the decelerator.

Obviously, selecting a velocity that is lower than the mean velocity of the beam results in a lower phase-space density of the decelerated package than the peak phase-space density of the molecular beam. Using Xe as a carrier gas instead of Kr, the mean velocity of the beam can be reduced to approximately 365 m/s, enabling the operation of the decelerator at significantly lower phase angles. However, Xe enhances cluster formation in the expansion, resulting in a lower beam intensity. Together with the increased spreading out of the beam before the entrance of the Stark decelerator, this reduces the advantages of the lower initial velocity. From a sequence of experiments using Kr and Xe as carrier gases, it is found that Xe is superior if final velocities lower than approximately 150 m/s are required. In experiments described in chapter 6, both Kr and Xe are used as a carrier gas to decelerate a bunch of OH radicals to a final velocity of approximately 20 m/s, before loading them into an electrostatic quadrupole trap.

3.4.3 Evolution of the beam through the Stark decelerator

In addition to demonstrating the operation principle of a decelerator, the TOF profiles of Fig. 3.7 to 3.10 indicate rich phase space dynamics of the untrapped molecules as well. A detailed understanding of the dynamics of the beam in the decelerator, both of the part that undergoes phase stable oscillations and of the molecules that are not trapped, can be obtained from the trajectory simulations. These simulations accurately reproduce the observed TOF profiles; the calculated phase space distributions should therefore be realistic as well. The details of the evolution of the phase space distribution of the beam throughout the deceleration process will depend on the exact settings of the decelerator, but a good understanding of the general features can be obtained by studying two limiting cases. In this section, the progression of the beam inside the decelerator is discussed, if the decelerator is operated with a time sequence that corresponds to the guiding experiment presented in Fig. 3.8 (the decelerator is operated at phase angle $\phi_0 = 0^\circ$), and to the deceleration experiment shown in

Fig. 3.9 ($\phi_0 = 70^\circ$). To test the validity of the (1 dimensional) model presented in section 3.2, 1 dimensional trajectory simulations were carried out for a beam of OH radicals that are exclusively in the $J = 3/2, M_J\Omega = -9/4$ state. The influence of transverse effects on the longitudinal phase space distributions will be discussed in chapter 5.

In Fig. 3.11 the evolution of the longitudinal phase space distribution of the beam of OH ($M_J\Omega = -9/4$) radicals is shown, that results from a one dimensional trajectory calculation of the measurement presented in Fig. 3.8. The decelerator is operated at a phase angle $\phi_0 = 0^\circ$ for a synchronous molecule with an initial velocity of 450 m/s. The phase space distribution is shown at the switch time when the synchronous molecule is in stage 1 ($T = 0.23$ ms after production of the beam), stage 21 ($T = 0.72$ ms), stage 41 ($T = 1.21$ ms), stage 81 ($T = 2.19$ ms), and stage 101 ($T = 2.68$ ms) of the Stark decelerator. In this notation stage i represents the region in the decelerator between electrode pairs i and $i + 1$. The entrance (center of electrode pair 1) and exit (center of electrode pair 102) are indicated by vertical dashed lines. The phase space diagrams that result from the model presented in section 3.2 are given as a overlay. In the simulations it is assumed that just after production ($T = 0.00$ ms), the beam has a Gaussian velocity profile with a mean velocity of 450 m/s and velocity spread of 15 %. The longitudinal position spread is determined by the width of the dissociation laser focus, and a Gaussian profile with a width of 4 mm is assumed. This results in a vertical phase space distribution centered around the position of the nozzle orifice (phase space distribution not shown). The upper graph in Fig. 3.11 shows the phase space distribution of the beam at $T = 0.23$ ms. At this time, the most intense part of the molecular beam is in the center of the first electric field stage, and the first high voltage pulse is applied to the Stark decelerator. The tilted phase space distribution results from the flight of the beam from the production region to the Stark decelerator. It is seen that the longitudinal acceptance of the decelerator encompasses a significant fraction of the emittance of the molecular beam. At $T = 0.72$ ms, the synchronous molecule has progressed to stage 21 in the decelerator. Molecules within the separatrix ('bucket') have rotated around the synchronous molecule, in agreement with the model of section 3.2. Molecules outside this bound region follow the lines of constant energy in the phase space diagram, resulting in a pronounced modulation of the phase space distribution of the beam. This modulation represents the influence of the switched electric fields on the molecules that are not trapped by the travelling potential well. In fact, the regions where the modulated distribution is 'horizontal' give rise to the small peaks in the wings of the TOF profiles of Fig. 3.7 and 3.8. The trajectory of the molecules outside the separatrix are not bound and the corresponding fraction of the molecular beam will continue to spread out as it progresses through the decelerator. This becomes increasingly apparent in the phase space distributions at $T = 1.21$ ms (stage 41), $T = 2.19$ ms (stage 81) and $T = 2.68$ ms (stage 101). In these graphs, only a selected fraction of the phase space distribution of the beam is shown for reasons of clarity. The bound molecules continue to rotate around the synchronous molecule, and are kept together throughout the decelerator. The unbound molecules spread out in position, and approach the separatrices of the buckets in front of and behind the bucket that contains the stable molecules. Obviously, for an infinite decelerator, the density of the unbound molecules will approach zero, resulting in a TOF profile that consists of a sharp narrow peak on a zero signal baseline. For the decelerator used in the present experiments, the 101 electric field stages that are used are sufficient to diminish the density of the beam close to the first neighboring separatrices to a undetectable value, as is seen in Fig. 3.7 and 3.8 by the region of zero signal in the TOF profiles on either side of the main peaks.

In analogy to Fig. 3.11, the longitudinal phase space dynamics of a beam of OH ($J = 3/2, M\Omega =$

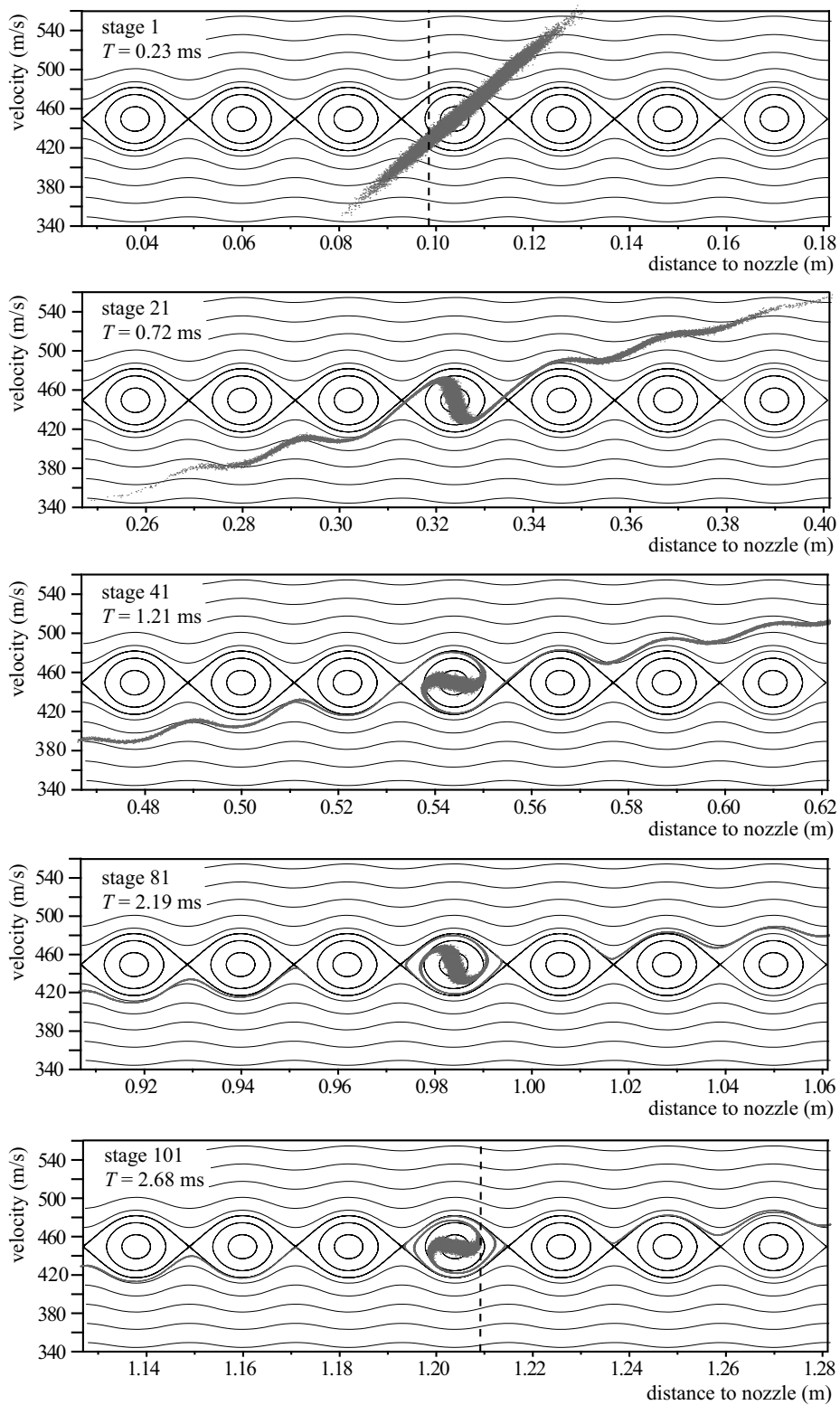


Figure 3.11: Evolution of the longitudinal phase space distribution of the beam of OH ($M_J\Omega = -9/4$) radicals that results from a one dimensional trajectory calculation of the measurement shown in Fig. 3.8. The decelerator is operated at a phase angle $\phi_0 = 0^\circ$. The distribution is shown at the switch time when the synchronous molecule is in stage 1, 21, 41, 81, and 101 of the Stark decelerator. The entrance and exit of the decelerator are indicated by the dashed lines.

$-9/4$) radicals, for settings of the decelerator that correspond to the deceleration experiment shown in Fig. 3.9, is depicted in Fig. 3.12. The Stark decelerator is operated at a phase angle of $\phi_0 = 70^\circ$ for a synchronous molecule with an initial velocity of 470 m/s, and the corresponding phase space diagrams of the decelerator are given as an overlay. The upper graph shows the distribution at $T = 0.24$ ms, when the synchronous molecule is in the center of the phase stable region in the first electric field stage of the decelerator. The center position of the first pair of electrodes is again indicated by the vertical dashed line. The nozzle to skimmer distance that is used in this experiment is slightly larger. In the discussion of the progression of the beam through the decelerator, three different regions in the phase space distribution of the beam in stage 1 will be considered separately, namely (i) molecules that are within the bucket bound by the separatrix; (ii) the part of the beam that is in position, and therefore also in velocity, ahead of the bucket; and (iii) the part of the beam that lags behind. The molecules within the bucket (part (i)) are phase stable, and oscillate around the velocity and phase of the synchronous molecule. The size of the separatrix is sufficiently small that the bucket is completely filled with molecules, and the spiral-like structure occurring in Fig. 3.11 is absent. The separatrix accurately describes the shape of the phase stable region, and the selected bunch of molecules leaves the decelerator with a velocity of 237 m/s, 3.36 ms after production of the beam.

Analogous to operating the decelerator at $\phi_0 = 0^\circ$, the part of the beam that was initially too fast (part (ii)) is modulated by the presence of empty buckets along the length of the entire decelerator. When the beam 'overtakes' the position of a bucket, the interaction with the fields results in a horizontal phase space distribution, ultimately leading to a peak in the TOF distribution. However, the pronounced oscillatory structure in the observed TOF profiles of the non-decelerated beam, shown enlarged in Fig. 3.10, cannot be understood from this alone and a full understanding of these oscillations is only obtained when higher order effects are included in the model for phase stability. This topic will be addressed in chapter 4.

Molecules just outside the bucket and that are initially too slow (part (iii)), are not captured by the decelerating potential well, and follow the curves of equal energy in the space space diagrams. These molecules accelerate with respect to the synchronous molecule, as can be seen from the phase space distribution of the beam at $T = 0.73$ ms (stage 21). Molecules that were initially even slower start interacting with the empty buckets that lag behind. The beam can not penetrate into the stable area, and evolves around the separatrix of the corresponding bucket. This leads to 'turning points' in the phase space distribution of the beam, that are most apparent in the diagram that corresponds to $T = 1.26$ ms (stage 41). These turning points result in the series of peaks in the TOF profile of the non-decelerated beam, indicated by stars in Fig. 3.9 of section 3.4.2. The tail in the distribution that connects the filled bucket containing the trapped package and the corresponding turning point becomes increasingly longer and less dense as the velocity of the synchronous molecule decreases. At $T = 2.54$ ms the decelerated package has a velocity close to 290 m/s, and is almost completely decoupled from the part of the beam that is not decelerated. At this time, the fastest molecules in the beam have already reached the detection zone.

3.4.4 Simultaneous deceleration of both $M_J\Omega$ components

In Ref [14] it was demonstrated using a beam containing various isotopomers of ammonia, that the simultaneous deceleration of bunches of molecules of different species, or molecules of the same species but with a different Stark shift, is possible. If the time-sequence is calculated for the molecule that can be least-well decelerated, a synchronous molecule with a different Stark effect and/or

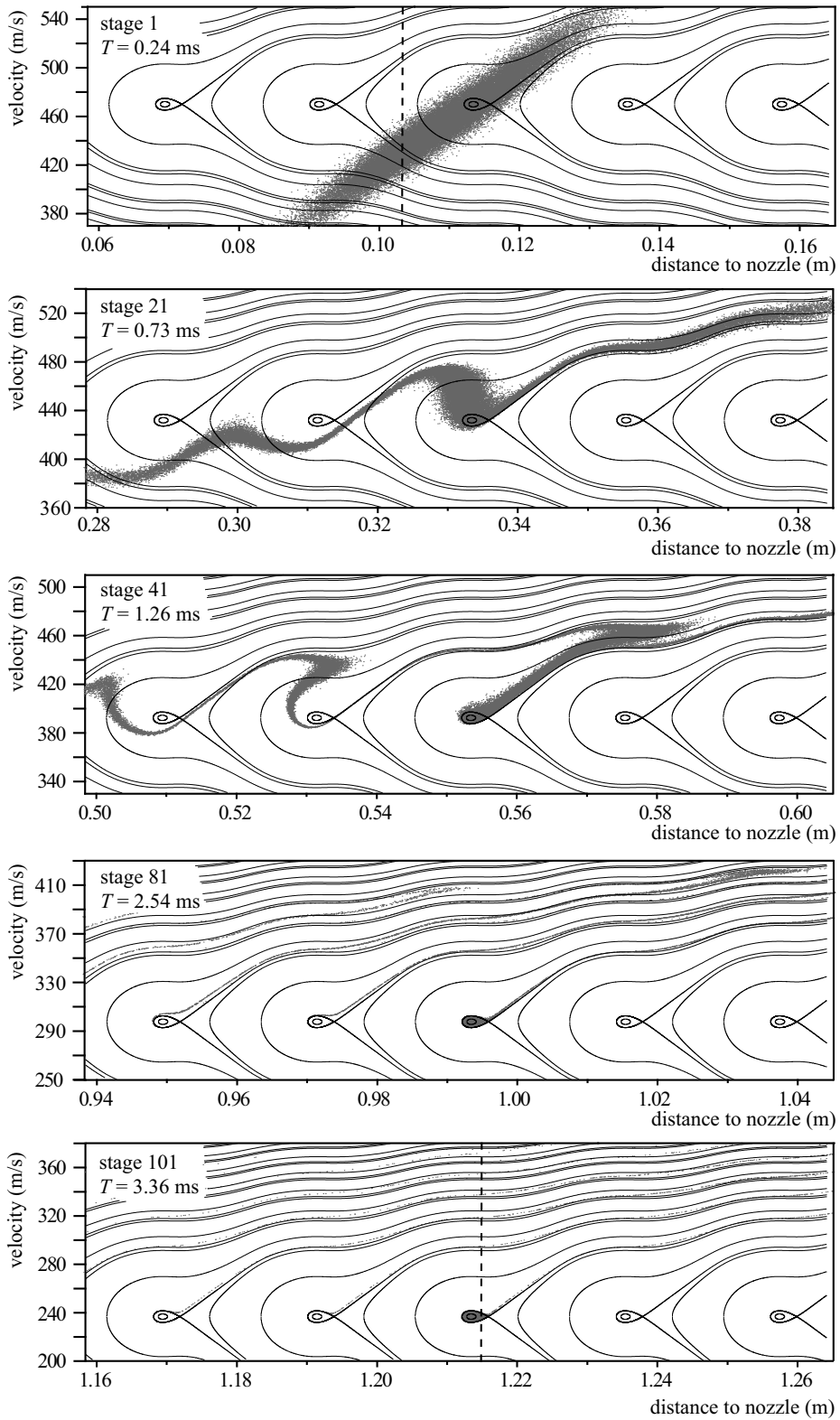


Figure 3.12: Evolution of the longitudinal phase space distribution of the beam that results from a one dimensional trajectory calculation of the deceleration experiment shown in Fig. 3.9. The decelerator is operated at a phase angle $\phi_0 = 70^\circ$.

different mass can be found as well. Both molecules are then matched to the time-sequence and simultaneously decelerated, although the acceptance of the decelerator will be different for both cases. The requirements for the existence of two different synchronous molecules for a given time sequence can be written as:

$$\frac{\Delta K'(\phi'_0)}{m'} = \frac{\Delta K(\phi_0)}{m}. \quad (3.6)$$

In this expression, the synchronous molecule for which the time sequence of the decelerator is calculated has mass m and loses a kinetic energy $\Delta K(\phi_0)$ per electric field stage. The corresponding parameters for the additional synchronous molecule are indicated by primes. For a beam of OH ($J = 3/2$) radicals equation 3.6 implies that molecules in both the $M_J\Omega = -3/4$ and the $M_J\Omega = -9/4$ component of the $J = 3/2$ state can be decelerated simultaneously. To a good approximation, the Stark shift of the $M_J\Omega = -3/4$ component is three times smaller than the shift of the $M_J\Omega = -9/4$ in identical electric fields, and eq. 3.6 reduces to

$$\sin(\phi_0)_{M_J\Omega=-9/4} = \frac{1}{3} \sin(\phi_0)_{M_J\Omega=-3/4}. \quad (3.7)$$

When the decelerator is operated with a time sequence that is calculated for OH ($J = 3/2$, $M_J\Omega =$

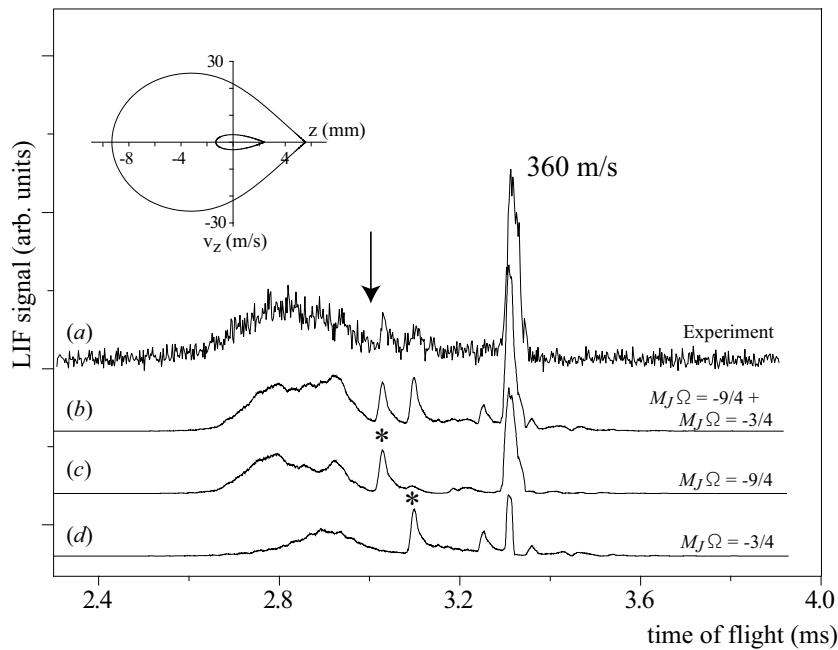


Figure 3.13: Observed TOF profile for OH ($J = 3/2$) radicals when the decelerator is operated with a time-sequence that is calculated for OH ($J = 3/2$, $M_J\Omega = -3/4$) at a phase angle of 70° . The result of a three dimensional trajectory simulation of the experiment is shown underneath the experimental profile for the $M_J\Omega = -3/4$ and $M_J\Omega = -9/4$ components combined, and separately. Molecules in both states are simultaneously decelerated from 430 m/s to 360 m/s. The longitudinal acceptance of the decelerator is given in the inset for OH ($J = 3/2$, $M_J\Omega = -3/4$) (inner curve) and OH ($J = 3/2$, $M_J\Omega = -9/4$) (outer curve).

$-3/4$) at a phase angle of 70° , a TOF profile as shown in Fig. 3.13 (a) is observed. In this experiment, the OH molecular beam was produced without the quartz capillary in front of the nozzle, reducing the mean velocity of the molecular beam to 430 m/s. From eqn. (3.7), the time-sequence that is applied

to the decelerator corresponds to a phase angle of 18° for OH in the $J = 3/2$, $M_J\Omega = -9/4$ quantum state. The corresponding longitudinal acceptance regions for molecules in both states are given in the inset. A synchronous molecule with an initial velocity of 430 m/s is decelerated to a final velocity of 360 m/s, and the decelerated package arrives in the detection region about 3.3 ms after production. The hole that is observed in the TOF profile of the part of the molecular beam that is not decelerated is again indicated by an arrow.

With the present LIF detection system we cannot discriminate between both $M_J\Omega$ components, but the contribution of the individual components can be deduced from the TOF profiles resulting from trajectory simulations, that are shown underneath the experimental profile. The simulated profile including both components, shown in curve (b) is seen to reproduce the observations. In curve (c) and (d) the individual contribution of both components to the TOF profile is depicted. Molecules in both $M_J\Omega$ components are decelerated to the same final velocity of 360 m/s. The TOF profile of the decelerated package for the $M_J\Omega = -9/4$ component has a higher peak intensity and is broader, reflecting the larger longitudinal acceptance of the decelerator for molecules in this state. In both cases, the profile of the beam that is not decelerated shows the characteristic structure discussed in the previous section. The peaks that originate from the 'turning points' in the longitudinal phase space distribution of the beam are indicated by stars, and appear at different times for both $M_J\Omega$ components.

3.5 Conclusions

A new generation Stark decelerator is developed, that is designed such that a large fraction of a molecular beam pulse can be selected and decelerated. This was demonstrated by decelerating a sizeable fraction of a molecular beam of OH ($J = 3/2$, $M_J\Omega = -9/4$) radicals with a mean velocity of 450 m/s to a final velocity of 95 m/s. Both the deceleration process and the phase-space dynamics of the molecules that are not pase-stable are studied in detail. The observed time-of-flight profiles of molecular beams passing through the Stark decelerator that are presented in this chapter are text book examples for the operation principles of a Stark decelerator.

CHAPTER 4

HIGHER-ORDER RESONANCES IN A STARK DECELERATOR

The motion of polar molecules can be controlled by time-varying inhomogeneous electric fields. In a Stark decelerator, this is exploited to select a fraction of a molecular beam that is accelerated, transported or decelerated. Phase stability ensures that the selected bunch of molecules is kept together throughout the deceleration process. In this chapter an extended description of phase stability in a Stark decelerator is given, including higher-order effects. This analysis predicts a wide variety of resonances that originate from the spatial and temporal periodicity of the electric fields. These resonances are experimentally observed using a beam of OH (${}^2\Pi_{3/2}, v = 0, J = 3/2$) radicals passing through a Stark decelerator.

Based on:

Higher-order resonances in a Stark decelerator

Sebastiaan Y.T. van de Meerakker, Nicolas Vanhaecke, Hendrick L. Bethlem, and Gerard Meijer
Phys. Rev. A **71**, 053409 (2005).

4.1 Introduction

In chapter 3 a one dimensional model, following the description given in the references [8, 14, 72], was presented for the motion of polar molecules through a Stark decelerator. In analogy to the operation of a LINAC [162], the concept of phase stability is essential for the operation of a Stark decelerator. Together with the transverse focussing in the decelerator, phase stability ensures that molecules in a selected (subset of) quantum state(s) can be accelerated, guided, or decelerated without loss, independent of the length of the decelerator; molecules within a certain position and velocity interval are selected and decelerated, keeping the phase space density of the selected bunch of molecules constant. Phase stability in a Stark decelerator quantitatively governs the dynamics of the selected package, and is fundamental to the understanding of the deceleration process. The same principle of phase stability is essential in the description of schemes for deceleration and bunching of molecules with pulsed travelling optical lattices [85, 87].

In recent experiments we have observed sharp and intense resonances in time-of-flight profiles of OH radicals exiting a Stark decelerator, where the available model for phase stability [8, 14, 72] predicts an almost structure-less profile. These features strongly suggest that phase stability beyond the current model is present. Numerical trajectory simulations of the experiment accurately reproduce the observations, but such simulations *a priori* yield no understanding of the physical origin of these features. In this chapter, an extended description of phase stability in a Stark decelerator is given, including higher-order terms in the analytical model. Additional phase stable regions are found that originate from the spatial and temporal periodicity of the electric fields. A comprehensive and intuitive picture of the physical background of these new resonances is presented.

4.2 Theory

4.2.1 Phase stability

Before extending the current model of phase stability in a Stark decelerator, the description of phase stability given in chapter 3 is briefly repeated here. The decelerator consists of an array of electric field stages centered a distance L apart, as schematically represented in Fig. 4.1. Opposing rods are connected to switchable power supplies with different polarity. All alternating electric field stages are electrically connected to each other. When the odd pairs of electrodes are switched to high voltage, the even pairs are switched to ground and vice versa. At any given time, the potential energy of a polar molecule as a function of its position has periodicity $2L$. In the extended description of phase stability presented in this paper, it is convenient to describe the motion of a molecule in terms of its reduced position θ , which has periodicity 2π . At a given time t , we define the reduced position $\theta = 0$ in between two adjacent pairs of electrodes such that the electrodes at $\theta = \pi/2$ are grounded, as shown in Figure 4.1. Switching of the electric field configuration corresponds to a phase shift of θ by π . The reduced position of the molecule at the time the fields are switched is defined as the phase-angle ϕ ; more precisely, ϕ coincides with θ immediately after the fields have been switched. This definition of ϕ thereby follows the earlier definition made in ref. [8] and [72].

By definition, a molecule with velocity v_0 is called *synchronous* if its reduced position is always the same at the time the fields are switched, i.e., ϕ_0 remains constant and the kinetic energy of the molecule will change by a constant amount $\Delta K(\phi_0)$ per stage. In the conventional operation of a

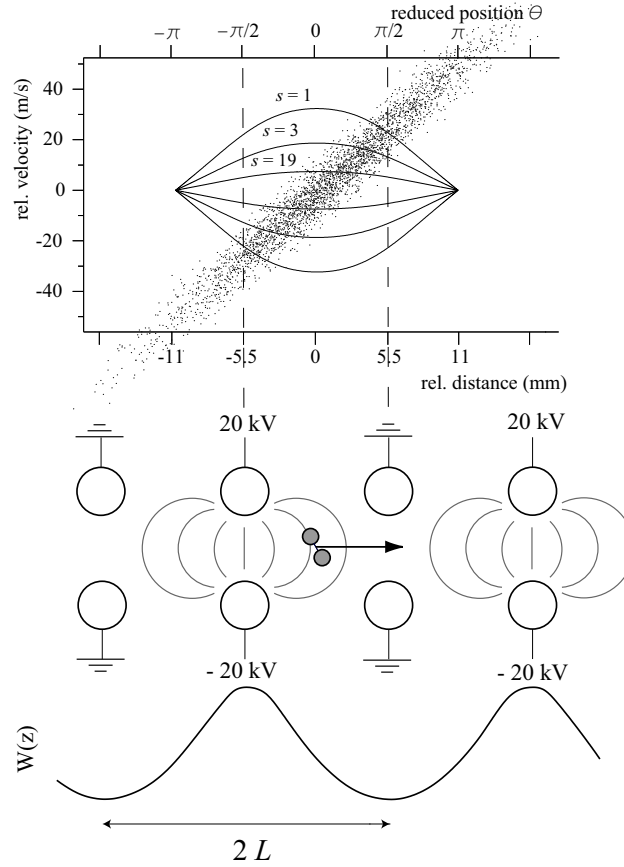


Figure 4.1: Scheme of the Stark decelerator, together with the Stark energy of a molecule as a function of position z along the molecular beam axis. Adjacent electric field stages are spaced a distance $L = 11$ mm apart. Each electric field stage consists of two parallel 6 mm diameter cylindrical rods with a center to center distance of 10 mm. A maximum voltage difference of 40 kV is applied to opposing rods in an electric field stage. The longitudinal phase space acceptance of the decelerator for OH($J = 3/2, M_J \Omega = -9/4$) is given for the resonances $s = 1, 3$ and 19 (see text), together with the longitudinal emittance of the OH beam (shaded area).

Stark decelerator, the synchronous molecule achieves this by travelling exactly a distance L in the time ΔT between two successive switch times. This means that the synchronous molecule is always 'in phase' with the switching of the decelerator. A molecule that has a slightly different phase ϕ and/or velocity v than the synchronous molecule will experience an automatic correction towards the equilibrium values ϕ_0 and v_0 . Molecules within a certain region in phase-space, bounded by the so-called separatrix, will undergo stable phase-space oscillations around the synchronous molecule, and a package of molecules is kept together throughout the deceleration process. Molecules outside this bounded region experience the switched potentials as well, but the force on these molecules is expected to be zero on average as they are sometimes accelerated and sometimes decelerated. It is shown in this chapter that synchronous molecules and phase stability can be found in this region as well. It is therefore convenient to distinguish between the "switching velocity" of the fields $v_{sw} \equiv$

$L/\Delta T$ and the velocity of the synchronous molecule v_0 . We will first derive the equation of motion for phase stable molecules with $v_0 = v_{sw}$, and then extend the description to the cases $v_0 \neq v_{sw}$. In the remainder of this chapter, we will refer to the presence of a phase stable region as a resonance.

4.2.2 First order resonances, $n = 1$

In the following, we consider molecules that move along the longitudinal axis of the decelerator. The Stark energy $W(\theta)$ of a polar molecule in a low-field seeking quantum state is symmetric around the position of a pair of electrodes and can be written as a Fourier series:

$$\begin{aligned}
 W(\theta) &= \frac{a_0}{2} + \sum_{n=1}^{\infty} a_n \cos(n(\theta + \pi/2)) \\
 &= \frac{a_0}{2} + \sum_{n \text{ odd}} (-1)^{\frac{n+1}{2}} a_n \sin n\theta \\
 &\quad + \sum_{n \text{ even}} (-1)^{n/2} a_n \cos n\theta \\
 &= \frac{a_0}{2} - a_1 \sin \theta - a_2 \cos 2\theta + a_3 \sin 3\theta + \dots
 \end{aligned} \tag{4.1}$$

Since the fields are switched after a time interval ΔT , the force on the molecules is a complicated function of position *and* time. The resulting force can only be integrated numerically, but an intuitive picture can be obtained by introducing the continuously acting *average* force \bar{F} that a molecule experiences between successive switch times. In general, the change in Stark energy of a molecule is small compared to the kinetic energy of the molecule ($\Delta W \ll K$). The change in kinetic energy per stage $\Delta K(\phi_0)$ for a synchronous molecule with phase ϕ_0 and velocity $v_0 = v_{sw}$ at a certain switch time is then given by the difference in potential energy at the reduced positions $\theta = \phi_0$ and $\theta = \phi_0 + \pi$:

$$\Delta K(\phi_0) = -\Delta W(\phi_0) = -(W(\phi_0 + \pi) - W(\phi_0)). \tag{4.2}$$

The average force \bar{F} that acts on the synchronous molecule is then simply $\bar{F}(\phi_0) = -\Delta W(\phi_0)/L$. This leads to an average force for a synchronous molecule

$$\bar{F}(\phi_0) = -\frac{2a_1}{L} \sin \phi_0, \tag{4.3}$$

if we only take the terms up to and including $n = 1$ in eqn. (1) into account. Under the approximation that a non-synchronous molecule with a velocity close to v_0 will also travel a distance L between two successive switch times, the average force acting on this molecule with phase $\phi = \phi_0 + \Delta\phi$ is then given by $-\frac{2a_1}{L} \sin(\phi_0 + \Delta\phi)$. The equation of motion with respect to the synchronous molecule then reads

$$\frac{mL}{\pi} \frac{d^2 \Delta\phi}{dt^2} + \frac{2a_1}{L} (\sin(\phi_0 + \Delta\phi) - \sin(\phi_0)) = 0, \tag{4.4}$$

where m is the mass of the molecule [8, 14, 72]. The outer contour in the phase stability diagram in Fig. 1 is obtained by numerically integrating eqn. (4.4) for $\phi_0 = 0^\circ$. The area inside this separatrix defines the region in phase-space for which non-synchronous molecules undergo stable oscillations

around the synchronous molecule, and gives the longitudinal acceptance of the decelerator. For molecules with a phase and velocity close to those of the synchronous molecule, the oscillation frequency is given by

$$\omega_z/2\pi = \sqrt{\frac{a_1 \cos \phi_0}{2m\pi L^2}}. \quad (4.5)$$

The size of the separatrix in the velocity direction Δv is proportional to $L\omega_z$. It is noted that operation of the decelerator at $\phi_0 = 0^\circ$ corresponds to transporting (part of) the beam through the decelerator without deceleration, while acceleration or deceleration of the beam occurs for $-90^\circ < \phi_0 < 0$ and $0 < \phi_0 < 90^\circ$, respectively.

Generally, to investigate the presence of phase-stable regions, we need to calculate ΔW for a molecule in a *given* time interval ΔT . For this, we need to calculate the distance that a molecule travels between successive switch times, which requires knowledge about the velocity of the molecule during the interval ΔT . In the treatment that we use in this chapter, we approximate the velocity of a molecule to be constant between two successive switch times. The change in potential energy per stage $\Delta W(\phi_0)$ for a synchronous molecule with phase ϕ_0 and a velocity $v_0 = v_{sw}$ at a certain switch-time is then given by $\Delta W(\phi_0) = 2a_1 \sin \phi_0$, if we again only take the terms up to and including $n = 1$ in eqn. (1) into account. In the first-order approximation it is assumed that a non-synchronous molecule with phase $\phi_0 + \Delta\phi$ and velocity v_0 will travel the same distance as the synchronous molecule. This then leads again to the equation of motion given above (eqn. (4.4)). In the remainder of this chapter, this approach is used to explore the existence of additional stable regions in phase-space.

Let's now assume that a synchronous molecule can also exist with a velocity $v_0 \neq v_{sw}$, and introduce the identity $v_0/v_{sw} \equiv s$. Let's again call the phase of the synchronous molecule at a certain switch time ϕ_0 . Instead of a distance L this molecule will now travel a distance sL between different switch times, and its reduced position θ on the potential after switching will be

$$\theta = \phi_0 + s\pi + \pi, \quad (4.6)$$

where the last term π accounts for the switching of the fields. It is readily seen from equation 4.6 that a molecule for which $s = \ell$ (ℓ odd) is indeed synchronous, since its phase on the potential is again ϕ_0 just after the fields are switched. An average force

$$\bar{F}(\phi_0) = -\frac{1}{\ell L}(W(\phi_0 + \ell\pi) - W(\phi_0)) = -\frac{2a_1}{\ell L} \sin \phi_0 \quad (4.7)$$

acts on the synchronous molecule. In this rather trivial case the synchronous molecule travels an integer number of periods further before the fields are switched than in the case where $v_0 = v_{sw}$. The force has an identical form as in eqn. (4.3), and we can directly use the equation of motion derived earlier and just replace a_1 by a_1/ℓ . This then leads to additional stable regions in phase space around $v_0 = \ell v_{sw}$. The size of the corresponding separatrices in velocity scales as $1/\sqrt{\ell}$ (see eqn. (4.5)). The separatrices for $\phi_0 = 0^\circ$ are depicted in Fig. 4.1 for $s = 3$ and $s = 19$ as well.

4.2.3 First-order resonances, $n > 1$

So far, only the leading term $a_1 \sin \theta$ in eqn. (4.1) has been included in the analysis, leading to the series of resonances with $s = \ell$ (ℓ odd). Including higher-order terms will not significantly change the

description for molecules whose velocity is close to either one of these resonances. The trajectory of a molecule inside, or close to, a separatrix is dominated by the term $a_1 \sin \theta$, and higher order terms will only slightly perturb the motion. For velocities further away from these regions, the influence of the a_1 -term on the trajectory rapidly decreases, and the terms $a_n \sin n\theta$ with $n > 1$ can gain in importance. The even terms in the spatial expansion of the potential energy in eqn. (4.1) have a maximum at the position of the pair of electrodes that is grounded *and* at the position of the pair that is at high voltage. The contribution of these terms to the potential energy of a molecule is therefore identical before and after switching. The even terms are therefore stationary, and no resonances due to these terms can occur.

The next term in eqn. (4.1) that needs to be considered is $a_3 \sin 3\theta$, which has a periodicity of $2L/3$. A molecule with phase ϕ_0 and velocity $v_0 = v_{sw}/3$ travels a distance $L/3$ in the time ΔT between two switch times. This molecule is therefore synchronous with respect to the term $a_3 \sin 3\theta$, although it is not synchronous with respect to the leading term $a_1 \sin \theta$. If, however, we switch two more times, the reduced position of the molecule will be $\theta = \phi_0 + 3\frac{\pi}{3} + 3\pi = \phi_0$, where the term 3π accounts for the three times switching of the fields. This means that the molecule is synchronous with *both* the $a_1 \sin \theta$ and the $a_3 \sin 3\theta$ term every *three* times the fields are switched. This, however, does not automatically imply that a phase stable region exists around this synchronous molecule. As before, we need to show that a non-synchronous molecule with position $\phi = \phi_0 + \Delta\phi$ and/or velocity $v = v_0 + \Delta v$ experiences a correction towards the equilibrium values ϕ_0 and v_0 . Analogous to eqn. (2) we need to calculate the energy $\Delta W(\phi)$ that a (non)synchronous molecule loses after 3 times switching. In general, a molecule with velocity sv_{sw} travels a distance $s\pi$ between successive switch times, and it can be shown that $\Delta W(\phi)$ after Q times switching can be written as:

$$\begin{aligned} \Delta W(\phi) = & \\ & \sum_{n \text{ odd}} (-1)^{\frac{n+1}{2}} \left\{ \sum_{q=0}^Q \left(-2a_n \sin(n\phi + qn(s+1)\pi) \right) \right. \\ & \quad \left. + a_n \sin(n\phi) + a_n \sin(n\phi + Qn(s+1)\pi) \right\} \\ & + \sum_{n \text{ even}} (-1)^{\frac{n}{2}} \left\{ a_n \cos(n\phi + Qn(s+1)\pi) - a_n \cos(n\phi) \right\} \end{aligned} \quad (4.8)$$

if we take into account all Fourier terms of eqn. (4.1). For the situation discussed above we have $s = 1/3$, leading to an energy loss for the synchronous molecule after three times switching ($Q = 3$) of

$$\begin{aligned} \Delta W(\phi_0) &= -3 \times 2a_3 \sin 3\phi_0 \\ &= 3 \times 2a_3 \sin 3\left(\phi_0 + \frac{\pi}{3}\right) \end{aligned} \quad (4.9)$$

if we take terms up to and including $n = 3$ in eqn. (4.1) into account. It is seen that the energy loss of the molecules due to the dominant term $a_1 \sin \theta$ in eqn. (4.1) is zero after *three* times switching, while the energy loss resulting from the term $a_3 \sin 3\theta$ adds up *every* time we switch. The situation can thus conveniently be described as if the potential energy of the molecule in the decelerator is only given by $W(\theta) = a_3 \sin 3\theta$. Hence, the equation of motion of molecules with respect to the synchronous

molecule is given by eqn. (4.4) when a_1 is substituted by a_3 , L by $L/3$ and ϕ by $3(\phi + \pi/3)$, respectively. The opposite sign in front of the term $a_3 \sin 3\theta$ with respect to the term $a_1 \sin \theta$ in eqn. (4.1) is equivalent to a phase shift of $\pi/3$. Inclusion of the term $n = 3$ in the analysis leads to additional stable regions in phase space around the velocity $v_0 = v_{\text{sw}}/3$. Like in the case $n = 1$ discussed in the previous section, a series of resonances is present around the velocities $v_0 = \ell v_{\text{sw}}/3$ (ℓ odd).

Including even higher order terms of eqn. (4.1) in the analysis, and with the help of eqn. (4.8), in general resonances occur at $s = \ell/n$ (both ℓ and n odd). For a given value of n , the force on a synchronous molecule due to the more dominant terms $< n$ cancels after n times switching, whereas the remaining leading term $a_n \sin n\theta$ results in a force $\frac{2a_n}{\ell L} \sin n\phi_0$ every time the fields are switched. The corresponding separatrices have periodicity $2L/n$, and the longitudinal oscillation frequency is given by

$$\omega_z/2\pi = \sqrt{\frac{a_n \cos n\phi_0}{2m\pi s L^2}}. \quad (4.10)$$

Since these resonances at velocities $v_0 = (\ell/n)v_{\text{sw}}$ can already be derived in the first-order approximation for the motion of the molecules through the Stark decelerator, we refer to these as first-order resonances.

An interpretation of the resonances $s = \ell/n$ can be obtained by representing both the spatial and the temporal dependence of the potential as a Fourier series. It was shown that the resulting force $F(\phi, t)$ that acts on the molecules can be written as

$$F(\phi, t) = \sum_{n \text{ even}}^{\infty} \frac{\pi n}{L} a_n \cos(n\phi) - \sum_{\ell \text{ odd}}^{\infty} \sum_{n \text{ odd}}^{\infty} \frac{2n}{\ell L} a_n \sin(n\phi - \ell\omega t), \quad (4.11)$$

where $\omega = 2\pi/\Delta T$ [163]. It is seen that the force is composed of a sum over stationary waves (n even) and propagating partial waves $\sin(n\phi - \ell\omega t)$ that move with phase velocity $v_\phi = \frac{\ell}{n}v_{\text{sw}}$. Resonances occur if the velocity v_0 of a molecule corresponds to the phase velocity v_ϕ of a propagating partial wave. Molecules with velocities that are close to this value interact strongly with the corresponding partial wave, while the more dominant partial waves have on average no effect on the motion; a synchronous molecule with $s = \ell/n$ is trapped at the center of the travelling potential well produced by the corresponding propagating partial wave ℓ, n .

4.2.4 Numerical simulations

In this section, numerical simulations of the trajectories of molecules through a Stark decelerator are discussed. The stable regions in phase space can be visualized by calculating the average velocity of a molecule during its trajectory through the decelerator. If a molecule is within a phase stable region, it will rotate in phase space around the corresponding synchronous molecule, and hence the average velocity of this molecule will be identical to the average velocity of the synchronous molecule [163]. Resonances therefore appear as regions in phase space where all the molecules have the same average velocity. The trajectories of molecules in a Stark decelerator are calculated by numerically integrating the equation of motion of the molecules. From a calculation of the electric field distribution in an electric field stage in combination with the (quantum state specific) Stark effect of the molecule of

interest, the coefficients of the spatial Fourier expansion as given in eqn. (4.1) are determined. For OH radicals in the $J = 3/2$, $M\Omega = -9/4$ component, the relevant odd coefficients are $a_1 = 0.618 \text{ cm}^{-1}$, $a_3 = 0.044 \text{ cm}^{-1}$, and $a_5 = 0.0037 \text{ cm}^{-1}$ for the geometry and voltage settings of the decelerator used in the present experiments (*vide infra*).

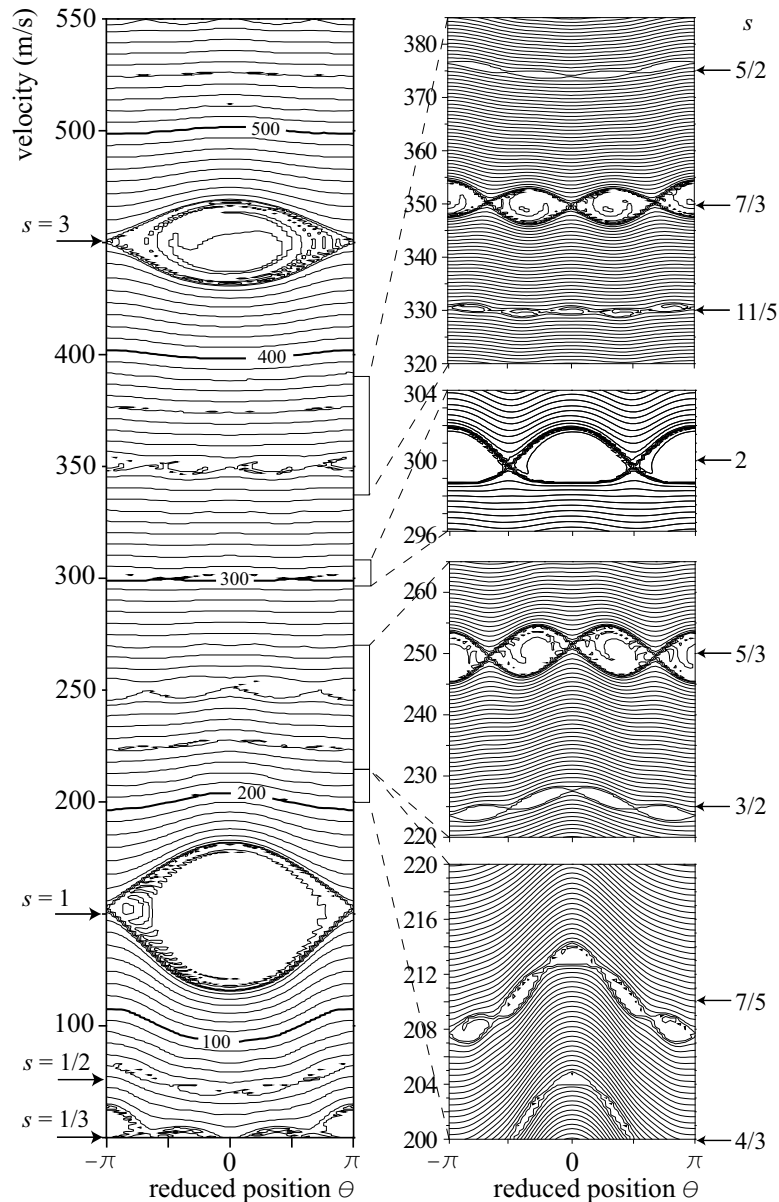


Figure 4.2: Contour-plot of the average velocity of $\text{OH}(J = 3/2, M\Omega = -9/4)$ radicals as a function of their initial position and velocity, that results from a one dimensional numerical simulation of their trajectories through a 300-stage decelerator. The decelerator is operated at a phase angle $\phi_0 = 0^\circ$ and a "switching velocity" $v_{sw} = 150 \text{ m/s}$. Resonances appear as regions in phase space where all the molecules have the same average velocity. The structure inside the separatrices is a result of the finite number of stages used in the simulation.

Fig. 4.2 depicts a contour-plot of the average velocity of $\text{OH}(J = 3/2, M\Omega = -9/4)$ radicals as

a function of their initial position and velocity, that results from a one dimensional numerical simulation of their trajectories through a 300-stage decelerator. The decelerator is operated at a phase angle $\phi_0 = 0^\circ$ and at a constant "switching velocity" $v_{sw} = 150$ m/s. The switching of the high voltage in the decelerator is assumed to be instantaneous. The initial positions and velocities of the molecules are deterministically distributed on a grid that covers two full stages in position (from $-\pi$ to $+\pi$ in reduced position θ) and that ranges from 50 m/s to 550 m/s in velocity. The first-order resonances $s = 1$ at velocity $v_0 = v_{sw}$ (150 m/s), and $s = 3$ ($v_0 = 3v_{sw} = 450$ m/s) are clearly identified. The structure inside the separatrices is a result of the finite number of stages used in the simulation. The size and shape of the separatrices is in quantitative agreement with the model described in sections 4.2.2 and 4.2.3. In particular, the compression of the separatrix along the velocity direction for $s = 3$ by $\sqrt{3}$ with respect to $s = 1$, as predicted by the model, is observed. The slight asymmetry of the separatrix for $s = 1$ is the result of higher order effects that are neglected thus far in the model.

In the panel on the right hand side of Fig. 4.2, four selected phase space regions are shown on an expanded vertical scale; note that the vertical scale for each of the regions is different. The resonances with $s = 5/3$ at $v_0 = 250$ m/s and $s = 7/3$ at $v_0 = 350$ m/s that belong to the series of first-order resonances with $n = 3$ are clearly visible and, as predicted by the model, have periodicity $2\pi/3$. The opposite sign in front of the term $a_3 \sin 3\theta$ with respect to the term $a_1 \sin \theta$ in eqn. (4.1) results in a phase shift of $\pi/3$, and the center of the separatrices are found at the reduced positions $\theta = -\pi$, $\theta = -\pi/3$, $\theta = \pi/3$ and $\theta = \pi$. The resonances with $s = 7/5$ and $s = 11/5$ that belong to the series $n = 5$ can be also clearly identified, even though the coefficient a_5 is about an order of magnitude smaller than a_3 . The centers of the corresponding separatrices are not phase shifted relative to the resonance $s = 1$ and are found at the positions $\theta = -4\pi/5, -2\pi/5, 0, 2\pi/5, \text{ and } 4\pi/5$.

In general, the size, shape and position of the phase stable regions in Fig. 4.2 that belong to the first-order resonances $s = \ell/n$ (ℓ and n odd) are quantitatively reproduced by the model. The distortions in the shape of the separatrices for, for instance, the resonances with $s = 5/3$ and $s = 7/5$ are due to the dominant term $a_1 \sin \theta$ in eqn. (4.1). The influence of this term on the motion of the molecules is *only* zero after an appropriate number of switch times, but for intermediate times, the trajectory of the molecules is predominantly determined by this term. This is most apparent for the resonance $s = 7/5$ as this resonance is very close to the resonance $s = 1$. The curve that connects the centers of the five separatrices is to be interpreted as the influence of the (dominant) term $a_1 \sin \theta$ on the velocity of the synchronous molecule. Only after five switch times this influence cancels, and the synchronous molecule has not lost, or gained, kinetic energy due to the term $a_1 \sin \theta$.

Apart from the resonances $s = \ell/n$ (ℓ and n odd) discussed in sections 4.2.2 and 4.2.3, additional resonances are observed. These resonances occur at $s = 1/2$ (75 m/s), $s = 3/2$ (225 m/s) and $s = 5/2$ (375 m/s) with a periodicity $2\pi/4$ and at $s = 2$ (300 m/s) with a periodicity $2\pi/2$. Applying eqn. (4.8) to these cases gives $\Delta W(\phi) = 0$ for all ϕ . Similarly, these resonances do not correspond to any propagating partial wave in the force $F(\phi, t)$ (eqn. (4.11)). Clearly, these resonances cannot be explained with the model used thus far, suggesting that more subtle effects in the dynamics of the molecules inside the Stark decelerator need to be taken into account. This is the topic of the next section.

4.2.5 Second-order resonances

So far, to calculate the change in potential energy ΔW in the time ΔT between two switch times, the approximation has been made that the velocity of a (non)synchronous molecule remains constant. With this approximation, a non-synchronous molecule with phase $\phi_0 + \Delta\phi$ and a synchronous molecule, both with velocity v_0 at a certain switch time, will travel the same distance $v_0 L/v_{sw}$ in the time ΔT . The change in potential energy $\Delta W(\phi)$ for (non)synchronous molecules after Q times switching is then given by eqn. (4.8), and leads to the resonances $s = \ell/n$ (ℓ and n odd).

A more accurate description of the motion of molecules in a Stark decelerator is obtained when the approximation that the velocity of a molecule during the time interval ΔT is constant, is refined. In the following we will discriminate between the *average* velocity $\langle v \rangle$ of a molecule during ΔT and the *instantaneous* velocity v of a molecule at the time the fields are switched. Again we compare a non-synchronous molecule with phase $\phi_0 + \Delta\phi$ and a synchronous molecule with phase ϕ_0 , both with the same instantaneous velocity v_0 at the time the fields are switched. The non-synchronous molecule traverses a different part of the potential and will have a *different* average velocity in the time ΔT than the synchronous molecule. In contrast to the approximation used before, the distance that a non-synchronous and a synchronous molecule travel in the time ΔT will now be different, and higher-order terms appear in the expression for $\Delta W(\phi)$ in eqn. (4.8). These higher order terms can lead to $\Delta W(\phi) \neq 0$ for those cases where eqn. (4.8) leads to $\Delta W(\phi) = 0$, and it is shown in the remainder of this section that these terms can explain the additional resonances discussed in section 4.2.4.

The series $s = 2, 4, 6, \dots$

Referring back to fig. 4.2, the resonance at $s = 2$ with periodicity π suggests that the corresponding synchronous molecule with phase ϕ_0 at a certain switch time k has an average velocity $\langle v_0 \rangle = 2v_{sw}$ between switch times k and $k + 2$, and that its change in kinetic energy is proportional to $\sin(2\phi_0)$. However, neither the instantaneous velocity v_0 of the synchronous molecule at the switch time k , nor the average velocity between the switch times k and $k + 1$ nor between the switch times $k + 1$ and $k + 2$ is known. It is therefore convenient to use the superscript k in the expressions for the phase ϕ , for the potential energy W , for the kinetic energy K and for the velocity v of a molecule at the switch time k .

Let's consider a molecule that at a certain switch time k has an *instantaneous* velocity v_0^k and a phase ϕ_0^k . For this molecule to be synchronous, its average velocity between switch times k and $k + 2$ has to obey $\langle v_0 \rangle^{k,k+2} = 2v_{sw}$. Like before, to study the possible existence of a resonance, we need to calculate the difference in potential energy $\Delta W^{k,k+2}$ of this molecule between switch times k and $k + 2$:

$$\Delta W^{k,k+2} = \Delta W^{k,k+1} + \Delta W^{k+1,k+2} \quad (4.12)$$

When we only take terms up to and including $n = 1$ of eqn. (4.1) into account, the change in potential

energy $\Delta W^{k,k+1}$ of the synchronous molecule between switch times k and $k + 1$ is given by

$$\begin{aligned}\Delta W^{k,k+1} &= W(\phi_0^k + \Delta\theta^{k,k+1}) - W(\phi_0^k) \\ &= -a_1 \sin(\phi_0^k + \Delta\theta^{k,k+1}) + a_1 \sin \phi_0^k \\ &\approx -a_1(\Delta\theta^{k,k+1} - 2\pi) \cos \phi_0^k.\end{aligned}\quad (4.13)$$

In this expression $\Delta\theta^{k,k+1}$ is the distance the molecule travels between switch times k and $k + 1$. The approximation in the last line of eqn. (4.13) is made because $\Delta\theta^{k,k+1}$ is close to 2π in this case (*vide infra*). The distance $\Delta\theta^{k,k+1}$ follows from the *average* velocity of the molecule between the switch times k and $k + 1$, which will be close, but not necessarily equal, to $2v_{\text{sw}}$. The average velocity $\langle v \rangle^{k,k+1}$ of the synchronous molecule follows from the conservation of energy:

$$K(v_0^k) + W(\phi_0^k) = \frac{1}{2}m \langle v^2 \rangle^{k,k+1} + \langle W \rangle^{k,k+1} \quad (4.14)$$

in the approximation that $(\langle v \rangle^{k,k+1})^2$ equals $\langle v^2 \rangle^{k,k+1}$. It can be shown that in this approximation $\langle W \rangle^{k,k+1}$ is equal to zero for the series $s = 2, 4, 6, \dots$ (proof available upon request), resulting in

$$\begin{aligned}\langle v \rangle^{k,k+1} &\approx \sqrt{\frac{2}{m} (K(v_0^k) + W(\phi_0^k))} \\ &= v_0^k \sqrt{1 + \frac{W(\phi_0^k)}{K(v_0^k)}} \\ &\approx v_0^k \left(1 - \frac{a_1 \sin \phi_0^k}{m(v_0^k)^2} \right)\end{aligned}\quad (4.15)$$

The distance $\Delta\theta^{k,k+1}$ that the molecule travels between switch times k and $k + 1$ is then given by

$$\begin{aligned}\Delta\theta^{k,k+1} &= \pi \left(\frac{\langle v \rangle^{k,k+1}}{v_{\text{sw}}} \right) \\ &\approx 2\pi \frac{v_0^k}{2v_{\text{sw}}} \left(1 - \frac{a_1 \sin \phi_0^k}{m(v_0^k)^2} \right).\end{aligned}\quad (4.16)$$

To calculate the change of potential energy $\Delta W^{k+1,k+2}$ of the synchronous molecule between switch times $k + 1$ and $k + 2$, the analysis given above is repeated for a molecule at reduced position θ^{k+1} and velocity v_0^{k+1} at switch time $k + 1$. The reduced position θ^{k+1} of the molecule on the potential just after switch time $k + 1$ is given by

$$\theta^{k+1} = \phi_0^k + \Delta\theta^{k,k+1} + \pi, \quad (4.17)$$

where the term π accounts for the switching of the fields. Therefore,

$$\begin{aligned}\Delta W^{k+1,k+2} &= W(\theta^{k+1} + \Delta\theta^{k+1,k+2}) - W(\theta^{k+1}) \\ &\approx -a_1(\Delta\theta^{k+1,k+2} - 2\pi) \cos \theta^{k+1} \\ &\approx a_1(\Delta\theta^{k+1,k+2} - 2\pi) \cos \phi_0^k,\end{aligned}\quad (4.18)$$

where in the last step the approximation has been used that $\Delta\theta^{k,k+1}$ is close to 2π . The distance $\Delta\theta^{k+1,k+2}$ follows from the *average* velocity of the molecule between the switch times $k+1$ and $k+2$. The average velocity $\langle v \rangle^{k+1,k+2}$ of the synchronous molecule follows from the conservation of energy:

$$K(v_0^{k+1}) + W(\theta^{k+1}) = \frac{1}{2}m \langle v^2 \rangle^{k+1,k+2} + \langle W \rangle^{k+1,k+2}. \quad (4.19)$$

Since $\langle W^{k+1,k+2} \rangle$ is again zero in this case, the average velocity $\langle v \rangle^{k+1,k+2}$ of the molecule between switch times $k+1$ and $k+2$ is approximated by:

$$\langle v \rangle^{k+1,k+2} \approx v_0^{k+1} \left(1 - \frac{a_1 \sin \theta^{k+1}}{m(v_0^{k+1})^2} \right). \quad (4.20)$$

It is convenient to express v_0^{k+1} in terms of v_0^k , which follows from the conservation of energy and eqn. (4.13) as:

$$v_0^{k+1} = \sqrt{(v_0^k)^2 + \frac{2a_1}{m}(\Delta\theta^{k,k+1} - 2\pi) \cos \phi_0^k}. \quad (4.21)$$

The synchronous molecule then travels a distance $\Delta\theta^{k+1,k+2}$ between switch times $k+1$ and $k+2$, given by

$$\begin{aligned} \Delta\theta^{k+1,k+2} &= \pi \left(\frac{\langle v \rangle^{k+1,k+2}}{v_{\text{sw}}} \right) \\ &\approx 2\pi \frac{v_0^k}{2v_{\text{sw}}} \left(1 + \frac{a_1 \sin \phi_0^k}{m(v_0^k)^2} \right). \end{aligned} \quad (4.22)$$

The reduced position θ^{k+2} of the synchronous molecule at switch time $k+2$, just after switching, is

$$\begin{aligned} \theta^{k+2} &= \phi_0^k + (\Delta\theta^{k,k+1} + \pi) + (\Delta\theta^{k+1,k+2} + \pi) \\ &\approx \phi_0^k + 4\pi \frac{v_0^k}{2v_{\text{sw}}} + 2\pi \end{aligned} \quad (4.23)$$

As mentioned before, the average velocity between switch times k and $k+2$ has to be $2v_{\text{sw}}$ for the molecule to be synchronous. With respect to the initial phase ϕ_0^k , its reduced position θ^{k+2} just after switch time $k+2$ therefore has to be $\phi_0^k + 4\pi + 2\pi$, where the term 2π accounts for the two times switching. From eqn. (4.23) it then follows that its instantaneous velocity v_0^k at switch time k needs to be *identical* to its average velocity $2v_{\text{sw}}$ between switch times k and $k+2$: $v_0^k = 2v_{\text{sw}}$. It is noted that this is coincidentally the case for the special series $s = 2, 4, 6, \dots$ discussed here, but that this is not generally true for the resonances of second-order (*vide infra*).

Finally, the total change in potential energy of the molecule between switch times k and $k+2$ can now be calculated:

$$\begin{aligned} \Delta W(\phi_0^k) &= \Delta W^{k,k+1} + \Delta W^{k+1,k+2} \\ &\approx a_1 (\Delta\theta^{k+1,k+2} - \Delta\theta^{k,k+1}) \cos \phi_0^k \\ &\approx \frac{4\pi a_1^2}{m(2v_{\text{sw}})^2} \sin \phi_0^k \cos \phi_0^k \\ &= \frac{2\pi a_1^2}{m(2v_{\text{sw}})^2} \sin 2\phi_0^k. \end{aligned} \quad (4.24)$$

The second-order terms in the derivation thus result in an expression for $\Delta W(\phi_0)$ that is similar to the expression found before for the first-order resonances $s = \ell/n$. The derivation given above is also valid for a non-synchronous molecule with phase $\phi^k = \phi_0^k + (\Delta\phi)^k$ and with velocity v_0^k at switch time k if the synchronous phase ϕ_0 in the expressions above is replaced by $\phi_0^k + (\Delta\phi)^k$. A non-synchronous molecule will therefore lose a kinetic energy $-\Delta W(\phi_0^k + (\Delta\phi)^k)$. For the resonances in Figure 4.2, the decelerator is operated at $\phi_0 = 0^\circ$, and the equation of motion for non-synchronous molecules with respect to the synchronous molecule in this case is again given by eqn. (4.4) with the appropriate substitutions. The size of the separatrix in the velocity direction depends now not only on the appropriate coefficient of the spatial Fourier expansion of the field, but has an additional factor that is proportional to the ratio of the potential energy to the kinetic energy. In contrast to the first-order resonances the size of the phase stable regions for these so-called second-order resonances rapidly decreases with higher "switching velocities" of the decelerator. The size of the separatrices belonging to the resonance $s = 2$ in Fig. 4.2 is quantitatively reproduced by the model. The derivation given in this section can be further generalized to describe additional resonances for $s = 2\ell$ (ℓ integer) as well.

The series $s = 1/2, 3/2, 5/2, \dots$

Referring back to Fig. 4.2, the observed resonances at $s = \ell/2$ (ℓ odd) with periodicity $2\pi/4$ suggest that the change in potential energy of the corresponding synchronous molecule, after four times switching, is proportional to $\sin(4\phi_0)$. To explain these resonances higher order terms in the Fourier expansion of eqn. (4.1) need to be included in the analysis. This series of resonances can be described when the terms $a_1 \sin \theta$ and $a_3 \sin 3\theta$ are taken into account; this derivation is not explicitly given here, but is available upon request. Again we consider a molecule with phase ϕ_0^k and velocity v_0^k at a certain switch time k , and we calculate the energy difference $\Delta W_0^{k,k+4}$ between switch times k and $k + 4$. For the resonance $s = 1/2$ the instantaneous velocity v_0^k at switch time k has to be

$$v_0^k = \frac{v_{sw}}{2} \left[1 - \frac{a_1}{mv_{sw}^2} \cos \phi_0^k - \frac{a_3}{mv_{sw}^2} \cos 3\phi_0^k \right] \quad (4.25)$$

in order for the synchronous molecule to have an average velocity of $\langle v_{synchr} \rangle = v_{sw}/2$ between switch times k and $k + 4$. The kinetic energy that the synchronous molecule loses after 4 times switching is

$$\Delta W(\phi_0^k) = \frac{2\pi a_1 a_3}{m(v_{sw}/2)^2} \left(4 - \frac{16}{3\pi} \right) \sin 4(\phi_0^k - \pi/4) \quad (4.26)$$

neglecting terms of higher order in (W/K) . This expression has again the familiar form that leads to phase stability. The resulting separatrices have periodicity $2\pi/4$, and are phase-shifted by $\pi/4$ with respect to $\phi_0^k = 0$ since the product $a_1 a_3 > 0$. Note that no terms $\propto a_1^2$ or $\propto a_3^2$ appear in the expression for $\Delta W(\phi_0^k)$, and that it is the cross-term $\propto a_1 a_3$ which gives rise to the resonance. A non-synchronous molecule with initial phase $\phi^k = \phi_0^k + (\Delta\phi)^k$ and with initial velocity v^k that obeys eqn. (4.25), loses a kinetic energy $-\Delta W(\phi_0^k + (\Delta\phi)^k)$, and will oscillate in phase space around the equilibrium values ϕ_0 and v_0 of the synchronous molecule.

The velocity of the synchronous molecule at every switch time between k and $k + 4$ is not constant, as is evident from the curved line that connects the four separatrices in Fig. 4.2. This curve $v_0(\theta)$ is given by eqn. (4.25), when ϕ_0^k is replaced by θ , and represents the influence of the leading

term $a_1 \sin \theta$ on the motion of the molecules, which only cancels after 4 times switching. It is clear that the entire series of second-order resonances with $s = \ell/2$ (ℓ odd) can be explained by this model. The phase stable regions obtained from the simulation for $s = 3/2$ and $s = 5/2$ (see Fig. 4.2) can be quantitatively reproduced.

Other resonances

In Fig. 4.2 a resonance is also seen at $s = 4/3$ ($v = 200$ m/s). Although the derivation has not been explicitly made for this, it is believed that, in analogy with the derivation for the series $s = 2\ell$ (ℓ integer), the term $a_3 \sin 3\theta$ gives rise to resonances at $s = 2\ell/3$ (ℓ integer). The corresponding kinetic energy loss for the synchronous molecule is proportional to $(a_3^2/mv_{sw}^2) \sin 6\phi_0^k$, and the separatrices have periodicity $2\pi/6$. This interpretation is supported by numerical simulations. In fact, the simulations indicate that many more resonances exist as well. For example, the resonances $s = 1/5$ and $s = 1/7$ already appear even if the terms $a_5 \sin 5\theta$ and $a_7 \sin 7\theta$ in the spatial Fourier expansion of the potential (eqn. (4.1)) are set to zero in the simulations, although the size of the separatrices is then rather small. Although speculative, these resonances are believed to originate from the neglected terms that are proportional to $(W/K)^2$, and $\Delta W(\phi_0^k)$ for a synchronous molecule takes the form

$$\Delta W(\phi_0^k) \propto \frac{a_1^2 a_3}{m^2 v_{sw}^4} \sin 5\phi_0^k \quad (4.27)$$

and

$$\Delta W(\phi_0^k) \propto \frac{a_1 a_3^2}{m^2 v_{sw}^4} \sin 7\phi_0^k \quad (4.28)$$

for the resonances $s = 1/5$ and $s = 1/7$, after switching 5 and 7 times, respectively. Including the terms $a_5 \sin 5\theta$ etc. in the analysis and/or taking even higher-order terms in W/K into account will lead to additional resonances, but this is beyond the scope of this chapter.

4.2.6 Summary

In the previous sections the longitudinal motion of molecules through a Stark decelerator is described using models with different levels of approximation. In the first-order approximation, the influence of the potential energy on the motion of the molecules in the time-interval ΔT between successive switch times is neglected, and the molecule is assumed to have a constant velocity during this time-interval. With this approximation, the resonances $s = \ell/n$ (both ℓ and n odd) can be explained. The change in potential energy of a synchronous molecule after n times switching can generally be expressed as

$$\Delta W(\phi_0) = -(-1)^{\frac{n+1}{2}} 2na_n \sin n\phi_0. \quad (4.29)$$

The corresponding separatrices have periodicity $2\pi/n$, and their size does not depend on v_{sw} . These resonances are referred to as first-order resonances.

In the second-order approximation, the influence of the potential energy on the motion of the molecules in the time-interval ΔT is taken into account. With this approximation, additional series of resonances are found; the derivation for the cases $s = 2\ell$ (ℓ integer) and $s = \ell/2$ (ℓ odd) has been

made. The expressions for $\Delta W(\phi_0)$ for the synchronous molecules are proportional to W/K . Even higher-order resonances exist as well, but a discussion of these is beyond the scope of this chapter.

4.3 Experiment

4.3.1 Experimental set-up

The experiments described in this chapter are performed in the molecular beam deceleration machine that was described in detail in chapter 3. The experiments reported here are performed on OH radicals as well, using the production method outlined in section 2.2 of chapter 2. Kr is used as a seed gas, resulting in a molecular beam that has a mean velocity around 450 m/s with a velocity spread (FWHM) of 15 %.

4.3.2 First-order resonances

In the experiments described in this chapter, the decelerator is operated with equal time intervals in a single time sequence, corresponding to transporting (part) of the beam through the decelerator without deceleration, i.e., the decelerator is operated at a phase angle of 0° . The advantage of that is that the interpretation of time-of-flight (TOF) profiles of the molecules exiting the decelerator is straightforward. A certain arrival time (almost) directly corresponds to a certain velocity of the molecule. The arrival time distribution (TOF profile) of the OH($J = 3/2$) radicals is recorded by scanning the time delay between the detection laser and the dissociation laser. The first pair of electrodes of the decelerator is switched to high voltage when the most intense part of the beam is at position $\theta = 0$ in the first electric field stage, thereby coupling in the molecular beam in the center of the longitudinal acceptance region of the decelerator. In Fig. 4.1, the longitudinal emittance of the molecular beam at the entrance of the Stark decelerator is shown as the gray area, together with the overlap with the separatrices for the resonances $s = 1, 3$ and 19.

When operating the decelerator at the "switching velocity" that corresponds to the mean velocity of the molecular beam ($v_{\text{sw}} = 450.0$ m/s), a TOF profile as presented in Fig. 4.3 *a* is observed (this Figure is identical to Figure 3.8 of chapter 3). The main portion of the beam is transported through the machine as a compact package, and arrives in the detection region about 2.9 ms after production. The TOF profile obtained from a three dimensional trajectory calculation, taking both $M_J\Omega$ components into account, is shown underneath the observed profile. The longitudinal phase space distribution for OH radicals in the $J = 3/2$, $M_J\Omega = -9/4$ state, close to the exit of the decelerator is shown in the inset. The separatrix that follows from the model for the case $s = 1$, centered around the synchronous velocity of 450 m/s, is shown in the figure as well. The separatrix quantitatively describes the region in phase space where molecules oscillate around the synchronous molecule.

The velocities $s = \ell/n$ of the higher-order resonances are not within the velocity distribution of the molecular beam, and these resonances can only be observed by operating the decelerator with a lower value of v_{sw} . The observed TOF profile is shown for (*b*) $v_{\text{sw}} = 151.1$ m/s, (*c*) 91.9 m/s, (*d*) 40.9 m/s, (*e*) 30.0 m/s and (*f*) 23.6 m/s. In each panel a resonance is observed at a time of flight of around 2.9 ms, corresponding to a velocity (close) to 450 m/s, and can be assigned $s = \ell = 1$,

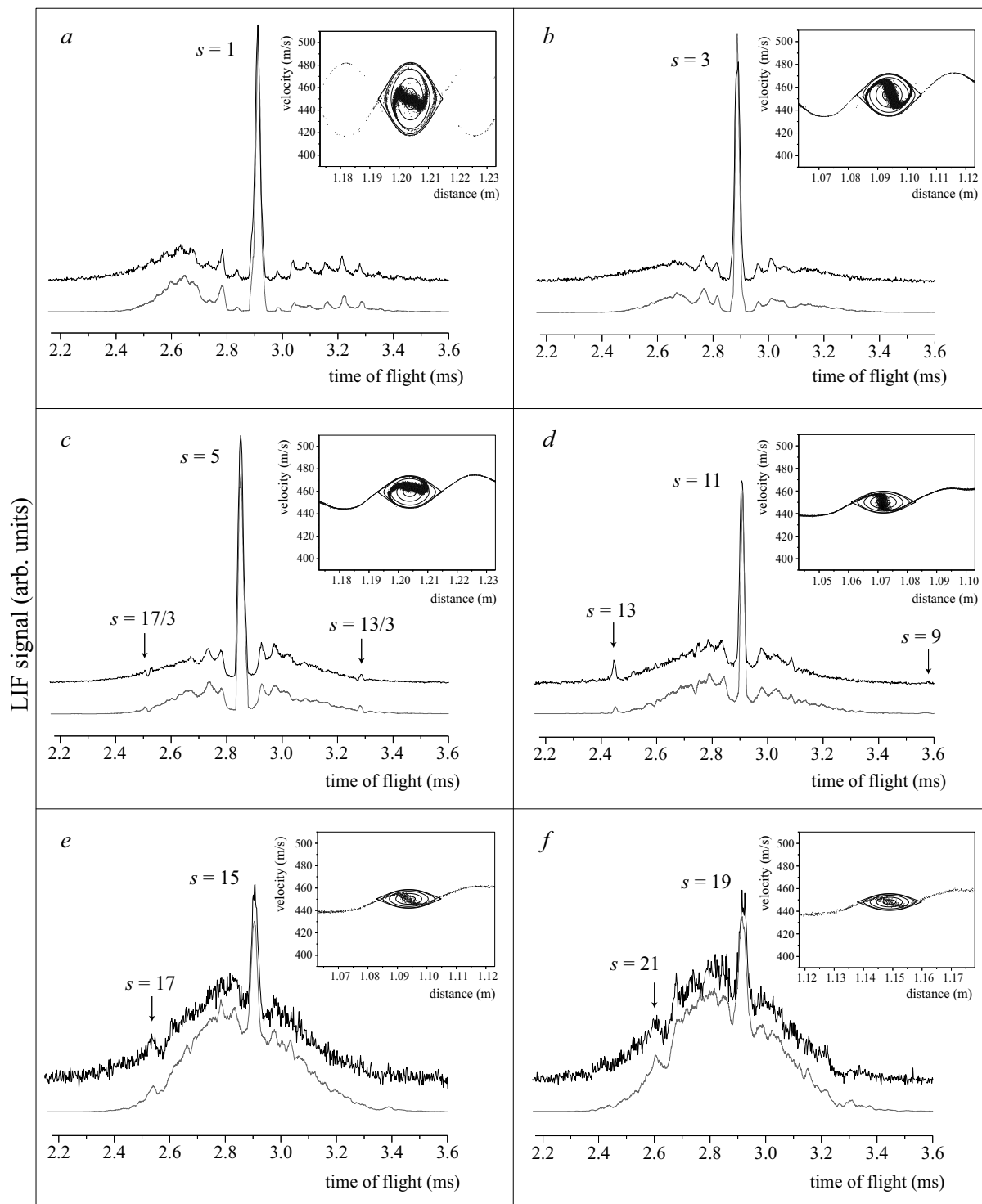


Figure 4.3: Observed and simulated TOF profiles showing a series of first-order resonances with $n = 1$. The decelerator is operated at phase angle $\phi_0 = 0^\circ$ and a "switching velocity" (a) $v_{sw} = 450.0$ m/s, (b) 151.1 m/s, (c) 91.9 m/s, (d) 40.9 m/s, (e) 30.0 m/s, and (f) 23.6 m/s. The TOF profiles that are obtained from three dimensional trajectory simulations of the experiment are shown underneath the experimental profiles. In the insets, the longitudinal phase space distributions for OH radicals in the $J = 3/2$, $M_J = -9/4$ state, close to the end of the decelerator, are shown. In these phase space plots the part of the beam that is responsible for the central feature in the observed TOF profiles is shown.

3, 5, 11, 15 and 19 of the series $n = 1$, respectively. The longitudinal acceptance of the decelerator for $\ell > 1$ is compressed in the velocity direction by a factor $\sqrt{\ell}$ compared to the case $s = \ell = 1$, and for increasing ℓ an ever smaller fraction of the beam is captured by the decelerator. In panels *c* through *f*, multiple resonances can be observed in a single TOF profile. The additional resonances $s = 17/3, 13/3, 13, 17$ and 21 can clearly be identified in the wings of the TOF profile. Three dimensional trajectory simulations again quantitatively reproduce the observed TOF profiles, and the resulting longitudinal phase space distributions for OH radicals in the $J = 3/2, M_J\Omega = -9/4$ state are shown in the insets, together with the corresponding separatrices. In the measurements presented in the panels *b* and *c*, the beam was not perfectly coupled in the center of the longitudinal acceptance region, resulting in a slightly asymmetric phase space distribution.

In Fig. 4.4, TOF profiles are shown that contain a number of first-order resonances with $n > 1$. The high-voltage circuitry of the decelerator does not allow to switch faster than $v_{sw} = 550$ m/s, limiting the resonances that can be observed to $s > 1$. In panel *a* the time sequence of the decelerator is set to $v_{sw} = 270.1$ m/s to observe the resonance $s = 5/3$ ($v_0 = 450.1$ m/s) at the center of the molecular beam distribution. To correct for the phase shift of the separatrices for $n = 3$, the first high voltage pulse is applied to the decelerator when the synchronous molecule is at position $\theta = \pi/3$ in the first electric field stage. The peak at an arrival time of 2.9 ms corresponds to the resonance $s = 5/3$. The full width half maximum (FWHM) of the peak is less than $10 \mu\text{s}$, reflecting the reduced size of the corresponding separatrix compared to the series $n = 1$. Again, the three dimensional trajectory simulation quantitatively reproduces the observed TOF profile, although the resonance $s = 5/3$ appears larger in the simulation than in the experiment. The separatrix that is obtained from the model presented in section 4.2.3 is shown in the inset, together with the longitudinal phase space distribution of OH ($J = 3/2, M\Omega = -9/4$) radicals near the exit of the decelerator. For reasons of clarity, the position and velocity scales are different compared to the insets of Fig. 4.3. In addition to the resonance $s = 5/3$, the first-order resonance $s = 9/5$ and the second-order resonances $s = 3/2$ and $s = 2$ can be identified in the wings of the TOF distribution.

Higher resonances of the series $n = 3$ can be observed by selecting a lower value of v_{sw} , as is shown for $v_{sw} = 71.1$ m/s in panel *b* of Fig. 4.4. With these settings, the resonance $s = 19/3$ appears at $v_0 = 450$ m/s (arrival time around 2.9 ms). The TOF profile is dominated by the nearby resonance $s = 7$ of the (much stronger) series $n = 1$. The resonance $s = 19/3$ is again over-estimated by the trajectory simulations, suggesting that the electric fields in the decelerator used in the experiment are slightly different from the calculated values. This discrepancy can be due to misalignments of the electrode array, and due to small fluctuations in the high voltage that is applied to the electrodes.

The resonances that belong to the series $n > 3$ are very weak as the coefficients a_n get increasingly smaller for higher values of n . In panel *c* of Fig. 4.4 the observed TOF profile is presented when the decelerator is operated with $v_{sw} = 321.5$ m/s, giving rise to the resonance $s = 7/5$ at $v_0 = 450$ m/s. The maximum extension Δv of the separatrix along the velocity axis is only 1 m/s, and the FWHM of the central peak is about $6 \mu\text{s}$. This corresponds to a longitudinal temperature of the selected molecules of about 0.3 mK. From the inset it is seen that the beam is coupled in slightly displaced from the center of the separatrix for the resonance $s = 7/5$. The oscillation frequency ω_z is too low to observe the phase stable rotation of the non-synchronous molecules around the synchronous molecule

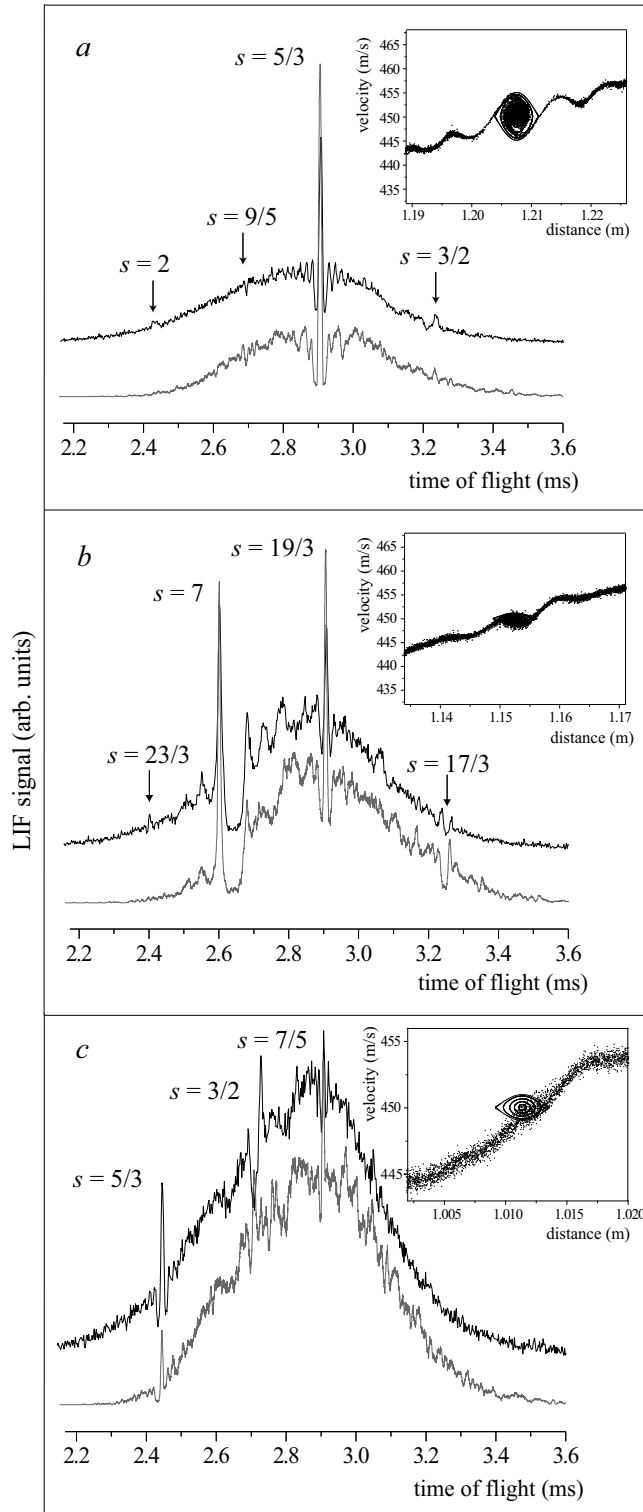


Figure 4.4: Observed and simulated TOF profiles when the decelerator is operated at values of v_{sw} such that $s = \ell/n$ (ℓ and n odd; $n > 1$) resonances appear at the center of the TOF distributions. The decelerator is operated with (a) $v_{sw} = 270.1$ m/s, (b) 71.1 m/s, and (c) 321.5 m/s, giving rise to the resonances $s = 5/3$, $s = 19/3$ and $s = 7/5$ at the center of the TOF distributions, respectively.

in the inset. In general the TOF distribution obtained from the trajectory simulations reproduces the observed distribution well, although the resonance $s = 7/5$ appears, like the resonances $s = 5/3$ and $s = 19/3$ in Fig. 4.4 *a* and *b*, too large in the simulated profile. The resonance $s = 5/3$ appears too small in the simulated TOF profile. This is due to the symmetric velocity distribution of the beam that is assumed in the simulations, that results in a systematic under estimation at early arrival times of the TOF distribution. No attempt was undertaken to observe resonances with $n > 5$.

4.3.3 Second-order resonances

From the description given in section 4.2.5 it is clear that the size of the second-order resonances is inversely proportional to the square of the "switching velocity" v_{sw} . For realistic values of v_{sw} , these resonances are therefore expected to be equally, or less strong than the resonance $s = 7/5$. In Fig. 4.5, the observed and simulated TOF profiles are presented when the time sequence that is applied to the decelerator is set to observe the second order resonances $s = 2$ (panel *a*; $v_{sw} = 225.0$ m/s) and $s = 3/2$ (panel *b*; $v_{sw} = 299.9$ m/s) at the center of the TOF distribution. In the observed profiles, these resonances are clearly identified at a TOF of around 2.9 ms. As expected, the resonance $s = 2$ is small, but the resonance $s = 3/2$ is surprisingly large. The agreement between the observed and simulated TOF profiles is reasonable for the resonance $s = 2$, but the size of the resonance $s = 3/2$ is not reproduced by the simulations. The longitudinal phase space distributions that are obtained from the trajectory calculations are shown in the insets, together with the expected separatrices from the analysis given in section 4.2.5. The oscillation frequency of these resonances is too low to observe the rotation of the phase space distribution, and only limited information on the dynamics of the molecules in the decelerator can be obtained from these figures. It is noted that the curvature around $v = 450$ m/s in the phase space distribution of panel *b* does not result from the resonance $s = 3/2$, but is a remnant from the remote resonance $s = 1$ (at $v = 299.9$ m/s).

The disagreement between the simulations and the experiment suggests that an amplification mechanism for the resonance $s = 3/2$ is present in the experiment, that is not included in the three dimensional trajectory simulations nor in the model given in section 4.2.5. Excluded in the simulated TOF profiles are, for example, the finite transient time τ of the high voltage switches, misalignments of the electrode array, and the slight voltage drop during the burst of switch times. For the decelerator used in this work $\tau \approx 450$ ns, and simulations indicate that no effect of the transient time is to be expected on the TOF distribution. Only for τ larger than approximately $5 \mu\text{s}$, the assumption that the fields are switched instantaneously is no longer valid. Due to the finite transient time, the separatrices become somewhat smaller, and, most importantly, are phase-shifted by approximately $v_{sw}\tau\frac{\pi}{L}$ with respect to the original separatrices. However, this does not lead to an amplification of a resonance, and we therefore conclude that the transient time of the high voltage switches cannot explain the discrepancy between the experiment and the trajectory simulations. Similarly, random misalignments of the electrode array and/or a voltage drop during the time sequence are only expected to result in a reduced size of the separatrices, and not in a larger resonance. The mechanical design of the decelerator is such that the distance between electrodes that are connected to the same high voltage switch is accurately known, e.g., $2L$ is equal to 22.00 ± 0.05 mm. The mutually orthogonal arrays of electrodes might be not as exactly centered relative to each other, however, as these arrays are mounted independently. It could therefore be that the electric field stages have alternately a length of $(L + \Delta L)$ and $(L - \Delta L)$, where we know ΔL mechanically only up to 0.2 mm. Simulations indicate that this can only lead to

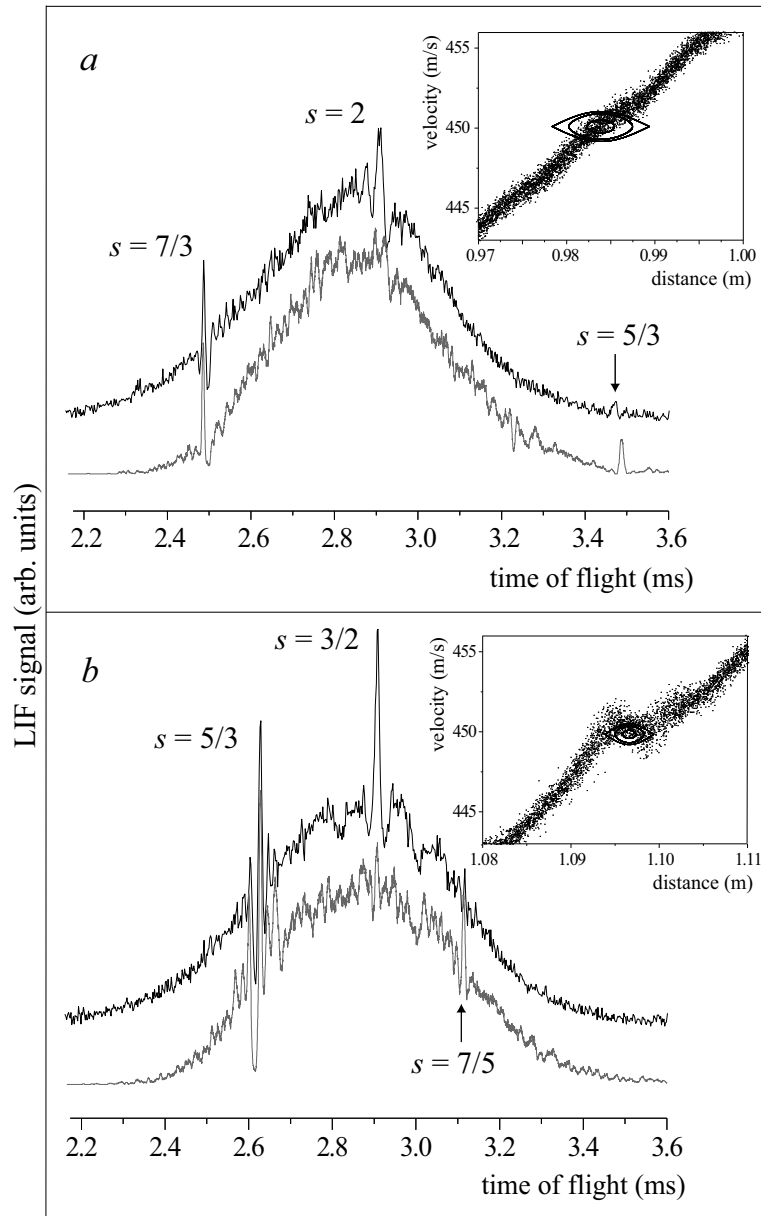


Figure 4.5: Observed and simulated TOF profiles showing second order resonances. The second-order resonances $s = 2$ (panel a) and $s = 3/2$ (panel b) are observed at the center of the TOF distribution when the decelerator is operated with a "switching velocity" of 225.0 m/s and 299.9 m/s, respectively.

a phase shift of the separatrices, but an amplification of a resonance cannot be explained. The origin of the magnitude of the resonance $s = 3/2$ in the experiment, also already observed in Fig 4.4 (panel c), is therefore at present not understood.

4.3.4 Molecular beam modulation

In the previous sections, the occurrence of *phase stability* at higher velocities than the "switching velocity" v_{sw} of the decelerator has been experimentally demonstrated. In this section it is shown that

these effects can also manifest themselves in the TOF profile that is observed in "normal" molecular beam deceleration experiments.

Consider a molecular beam with a mean velocity \bar{v} . We now apply a time-sequence to the decelerator that is calculated for a synchronous molecule with initial velocity close to \bar{v} and with a non-zero phase angle ϕ_0 . The package of molecules that is within the corresponding separatrix ($s = 1$) is decelerated from \bar{v} to the final velocity, which is determined by the phase angle that is used. This process has been documented in detail in several papers, and will not be further discussed here. Instead, we will focus on the part of the beam that is not decelerated. In the time sequence, the time ΔT between successive switch times gets increasingly longer to compensate for the ever slower travelling synchronous molecule. One may wonder, therefore, if in this case phase stable regions can be found at higher velocities than $v_{sw} = L/\Delta T$ as well. Obviously, this is not the case, as the analysis given in sections 4.2.2, 4.2.3 and 4.2.5 shows that *simultaneous* phase stability at different values of s can only occur if the decelerator is operated at a phase angle of 0° *. However, when the deceleration rate is low, the variation of ΔT is small, and the molecules moving with the resonance velocity of $sL/\Delta T$ are *almost* phase stable, i.e., the phase space distribution of these molecules rotates around an *almost* synchronous molecule for a considerable amount of time. As the velocity of the synchronous molecule for which $s = 1$ is lowered, the velocity of a "resonance" at $s > 1$ can move through the entire velocity distribution of the molecular beam, thereby inducing numerous rotations in the phase space distribution of the beam. This results in a pronounced modulation of the beam.

In Fig. 4.6(a), the TOF profile is shown that is observed when the molecular beam is modulated by the resonance $s = 3$ that originates from the term $a_1 \sin \theta$. The experiment is performed using Xe as a carrier gas, yielding a mean velocity of the beam of 365 m/s. The time-sequence is selected to obtain a maximum contrast in the TOF profile. The sequence is generated for a synchronous molecule with an initial velocity of 230 m/s and for a phase angle of 40° . With these settings for the decelerator, the velocity $L/\Delta T$ of the synchronous molecule is around 100 m/s when the most intense part of the beam is close to the end of the decelerator. The velocities in the beam are well above the velocity of the synchronous molecule, and there is no part of the beam that is selected and decelerated. The velocity of the "resonance" at $s = 3$, however, is lowered from 690 m/s to 300 m/s, and moves through the complete velocity distribution of the molecular beam. A pronouncedly modulated TOF profile results, consisting of a series of peaks, with (almost) zero signal between the peaks. In the inset, the phase space distribution of the OH($J = 3/2$, $M_J\Omega = -9/4$) radicals, close to the exit of the decelerator, is shown. With the time sequence used, the interaction of the beam with the $s = 3$ resonance results in regions in phase space where the phase space distribution is (nearly) vertical. A pulse train of spatially bunched molecules [10], trailing each other by 22 mm, develops, which results in the series of peaks in the TOF profile. The TOF profile that is obtained from a simulation of the experiment, taking both $M_J\Omega$ components into account, is shown underneath the experimental TOF profile, and is seen to be in quantitative agreement with the observations.

A similar modulation of the molecular beam can also be obtained when a resonance at other val-

*It is noted that phase stable deceleration of a packet of molecules using a resonance with $s \neq 1$ is possible, when the appropriate time-sequence is used. However, more deceleration stages compared to $s = 1$ are needed to obtain the required final velocity.

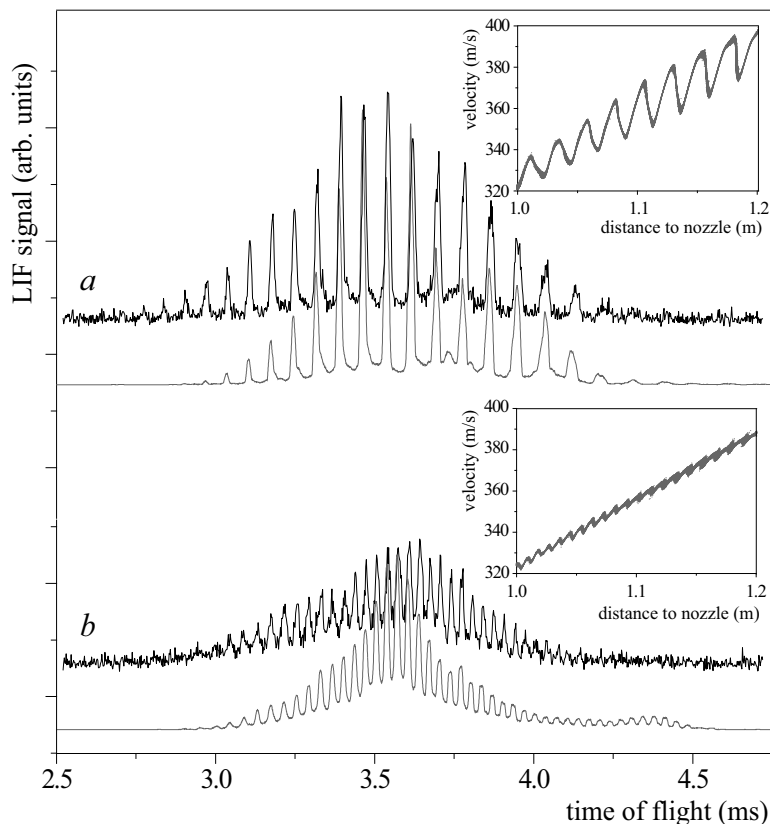


Figure 4.6: Observed (upper curves) and calculated (lower curves) TOF profiles when the molecular beam is modulated by *a* the resonance $s = 3$, and *b* the resonance $s = 5/3$. The time sequences that are applied to the decelerator have been carefully selected to obtain a maximum contrast in the TOF profile. In the insets, the phase space distributions of OH ($J = 3/2, M_J \Omega = -9/4$) radicals are shown, when the most intense part of the beam is close to the exit of the decelerator.

ues of s is used. In particular, the beam can be modulated by the term $a_3 \sin 3\theta$ when the velocity that corresponds to $(5/3)v_{\text{sw}}$ moves through the velocity distribution of the beam. This situation is depicted in Fig. 4.6 (*b*). The decelerator is operated with a time sequence that is calculated using a phase angle $\phi_0 = 35^\circ$ and for a synchronous molecule with an initial velocity of 290 m/s. When the beam is close to the end of the decelerator, about 3 ms after production, the synchronous molecule has a velocity of approximately 180 m/s. In this case, the velocity of the resonance $s = 5/3$ is lowered from 485 m/s to 300 m/s, and the molecular beam strongly interacts with the term $a_3 \sin 3\theta$. This results in a finer structured modulation of the phase space distribution of the beam (see inset) and the peaks in the TOF profile are closer spaced. The reduced contrast of the modulation is in part due to the smaller value of the coefficient a_3 compared to a_1 . Again, the TOF profile that results from a numerical trajectory simulation (lower curve) accurately reproduces the experimental profile (upper curve).

Similarly rich oscillatory structure on the TOF profile of the non-decelerated beam has been observed in molecular beam deceleration (and trapping) experiments before, but a clear explanation for this was lacking thus far. The oscillatory structure explicitly shown in the lower curve of Figure 3.10

of chapter 3, for instance, is caused by the resonance $s = 5/3$, which has (partly) moved into the velocity distribution of the non-decelerated part of the beam. Although smaller in amplitude than the modulations presented here in Fig 4.6, the earlier observed oscillations presented in chapter 3 have the same physical origin.

4.4 Conclusions

In this chapter, an extended description of phase stability in a Stark decelerator, including higher-order terms in the analysis, is given. These higher order terms give rise to a variety of phase stable regions (resonances), that originate from the spatial and temporal periodicity of the electric fields in the decelerator. These new resonances are experimentally observed using a molecular beam of OH ($^2\Pi_{3/2}, J = 3/2$) radicals. These additional resonances contribute significantly to a detailed understanding of the phase space dynamics of molecules in a Stark decelerator, and the observed TOF profiles explicitly demonstrate that ultimate control over the phase space distribution of the entire molecular beam can be obtained. This is also the main message of this chapter. In the following, some possible applications are nevertheless mentioned.

The resonances presented in the Figures 4.3, 4.4 and 4.5 are excellent velocity markers in the velocity distribution of the molecular beam. In general, an accurate measurement of the velocity and velocity distribution of a molecular beam is difficult. Both the distance between nozzle and detector and the total time of flight of the molecules are often not accurately known. For the resonances described here, the velocity of the resonances is determined by two well calibrated variables, namely the length of the decelerator, and the total time of a burst sequence. The length of the decelerator used in this experiment is 1111 ± 0.2 mm and the accuracy of the burst sequence (with a typical duration of 2.5 ms) is given by the transient time τ of the high voltage switches, which is about 450 ns. The accuracy with which we can determine the absolute velocity of selected resonances is therefore on the order of a few times 10^{-4} .

The observed resonances can be used to map out the electric field geometry of the decelerator; from the magnitudes of the resonances, the relative contributions of the terms $a_1 \sin \theta$, $a_3 \sin 3\theta$, $a_5 \sin 5\theta$, etc. to the potential energy of a molecule in the Stark decelerator, can be obtained. This thereby also provides a method to test the mechanical details of the electrode array.

In most experiments performed with a Stark decelerator to date, the decelerator is used either to guide ($\phi_0 = 0$), or to decelerate ($0 < \phi_0 < \pi/2$) a bunch of molecules. In principle, however, a Stark decelerator can also be used to accelerate ($-\pi/2 < \phi_0 < 0$) molecules. Although there are no intrinsic limitations to the final velocity (other than the speed of light), there are several technical constraints that are associated with the switching of the high voltage. In the decelerator used in this work, for instance, the minimum time ΔT between two successive switch times is about $20 \mu\text{s}$, limiting the attainable final velocity to only 550 m/s if the distance L between adjacent stages is kept constant. Changing to a resonance with $s > 1$ allows one to accelerate the molecules further when the minimum allowed value of ΔT is reached, although more electric field stages are needed to obtain the required final velocity. This might be particularly important when molecules are manipulated using microstructured electrodes that are separated by only a few μm [76]. It is noted that in LINAC's the use of multiple periods of the field for one acceleration step ($s > 1$) is very common [162].

CHAPTER 5

TRANSVERSE STABILITY IN A STARK DECELERATOR

The concept of phase stability in a Stark decelerator ensures that polar molecules can be accelerated, guided or decelerated without loss; molecules within a certain position and velocity interval are kept together throughout the deceleration process. In this chapter the influence of the transverse motion on phase stability in a Stark decelerator is investigated. For typical deceleration experiments, i.e., for high values of the phase angle ϕ_0 , the transverse motion considerably enhances the region in phase-space for which phase stable deceleration occurs. For low values of ϕ_0 , however, the transverse motion reduces the acceptance of a Stark decelerator and unstable regions in phase-space appear. These effects are quantitatively explained in terms of a coupling between the longitudinal and transverse motion. The predicted longitudinal acceptance of a Stark decelerator is verified by measurements on a beam of OH ($X^2\Pi_{3/2}$, $J = 3/2$) radicals passing through a Stark decelerator.

Based on:

Transverse stability in a Stark decelerator

Sebastiaan Y.T. van de Meerakker, Nicolas Vanhaecke, Hendrick L. Bethlem, and Gerard Meijer

Submitted to Phys. Rev. A

5.1 Introduction

In chapter 3 the concept of phase stability was used to describe the longitudinal motion of polar molecules in a Stark decelerator. Assuming that the trajectory of the molecules is always along the molecular beam axis, a one dimensional model for phase stability was presented, that follows the original description of phase stability in a Stark decelerator given by Bethlem *et al.* [8, 14, 72]. In chapter 4, this model was refined by including higher order terms in the analysis, with different levels of approximation. This extended model for phase stability predicts a wide variety of additional phase stable regions, referred to as resonances. The existence of these resonances has experimentally been verified. Although presenting a deeper understanding of phase stability in a Stark decelerator, the extended model still assumes the molecules to travel on the molecular beam axis. In a laboratory Stark decelerator, however, the molecular beam has a velocity component transverse to the molecular beam axis. Since the electric field is always maximum close to the surface of the electrodes, the field drives the molecules back towards the molecular beam axis, resulting in a transversal oscillatory motion around the beam axis. One may wonder, if and how this transverse motion effects the longitudinal motion of the molecules in a Stark decelerator, and hence the longitudinal phase stability. In this chapter, the influence of the transverse motion on phase stability in a Stark decelerator is studied using numerical simulations. The simulations indicate that for low values of the phase angle ϕ_0 the acceptance of a Stark decelerator is smaller than the one dimensional model for phase stability predicts, while the acceptance is enhanced for high values of ϕ_0 . Both effects are quantitatively explained in terms of the coupling between the transverse and longitudinal motion of molecules in a Stark decelerator. The deviation of the longitudinal acceptance of a Stark decelerator from the acceptance that follows from the one dimensional model, is experimentally verified by dedicated measurements on the integrated intensity of a beam of OH ($X^2\Pi_{3/2}, J = 3/2$) radicals passing through a Stark decelerator.

5.2 Longitudinal phase stability

For convenience, the main results of the one dimensional description of longitudinal phase stability in a Stark decelerator presented in section 3.2.1 of chapter 3 is briefly repeated here. In this description the phase angle ϕ_0 plays an essential role. The phase angle indicates the position of the synchronous molecule with respect to the electrodes of the electric field array at the moment the fields are switched. For deceleration, the phase angle ranges from 0° and 90° and determines both the deceleration rate and the longitudinal acceptance of the decelerator. High deceleration rates can be obtained for high values of ϕ_0 , although the longitudinal acceptance of the decelerator rapidly decreases for increasing values of ϕ_0 . This is summarized in Figure 5.1 where the longitudinal acceptance of the decelerator is shown for different values of ϕ_0 . When the decelerator is operated at a phase angle $\phi_0 = 90^\circ$, a maximum amount of kinetic energy can be extracted from the synchronous molecule in an electric field stage, but the longitudinal acceptance of the decelerator vanishes. For low values of ϕ_0 , the acceptance is large, but the corresponding deceleration rate is only modest. For $\phi_0 = 0^\circ$ the deceleration rate vanishes, and the beam is transported through the Stark decelerator without deceleration.

For a given value of ϕ_0 , molecules that have a position in phase-space that is within the closed contour (called separatrix) are phase stable and are selected by the decelerator. These molecules will rotate in longitudinal phase-space around the position of the synchronous molecule. The longitudinal

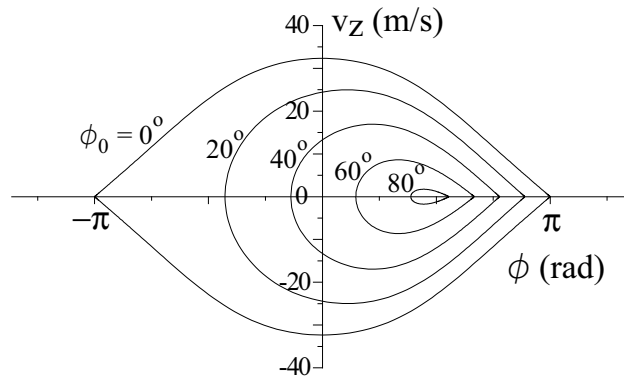


Figure 5.1: Longitudinal acceptance of the decelerator for different values of the phase angle ϕ_0 . The velocity v_z corresponds to the velocity of the synchronous molecule. The center of the electrodes of two adjacent electric field stages are positioned at the relative distances 0 and 11 mm.

oscillation frequency $\omega_z/2\pi$ follows directly from the longitudinal equation of motion (eqn. 3.4 of chapter 3), and depends on the initial longitudinal phase-space position of the molecule. In the remainder of this chapter the initial longitudinal phase-space position is taken along the line with constant velocity, given by the velocity of the synchronous molecule (the line $v_z = 0$ m/s in Fig. 5.1). The position along this line is indicated with z_i , such that the electrodes of adjacent stages are at $z_i = 0$ mm and $z_i = 11$ mm and such that the synchronous molecule for $\phi_0 = 0^\circ$ is initially at $z_i = 5.5$ mm. Restriction of the initial position to points along this line can be done without loss of generality, as any iso-energy contour within the separatrix crosses this line. The natural longitudinal frequencies are shown in Figure 5.2 as a function of z_i , for the phase angles $\phi_0 = 0^\circ, 40^\circ$ and 80° . The separatrices that determine the longitudinal acceptance of the decelerator for these phase angles are given in the upper part of this figure for convenience. As expected from the 1 dimensional model for phase stability, the longitudinal oscillation frequency is maximal when the initial longitudinal position of a molecule is close to the position of the synchronous molecule. Further outward, the oscillation frequency is lowered, reaching zero on the separatrix. For OH radicals in the $M_J\Omega = -9/4$ component of the $X^2\Pi_{3/2}, v = 0, J = 3/2$ rotational ground state, the maximum longitudinal frequency is approximately 700 Hz when the Stark decelerator is operated at a phase angle $\phi_0 = 0^\circ$. The slightly reduced frequency around the synchronous molecule when the decelerator is operated at $\phi_0 = 0^\circ$ is caused by the non-linear Stark effect of the OH radical for low values of the electric field strength, but simulations indicate that this effect hardly influences the structure of the phase-space distributions discussed in this chapter.

5.3 Transverse stability

5.3.1 Transverse motion

In a Stark decelerator, the electric field is maximal close to the surfaces of the opposing electrodes in a field stage. Consider an electric field stage where the electrodes are oriented along the x direction. Molecules in a low-field seeking state that approach (along the z axis) these electrodes experience a focussing force towards the molecular beam axis in the y direction; the force in the x direction

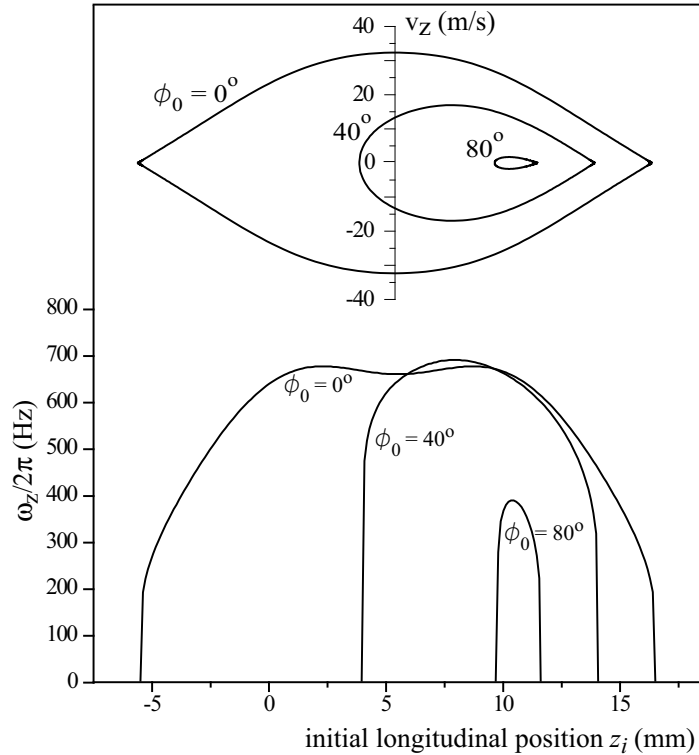


Figure 5.2: The natural longitudinal frequencies $\omega_z/2\pi$ for the phase angles $\phi_0 = 0^\circ$, 40° and 80° , as a function of the initial longitudinal position z_i . For these phase angles, the longitudinal phase-space acceptance diagrams that follow from the 1D model for phase stability are shown in the upper part.

is negligible. The electric field stages in the decelerator are alternately positioned in the x and y direction to obtain a focussing force in both transverse directions. As a consequence, molecules that have an off-axis position and/or velocity component will follow an oscillatory trajectory around the molecular beam axis. This property is as essential for the operation of a Stark decelerator as the longitudinal phase stability; the spreading out of the selected part of the molecular beam is prevented in both the transverse and longitudinal direction.

A quantitative analysis of the intrinsic focussing properties of the decelerator can be obtained when the transverse force is calculated that a molecule experiences during its flight through the decelerator. We will follow here the method that has been used before to calculate the average transverse force for the ND_3 molecule in a Stark decelerator [14] *. The actual transverse force experienced by a molecule depends in general on its position and time. In this chapter, we assume that the motions in the x and y direction are uncoupled and can be treated independently. The validity of this approach is confirmed by numerical simulations. The transverse oscillation time is much larger than the time it takes the molecule to traverse one period (two stages) of the decelerator. The transverse motion can therefore be described by introducing the average force components $\bar{F}_{x,y}$, that are obtained by integrating over one period of the decelerator. The average transverse force only depends on the phase angle ϕ . The longitudinal oscillation frequency $\omega_z/2\pi$ is sufficiently low that, to a good approximation, all molecules within the longitudinal acceptance area travel a distance $2L$ in the time-

*In ref. [14] an error was made when performing the integral (eqn. 5 of ref. [14]), leading to too high values for the force constants.

interval $2\Delta T$. In the calculation of the average force the transverse position is taken constant in the time-interval $2\Delta T$, since the transverse motion is slow. The average force $\bar{F}_y(\phi)$ then reads:

$$\begin{aligned}\bar{F}_y(\phi) &= \frac{1}{2\Delta T} \int_t^{t+2\Delta T} F_y(z(t'), t') dt' \\ &\approx \frac{1}{2L} \int_{\phi L/\pi}^{(\phi+2\pi)L/\pi} F_y(z) dz.\end{aligned}\quad (5.1)$$

To a good approximation, the transverse force \bar{F}_y is linear in the displacement y from the molecular beam axis. The strength of the transverse force can therefore be expressed in terms of a frequency $\omega_y(\phi)$, referred to as the natural transverse frequency, using the relation:

$$\bar{F}_y = -m\omega_y^2(\phi) y. \quad (5.2)$$

In Figure 5.3, the natural transverse oscillation frequency of the Stark decelerator is shown for an OH ($X^2\Pi_{3/2}$, $J = 3/2$, $M_J\Omega = -9/4$) radical as a function of the phase ϕ . For a molecule at $\phi = 0^\circ$,

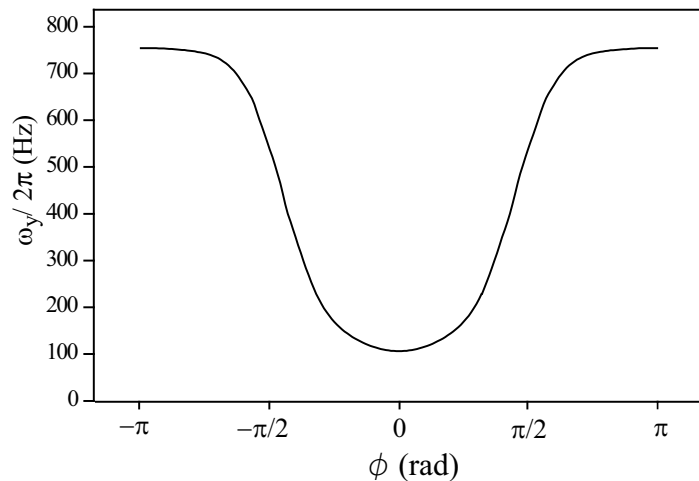


Figure 5.3: Natural transverse oscillation frequency $\omega_y/2\pi$ of the Stark decelerator for an OH ($X^2\Pi_{3/2}$, $J = 3/2$, $M_J\Omega = -9/4$) radical as a function its phase ϕ .

the natural transverse oscillation frequency is minimal and has a value of only 110 Hz. For increasing longitudinal phases, the natural transverse frequency increases quickly, reaching a maximum of about 750 Hz for $\phi = 180^\circ$.

The increasing transverse oscillation frequency for increasing values of ϕ can be understood from the longitudinal motion of the molecules. When the Stark decelerator is operated at $\phi_0 = 0^\circ$, the synchronous molecule will only fly a maximum distance $L/2$ (5.5 mm for the decelerator discussed here) away from the electrodes that are grounded before the fields are being switched. The synchronous molecule is therefore always closer to the set of electrodes that is grounded than to the set that is at high voltage. This implies that the synchronous molecule is always in the region where the transverse focussing force is only modest, and the corresponding transverse oscillation frequency is low. Non-synchronous molecules oscillate in longitudinal phase-space around the position of the synchronous molecule and hence come closer to the position of the electrodes that are at high voltage. Molecules

with an ever larger displacement in longitudinal phase-space from the position of the synchronous molecule, will be focussed more efficiently, and follow a transverse oscillatory motion with a higher oscillation frequency.

Generally, a molecule oscillates in phase around the synchronous molecule. The time-dependence of the transverse force that a (non-synchronous) molecule experiences during its flight through the decelerator can be calculated if the phase $\phi(t)$ of the molecule as a function of time, that follows from the natural longitudinal frequency $\omega_z/2\pi$, is known. The natural longitudinal and transverse frequencies, presented in the Figures 5.2 and 5.3, together in principle govern the complete dynamics of molecules in the Stark decelerator. It is seen from these figures that the longitudinal and transverse oscillation frequencies can become rather similar. One can expect, therefore, that a coupling between the longitudinal and transverse motion can result in parametric amplification, leading to unstable operation of the decelerator. In the next section numerical trajectory simulations are presented, to investigate the influence of the transverse motion on the longitudinal acceptance of a Stark decelerator.

5.3.2 Longitudinal phase stability; 3D versus 1D

The effect of the transverse motion of the molecules on the longitudinal acceptance of the decelerator can be studied by comparing the longitudinal acceptance of the Stark decelerator, that is calculated assuming (i) that the molecules fly along the molecular beam axis (referred to as a 1D calculation), and (ii) taking the real trajectories of the molecules into account (3D calculation). A comparison that is generally valid is difficult, however, as the motion of a molecule in a Stark decelerator critically depends on the Stark effect of the molecule, the electric field strengths in a deceleration stage, the actual velocity of the molecule as it progresses through the decelerator, and hence the value of the phase angle that is used. In addition, a possible influence of the transverse motion can only manifest itself when the molecule spends sufficient time in the decelerator. We restrict ourselves here to numerical studies of the trajectories of OH ($X^2\Pi_{3/2}, v=0, J=3/2, M_J\Omega = -9/4$) radicals that pass through a Stark decelerator. Furthermore, we limit ourselves in this section to the resonance $s=1$, as this is of most practical interest if a Stark decelerator is operated with the aim to decelerate a molecular beam. The influence of the transverse motion on resonances with $s > 1$ will be discussed in section 5.3.6. In the calculations presented in this chapter, the Stark decelerator that is described in chapter 3 is simulated. In the simulations only the length of the decelerator is varied, as will be described below.

A profound difference in the longitudinal acceptance of the decelerator is found for the one and the three dimensional trajectory calculations. This is illustrated in Figure 5.4. For different values of the phase angle ϕ_0 , the trajectories of a package of molecules are simulated using a 1D and a 3D trajectory simulation. The resulting longitudinal phase-space distributions of the molecules in the last electric field stage of the decelerator are shown on the left (3D) and on the right (1D) hand side of Figure 5.4. The separatrices that follow from the 1D model for phase stability are given as an overlay. The horizontal and vertical scale for each distribution are different for reasons of clarity. For each value of ϕ_0 , the time sequence of the decelerator is chosen such that the total time of flight of the synchronous molecule in the decelerator is approximately 8 ms, and the final velocity of the synchronous molecule is about 70 m/s. This is achieved by an appropriate choice of the initial velocity of the synchronous molecule and the length of the decelerator. This strategy allows for a good comparison between the observed phase-space distributions for different values of ϕ_0 . For the phase angle $\phi_0 = 0^\circ$ a velocity of 250 m/s for the synchronous molecule is chosen. In Table 5.1, the initial velocity v_i and the final

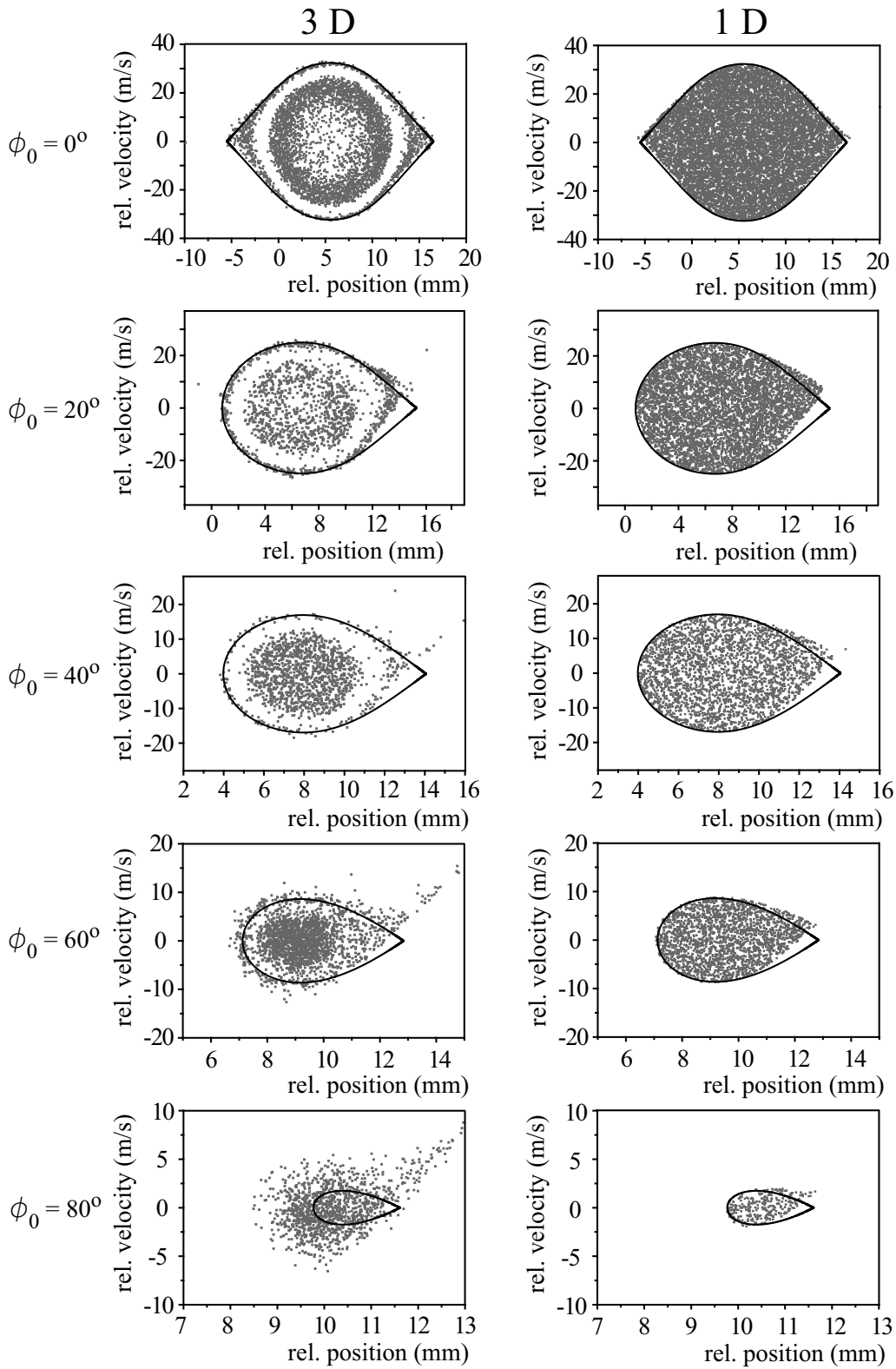


Figure 5.4: Longitudinal phase-space distributions of OH ($X^2\Pi_{3/2}$, $J = 3/2$, $M_J\Omega = -9/4$) radicals inside the decelerator that result from 1D and 3D trajectory simulations when the Stark decelerator is operated at $\phi_0 = 0^\circ$, 20° , 40° , 60° and 80° . In all simulations, the molecules spend approximately 8 ms in the decelerator.

velocity v_f of the synchronous molecule, and the number of stages of the decelerator that are used in the simulations for each value of ϕ_0 , are summarized. In the 1D (3D) simulations, the molecules

Table 5.1: Relevant parameters of the trajectory simulations that are performed to calculate the longitudinal phase-space distributions presented in Figure 5.4. The initial velocity v_i and the final velocity v_f of the synchronous molecule, and the number of stages of the decelerator are given for each value of ϕ_0 .

ϕ_0	v_i (m/s)	v_f (m/s)	# stages
0°	250	250	180
20°	250	65	120
40°	450	74	201
60°	545	79	201
80°	665	68	249

are homogeneously distributed over a 2D surface (6D volume) in phase-space at the entrance of the decelerator that largely exceeds the 2D (6D) acceptance of the decelerator. It is important to note that the phase-space densities (number of molecules that are used in the simulation per unit area/volume) in each of the simulations is different to limit the computational time. Therefore, no comparison is possible between the density of molecules in the different phase space diagrams. Only the structure of the phase-space distributions is of relevance here.

From Figure 5.4 it is seen that for all values of ϕ_0 , the separatrix accurately describes the longitudinal acceptance of the decelerator if the trajectories of the molecules are restricted to the molecular beam axis. The longitudinal phase-space distributions in the last stage of the decelerator (some 8 ms after the molecules have entered the decelerator) are homogeneous, and no structure in the distribution is observed. The deviation of the phase-space distribution from the separatrix for $\phi_0 > 0^\circ$ results from the relatively low velocity (~ 70 m/s) of the synchronous molecule in the last electric field stage of the decelerator. For these velocities, the Stark energy of the molecules in the field is not negligible compared to the kinetic energy, and the assumptions that are used in the derivation of the model for phase stability are not valid anymore. The phase-space distribution changes from a 'fish-like' to a 'golf-club-like' shape [14]. However, this deviation from the model is unrelated to the three dimensional motion of the molecules through the decelerator, and will not be further discussed here.

In contrast to the 1D simulations, the phase-space distributions that result from the three dimensional trajectory simulations are highly structured, and this structure differs depending on the phase angle ϕ_0 . For $\phi_0 = 0^\circ$ the longitudinal phase-space distribution shows regions that are alternately empty and filled. In the center of the separatrix, only a limited number of molecules can be found that are phase stable. This is counter-intuitive, as this implies that molecules that have a position in phase-space close to the synchronous molecule are actually not so well transported through the decelerator. Surrounding this empty center, a stable ring is found. Even further away from the center, the stable ring suddenly changes into an empty ring, referred to as a halo. Hardly any molecules exist in the last stage of the decelerator that have a position in phase-space that is within this halo. Particularly interesting is the sharp boundary between the stable ring and the halo. Close to and on the separatrix, a thin outer stable ring appears.

For higher values of ϕ_0 , the structure in the phase-space distribution changes. The empty area in the center vanishes rapidly, and is already almost absent for $\phi_0 = 20^\circ$. A stable region in the center

of the separatrix, followed by an empty halo and a stable ring close to the separatrix is observed for the phase angles $\phi_0 = 20^\circ$ and $\phi_0 = 40^\circ$. For $\phi_0 = 60^\circ$, the halo gains in stability, although the highest stability can still be found in the center of the separatrix. Although exhibiting a structured distribution, the extent of the phase-space distribution for phase angles up to 60° is well described by the separatrix. For $\phi_0 = 80^\circ$, however, the majority of the molecules have a position in phase-space that is outside the separatrix, and the total area of the phase-space distribution largely exceeds the area of the separatrix.

The phase-space distributions of the molecules in the last stage of the decelerator for different values of ϕ_0 , presented in Figure 5.4, have important implications for the operation of a Stark decelerator. For low values of the phase angle ϕ_0 , the acceptance of the decelerator is less than the model of phase stability suggests. Indeed, the simulations show that molecules with a position in phase-space originally within the halo crash onto the electrodes somewhere during their path through the decelerator. For high values of ϕ_0 , however, the acceptance of the Stark decelerator is actually significantly higher than can be expected from the model; a larger fraction of the molecular beam can be selected than indicated by the separatrix. Apart from these implications, the observed structure in the phase-space distributions, and in particular the structure for $\phi_0 = 0^\circ$, indicates that interesting (and complex) six dimensional phase-space dynamics of molecules in a Stark decelerator is present. In the following sections, the structure of the observed phase-space distribution for different values of ϕ_0 is explained in terms of a coupling between the transverse and longitudinal motion of the molecules in the decelerator.

5.3.3 Effective phase angle

The enhanced stability that occurs when the decelerator is operated at high phase angles can be understood from the potential energy of a molecule during its trajectory between two adjacent electric field stages. In Figure 5.5 the Stark energy of an OH ($X^2\Pi_{3/2}$, $J = 3/2$, $M_J\Omega = -9/4$) radical is shown as a function of its position in an electric field stage, for two different trajectories of the molecule. The electrode positions are indicated by the vertical dashed lines. The electrodes at the positions 0 mm and 11 mm are grounded and placed at high voltage, respectively. In the dashed curve of Figure 5.5, the Stark energy is shown when the trajectory of the molecule is parallel to, but 1.5 mm away from the molecular beam axis. In the solid curve, the molecule is assumed, like in the one dimensional model for phase stability, to fly along the beam axis. Clearly, for longitudinal positions close to the position of the electrodes that are placed at high voltage, the Stark energy of a molecule that has an off-axis position deviates significantly from the Stark energy on the molecular beam axis. This is expected, as the electric field close to the surface of the electrodes is higher than the electric field on the molecular beam axis. However, the time sequence for a given phase angle ϕ_0 that is applied to the decelerator is normally calculated for a synchronous molecule that flies along the molecular beam axis. We recall here the physical meaning of the phase angle ϕ_0 : the electric fields are switched when the synchronous molecule has reached the same longitudinal position, indicated by ϕ_0 , in an electric field stage. The positions 5.5 mm and 11 mm in Figure 5.5 correspond to the phase angles $\phi_0 = 0^\circ$ and $\phi_0 = 90^\circ$, respectively. However, Figure 5.5 implies that the synchronous molecule actually observes the *lowest* difference in Stark energy during its trajectory between two successive switch times. For molecules that have off-axis velocity components, the time sequence that is applied actually matches with a time sequence that would have been obtained for a synchronous molecule with a lower value of ϕ_0 . This situation is analogous to the discussion of the simultaneous deceleration of

OH radicals in different quantum states presented in chapter 3 and the simultaneous deceleration of different ammonia isotopomers [14]. If a time sequence is generated for a molecule that can be least-well decelerated, a molecule with a different Stark effect and/or different mass that is synchronous with this time sequence can be found as well. The longitudinal acceptance of the decelerator is smallest, however, for the molecule that can be least-well decelerated. In the situation discussed here this implies that, for a given time sequence, molecules that do not fly along the molecular beam axis observe a larger longitudinal acceptance of the decelerator. Since in a laboratory molecular beam a large distribution of off-axis positions and velocity components is present, the longitudinal acceptance of the decelerator at high phase angles is best described by an 'effective phase angle' $\phi_{0,eff}$ instead of ϕ_0 , with $\phi_{0,eff} < \phi_0$. In section 5.4.1 experiments are described where phase stable deceleration of a package of OH radicals is observed when the Stark decelerator is operated at a phase angle $\phi_0 = 90^\circ$.

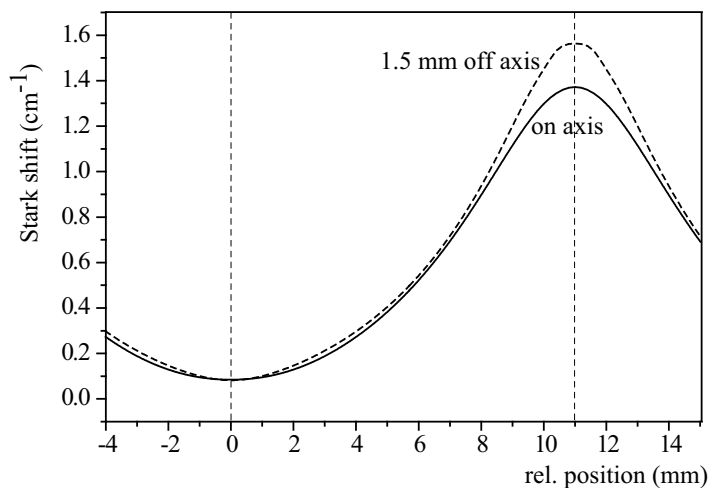


Figure 5.5: Stark energy of an OH ($X^2\Pi_{3/2}$, $J = 3/2$, $M_J\Omega = -9/4$) radical as a function of its longitudinal position in an electric field stage, when the molecule flies on (solid curve) and 1.5 mm away from (dashed curve) the molecular beam axis. The positions of the electrodes are indicated by the vertical dashed lines.

5.3.4 Transverse stability

The structure in the longitudinal phase-space distribution that is observed when the Stark decelerator is operated at low phase angles is more complex. A good understanding of the processes that lead to this structure can be obtained by studying the three dimensional trajectories of molecules in a Stark decelerator when the decelerator is operated at a phase angle $\phi_0 = 0^\circ$. For this value of ϕ_0 , the contrast between stable and unstable regions is maximal. In Figure 5.6, the transverse trajectory of an OH ($X^2\Pi_{3/2}$, $J = 3/2$, $M_J\Omega = -9/4$) radical is shown, for different initial longitudinal positions z_i in the first electric field stage of the decelerator. The Stark decelerator is operated at a phase angle of 0° for a synchronous molecule with a longitudinal velocity of 250 m/s. These values are identical to the parameters that were used for the simulations presented in the upper phase-space distributions in Figure 5.4. The Stark decelerator simulated here consists of 500 stages, increasing the total time of flight to about 22 ms. The longitudinal phase-space acceptance of the decelerator in this case is identical to the distribution in the top left corner of Figure 5.4, and is shown on the left hand side

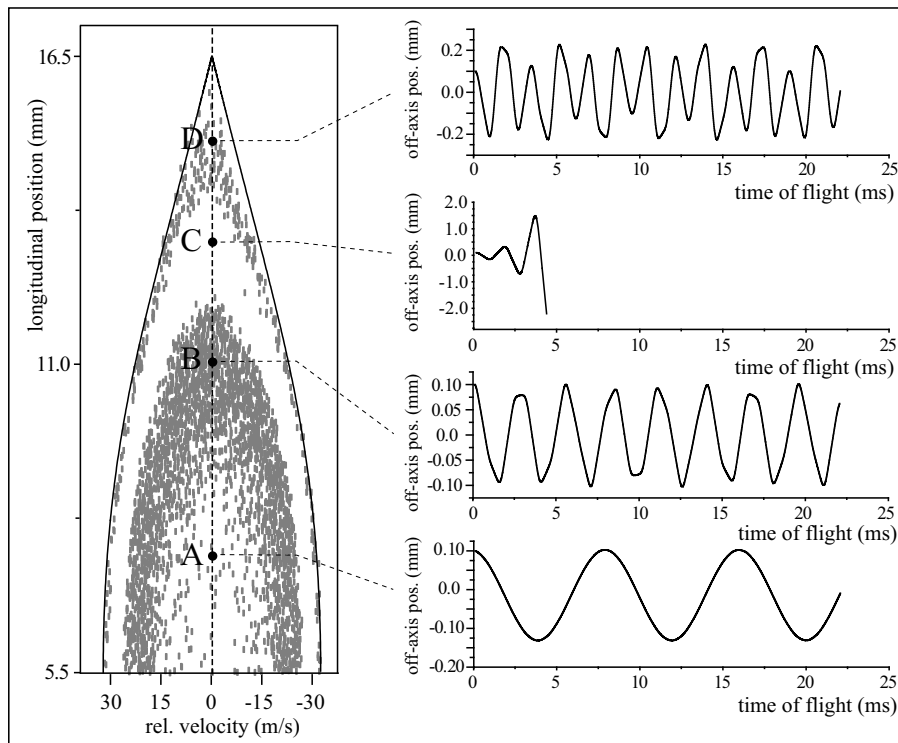


Figure 5.6: The transverse trajectory of an OH ($X^2\Pi_{3/2}$, $J = 3/2$, $M_J\Omega = -9/4$) radical in the decelerator, for different initial longitudinal positions in the first electric field stage of the decelerator. The Stark decelerator is operated at a phase angle of 0° for a synchronous molecule with a longitudinal velocity of 250 m/s. For each of the initial longitudinal positions, the molecule is given a small initial off-axis position of 0.1 mm, a longitudinal velocity of 250 m/s and a transverse velocity of 0 m/s. Note the different vertical scales that are used in each graph.

of Figure 5.6; note that the longitudinal position axis is placed vertical in this figure. For each of the initial longitudinal positions, indicated by the black points, the molecule is given a small initial off-axis position of 0.1 mm, a longitudinal velocity of 250 m/s and a transverse velocity of 0 m/s. The initial position of the molecule is thus very close to the molecular beam axis and the initial velocity direction is parallel to the beam axis. The off-axis position is then calculated as a function of time, and is shown for each initial longitudinal position z_i on the right hand side of Figure 5.6. It is seen that the transverse trajectory of the molecule strongly depends on z_i . When the molecule is initially within the empty region in the center of the separatrix (position A in Figure 5.6), the molecule exhibits an oscillatory motion around the beam axis. The maximum amplitude is approximately given by the initial off-axis position, and the oscillation frequency is about 125 Hz. When the molecule starts at position B, inside the stable ring, the oscillation frequency is about a factor three larger, although the transverse motion is less periodic. The maximum off-axis position is again given by the initial value of 0.1 mm. When the molecule has an initial longitudinal position that is inside the halo (position C), the transverse oscillation frequency is again higher, but the transverse trajectory shows a behavior that is fundamentally different. The amplitude of the transverse motion is repeatedly enhanced, until the

off-axis position reaches the surface of an electrode that is located 2.0 mm from the molecular beam axis. Note the different vertical scale that is used in this graph. When the molecule starts at position D, in the stable region close to the separatrix, the transverse trajectory is similar to the transverse trajectory that is observed for the initial position B. However, the transverse oscillation frequency is again increased.

The reason for the low number of molecules that is found in the central region of the phase-space distribution can be directly inferred from Figure 5.3. In this region, the phase of a molecule oscillates around the synchronous molecule with only a limited amplitude. The transverse frequency in this region is then too low to restrict the transverse trajectory to the $4 \times 4 \text{ mm}^2$ transverse spatial area that is given by the surfaces of the electrodes. Only molecules that have small transverse velocity components do not crash onto the electrodes somewhere downstream from the entrance of the decelerator. Although being inherently stable, the transverse acceptance of the decelerator in this region is small. Non-synchronous molecules that have an ever larger displacement from the synchronous molecule in longitudinal phase-space experience a higher transverse force, and the transverse acceptance of the Stark decelerator increases. The number of molecules that do not crash on the electrodes rises rapidly, and the phase-space distribution becomes more filled. When the Stark decelerator is operated at higher values of ϕ_0 , the synchronous molecule approaches closer the set of electrodes that are at high voltage when the fields are switched. Compared to $\phi_0 = 0^\circ$, phase-stable molecules are in a region where the transverse oscillation frequency is higher. The molecules are therefore more efficiently focussed, and the empty central region becomes smaller for increasing values of ϕ_0 . In the phase-space distributions of Figure 5.4 it is seen that for $\phi_0 > 20^\circ$, the empty central region in the longitudinal phase-space distribution already vanishes.

Referring back to Figure 5.4, the halo in the longitudinal phase-space distribution for $\phi_0 = 0^\circ$ cannot be understood from the argumentation that is presented above. On the contrary, for molecules with an ever larger displacement from the synchronous molecule, the Stark decelerator is expected to have a larger transverse acceptance. Obviously, the appearance of the halo is the result of an unstable behavior of the transverse trajectory of molecules (see Figure 5.6). This strongly suggests that the coupling between the longitudinal and transverse motion can indeed result in a parametric amplification of the (transverse) motion. In the next section a model is presented for the transverse motion of molecules in a Stark decelerator, based on the time-dependence of the transverse force, that leads to a quantitative understanding of the presence and location of the halo.

5.3.5 Transverse equation of motion, $\phi_0 = 0^\circ$

In the derivation of the transverse equation of motion that is presented in this section, we will again limit ourselves to $\phi_0 = 0^\circ$. It is clear from Figure 5.5 that, in particular for low and moderate phase angles, the potential energy of a molecule that flies on or off axis is almost identical. In the model for the transverse motion presented in this section, we will therefore assume that the longitudinal frequency $\omega_z/2\pi$ does not depend on the transverse position of the molecule. The transverse oscillation frequency $\omega_y/2\pi$ as a function of time for a non-synchronous molecule with a given initial longitudinal position z_i , can then be calculated as is illustrated in Figure 5.7. Let's consider a molecule with a certain initial longitudinal position z_i and some initial transverse position. The transverse oscillation frequency $\omega_y/2\pi$ as a function of the phase ϕ of this molecule, as already presented in Figure 5.3, is shown on the right top corner of Figure 5.7. The phase $\phi(t)$ oscillates with the longitudinal frequency $\omega_z/2\pi$ and is shown in the left top corner of Figure 5.7. The value of $\omega_z/2\pi$ follows from the value of

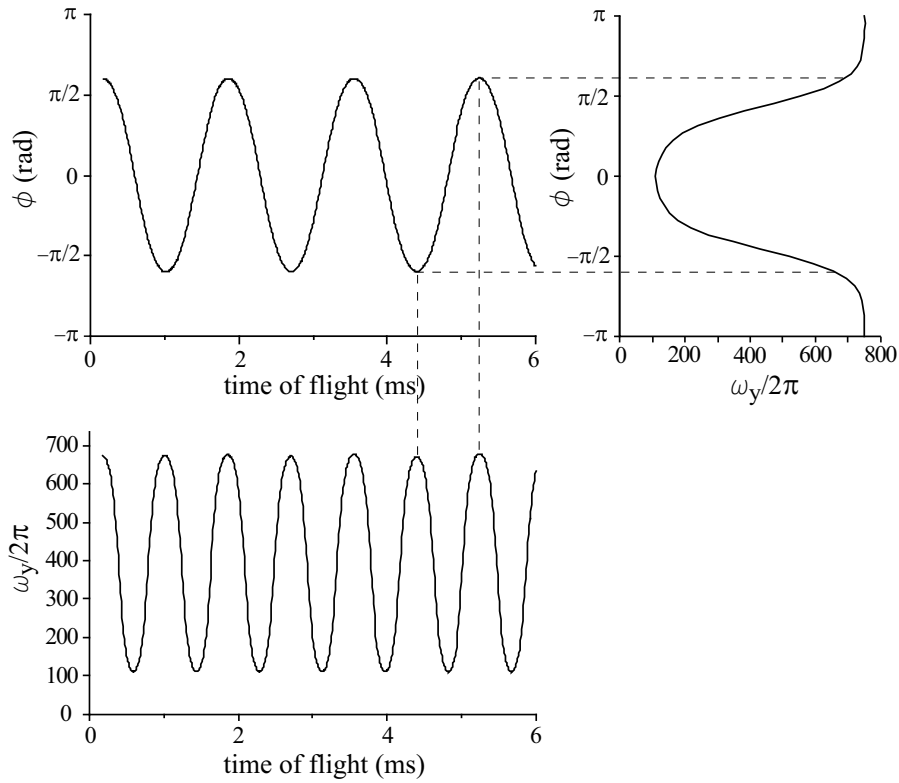


Figure 5.7: The temporal dependence of the transverse oscillation frequency ω_y can be constructed from the temporal dependence of the phase ϕ in combination with the dependence of ω_y on ϕ (Figure 5.3).

z_i (see Figure 5.2). The outer turning points of the motion of the molecule are indicated by the horizontal dashed lines in Figure 5.7. The temporal dependence of the transverse oscillation frequency $\omega_y(t)/2\pi$ can now easily be constructed, and is shown in the lower curve of Figure 5.7. It is readily seen that $\omega_y(t)$ oscillates with twice the longitudinal oscillation frequency. The transverse trajectory of the molecule can be calculated by solving the equation of motion

$$\frac{d^2y}{dt^2} + \omega_y^2(t)y = 0. \quad (5.3)$$

To a good approximation, $\omega_y^2(t)$ can be represented as an oscillatory function:

$$\omega_y^2(t) = \omega_0^2 - A \cos(2\omega_z t). \quad (5.4)$$

The transverse motion is driven by the longitudinal motion, and the transverse equation of motion is given by the well-known Mathieu equation [164]

$$\frac{d^2y}{d\tau^2} + (a - 2q \cos(2\tau))y = 0, \quad (5.5)$$

with

$$a = \left(\frac{\omega_0}{\omega_z}\right)^2; \quad q = \frac{A}{2\omega_z^2}; \quad \tau = \omega_z t. \quad (5.6)$$

Depending on the values of a and q , the solutions of the Mathieu equation exhibit stable or unstable behavior. This is shown in the Mathieu stability diagram in the left top corner of Figure 5.8. The regions where stable solutions exist are indicated as gray areas; in the white regions the solutions are exponentially unstable. For the equation of motion (5.5), $a \geq 0$ and the largest unstable region appears around $a = 1$. For this value $\omega_0 = \omega_z$, i.e., the time-integrated transverse frequency $\omega_y/2\pi$ is equal to the longitudinal oscillation frequency $\omega_z/2\pi$, leading to parametric amplification of the transverse trajectory. In general, instable regions appear as "tongues" that touch the a axis at $a = p^2$ ($p \in \mathbb{N}$) [165]. The value of q determines the width of the unstable region. The description of the transverse motion of molecules in a Stark decelerator as presented here is very similar to the description of ions that are stored in a Paul trap [166, 167], or of ions that pass through a quadrupole mass spectrometer [168].

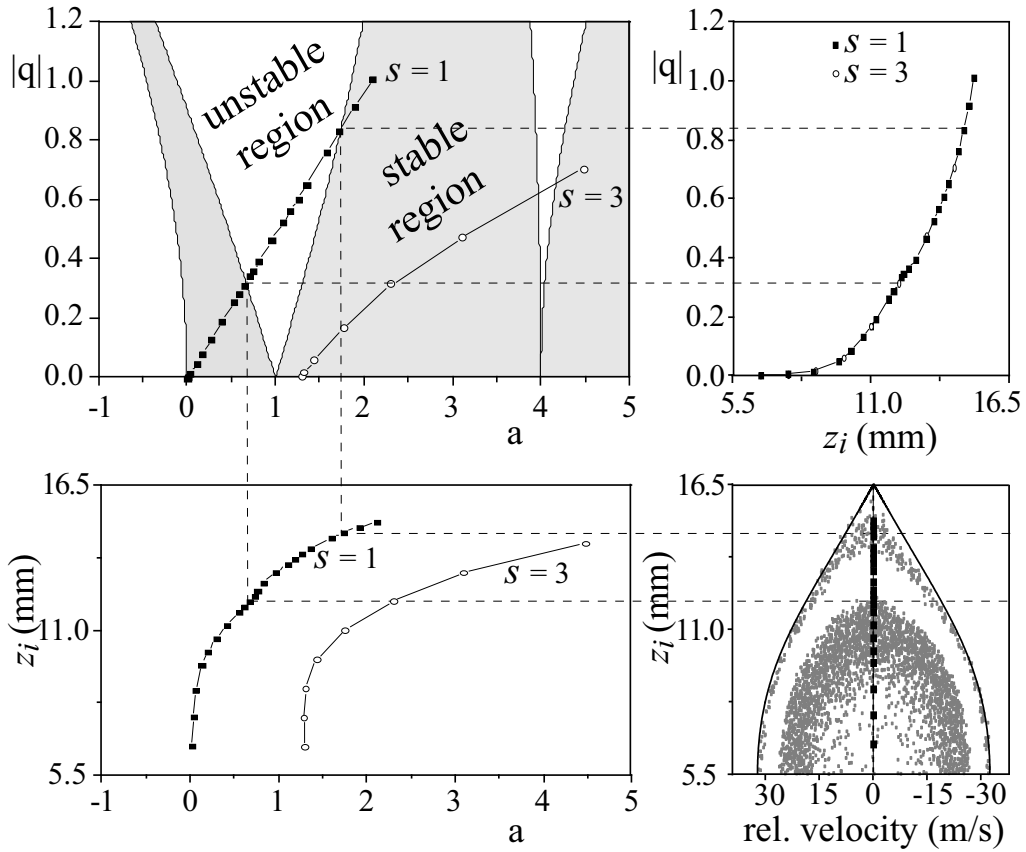


Figure 5.8: Mathieu stability diagram, indicating whether the solutions of the transverse equation of motion are stable or unstable. The position in the stability diagram of a non-synchronous molecule as a function of the initial longitudinal position z_i , is indicated by the filled squares (open circles), if the Stark decelerator is operated at phase angle $\phi_0 = 0^\circ$ using the resonance with $s = 1$ ($s = 3$). The longitudinal phase-space distribution of molecules that results from three dimensional trajectory calculations is given for $s = 1$ in the right bottom corner.

For different values of z_i , indicated by the filled black squares in the phase-space distribution in the right bottom corner of Figure 5.8, the values of ω_z , ω_0 , and A , and hence the parameters a and q , can be determined following the methodology as outlined in Figure 5.7. The resulting values of

a and q as a function of z_i are indicated in the left bottom corner and the right top corner of Figure 5.8, respectively. The corresponding locations in the Mathieu stability diagram are indicated as well. For molecules with an initial longitudinal position z_i that is close to the synchronous molecule, a and q are small, and the Mathieu equation has stable solutions. For values of z_i that are further away from the synchronous molecule, however, both a and q significantly increase. Above a critical value, the trajectories suddenly become unstable. The value of z_i at which this resonance occurs, is in quantitative agreement with the position of the appearance of the halo in the phase-space distribution of the 3D trajectory simulation of molecules in a Stark decelerator. For even larger values of z_i (closer to the separatrix), the values of a and q are within a stable region in the stability diagram again. This is also observed in the phase-space distribution. The corresponding threshold value, however, does not exactly match to the point where the halo changes into a stable region. This is mainly because the longitudinal motion is not harmonic, and for large values of z_i , $\omega_y^2(t)$ cannot accurately be represented by eqn. (5.4). In these regions, a quantitative prediction from the model presented above cannot be expected.

The model for the transverse trajectory of molecules in a Stark decelerator presented above provides a clear understanding of the physical background for the presence of the halo. Molecules with a position in phase-space within this halo experience a transverse force that is driven by the longitudinal motion in such a way that the transverse amplitude of the motion exponentially grows until the molecules crash onto the electrodes of the decelerator. This part of longitudinal phase-space is therefore inherently unstable. Outside the halo, however, molecules within a certain transverse position and velocity interval, i.e., within the transverse acceptance of the Stark decelerator, will be bound within the $4 \times 4 \text{ mm}^2$ spatial area that is given by the electrode array. The maximum transverse velocity component that is allowed for a molecule follows from the transverse force (eqn. (5.4)) that a molecule experiences during its flight through the decelerator. The time averaged transverse force constant is given by $m\omega_0^2$, leading to a maximum transverse well depth of $\frac{1}{2}m\omega_0^2(2\text{mm})^2$. The maximal transverse velocity v_{max} that can be captured can then be estimated via $\frac{1}{2}mv_{\text{max}}^2 = \frac{1}{2}m\omega_0^2(2\text{mm})^2$. The dependence of ω_0^2 on the initial longitudinal position z_i is shown in Figure 5.9. The range of initial longitudinal positions z_i in which the decelerator is unstable, is indicated by the gray area. For molecules with an initial longitudinal position z_i that is close to the synchronous molecule (position 5.5 mm in Figure 5.9), the maximal transverse velocity is approximately 1 m/s. For initial positions z_i of 11 mm and 15 mm, the transverse velocity acceptance is approximately 5 m/s and 7 m/s, respectively.

Strictly spoken, the model described above is only valid when the Stark decelerator is operated at phase angle $\phi_0 = 0^\circ$. Only then $\omega_y^2(t)$ can, in a good approximation, be represented as a sinusoidally oscillating function, leading to the Mathieu equation for the transverse equation of motion. For higher values of ϕ_0 , the function $\omega_y^2(t)$ is still periodic, but additional terms in the equation of motion eqn. (5.5) are needed to account for the non-sinusoidal character of ω_y^2 . The equation of motion then transforms from the Mathieu equation into the less well-known Hill [169] equation. Again, the solutions of this equation exhibit stable and unstable behavior, although more parameters than just a and q determine the stability. A detailed analysis of the corresponding equations of motion is beyond the scope of this chapter, but it is believed that a quantitative description of the halo's that appear for the phase angles $\phi_0 = 20^\circ$, 40° , and 60° in Figure 5.4 can be obtained as well. For (much) higher values of ϕ_0 , the y -dependence of ω_z becomes important, and will determine the acceptance of the Stark decelerator, as described in section 5.3.3.

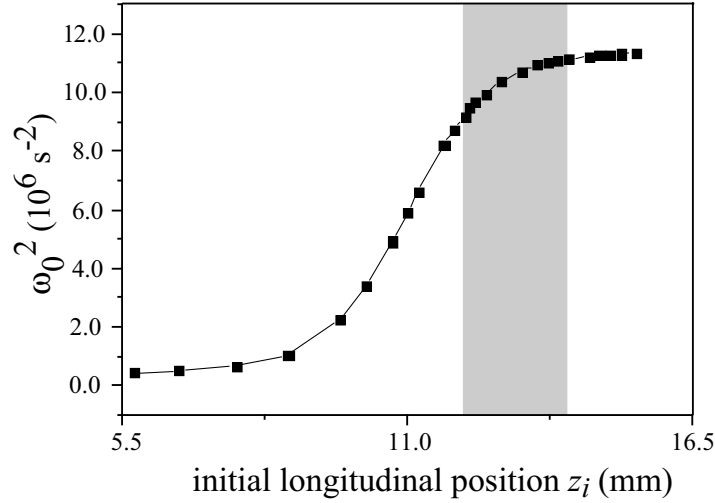


Figure 5.9: The time-averaged transverse oscillation frequency ω_0^2 for an OH ($X^2\Pi_{3/2}, J = 3/2, M\Omega = -9/4$) radical, as a function of the initial longitudinal position in the Stark decelerator, if the decelerator is operated at $\phi_0 = 0^\circ$. The range in which the decelerator is unstable is indicated by the gray area.

5.3.6 Higher-order resonances

So far, the transverse motion is analyzed in situations where the Stark decelerator is operated using the resonance with $s = 1$, i.e., the situation where the synchronous molecule travels a distance L before the fields are switched. In this section the influence of the transverse motion of the molecules on the longitudinal acceptance of the decelerator is discussed, if the decelerator is operated at $\phi_0 = 0^\circ$ on a resonance with $s > 1$. The strongest of these higher-order resonances is the resonance with $s = 3$. The longitudinal motion of the molecules through the decelerator is fundamentally different if the decelerator is operated at a higher-order resonance. For instance, compared to normal ($s = 1$) operation of the Stark decelerator, the synchronous molecule travels a distance that is equal to 3 instead of 1 electric field stage(s) before the fields are switched if the decelerator is operated at $s = 3$. The synchronous molecule therefore always traverses a set of electrodes that is at high voltage during its path between successive switch times. The transverse focussing properties of the decelerator are therefore fundamentally different as well: the synchronous molecule is more strongly focussed, and the transverse oscillation frequency of molecules that are close to the synchronous molecule will be higher.

In the left hand side of Figure 5.10, the longitudinal phase-space acceptance, and the corresponding natural longitudinal and transverse oscillation frequencies are summarized, that are present when the decelerator is operated at $\phi_0 = 0^\circ$ using the resonance with $s = 1$. The initial longitudinal positions z_i that lead to the empty center or the halo, are indicated by the gray areas. In the right hand panel of Figure 5.10, the longitudinal and transverse natural frequencies of the decelerator are shown for an OH ($X^2\Pi_{3/2}, J = 3/2, M_J\Omega = -9/4$) radical, if the Stark decelerator is operated at $\phi_0 = 0^\circ$ using the first-order resonance with $s = 3$. All other parameters are identical to the parameters used in the numerical simulations before. The transverse oscillation frequency for a molecule that is close to the synchronous molecule is indeed much larger compared to operation of the decelerator at $s = 1$. In addition, the value of the natural transverse frequency depends less on the phase ϕ of the molecule. The natural longitudinal frequency is scaled down by a factor $\sqrt{3}$ compared to $s = 1$, as predicted

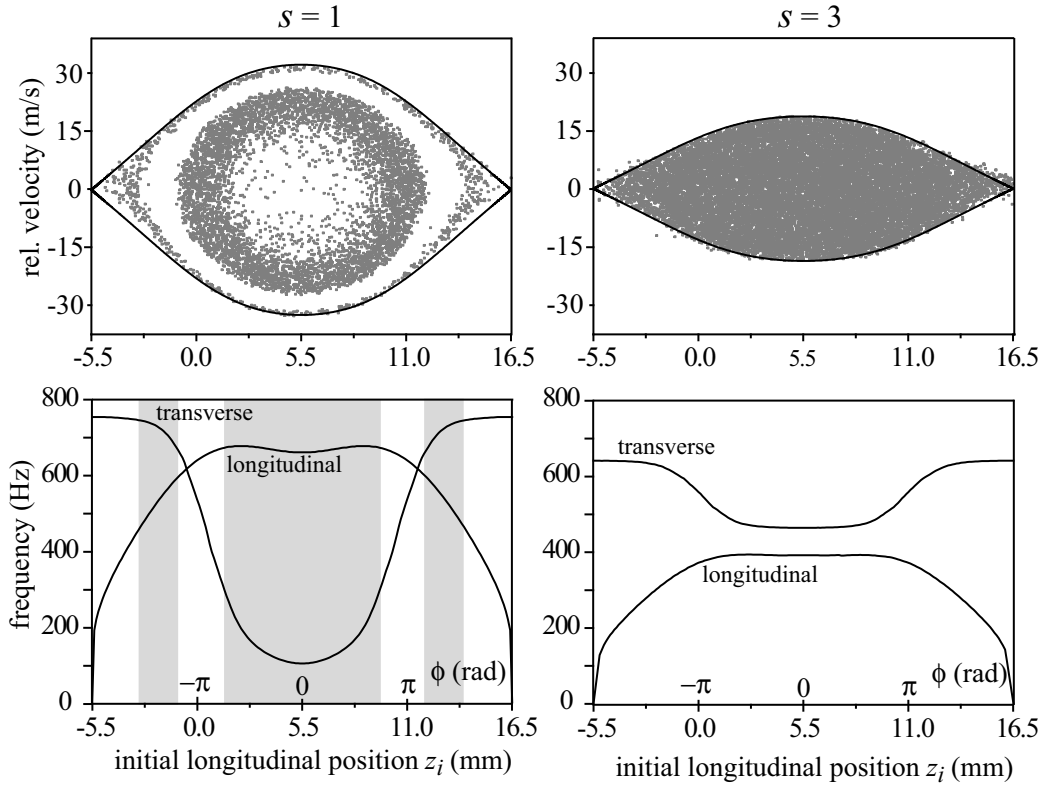


Figure 5.10: Natural transverse and longitudinal oscillation frequency of an OH ($X^2\Pi_{3/2}, J = 3/2, M_J\Omega = -9/4$) radical as a function of the initial longitudinal position z_i in the first electric field stage of the Stark decelerator. The decelerator is operated at $\phi_0 = 0^\circ$ using the resonance $s = 1$ (left hand side) and $s = 3$ (right hand side). In the upper part the longitudinal phase-space acceptance of the Stark decelerator is shown for both cases. The initial longitudinal positions that lead to the empty center or the halo, are indicated by the gray areas.

by the extended 1D model for phase stability (see chapter 4). During the motion of a molecule in the decelerator, the transverse natural frequency always exceeds the longitudinal natural frequency. Consequently, the coupling between the longitudinal and transverse motion will be profoundly different than if the Stark decelerator is operated at $s = 1$. In the right upper corner of Figure 5.10, the longitudinal phase-space distribution of the molecules in the last stage of the decelerator is shown, that results from a three dimensional trajectory simulation. The phase-space distribution is homogeneous, and no regions of instability or reduced acceptance are observed. The transverse acceptance at the center of the phase-space region is enhanced by the improved transverse focussing that is present in this region, and no empty center is observed. In addition, the halo is absent due to the (more) uncoupled longitudinal and transverse motion. Analogous to the methodology that was used in section 5.3.5, the parameters a and q of the transverse equation of motion can be determined. These are shown by the open circles in the Mathieu stability diagram of Figure 5.8 as a function of z_i . Indeed, when the Stark decelerator is operated using the resonance with $s = 3$, the large unstable region centered around $a = 1$ is avoided, and the equation of motion has stable solutions. Only for large initial longitudinal positions, there exists a small unstable region, centered around $a = 4$. A region of reduced stability is indeed observed close to the separatrix in the numerical trajectory simulations, but a much larger number of stages in the decelerator is required before the molecules in this region

are completely depleted.

Although the 1D model for phase stability predicts a phase stable region that is scaled down by a factor $\sqrt{3}$ if the Stark decelerator is operated at the resonance $s = 3$, the improved focussing properties of the decelerator, and the absence of the halo, actually result in a number of molecules that exit the decelerator that is more than a factor 2 increased compared to 'normal' operation of the decelerator. A significant increase of signal intensity has indeed been observed in the measurements presented in chapter 4, when the Stark decelerator was operated at $\phi_0 = 0^\circ$ using the resonance with $s = 3$ instead of $s = 1$. One may wonder if operation of the decelerator using $s > 3$ yields even larger signal intensities. In Figure 4.3 of chapter 4 a series of TOF profiles is presented that is obtained when the Stark decelerator is operated at $\phi_0 = 0^\circ$ for the resonances with $s = 1, 3, 5, 11, 15,$ and 19 . Referring back to this figure, the change in signal intensity for the series of measurements

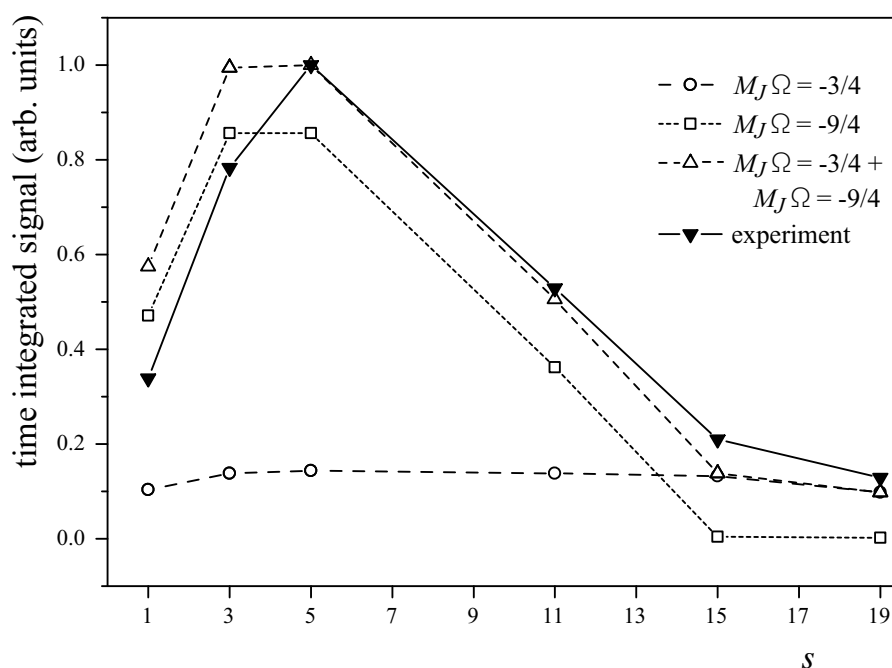


Figure 5.11: The normalized time-integrated intensity of the experimental TOF profiles of Figure 4.3 of chapter 4 (full line), as a function of the ratio s of the velocity of the synchronous molecule to the 'switching' velocity. The integrated intensity that results from a three dimensional trajectory calculation of the experiment is shown, together with the individual contributions of both $M_J\Omega$ components.

directly reflects the different transverse focussing properties of the decelerator, when the decelerator is operated at resonances with different values of s . The normalized time integrated intensity of the experimental TOF profiles is shown in Fig. 5.11. As mentioned in the previous paragraph, it is seen that the number of OH radicals that exit the decelerator is more than a factor 2 larger when the decelerator is operated at $s = 3$ instead of $s = 1$. Operation at $s = 5$ even yields a higher signal intensity. For $s > 5$, however, the time integrated signal rapidly decreases. The time integrated intensity of the TOF profiles as a function of s that is obtained from three dimensional trajectory simulations of the experiment, is shown in Fig. 5.11 as well, together with the individual contributions of both $M_J\Omega$ components to the LIF signal. The agreement between the relative integrated intensities of the experimental TOF profiles and the simulated intensities is good. It is noted that, although

all TOF profiles of Fig. 4.3 of chapter 4 were recorded the same day, the stability of the OH beam intensity and detection laser frequency result in a 20% uncertainty of the given experimental values in Fig. 5.11.

The numerical trajectory simulations indeed confirm that the larger integrated signal intensity when the decelerator is operated at $s = 3$ or $s = 5$, is a result of a larger transverse acceptance of the Stark decelerator and the absence of instability regions in the longitudinal acceptance. The decreasing signal intensity for $s > 5$ is due to over-focussing of the beam. Since adjacent electric field stages are orthogonally placed with respect to each other, the transverse direction in which the beam is focussed is changed by 90° every time the fields are switched. In general, the beam is therefore focussed in one transverse direction for a duration proportional to s , before the focussing direction is reversed. For $s > 5$, the molecules become too strongly focussed in one direction before the focussing direction is changed, and crash onto the electrodes further downstream. For $s > 13$, the focussing in one transverse direction for molecules in the $M_J\Omega = -9/4$ component is so strong that this component hardly contributes to the signal intensity anymore. Only OH radicals that are in the $M_J\Omega = -3/4$ component, and that experience a factor 3 lower focussing force, exit the decelerator for these high values of s .

5.4 Experiment

It is very difficult to experimentally study the influence of the transverse motion of the molecules on the longitudinal phase stability in a Stark decelerator. Obviously, it is impossible to create a molecular beam in which all molecules exclusively fly along the molecular beam axis to make a comparison between the 1D and the 3D case. Nor is it possible to directly measure the longitudinal phase-space distribution of the molecules in the decelerator. At best, one can measure the spatial distribution of the molecular cloud in an electric field stage [79], but this does not yield the desired information on the phase-space distribution. The molecular beam deceleration machine used in this thesis is best suited to record the time-of-flight (TOF) profile of the molecules that exit the decelerator. From the structure and the intensity of these TOF profiles, and from a comparison between the experimental profile and the profile that results from a 1D or a 3D trajectory simulation, a good insight in the phase-space distribution of the beam inside the decelerator can be obtained. This strategy is followed in the experiments reported here, in which the decelerator is operated in two limiting cases. In section 5.4.1 experiments are described in which the decelerator is operated at a high value of ϕ_0 to verify the enhanced acceptance of the decelerator at these phase angles. In section 5.4.2 the decelerator is operated at $\phi_0 = 0^\circ$ to demonstrate the existence of the stable ring and the halo in the acceptance of the Stark decelerator. In all experiments reported here, Xe is used as a seed gas, resulting in a molecular beam of OH radicals that has a mean velocity around 365 m/s with a velocity spread (FWHM) of 15 %.

5.4.1 High phase angles; $\phi_0 = 90^\circ$

To demonstrate the enhanced longitudinal acceptance of the decelerator for high values of ϕ_0 , the decelerator can be operated with a time sequence that is calculated for a phase angle equal to 90° . In this case, phase stability vanishes in the one dimensional model for phase stability, i.e., *only* the trajectory of the synchronous molecule is stable. In the upper curve of Figure 5.12, the observed

TOF profile is shown when the Stark decelerator is operated at a phase angle of $\phi_0 = 90^\circ$ for a synchronous molecule with an initial velocity of 370 m/s. With these settings of the decelerator, the synchronous molecule is decelerated to a velocity of 144.7 m/s in electric field stage number 65. The remaining stages are operated at $\phi_0 = 0^\circ$ to transport the decelerated molecules to the detection region, where the synchronous molecule is expected to arrive about 6.4 ms after production. From the experimental profile it is clear that indeed a package of molecules is captured by the decelerator, and arrives in the detection region at the predicted arrival time. The observed TOF profile is accurately reproduced by the TOF profile that is obtained from a three dimensional trajectory simulation of the experiment, shown underneath the experimental TOF profile. In the insets, the longitudinal phase-space distributions of OH ($X^2\Pi_{3/2}, J = 3/2, M_J\Omega = -9/4$) radicals in one of the last deceleration stages are shown, that result from a 1D (left inset) and 3D (right inset) trajectory simulation. The separatrices that correspond to $\phi_0 = 70^\circ, \phi_0 = 75^\circ$ and $\phi_0 = 80^\circ$ are given as an overlay. The 1D trajectory simulation shows the presence of decelerated molecules if $\phi_0 = 90^\circ$ is used, as our decelerator has a limited number of stages. These molecules, however, are not phase stable and spread out in phase space for increasing lengths of the decelerator. From the right inset it follows that when the decelerator is operated at $\phi_0 = 90^\circ$, the decelerated molecules occupy an area in longitudinal phase-space that is best described by an effective phase angle of 75° . This indicates that the transverse motion of the molecules through the decelerator results in an enhanced area of phase stability when the decelerator is operated at high phase angles.

5.4.2 Low phase angles; $\phi_0 = 0^\circ$

When the Stark decelerator is operated at high phase angles like in the previous section, the longitudinal emittance of the molecular beam pulse largely exceeds the longitudinal acceptance of the Stark decelerator. The TOF profile of the decelerated molecules that exit the decelerator therefore directly reflects the (structure of) the phase-space distribution of the molecules in the last electric field stage of the decelerator. For low values of ϕ_0 , however, the longitudinal acceptance of the decelerator can be much larger than the emittance of the beam. In particular, for the Stark decelerator and OH molecular beam used in this thesis, the beam overlaps completely with the velocity interval of the longitudinal acceptance, but has a relatively narrow spatial distribution, that is predominantly determined by the spatial extent of the dissociation laser. If the molecular beam pulse (partially) overlaps with regions in longitudinal phase-space that are unstable, the intensity of the TOF profile of the molecules that exit the decelerator will be reduced. By measuring the time-integrated intensity of the TOF profile at the exit of the decelerator, as a function of the initial longitudinal position of the beam in the first electric stage, the overlap of the emittance of the beam with the longitudinal acceptance of the decelerator is probed. This strategy is used in the experiments that are described in this section. The experimental procedure is schematically represented in Figure 5.13. In the inset in the upper left part of this figure, the longitudinal acceptance of the decelerator is shown if the decelerator is operated at phase angle $\phi_0 = 0^\circ$. The initial position of the beam within this acceptance region can be selected by a proper choice of the time at which the decelerator is switched on with respect to the time that the OH radicals are produced. This is shown in the inset of Figure 5.13 for three different initial longitudinal positions, referred to as A, B and C. The longitudinal phase-space distribution of the beam is tilted as a result of the spreading of the beam between the nozzle and the entrance of the Stark decelerator. The spatial extent of the dissociation laser in the experiments is reduced to 0.7 mm. As a result, the molecular beam only overlaps with the acceptance region in a spatially narrow, and

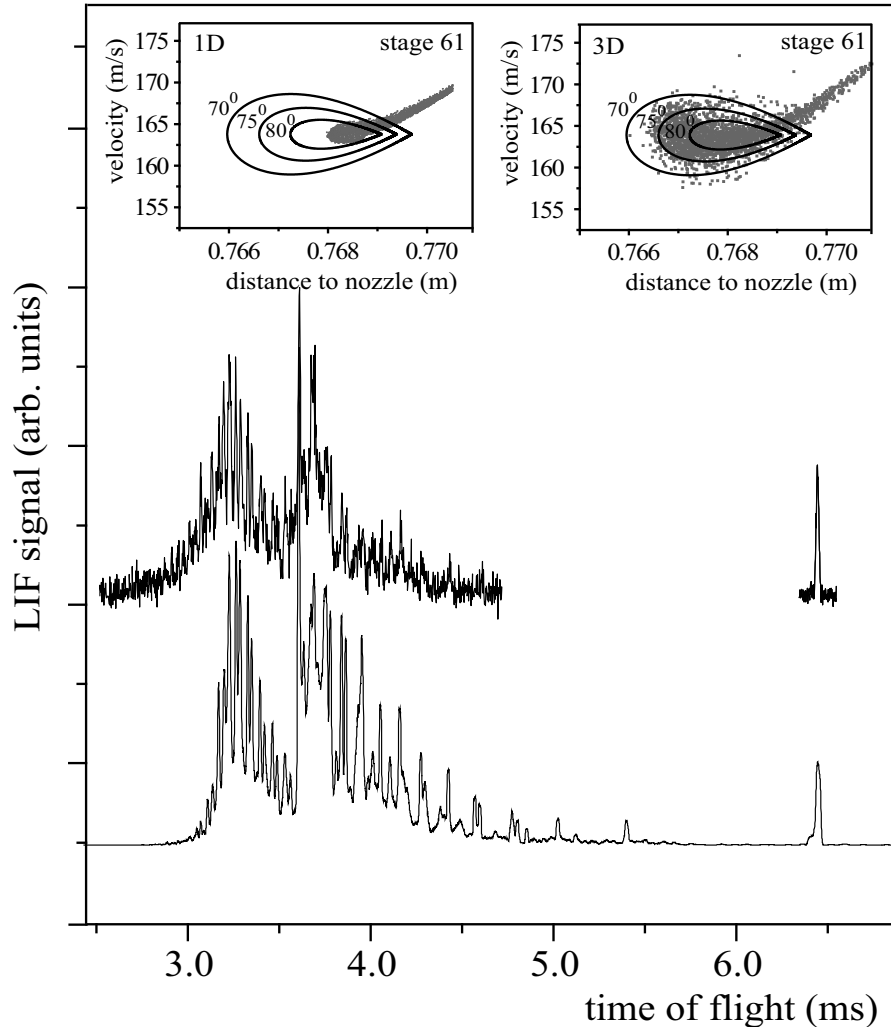


Figure 5.12: Observed TOF profile of OH radicals that exit the decelerator, when the decelerator is operated at a phase angle $\phi_0 = 90^\circ$. The TOF profile that results from a three dimensional trajectory simulation of the experiment is shown underneath the experimental profile. In the left and right inset, the longitudinal phase-space distribution of OH ($X^2\Pi_{3/2}, J = 3/2, M_J\Omega = -9/4$) radicals in one of the last deceleration stages is shown, that result from a 1D and a 3D trajectory simulation, respectively. The separatrices that correspond to the phase angles $\phi_0 = 70^\circ$, $\phi_0 = 75^\circ$ and $\phi_0 = 80^\circ$ are given as an overlay.

well defined region. The integrated TOF profile of the molecules that exit the decelerator for a given initial longitudinal position of the beam, therefore directly reflects the stability of that particular part of the phase-space acceptance region. By measuring the TOF-profiles for various initial longitudinal positions of the beam, the structure within the longitudinal phase-space acceptance of the Stark decelerator can be probed. In the upper part of Figure 5.13, a typical TOF profile is shown that is obtained if the decelerator is operated at phase angle $\phi_0 = 0^\circ$. The central peak in this profile corresponds to phase-stable molecules, i.e., to those molecules that were within the longitudinal acceptance of the decelerator when the decelerator was switched on. For each initial longitudinal position of the beam, the TOF profile is recorded and integrated in a $200 \mu\text{s}$ time window around the mean arrival time of the central peak. This is indicated in the lower part of Figure 5.13, where the TOF-profiles are shown

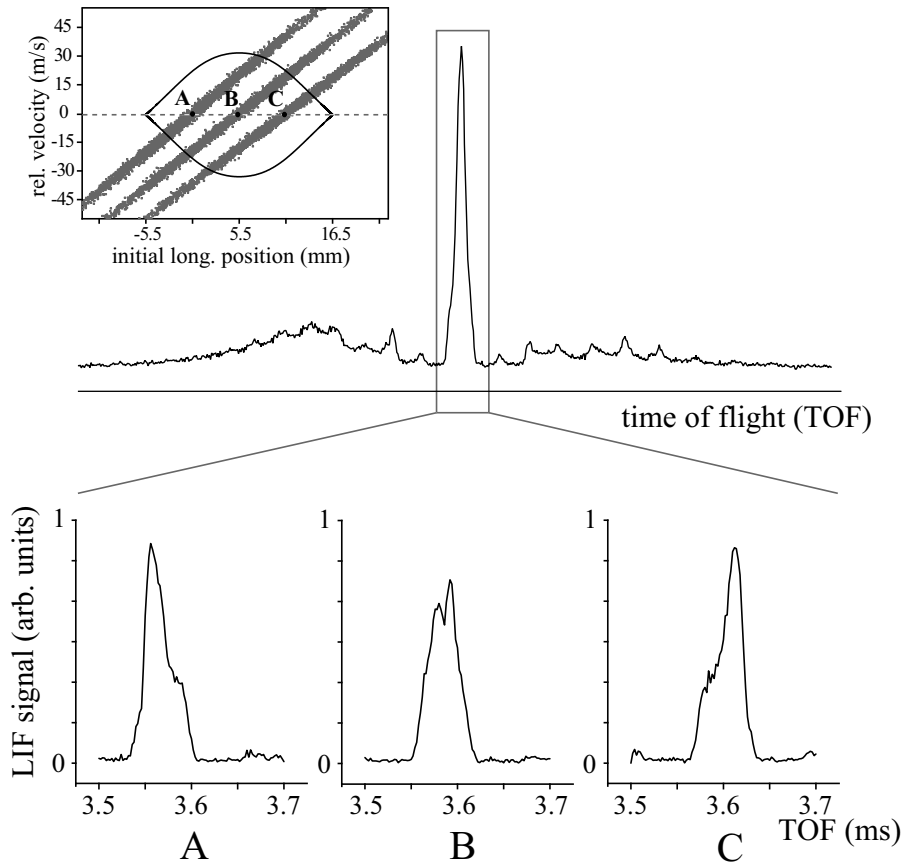


Figure 5.13: Schematic representation of the experimental procedure to study the structure in the longitudinal phase-space acceptance when the Stark decelerator is operated at phase angle $\phi_0 = 0^\circ$. In the upper part of the figure, the overlap of the acceptance of the Stark decelerator with the emittance of the molecular beam is shown, for different initial longitudinal positions of the beam. For each of these initial positions, the TOF profile of molecules exiting the Stark decelerator is recorded and integrated in a $200 \mu\text{s}$ time window around the central peak.

that are obtained when the beam is at the initial longitudinal positions A, B and C.

On the left hand side of Figure 5.14, the integrated signal intensity of the experimentally obtained TOF-profile is shown as a function of the initial longitudinal position of the beam in the Stark decelerator, when the decelerator is operated at the phase angle $\phi_0 = 0^\circ$, using the resonance $s = 1$. For each longitudinal position of the beam, the TOF profile is recorded and integrated as discussed above. The resulting experimental data is represented by the filled black squares in the lower panel of the figure. As a reference signal, after every two measured TOF profiles, the TOF profile is recorded when the beam has an initial position of 5.5 mm with respect to the first pair of electrodes of the decelerator. From these reference signals, a long-term drift in the experimental apparatus and detection efficiency can be corrected for. The error bars that accompany the experimental data points in Figure 5.14 represent the spread in the reference signals. The longitudinal acceptance of the Stark decelerator for this case, already discussed before and shown in Figure 5.10, is shown once more in the left upper panel of Figure 5.14. The position of the electrodes is again indicated by the vertical dashed lines. It is noted that this phase-space distribution results from a simulation that is performed for a beam with a mean

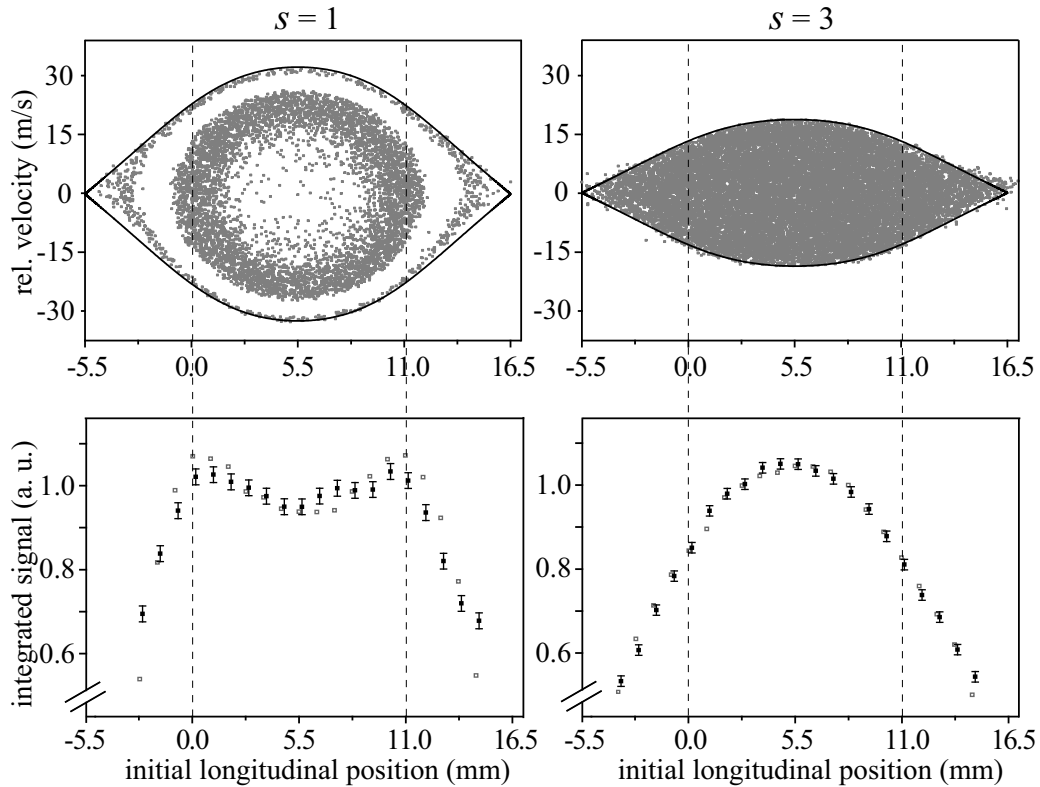


Figure 5.14: Integrated signal intensity of a selected part of the TOF-profile as a function of the initial longitudinal position of the beam, that is obtained when the Stark decelerator is operated at $\phi_0 = 0^\circ$ using the resonance $s = 1$ (left hand side) and the resonance $s = 3$ (right hand side). The integrated signal intensities that result from a three dimensional trajectory calculation of the experiment are indicated by the open gray squares. The longitudinal phase-space acceptance of the Stark decelerator for OH ($X^2\Pi_{3/2}, J = 3/2, M_J\Omega = -9/4$) radicals is shown in the upper part for both cases. The positions of the electrodes of the Stark decelerator are indicated by the vertical dashed lines.

velocity of 250 m/s and a Stark decelerator that consists of 180 stages. In the experiments, however, the OH beam has a mean velocity of 365 m/s, and the Stark decelerator that is used in the experiments consists of only 101 stages. This does not affect the inherent longitudinal acceptance of the Stark decelerator, but the relatively short amount of time that the molecules spend in the decelerator may result in a reduced contrast between the stable and unstable regions. Nevertheless, Figure 5.14 shows that the molecules are most efficiently transported through the decelerator if the beam is coupled in at the longitudinal positions where the beam has most overlap with the stable ring in the phase-space acceptance. A clear decrease in signal is observed when the beam is initially in between these positions, at the center of the acceptance region. A sharp decrease in signal results when the beam has an initial position that is within the halo. The relatively small stable region that is close to the separatrix cannot be probed, as the TOF profiles that result when the beam is coupled in in this region are difficult to interpret and cannot be accurately quantified. The dependence of the observed signal intensity on the initial longitudinal position of the beam in the first stage of the decelerator, is a clear indication of the existence of both the small transverse acceptance at the center of the phase-space acceptance and of the halo. The integrated intensities of the selected intervals of the TOF profiles that result from a three

dimensional trajectory simulation of the experiment, taking both low-field seeking $M_J\Omega$ components of the $X^2\Pi_{3/2}, J = 3/2$ state of OH into account, are represented by the open gray squares in Figure 5.14. Quantitative agreement between the observations and the simulations is obtained.

The experiments described above are repeated with the Stark decelerator operating at $\phi_0 = 0^\circ$ using the resonance with $s = 3$. The experimental results are shown on the right hand side of Figure 5.14. The homogeneous longitudinal phase-space acceptance that is present in this case results in a different dependence of the signal intensity on the initial longitudinal position of the beam. The largest fraction of the beam is selected and transported through the machine when the beam is coupled in at the center of the acceptance region, and this decreases further outward. The signal intensities that result from three dimensional trajectory simulations are given as an overlay. Again, quantitative agreement is obtained between the observations and the simulations.

5.5 Conclusions

In this chapter, the influence of the transverse motion on the longitudinal phase stability in a Stark decelerator is studied, using OH radicals as a model system. For high values of the phase angle ϕ_0 ($\phi_0 > 70^\circ$), the longitudinal phase-space acceptance of the decelerator is significantly enhanced by the transverse motion; a much larger part of the beam can be decelerated than the one dimensional model for phase stability suggests. For low values of the phase angle ϕ_0 , however, the transverse motion reduces the acceptance of the decelerator; weak transverse focussing of the molecules results in a small transverse acceptance in the phase-space region around the synchronous molecule. In addition, coupling between the transverse and longitudinal motion can result in inherently unstable regions in phase-space; driving of the transverse motion by the longitudinal motion can lead to unstable trajectories. A comprehensive model for the combined transverse and longitudinal phase stability, that provides a clear physical understanding of the presence of these effects, is presented.

The influence of the transverse motion on the longitudinal acceptance that is studied in this chapter is generally present in Stark decelerators with the original design of the electrode array. The extent to which this results in a significant enhancement of the acceptance, or in an unacceptable reduction in efficiency of the decelerator, critically depends on a variety of parameters. Reduction of the longitudinal phase-space stability for low values of ϕ_0 will be more severe if molecules spend a longer time in the decelerator, i.e., for long Stark decelerators, and/or for low velocities of the molecular beam. The structure of the phase-space distribution does not depend critically on the ratio of the (electric field dependent) Stark shift over mass of the molecule, however. The effects as discussed in this chapter for the OH ($J = 3/2, M_J\Omega = -9/4$) radical, with its (near) linear Stark effect, are generally present for molecules that exhibit a linear Stark effect. In particular, the halo is found at exactly the same position for OH radicals in the ($J = 3/2, M_J\Omega = -3/4$) level, even though these experience a three times smaller Stark shift. This is readily understood as only the ratio of the transverse and the longitudinal force determines the unstable regions in phase-space. But also for the molecules SO₂, H₂O and H₂CO, that exhibit non-linear Stark shifts, the phase-space distributions that result from three dimensional trajectory simulations show a similar structure as the distributions that are obtained for OH. Only the overall longitudinal and transverse acceptance is different for the various molecules.

Stark decelerators are developed and built with the aim to decelerate (and ultimately trap) molecules. Apart from revealing complex and interesting six dimensional phase-space dynamics of molecules in a Stark decelerator, the deviations from the acceptance that is predicted by the one di-

mensional model for phase stability have profound consequences for the efficiency of the deceleration process. So far, in most of our trapping experiments, the phase angles that are used are equal to or exceed 70° , exploiting the increased acceptance of the decelerator that is present at these phase angles. An apparent obvious strategy to construct a Stark decelerator with a large number of stages, such that it can be operated at rather low phase angles [170], should be carefully considered; the increase in longitudinal phase-space acceptance that is present at lower phase angles might be undone by the inferior focussing properties of the decelerator, and by the existence of inherently unstable regions. With the present design of the electrode geometry, a significant gain in the inherent longitudinal phase-space acceptance can only be obtained if the geometry and/or the applied electric fields are scaled up, although this is accompanied by severe technical difficulties. When a decelerator with a design of the electrode geometry that allows for independent control over the transverse and longitudinal motion of the beam, as for instance applied in decelerators of the 'Alternating Gradient'-type [9], is used, a significant increase of the longitudinal phase-space acceptance of the decelerator can be obtained. This can also be achieved in the present design by operation of the decelerator using resonances with $s \geq 3$, although a larger number of electric field stages is required to obtain the same final velocity of the molecular beam. Whatever strategy is followed, detailed three dimensional numerical trajectory simulations should be an integral part in the design of a new Stark decelerator apparatus.

CHAPTER 6

ELECTROSTATIC TRAPPING OF OH RADICALS

A pulsed beam of ground state OH radicals is slowed down using a Stark decelerator and is subsequently loaded into an electrostatic trap. Characterization of the molecular beam production, deceleration and trap loading process is performed via laser induced fluorescence detection inside the quadrupole trap. Depending on details of the trap loading sequence, typically 10^5 OH ($X^2\Pi_{3/2}, J = 3/2$) radicals are trapped at a density of around $10^7 - 10^8 \text{ cm}^{-3}$ and at temperatures in the 50-500 mK range. The $1/e$ trap lifetime is around 1.0 second.

Based on:

Deceleration and electrostatic trapping of OH radicals

Sebastiaan Y.T. van de Meerakker, Paul H.M. Smeets, Nicolas Vanhaecke, Rienk T. Jongma, and Gerard Meijer
Phys. Rev. Lett. **94**, 23004 (2005).

6.1 Introduction

In chapter 3 a new generation Stark decelerator was described that enables the deceleration of a significant fraction of a pulsed molecular beam. This was explicitly demonstrated by decelerating a molecular beam of OH ($X^2\Pi_{3/2}, J = 3/2, M_J = -9/4$) radicals from 450 m/s to 95 m/s. To be able to exploit the possibilities that this new Stark decelerator offers to study molecules at (ultra)low temperatures and for collision and reactive scattering experiments at these temperatures, the slow beam needs to be decelerated further and confined in a trap. For this, the new generation molecular beam deceleration machine described in chapter 3 is extended with an electrostatic quadrupole trap [11, 14]. In this chapter, the deceleration and electrostatic trapping of ground state OH ($X^2\Pi_{3/2}, J = 3/2$) radicals is reported.

6.2 Experiment

6.2.1 The experimental set-up

The experimental setup is schematically shown in Fig. 6.1. A pulsed beam of OH with a mean velocity of 460 m/s and with a velocity spread of 15 % (full width half maximum, FWHM) is produced via ArF-laser dissociation of HNO_3 seeded in Kr near the orifice of a pulsed valve, as described in detail in chapter 2. Part of the beam is decelerated using the Stark decelerator described in chapter 3. As before, the decelerator is operated with a voltage difference of 40 kV between the opposing electrodes in a deceleration stage. To confine the OH radicals, the Stark decelerator is extended with an electrostatic quadrupole trap. The trap consists of a ring electrode, centered 21 mm downstream from the last electrodes of the decelerator, with an inner radius R of 10 mm and two hyperbolic end-caps with a half-spacing of $R/\sqrt{2}$. This trap is scaled up by a factor two compared to the trap that was used to trap ND_3 molecules [11, 14]. The molecular beam enters the trap through a 4 mm diameter hole in the first end-cap. This hole is the only vacuum connection between the deceleration chamber and the trap chamber, and the pressure in the trap chamber can be kept at about 3×10^{-9} Torr under operating conditions. Optical access to the trap is provided by two 6 mm diameter holes in the ring electrode. The beam of a frequency doubled pulsed dye laser is sent through these holes to perform LIF detection of the OH radicals at the center of the trap. Excitation is performed on the $Q_1(1)$ transition of the $A^2\Sigma^+, v = 1 \leftarrow X^2\Pi_{3/2}, v = 0$ band around 282 nm, selectively detecting OH ($J = 3/2$) radicals in the upper Λ -doublet component. Off-resonant fluorescence on the $A^2\Sigma^+, v = 1 \rightarrow X^2\Pi, v = 1$ band around 313 nm is imaged through a 6 mm diameter opening in the second end-cap onto a photomultiplier tube (PMT). Stray light from the laser is largely avoided by using light baffles and is suppressed by optical filtering in front of the PMT. Only molecules in (both $|M_F|$ hyperfine sublevels of) the $J = 3/2, M_J\Omega = -9/4$ component are decelerated and trapped in the present experiments, although molecules in both $M_J\Omega$ components contribute to the laser induced fluorescence (LIF) signal of the non-decelerated beam that is passing through the trap.

6.2.2 Deceleration and trapping experiments

In Fig. 6.2 the intensity of the LIF signal of OH ($J = 3/2$) radicals at the center of the trap is shown as a function of time after firing the dissociation laser, using different deceleration and trap loading sequences. In the measurement shown in the upper curve, the decelerator is operated at a phase angle

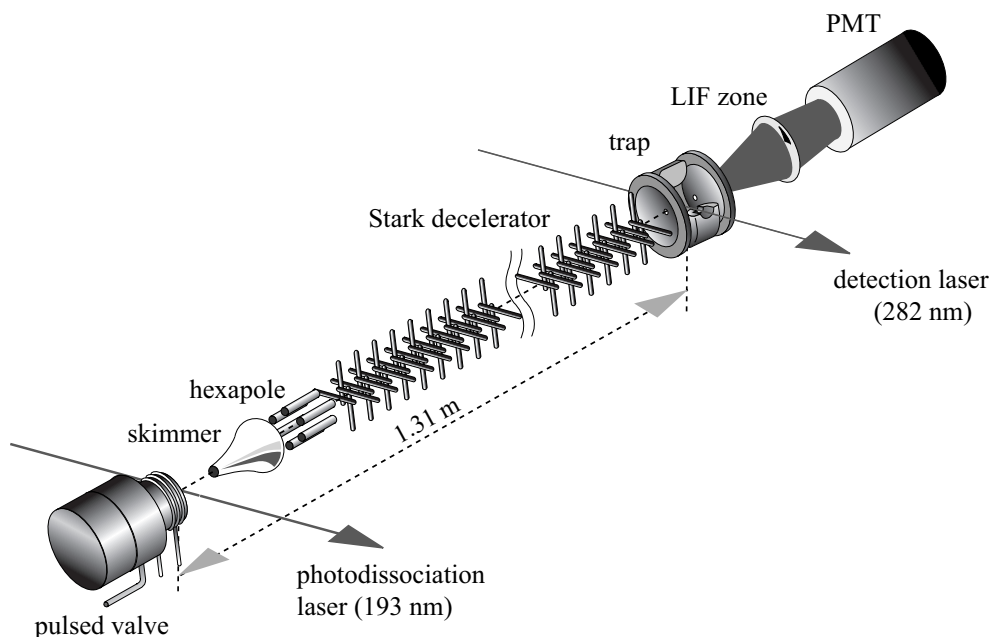


Figure 6.1: Scheme of the experimental setup. A beam of OH ($X^2\Pi_{3/2}, J = 3/2$) radicals is produced via ArF-laser dissociation of HNO_3 near the orifice of a pulsed valve. The OH radicals pass a skimmer and hexapole, and are decelerated in the Stark decelerator. Subsequently, the OH radicals are loaded into an electrostatic quadrupole trap. LIF detection of the OH radicals is performed at the center of the trap.

of $\phi_0 = 50^\circ$, extracting about 0.9 cm^{-1} of kinetic energy from the synchronous molecule in every deceleration stage; OH radicals with an initial velocity of around 465 m/s are decelerated to a final velocity of around 305 m/s. Due to a better spatial confinement, the peak density of the decelerated portion of the molecular beam is higher than the peak density of the non-decelerated beam that passes through the trap. The hole in the TOF profile of the fast beam due to the removal of OH radicals that are decelerated is indicated by an arrow. In the measurement shown in the middle curve, OH radicals with an initial velocity around 440 m/s are decelerated to 170 m/s, operating the decelerator at a phase angle of $\phi_0 = 70^\circ$. In both the measurements presented in the upper and middle curve, the last 7 electric field stages of the decelerator were grounded. The lower intensity of the decelerated molecules in the middle curve compared to the upper curve, is in part due to the almost 10 cm long free flight from the last electric field stage that is used in the experiment and the detection zone.

To be able to load the OH radicals into the electrostatic trap, the beam needs to be decelerated further to approximately 20 m/s. For this, the last 7 stages can be used with a maximum voltage difference of 30 kV between the electrodes in a deceleration stage. In the lower curve of Figure 6.2, the observed TOF profile is shown when the first 101 stages of the decelerator are operated at $\phi_0 = 77^\circ$, extracting about 1.2 cm^{-1} of kinetic energy per deceleration stage. OH radicals with an initial velocity of 428 m/s ($E_{kin} = 130.4 \text{ cm}^{-1}$) are decelerated to a velocity of 95 m/s in stage 101. The remaining 7 stages of the decelerator are operated at the lower phase angle of $\phi_0 = 72^\circ$ to compensate for the reduced acceptance of the decelerator in these last stages. Here, the decelerator extracts about 0.9 cm^{-1} of kinetic energy per deceleration stage, and the OH radicals exit the decelerator with a

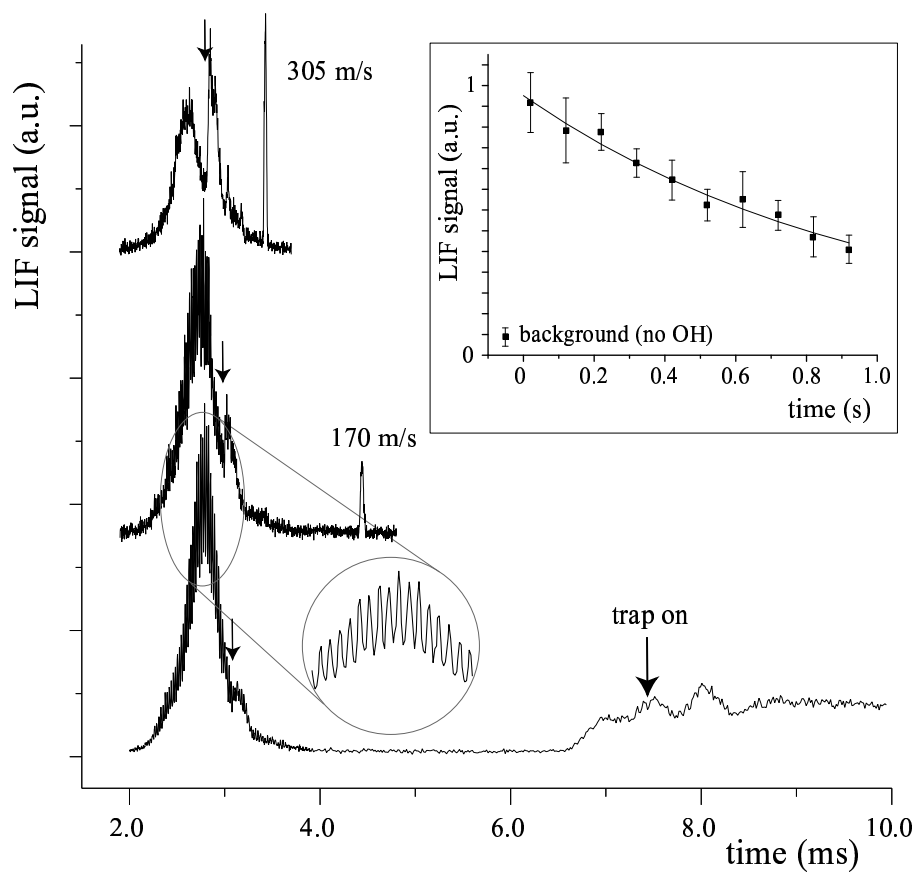


Figure 6.2: LIF signal of OH ($J = 3/2$) radicals at the center of the quadrupole trap as a function of time after OH production for two different deceleration sequences (upper two curves) and for a deceleration and trapping sequence (lower curve). In the inset, the LIF signal intensity of the electrostatically trapped OH radicals is shown on a longer time-scale.

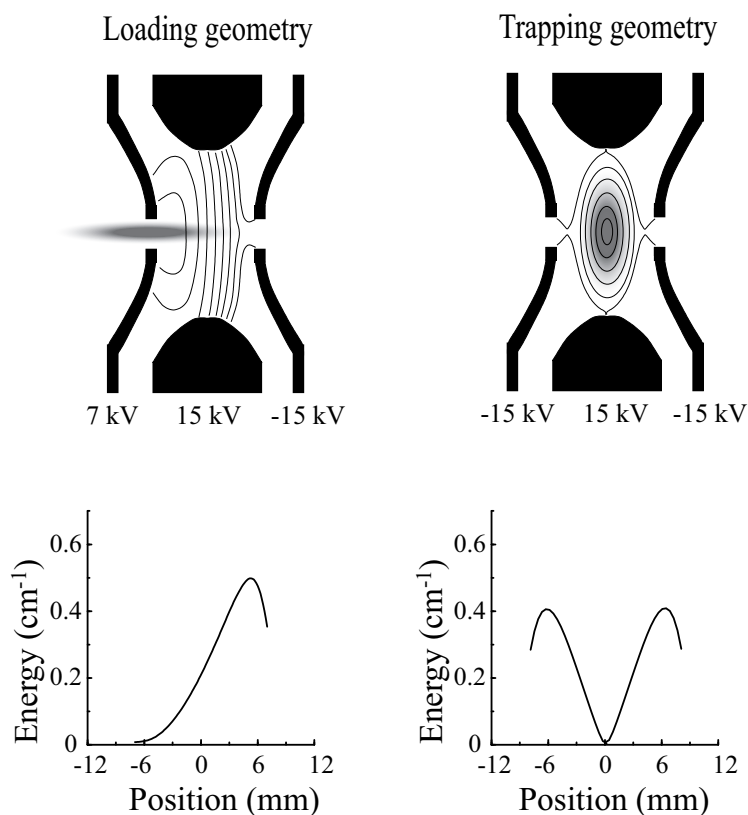


Figure 6.3: Schematic representation of the loading procedure of the electrostatic trap. In the "loading geometry", the potentials on the trap electrodes are chosen such that a potential hill is created in the trap that is higher than the remaining kinetic energy of the incoming molecules. At the time the molecules come to a stand-still in the center of the trap, the trap is switched into the "trapping geometry". In this geometry a (nearly) symmetric 500 mK deep potential well is created, in which the molecules are confined.

velocity of around 21 m/s ($E_{kin} = 0.3 \text{ cm}^{-1}$). The OH radicals in the non-decelerated part of the beam also experience the switched electric fields inside the decelerator. This leads to a highly structured phase-space distribution and results in rich oscillatory structure on the TOF profile of the fast beam, as shown enlarged in the figure. These oscillations again result from the resonance $s = 5/3$ that has partially moved into the velocity distribution of the non-decelerated beam (see chapter 4).

The slow beam of OH radicals is loaded into the electrostatic trap with voltages of 7 kV, 15 kV and -15 kV on the first end-cap, the ring electrode and the second end-cap, respectively. This "loading geometry" of the trap is schematically represented on the left side of Figure 6.3. In the loading geometry, a potential hill in the trap is created that is higher than the remaining kinetic energy of the molecules. The OH radicals therefore come to a standstill near the center of the trap, around 7.4 ms after their production. At that time, indicated by an arrow in Fig. 6.2, the trap is switched into the "trapping geometry", as schematically represented on the right side of Figure 6.3; the first end-cap is switched from 7 kV to -15 kV to create a (nearly) symmetric 500 mK deep potential well. After some initial oscillations, a steady LIF signal is observed from the OH radicals in the trap. The LIF intensity of the trapped OH radicals is about 20 % of the peak LIF intensity of the non-decelerated beam of OH that passes through the trap. Quantifying LIF signals is notoriously difficult. The observed LIF signal

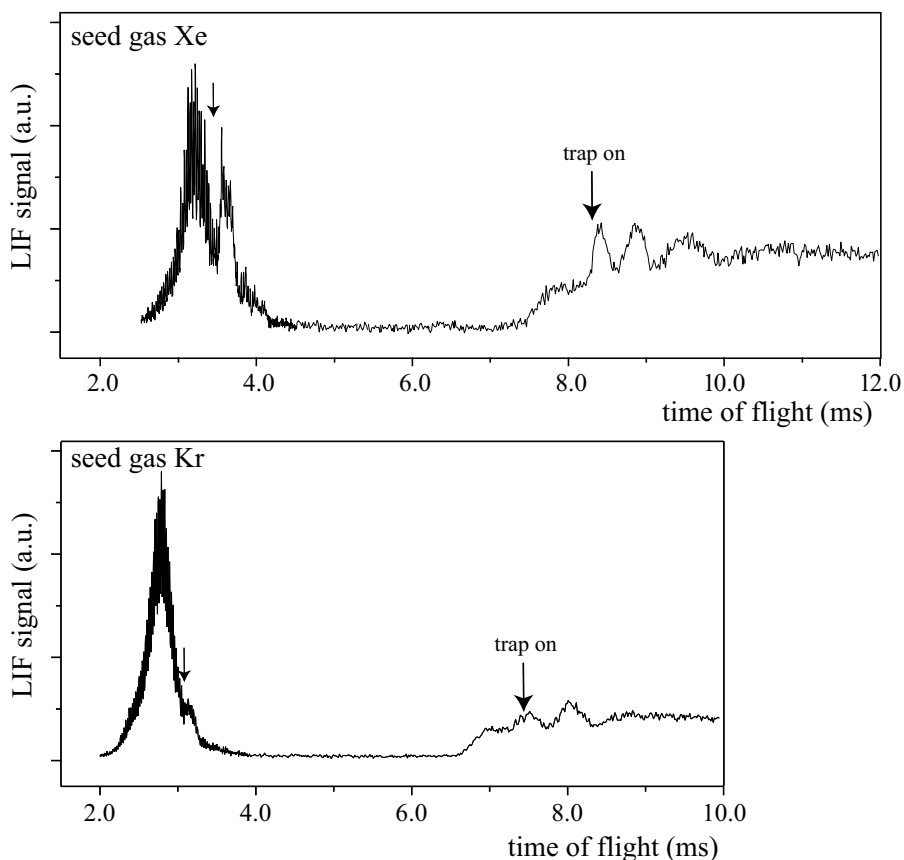


Figure 6.4: Measured TOF profiles of OH ($J = 3/2$) radicals when trapping experiments are performed using Kr (lower curve) and Xe (upper curve) as a carrier gas. The hole in the TOF profile of the fast beam due to the removal of OH radicals that are decelerated is indicated by an arrow in both curves. The time at which the trap is switched on is indicated by a vertical arrow as well.

of the trapped OH radicals corresponds to a total number of about 10^5 OH ($J = 3/2$, $M_J\Omega = -9/4$) radicals, in the approximately 0.03 cm^3 detection volume in the trap. In the inset, the LIF signal intensity is shown on a longer time-scale. The latter experiments are performed while running the experiment at a repetition rate of 1 Hz, limiting the maximum time-of-flight that can be measured to 1.0 second. From these experiments, a $1/e$ trap lifetime on the order of 1.0 second, limited by collisions with background gas, is deduced.

The molecular beam deceleration and trapping experiment presented in Figure 6.2 are performed using Kr as a carrier gas, producing a molecular beam with a mean velocity of 460 m/s. To decelerate OH radicals to the final velocity of 20 m/s that is required for loading the beam into the trap, only OH radicals with a maximum initial velocity of approximately 428 m/s can be selected by the decelerator. Obviously, selection of a package of molecules around the mean velocity of the beam could lead to a higher phase-space density of the trapped molecules. In the lower and upper panel of Figure 6.4, the TOF profiles of trapping experiments are shown when the carrier gases Kr and Xe are used, respectively (the TOF profile when Kr is used is identical to the lower curve in Figure 6.2). The reduced mean velocity of the beam of about 365 m/s when Xe is used as a carrier gas allows the selection of the most intense part of the molecular beam. In addition, the Stark decelerator can be

operated at much lower phase angles, increasing the longitudinal acceptance of the decelerator. The decelerator is operated at $\phi_0 = 53^\circ$ and $\phi_0 = 48^\circ$ in the first 101 stages and the last 7 stages, respectively. A significant part of the original molecular beam is decelerated from 371 m/s to 21 m/s, and subsequently loaded into the electrostatic trap. The hole in the TOF profile of the fast beam due to the removal of OH radicals that are decelerated is again indicated by an arrow, as well as the time at which the trap is switched into the trapping configuration. The LIF intensity of the trapped OH radicals is about 40 % of the peak LIF intensity of the non-decelerated beam of OH that passes through the trap, i.e. a much larger fraction of the beam can be trapped when Xe is used. Compared to Kr, and using similar trap loading sequences, the density of OH radicals in the trap is about a factor 2 larger when Xe is used as a carrier gas.

6.2.3 Trap-loading characterization

The absolute number of OH radicals that can be trapped as well as the phase space distribution of the trapped molecules critically depends on the details of the trap loading sequence. In Fig. 6.5 measurements are shown for two slightly different trap loading conditions, referred to as case A and case B. These measurements are performed using Kr as a carrier gas. Curve A(i) and B(i) show the TOF profile of the slow beam of OH radicals that passes through the trap when no voltages are applied to the trap electrodes. Due to the lower beam velocity of around 15 m/s in case B compared to the 21 m/s in case A, the beam arrives later at the center of the trap, is spread out more and has a lower peak density. Curve A(ii) and B(ii) show the TOF profile when the voltages for trap loading as given earlier are constantly applied to the trap electrodes. In case A the molecules enter the trap too fast, and move past the center of the trap; the observed double-hump structure in the TOF profile is to be interpreted as the signal from first the incoming and then the reflected beam. In case B the molecules are reflected almost exactly at the center of the trap. Curve A(iii) (identical to the lower curve in Fig. 6.2) and B(iii) show the resulting TOF profile when we switch from the loading geometry to the trapping geometry at the time indicated by the arrow. The higher initial velocity in case A leads to approximately a factor three more molecules in the trap, but also results in clear oscillations in the TOF profile. When the molecules are (more) correctly coupled into the trap, as in case B, hardly any oscillations are observed. The TOF profiles that result from three dimensional trajectory simulations of the experiment are shown underneath the experimental profiles. In these simulations, the geometry of the trap electrodes and the different fluorescence collection efficiencies at different regions in the trap are taken into account. The simulations accurately reproduce the observed TOF profiles. The calculated longitudinal phase space distribution of the molecules in the trap at $t = 30$ ms, shown in Fig. 6.5 for both cases, should therefore also be realistic. From this, the FWHM of the velocity distribution of the trapped molecules is deduced to be around 30 m/s in case A and around 10 m/s in case B, corresponding to a temperature of 450 mK and 50 mK for the trapped OH radicals, respectively. The density is rather similar in both cases, and is about $10^7 - 10^8 \text{ cm}^{-3}$.

The measurements presented in Figure 6.5 clearly indicate that the trap-loading process is less optimal when the beam is better coupled into the trap. This is due to the inferior transverse focussing of the beam in this case while travelling the 21 mm distance between the last stage of the decelerator and the center of the trap. The better (longitudinal) phase-space matching of the OH radical beam to the (longitudinal) acceptance of the quadrupole trap is stultified by the lower longitudinal velocity of the package and the corresponding increased transverse spreading. A way to improve this situation is to install a buncher [10] and a hexapole in front of the electrostatic trap, that allows the independent

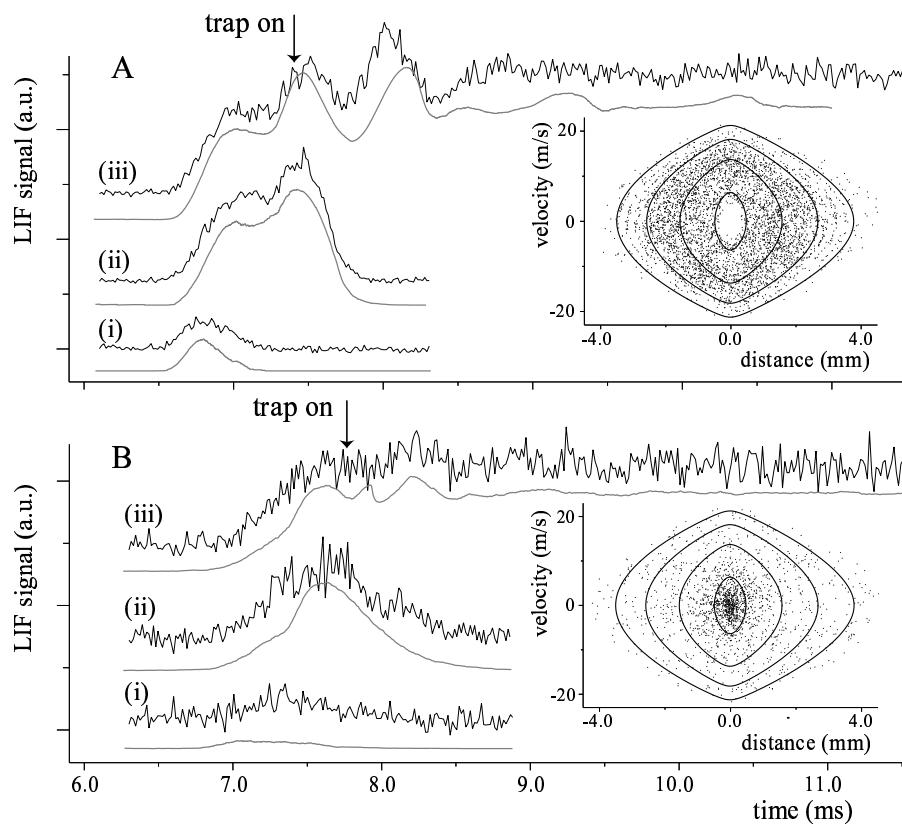


Figure 6.5: LIF signal of OH ($J = 3/2$) radicals at the center of the trap as a function of time after OH production for two different trap loading sequences (case A and B), together with the numerically simulated curves. The calculated longitudinal phase space distribution of the OH radicals in the trap at $t = 30$ ms is shown for both cases.

control over the longitudinal focussing (buncher) and the transverse focussing (hexapole) of the slow package of molecules [14]. However, these elements significantly increase the distance between the Stark decelerator and the electrostatic trap, raising the requirements to the ability of both elements to control the spreading of the whole package of molecules. Another approach is to 'merge' the Stark decelerator with the electrostatic trap, either by changing the electrode geometry of the last stages of the decelerator to allow trapping, or by changing the electrode geometry of the trap to allow improved deceleration and transverse focussing. Design studies of such traps are currently underway.

6.3 Conclusions and outlook

The experiments reported here are performed in a molecular beam deceleration and trapping machine that is designed such that almost the complete molecular beam pulse that passes through the skimmer in the right quantum-state can be transported through the trap at a tunable absolute velocity while staying together as a compact package. Alternatively, a sizeable fraction of this molecular beam pulse can be slowed down to a near standstill and loaded into the electrostatic trap, where the molecules can then be trapped up to seconds. Sensitive quantum-state specific detection of the molecules can be performed inside the quadrupole trap. As the molecular beam machine typically runs at a 10 Hz repetition rate, and as different high voltage switching sequences can be applied to adjacent molecular beam pulses, this together offers the unique possibility to perform "in-beam" collision and reactive scattering experiments as a function of the continuously tunable collision energy and with an unprecedented energy resolution.

CHAPTER 7

DIRECT MEASUREMENT OF THE RADIATIVE LIFETIME OF VIBRATIONALLY EXCITED OH RADICALS

Neutral molecules, isolated in the gas-phase, can be prepared in a long-lived excited state and stored in a trap. The long observation time afforded by the trap can then be exploited to measure the radiative lifetime of this state by monitoring the temporal decay of the population in the trap. This method is demonstrated here and used to benchmark the Einstein A-coefficients in the Meinel system of OH. A pulsed beam of vibrationally excited OH radicals is Stark decelerated and loaded into an electrostatic quadrupole trap. The radiative lifetime of the upper Λ -doublet component of the $X^2\Pi_{3/2}, v = 1, J = 3/2$ level is determined as 59.0 ± 2.0 ms, in good agreement with the calculated value of 58.0 ± 1.0 ms.

Based on:

Direct measurement of the radiative lifetime of vibrationally excited OH radicals
Sebastiaan Y.T. van de Meerakker, Nicolas Vanhaecke, Mark P.J. van der Loo, Gerrit C. Groenenboom, and Gerard Meijer
Phys. Rev. Lett. **95**, 013003 (2005).

7.1 Introduction

Infrared absorption and emission spectroscopy has a long and rich history in the development and application of molecular physics. Absorption and emission of infrared radiation is an important diagnostic means in determining the presence and concentration of molecular species in various environments, ranging from plasmas and flames to the earth's atmosphere and interstellar space. A quantitative analysis of these observations relies on a detailed knowledge of the Einstein A -coefficients that characterize the spontaneous emission rates. These A -coefficients can generally be inferred from absorption measurements, provided the (line-integrated) number density and the temperature of the absorbing species are accurately known. The unstable nature of many chemically highly relevant molecules severely limits the accuracy of this approach for these species, however. The most direct and generally applicable route to accurately determining the A -coefficients is to measure the radiative lifetimes of individual ro-vibrational levels. Molecules isolated in the gas-phase and at low densities are needed for this, as interactions with a medium and quenching by collisions have to be avoided. The preferred way to measure the radiative lifetime is to prepare molecules in the quantum state of interest, and to measure the state-specific population as a function of time. The problem with this approach is that infrared radiative lifetimes are typically in the millisecond to second range, much longer than the observation times that are commonly available in experiments. Ingenious schemes have been developed that nevertheless enable a measurement of long radiative lifetimes of neutral molecules in a molecular beam [171, 172]. Only for lifetimes up to a few milliseconds it has been possible to measure the population decay directly [173].

For charged particles, the greatly enhanced observation times that became available when traps were developed opened up the possibility to directly measure radiative lifetimes of metastable states [174]. For neutral atoms and neutrons, trapping has been used to directly measure long lifetimes as well [175]. Methods to confine neutral gas-phase molecules in magnetic [42], optical [46], and electrostatic traps [11] for times up to seconds have recently been developed. In this chapter, the first direct measurement of the infrared radiative lifetime of a vibrationally excited trapped molecule is reported. By measuring the temporal decay of the population of OH ($X^2\Pi_{3/2}, v = 1, J = 3/2$) radicals in an electrostatic trap, an accurate value for the A -coefficient of the fundamental $1 - 0$ band of OH is obtained.

The infrared radiative properties of the OH radical are of particular importance. Vibrationally excited OH ($X^2\Pi, v \leq 9$) radicals, produced in the upper atmosphere via the reactive depletion of ozone [25–27], are responsible for the near-infrared night-time air-glow [176]. Recently, this OH Meinel band emission has also been observed from artificial aurora at higher altitudes, offering new possibilities to study ionospheric interactions [177]. OH vibrational emission has also been observed from stellar and interstellar space [28]. The so-called ‘prompt emission’ in the $1 - 0$ band of the OH radical (around $3.3 \mu\text{m}$), produced by photodissociation of water, is used as a tracer for water produced in comets [178]. The radiative lifetimes of the vibrational states of OH ($X^2\Pi$) are essential for a quantitative interpretation of all these observations, and have therefore received considerable experimental and theoretical attention. Over the years, the values have scattered over a wide range and have only slowly converged [179]. The most recent values for the lifetimes, based on experimental absorption line intensities, are given in the HITRAN 2004 database [180]. For the $X^2\Pi_{3/2}, v = 1, J = 3/2$ level of OH, this database gives a lifetime of 56.6 ms with an error of 10-20%.

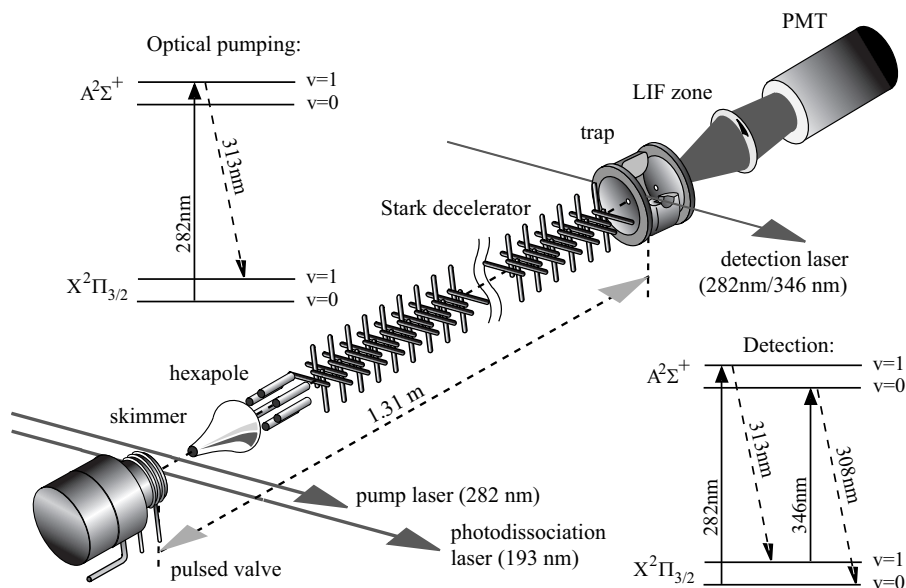


Figure 7.1: Scheme of the experimental setup. A pulsed beam of OH ($v = 0$) radicals is produced via photodissociation (193 nm) of HNO₃ molecules seeded in Xe. Prior to entering the decelerator, part of the OH radicals are prepared in the $v = 1$ state by Franck-Condon pumping via the $A^2\Sigma^+$ state (upper left). OH radicals in the $J = 3/2$ level of both the $v = 0$ and $v = 1$ vibrational states of the $X^2\Pi_{3/2}$ electronic ground state are Stark decelerated and subsequently loaded into the electrostatic trap. Molecules in the trap are state-selectively detected by imaging the laser induced fluorescence onto a PMT.

7.2 Experiment

The experiments are performed in the molecular beam deceleration and trapping machine that was used for the electrostatic trapping experiments of OH ($X^2\Pi_{3/2}, v = 0$) radicals that are described in chapter 6. This machine is schematically shown in Figure 6.1. A pulsed beam of OH radicals with a mean velocity of 360 m/s is produced via ArF-laser dissociation of HNO₃, seeded in Xe, near the orifice of a pulsed solenoid valve. In the experiments, the population in the $J = 3/2$ rotational level of the $v = 0$ and $v = 1$ vibrational states of the $X^2\Pi_{3/2}$ electronic ground state is of relevance. During the expansion, most of the OH radicals cool down to the ro-vibrational ground state $v = 0, J = 3/2$. Just after the expansion region, approximately 15% of the OH ($v = 0$) radicals are promoted to the $X^2\Pi_{3/2}, v = 1$ state by Franck-Condon pumping via the $A^2\Sigma^+$ state at 282 nm [181]. This optical pumping scheme is shown in the upper left of Figure 7.1. In the presence of an electric field, the upper Λ -doublet components of the $J = 3/2$ levels split into a low-field seeking $M_J\Omega = -3/4$ and a $M_J\Omega = -9/4$ component. Only OH radicals in the $J = 3/2, M_J\Omega = -9/4$ component of either vibrational state are Stark decelerated and subsequently loaded into the quadrupole trap, as is described in detail in chapter 6.

The Stark shifts of the $v = 0$ and $v = 1$ states of OH are very similar [182], and molecules in both vibrational states are simultaneously decelerated and loaded into the quadrupole trap with equal efficiency. In the present experiments, the pressure in the trap chamber does not exceed 2×10^{-9} mbar under operating conditions. The density of OH radicals at the center of the trap is measured using laser induced fluorescence (LIF) detection schemes, shown in the lower right of Figure 7.1. The population

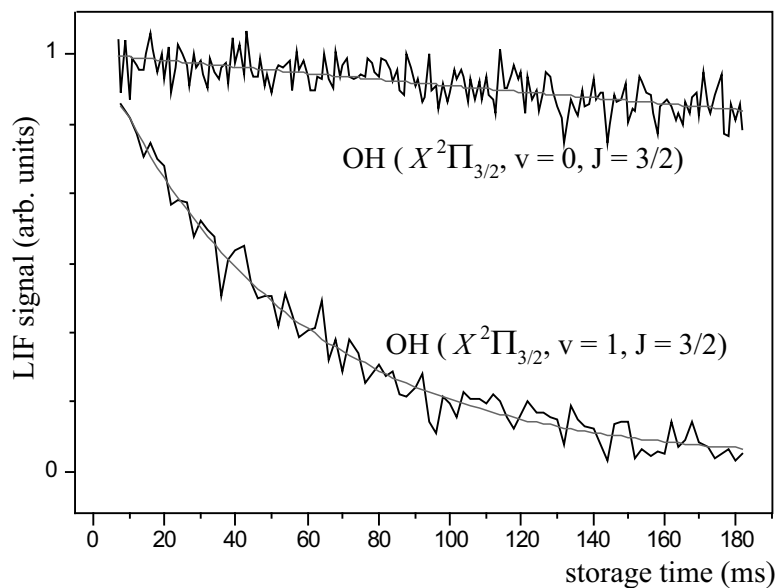


Figure 7.2: Population of trapped OH radicals in the $X^2\Pi_{3/2}, v = 0, J = 3/2$ level (upper curve) and in the $X^2\Pi_{3/2}, v = 1, J = 3/2$ level (lower curve), as a function of the storage time t . The trapping potential is switched on at $t = 0$ ms.

of the OH radicals in the $v = 0, J = 3/2$ and $v = 1, J = 3/2$ levels is state-selectively probed by inducing the $Q_1(1)$ transitions of the $A^2\Sigma^+, v = 1 \leftarrow X^2\Pi, v = 0$ band around 282 nm and the $A^2\Sigma^+, v = 0 \leftarrow X^2\Pi, v = 1$ band around 346 nm, respectively. The off-resonant fluorescence around 313 nm (when probing $v = 0$) and 308 nm (when probing $v = 1$) is imaged through a 6 mm diameter opening in the second end-cap onto a photomultiplier tube (PMT).

In Figure 7.2, the LIF signal of the trapped cloud of OH radicals in the $v = 0, J = 3/2$ level (upper curve) and in the $v = 1, J = 3/2$ level (lower curve) is shown as a function of the storage time t . The trapping potential is switched on at $t = 0$ ms. The experiment runs at a repetition rate of 5 Hz to allow for a maximum observation time of (almost) 200 ms in the trap. On this time-scale, OH radicals in the $v = 0$ state mainly leave the trap via collisions with background gas; both elastic and inelastic collisions with the thermal background gas transfer an amount of kinetic energy to the OH radicals that largely exceeds the trap depth. From a separate series of measurements, running the apparatus at lower repetition rates while maintaining the same background pressure, a $1/e$ trap lifetime of 1.3 ± 0.1 s is deduced. The population of trapped OH radicals in the $v = 1$ state, on the other hand, is mainly depleted via spontaneous emission to the $v = 0$ state, in addition to collisions with background gas. The observed exponentially decaying curve therefore almost directly reflects the radiative lifetime of the $X^2\Pi_{3/2}, v = 1, J = 3/2$ level of OH. From a series of measured decay curves, taking carefully the baseline and the signal-to-noise ratio of the LIF signal into account, an exponential decay time of 56.4 ± 1.9 ms is deduced. The inherent trap lifetime can be assumed to be identical for OH radicals in the $v = 0$ and $v = 1$ vibrational states, as the total collision cross-sections with thermal background gas will be very similar for OH in either one of the vibrational states. Under this assumption, a radiative lifetime τ for OH radicals in the upper Λ -doublet component of the $X^2\Pi_{3/2}, v = 1, J = 3/2$ level of $\tau = 59.0 \pm 2.0$ ms is obtained. In a non-decelerated beam of OH radicals that passes through the trap about 3.6 ms after production, the population of OH radicals in the $v = 2$ state is measured to

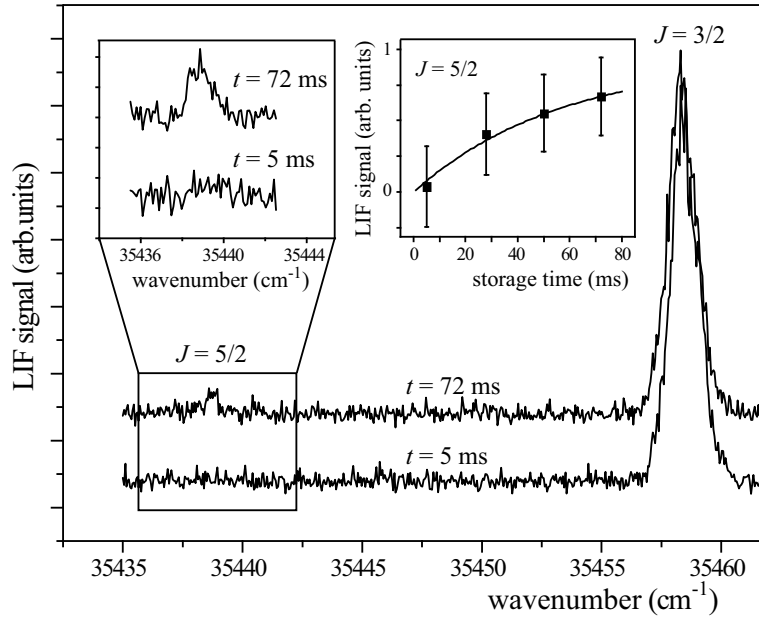


Figure 7.3: Excitation spectrum of trapped OH ($v = 0$) radicals that is recorded 5 ms (lower curve) and 72 ms (upper curve) after switching on of the trap. In the central inset, the population of trapped OH radicals in the $v = 0, J = 5/2$ level is shown as a function of the storage time.

be more than an order of magnitude less than the population in the $v = 1$ state. Re-population of the $v = 1$ state in the trap via cascading spontaneous emission from higher vibrational states is therefore negligible in our experiment.

OH radicals in the $v = 1, J = 3/2$ level that are confined in the trap undergo infrared spontaneous emission to the $v = 0$ state, following the selection rules of the electric dipole allowed transitions in the presence of an electric field. The molecules can make a transition to all $M_J\Omega$ components of the $J = 1/2, J = 3/2$ and $J = 5/2$ rotational levels of the $X^2\Pi, v = 0$ electronic ground state. Of these, only molecules that end up in the $M_J\Omega = -15/4, -9/4$ and $-3/4$ components of the $J = 5/2$ level or in the $M_J\Omega = -9/4$ and $-3/4$ component of the $J = 3/2$ level are (partially) recaptured and confined in the trap. In Figure 7.3, the excitation spectrum of trapped OH ($v = 0$) radicals is shown that is recorded 5 ms (lower curve) and 72 ms (upper curve) after switching on of the trap. The detection laser is scanned over the $Q_1(1)$ and $Q_1(2)$ transitions of the $A^2\Sigma^+, v = 1 \leftarrow X^2\Pi_{3/2}, v = 0$ band, probing the population in the $v = 0, J = 3/2$ and $v = 0, J = 5/2$ levels, respectively. Initially, the trapped OH $v = 0$ radicals exclusively reside in the $J = 3/2$ level, the only rotational state that is selected by the Stark decelerator. After 72 ms of trapping, a small but significant population of OH radicals in the $v = 0, J = 5/2$ level is detected in the trap. In the central inset of Figure 7.3, the accumulation over time of the trapped OH ($v = 0, J = 5/2$) radicals is shown. The expected exponential growth of the population in the $J = 5/2$ level, as deduced from the measurements shown in Figure 7.2, is shown as well. The relative population of trapped OH radicals in the $v = 0, J = 3/2$ and $v = 0, J = 5/2$ levels is also consistent with the expectations. An overall factor of about 20 is expected, based on the initial relative population of $v = 0$ and $v = 1$ in the trap and the Hönl-London factor for fluorescence from the $v = 1, J = 3/2$ to the $v = 0, J = 5/2$ level, in combination with the larger size of the trapped cloud of $J = 5/2$, e.g. the reduced overlap with the detection laser.

The radiative properties of the OH radical can be calculated from its dipole moment function and the potential energy curve. The radiative lifetime τ of the upper Λ -doublet component (of $f(+)$ parity) of the $X^2\Pi_{3/2}(v = 1, J = 3/2)$ level of OH is given by

$$\tau^{-1} = \sum_f A^{fi} = \sum_f \frac{4\alpha\omega_{fi}^3}{3c^2e^2} |\langle f|\mu|i\rangle|^2, \quad (7.1)$$

where A^{fi} are the Einstein A -coefficients for the $X^2\Pi, v = 1 \rightarrow X^2\Pi, v = 0$ transitions, α is the fine structure constant, ω_{fi} the angular frequency of the emitted photon, c the speed of light, and e the elementary charge. In the calculation of the initial ($|i\rangle$) and final ($|f\rangle$) states, Λ -type doubling and spin-orbit, spin-rotation, and rotation-vibration coupling is taken into account. The sum over final states includes all spin-orbit levels with $J \leq 5/2$. The $X^2\Pi$ potential energy curve and the r -dependent dipole moment μ are obtained from an internally contracted multireference configuration interaction calculation with the MOLPRO [183] program package. Special relativistic effects are taken into account by using Douglas-Kroll one-electron integrals. The molecular orbitals are obtained from a 1-5 σ , 1-2 π complete active space self consistent field calculation, employing an augmented correlation consistent polarized valence 6-zeta (aug-cc-pV6Z) one-electron basis set. The r -dependent spin orbit couplings are obtained in a similar calculation employing an uncontracted aug-cc-pVQZ basis. The Λ -type doubling parameters are taken from spectroscopic observations [184]. The result that is obtained for the radiative lifetime in the presence of a full parity mixing electric field is $\tau = 58.0$ ms (in field free conditions $\tau = 57.7$ ms), in good agreement with the experimentally determined value. As the computed ro-vibrational energy levels agree with experiments to better than 0.02% and as our dipole moments agree with previous high level *ab initio* calculations [185] to about 0.7%, we estimate the error in τ to be about 1 ms.

7.3 Conclusions

In this chapter, the first direct measurement of the quantum-state specific infrared radiative lifetime of a trapped molecule is reported. The technique reported here can generally be applied to directly measure lifetimes of metastable states of neutral molecules up to seconds, with an unprecedented accuracy. A requirement is that it must be possible to confine the molecules in the desired quantum state in a trap. The molecules can be prepared in the metastable state prior to deceleration and trapping, as reported here. Alternatively, they can first be trapped in the quantum-state that is best suited for it, and preparation of the desired metastable state can then be performed inside the trap. By recording the decay of the population of vibrationally excited OH ($X^2\Pi_{3/2}, v = 1, J = 3/2$) radicals in an electrostatic quadrupole trap, the radiative lifetime of this level is determined as 59.0 ± 2.0 ms, in good agreement with the theoretically predicted value of 58.0 ± 1.0 ms. This provides a benchmark for the Einstein A -coefficients in the Meinel system of OH. This is of particular importance in, for instance, combustion, atmospheric science and in astrophysics.

CHAPTER 8

ACCUMULATING NH RADICALS IN A MAGNETIC TRAP

We propose a novel scheme to accumulate fermionic or bosonic NH radicals (^{14}NH or ^{15}NH , respectively) in a magnetic trap in order to increase the phase-space density. NH molecules prepared in the long-lived metastable $a^1\Delta$ state that exhibits a large Stark effect can be brought to a standstill using Stark deceleration. By inducing the hitherto unobserved spin-forbidden $A^3\Pi \leftarrow a^1\Delta$ transition, followed by spontaneous emission to the $X^3\Sigma^-$ state, a unidirectional pathway for population transfer from the metastable state into the electronic ground state is obtained. In the ground state the NH molecules are no longer sensitive to electric fields but show a significant Zeeman effect instead, enabling confinement and reloading of ground state molecules in a magnetic trap. In a preliminary deceleration experiment, a beam of $\text{NH}(a^1\Delta, J = 2)$ radicals is decelerated from 550 to 330 m/s.

Based on:

Accumulating NH radicals in a magnetic trap

Sebastiaan Y.T. van de Meerakker, Rienk T. Jongma, Hendrick L. Bethlem, and Gerard Meijer
Phys. Rev. A. **64**, 041401(R) (2001); and

Optical pumping of metastable NH radicals into the paramagnetic ground state

Sebastiaan Y.T. van de Meerakker, Boris G. Sartakov, Allard P. Mosk, Rienk T. Jongma, and Gerard Meijer
Phys. Rev. A. **68**, 032508 (2003).

8.1 Introduction

In chapter 6 it was demonstrated that after Stark deceleration, a beam of ground-state OH radicals can be electrostatically trapped for times up to seconds. These experiments could in principle be performed with any polar molecule that has a positive Stark shift. A selection of these were given in Table 2.1 of chapter 2. To be able to study molecular interactions and collective effects in these trapped cold molecular gases, the phase-space density needs to be further increased, i.e., the number density needs to be made higher and/or the temperature needs to be reduced. The Liouville theorem dictates that an increase of phase-space density is not possible without dissipation. Consequently, non-conservative forces are required to increase the phase-space density. Evaporative cooling [186], a method that has been very successful for cold atoms, might be applicable to molecules as well once the number density in the trap is large enough that collisions occur. Alternatively, the trapped sample can be sympathetically cooled by inducing collisions between the trapped molecules and (much colder) trapped atoms [187, 188]. The efficiency of these methods depends on a sufficiently large ratio of elastic-to-inelastic cross sections at the relevant temperatures. Most of these are at present unknown, although considerable theoretical progress has been made in this field in recent years [75, 93, 189–191]. Although not experimentally realized yet, other cooling schemes like laser-cooling on ro-vibrational transitions [192] or cavity-mediated cooling [193], have been suggested. For our technique, the most straightforward method to increase the phase-space density of trapped molecules would be the accumulation of several packages of molecules in the trap; the density that is reached so far is obtained employing a single loading cycle. Simply re-loading the trap, however, requires opening up the trapping potential thereby losing the molecules that are already stored. In this chapter a scheme is described to re-load a magnetic trap which circumvents this fundamental obstacle. This scheme works specifically for the NH radical, and can be realized by producing NH molecules in the $a^1\Delta$ state, which can be slowed down to a complete standstill using the Stark decelerator. Subsequently, the molecules are forced to decay to the $X^3\Sigma^-$ electronic ground state by exciting the spin-forbidden $A^3\Pi \leftarrow a^1\Delta$ transition. In the ground state, the NH molecules interact strongly with magnetic fields and can be readily trapped in inhomogeneous magnetic fields. In the ground state the molecules are rather insensitive to electric fields, and the electric fields of the decelerator hardly effect the magnetic trapping potential. The magnetic trap can therefore be directly superimposed with the point where the NH radicals have been electrostatically stopped. The ‘laser-driven’ spontaneous decay process effectively switches off the electric field interaction of the molecules enabling the accumulation of several packages of molecules in the magnetic trap, and automatically fulfills the requirement of a uni-directional pathway to the ground state.

There are additional features that make the NH radical an interesting system to the field of cold molecules. Its $2 \mu_B$ magnetic moment in the $^3\Sigma^-$ electronic ground state actually makes the NH radical one of the prime candidates in molecular magnetic trapping experiments. Magnetic trapping of molecules is important, since theoretical studies indicate that the cross sections for inelastic collisions between two dipolar molecules causing trap-loss is greatly enhanced in the presence of an electric field [75]. NH radicals are therefore at the center of interest in several experimental and theoretical studies. Currently, an effort is undertaken to load a molecular beam of NH($^3\Sigma^-$) radicals into a cryogenic He buffer gas, and to subsequently trap the molecules at the center of an inhomogeneous magnetic field. Although the trapping has not been achieved yet, up to 10^{12} molecules in the beam could be buffer-gas cooled to temperatures below 6 K [45]. The interactions of NH ($X^3\Sigma^-$) radicals

with Rb atoms, and the implications for sympathetic cooling, have been theoretically investigated [194]. In experiments, two bosonic (^{15}NH , ^{14}ND) and two fermionic (^{14}NH , ^{15}ND) isotopomers can be produced, of which in particular ^{15}NH has a relatively simple hyperfine structure. Molecules in both the electronic ground state and in the electronically excited metastable state can be sensitively detected using Laser Induced Fluorescence (LIF) on strong, electric dipole allowed, transitions in the ultraviolet spectral region. Moreover, the $A^3\Pi, v=0 \leftarrow X^3\Sigma^-, v=0$ transition around 336 nm has a Franck-Condon factor of better than 0.999 [195]. As in addition a closed rotational transition can be found, this offers interesting prospects for direct laser-cooling. It should be remarked, however, that in this highly diagonal system the actual ratio of the oscillator strengths of the diagonal to the off-diagonal transitions depends sensitively on the r -dependence of the transition dipole moment. But even so, measurements indicate that the ratio of the transition probabilities of the ($v=0 \rightarrow v=0$) and the ($v=0 \rightarrow v=1$) transition is better than 0.993 [196]. The NH radical is also an interesting species for cold chemistry studies. NH radicals in their metastable $a^1\Delta$ state, which are isoelectronic with O (^1D) and CH_2 (\tilde{a}^1A_1) and isovalent with NF ($a^1\Delta$) and NCl ($a^1\Delta$), are regarded as a model system to study elementary reactions of electronically excited species [197].

This chapter is organized as follows. In section 8.2, the accumulation scheme is discussed in more detail. The hitherto unobserved spin-forbidden $A^3\Pi \leftarrow a^1\Delta$ transition is characterized in section 8.3. In section 8.4 a production method for a molecular beam of NH ($a^1\Delta$) radicals is described, that is suited to be injected into a Stark decelerator. In section 8.5 a preliminary deceleration experiment is described, in which part of this beam is decelerated from 550 to 330 m/s.

8.2 Accumulation scheme

In the scheme proposed here, ^{14}NH is used throughout, although the arguments hold equally well for ^{15}NH . The electronic states of NH that are of relevance to the proposed scheme are schematically shown in the left part of Fig. 8.1. The Stark shift of the $a^1\Delta$ ($v=0, J=2$) state, located some 1.5 eV above the electronic ground state, is plotted as a function of the electric field strength in the upper inset to Fig. 8.1. The Λ -doublet splitting of this level is only 115 kHz [198], and a nearly linear Stark shift is observed. The $a^1\Delta$ ($v=0, J=2, M\Omega = -4$) level, originating from the upper Λ -doublet component of f -parity, experiences a positive Stark shift of more than 3 cm^{-1} in an electric field of 200 kV/cm. Therefore, molecules in this state are excellent candidates to be slowed down with the Stark decelerator. It should be noted that the radiative lifetime of the $a^1\Delta$ state is very long (12.5 s [199]) compared to the typical duration of the deceleration process.

A setup that can be used to test the proposed scheme is schematically depicted in Fig. 8.2. NH molecules in their metastable $a^1\Delta$ state are produced in a pulsed supersonic gas expansion from a precursor molecule. Making use of the process of adiabatic cooling, the rotational ground state ($J=2$) will be predominantly populated in the beam, and high densities of molecules in this state at a translational temperature of typically 1 K can be reached. The absolute velocity of the NH molecules needs to be largely reduced before the molecules can be trapped. This can be realized by passing the molecular beam through the Stark decelerator, thus producing high densities of slow, velocity-selected molecules. The NH molecules can be brought to a complete standstill in the last, enlarged electric field section of the decelerator in which the electric field will only go up to about 20 kV/cm. A con-

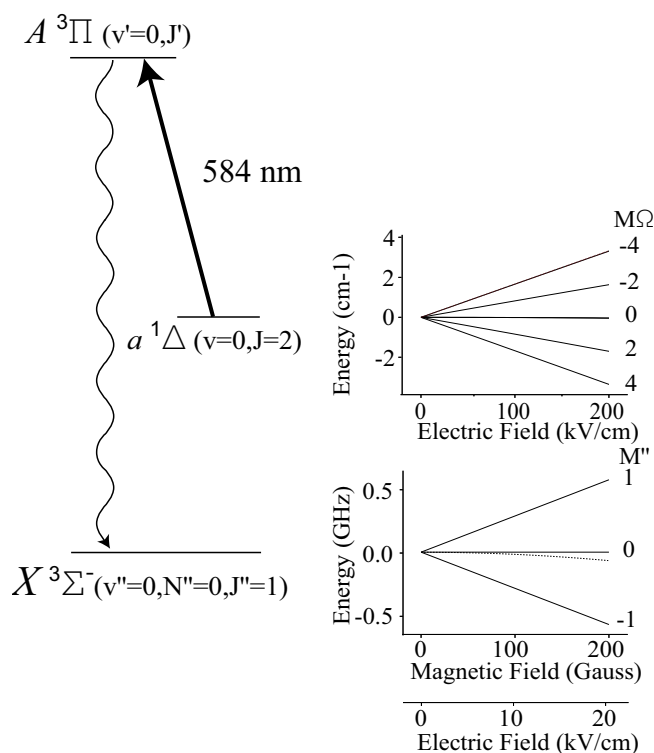


Figure 8.1: The electronic states of NH that are of relevance to the proposed scheme. The NH molecules prepared in the long-lived $a^1\Delta(v = 0, J = 2)$ state exhibit a large Stark shift, as shown in the inset. By inducing the spin-forbidden $A^3\Pi(v' = 0) \leftarrow a^1\Delta(v = 0)$ transition around 584 nm, the molecules are forced to spontaneously decay to the $X^3\Sigma^-(v'' = 0)$ state. Both the Stark shift (dashed curve) and Zeeman shift (solid curves) of the lowest rotational level in this state is shown. For the Stark shift, the different M -components are unresolved. Note the different energy scale for both insets.

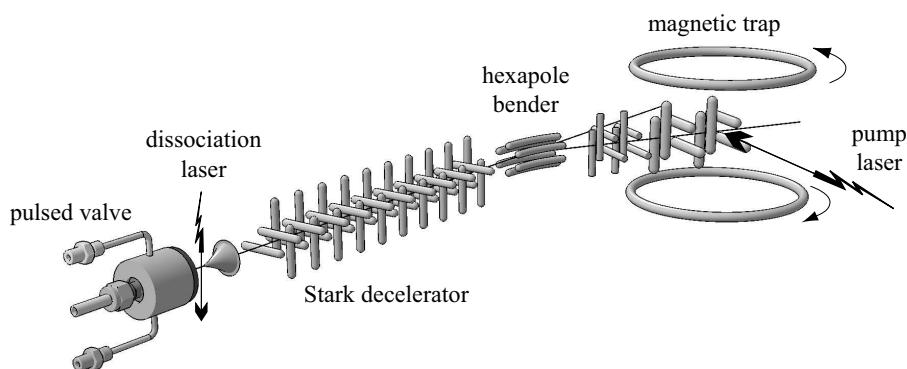


Figure 8.2: A typical setup that can be used to accumulate NH molecules in a magnetic trap. NH molecules in the $a^1\Delta$ state are produced in a pulsed molecular beam from a precursor, and slowed down with the Stark decelerator. A hexapole bender injects only the selected bunch of molecules into the final part of the decelerator, where the molecules are stopped in the last, enlarged electric field section. A pump laser provides the molecules a uni-directional path to the electronic ground state, where they are accumulated in a magnetic trap.

ventional magnetic trap, for instance formed by two coils in the anti-Helmholtz configuration, creates a magnetic field minimum exactly at the position where the molecules are stopped. The Zeeman effect in the $a^1\Delta$ state due to the presence of the magnetic field is negligible small compared to the Stark effect. As soon as the molecules in the $a^1\Delta$ state are brought to a standstill, the electric fields of the decelerator are switched off, while the magnetic field is permanently on. Immediately after switching off the electric field, the decelerated molecules can be pumped via a laser induced spin-forbidden transition from the $a^1\Delta$ state to the lowest vibrational level of the $A^3\Pi$ state. In section 8.3 experiments are described where this hitherto unobserved transition has been found and characterized. It is shown that this transition can be efficiently induced using high-intensity narrow-band radiation. The lifetime of the electronically excited $A^3\Pi(v' = 0)$ state is around 450 ns [200], and a transition from this state to the $X^3\Sigma^-(v'' = 0)$ ground state will occur via spontaneous emission of a photon. The allowed $A^3\Pi \rightarrow X^3\Sigma^-$ transition is almost perfectly ‘vertical’ (the Franck-Condon factor for this vibrational transition is better than 0.999 [195]), and consequently molecules will end up in the lowest vibrational level of the electronic ground state with almost unit efficiency. Selected $A^3\Pi(v' = 0, J') \leftarrow a^1\Delta(v = 0, J)$ transitions will cause a major fraction (up to 62%, see section 8.3) of the excited molecules to end up in the $X^3\Sigma^-(v'' = 0, N'' = 0, J'' = 1, M'' = 1)$ level.

Both the Zeeman shift (solid curves) and the Stark shift (dashed curve) of this rotational state are indicated in the lower inset to Fig. 8.1. The hyperfine structure is not included in the figure as calculations show that it does not significantly influence the overall picture. It is observed that even in electric fields as high as 20 kV/cm the Stark shift is very small, making ground state NH molecules rather insensitive to electric fields. Due to the non-zero electron spin ($S = 1$), there is a significant Zeeman shift, allowing confinement of ground state NH molecules in a magnetic trap. Using conventional coils, magnetic fields up to 100 Gauss are readily achieved, creating a 300 MHz, or 15 mK, deep trap that can store molecules in states that experience a positive Zeeman shift. The trap depth is nicely matched to the typical translational temperature of the decelerated package of molecules exiting the Stark decelerator, which can be as low as a few mK. The absence of a significant Stark shift in the electronic ground state allows switching of the Stark decelerator to stop the next pulse of NH molecules in the $a^1\Delta$ state without losing the magnetically trapped ground state molecules. The spontaneous emission step makes that the transfer of molecules from the $a^1\Delta$ to the $X^3\Sigma^-$ state is uni-directional. Via this mechanism, an increase of phase-space density is obtained with every pulse of molecules that is stimulated to the $X^3\Sigma^-$ state.

Referring back to Fig. 8.2, collisions of molecules in the magnetic trap with the fast part of the next gas pulse that is not sufficiently decelerated, can be prevented by placing the last few stages of the decelerator under a small angle relative to the molecular beam axis. By using a pulsed hexapole bender [13] as indicated in Fig. 8.2, only the decelerated bunch of molecules, which is suitable to be trapped, will be coupled into the last few stages, while the remainder of the gas pulse passes in a straight line. The presence of NH molecules in the trap in either the $a^1\Delta$ or the $X^3\Sigma^-$ state can be conveniently monitored via laser induced fluorescence (LIF) detection on strong electronic transitions in the near-UV [201, 202]. Considering the (almost) unity Franck-Condon factor for the $A^3\Pi(v' = 0) \leftarrow X^3\Sigma^-(v'' = 0)$ transition [195], it is emphasized that an (almost) closed ro-vibrational transition can be found allowing further reduction of the temperature of NH radicals using conventional laser cooling after application of the Stark deceleration technique, although ad-

ditional microwave transitions between hyperfine components will be needed to effectively close the absorption-emission cycle [192].

Compared to a single pulse, the gain in intensity of trapped molecules via accumulating molecules from consecutive cycles equals the product of the trapping time and the repetition rate at which the experiment is operated. Trapping times exceeding 10 s are anticipated at ultra-high vacuum ($< 10^{-10}$ Torr) conditions. The setup we are currently using has a maximum repetition rate of 10 Hz, yielding a gain in intensity of at least two orders of magnitude via the proposed accumulation process. The short duration of the deceleration process (on the order of 1 ms) implies that the whole experiment can in principle be operated at higher repetition rates, increasing the gain correspondingly.

8.3 Optical pumping of NH ($a^1\Delta$) radicals into the $X^3\Sigma^-$ state

Obviously, a critical step in the proposed accumulation scheme is the realization of the spin-forbidden $A^3\Pi(v' = 0) \leftarrow a^1\Delta(v = 0)$ transition. Although this transition has never been experimentally observed, the singlet-triplet splitting in NH is known quite well. The singlet and triplet systems of NH were first connected by the observation of the $b^1\Sigma^+ \rightarrow X^3\Sigma^-$ transition [203] in emission. The most accurate value of the singlet-triplet splitting to date is derived from a direct measurement of the $a^1\Delta \rightarrow X^3\Sigma^-$ transition [199]. Based on these measurements, the $A^3\Pi, v = 0 \leftarrow a^1\Delta, v = 0$ transition is expected around 584 nm, and can be recorded using LIF detection. In this section, experiments are described that demonstrate that efficient transfer of NH ($a^1\Delta$) radicals to the electronic ground state $X^3\Sigma^-$ by optical pumping via the spin-forbidden $A^3\Pi \leftarrow a^1\Delta$ transition is possible. These experiments are performed in a small molecular beam machine using a pulsed discharge source to produce a molecular beam of NH ($a^1\Delta$) radicals.

8.3.1 Experiment

The molecular beam machine consists of two differentially pumped vacuum chambers. The NH molecules are formed in an electrical discharge during the expansion of a mixture of about 1% NH_3 in He into vacuum through a commercially available pulsed supersonic valve (R.M. Jordan, Inc.). The valve has a pulse duration of approximately 40 μs and operates at a repetition rate of 10 Hz. With a stagnation pressure of 1.5 bar, the pressure in the source chamber does not exceed $3 \cdot 10^{-6}$ Torr under operating conditions. The geometry of the discharge source is similar to that used by Van Beek *et al.* for the production of a pulsed beam of OH radicals [117]. To confine the discharge, a sharp-edged nozzle with an orifice of 0.5 mm diameter is used. A 0.5 mm diameter stainless steel ring with an inner diameter of 4.5 mm is mounted 2.5 mm in front of the nozzle. A voltage difference of 4.0 kV is applied between the ring and the valve body and can be pulsed using a fast high voltage switch (Behlke Electronic, HTS 61-03-GSM). The discharge has a duration of typically 10 μs . In the discharge, the NH molecules are produced in various electronic states, with only a fraction occupying the long-lived $a^1\Delta$ state. The quenching rate for the removal of NH molecules from this state by collisions with the He atoms is sufficiently low [204] that a beam of metastable NH can be produced. The beam passes through a 1.5 mm diameter skimmer and enters the detection chamber where the molecules can be state-selectively detected in a LIF-zone, 24 cm downstream from the nozzle. Here, a pulsed laser beam crosses the molecular beam at right angles. Laser induced fluorescence from this interaction

region is spatially filtered and imaged on a photomultiplier tube (Electron Tubes B2/RFI, 9813 QB). A near-UV bandpass filter (Schott glass; UG11 filter) is used to block the ambient laboratory light. Stray light from the laser is reduced by using several 4 mm diameter light baffles. To reduce stray light further, the LIF optics are mounted inside a hollow, blackened stainless steel tube. Blackening of the surfaces is performed by growing a 10 to 20 μm thick copper film on the surfaces using electrolysis in a copper sulphate bath. A black copper-(II)oxide layer is formed when placing the product in a 100 $^{\circ}\text{C}$ bath containing sodium hydroxide and a strong oxidizer. The black surface attaches very well to the stainless steel and is, after baking, compatible with ultra high vacuum applications ($\leq 10^{-10}$ Torr), i.e. for trapping experiments.

8.3.2 Characterization of the molecular beam

To characterize the rotational state distribution of the metastable NH radicals in the molecular beam, the NH ($a^1\Delta$) radicals are detected by inducing the strong dipole allowed $c^1\Pi, v=0 \leftarrow a^1\Delta, v=0$ transition around 326 nm. Pulsed laser radiation is generated by frequency-doubling the output of a Nd:YAG laser pumped dye laser system (Spectra Physics GCR-170/PDL3 combination) operating on DCM dye; typically some 10 mJ of tunable UV radiation with a bandwidth of 0.07 cm^{-1} is produced. In the experiment a pulse energy of only 0.5 mJ in a 4 mm diameter beam is used, sufficient to saturate the transition. Although the rotational levels in the $c^1\Pi, v=0$ state are predissociated, the lifetime is still around 460 ns and the total fluorescence quantum yield of these levels is about 90 % [205, 206]. Radiative decay from the $c^1\Pi, v=0$ state can occur via the $c^1\Pi \rightarrow b^1\Sigma^+$ and the $c^1\Pi \rightarrow a^1\Delta$ transitions. Only a few % of the total fluorescence is in the $c^1\Pi \rightarrow b^1\Sigma^+$ channel around 450 nm [207], which is suppressed by the optical filter in our experiment. The observed $c^1\Pi \leftarrow a^1\Delta$ excitation spectrum is depicted in Figure 8.3.

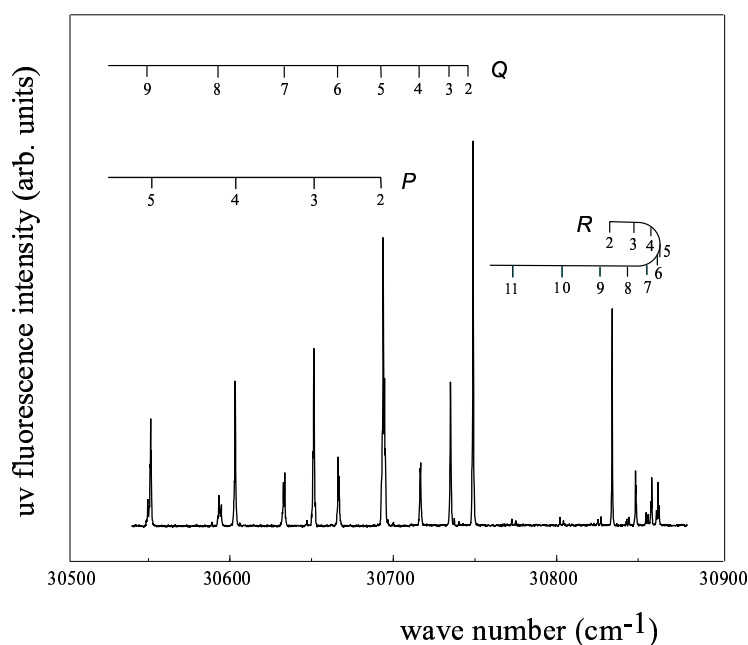


Figure 8.3: The observed $c^1\Pi, v=0 \leftarrow a^1\Delta, v=0$ excitation spectrum for ^{14}NH , together with the assignment of the spectral lines.

The observed lines are readily assigned using the line positions given by Ram *et al.* [202]. The ground rotational state $J = 2$ is the most populated in the beam, but population of states up to $J = 11$ is observed. The splitting of the lines due to the combined Λ -doublet splitting in the $c^1\Pi$ and the $a^1\Delta$ state is only resolved for high J -levels. Although no single rotational temperature can be fitted to the observed spectrum, a rotational temperature of about 120 K can be used to describe the relative population distribution of the lowest rotational levels. This relatively high rotational temperature is not unexpected in view of the limited cooling capacity of He in the expansion region combined with the hot discharge source. For the present study, the relatively wide rotational population distribution in the beam has the advantage that a rich $A^3\Pi \leftarrow a^1\Delta$ spectrum can be expected from which the relative rotational transition probabilities can be accurately determined. In successive experiments the population in the lowest rotational level in the metastable state and in the electronic ground state, i.e., the population in the $a^1\Delta, v = 0, J = 2$ level and in the $X^3\Sigma^-, v = 0, N = 0, J = 1$ level, were measured. The latter is measured by recording (part of) the $A^3\Pi \leftarrow X^3\Sigma^-$ excitation spectrum around 336 nm. From these measurements it is deduced that with the present production method the population in the metastable state is about an order of magnitude less than the population in the electronic ground state. In section 8.5 a production method for a slow molecular beam of NH radicals, that are almost exclusively produced in the ($a^1\Delta, J = 2$) state, is described. This beam is suited to be injected into a Stark decelerator.

8.3.3 The $A^3\Pi \leftarrow a^1\Delta$ transition

The spin-forbidden $A^3\Pi \leftarrow a^1\Delta$ transition around 584 nm is induced by the fundamental output of the same dye laser system, now operating on Rhodamine B dye. The radiative lifetime of the $A^3\Pi$ state is around 425 ns [200] and the far off-resonant $A^3\Pi \rightarrow X^3\Sigma^-$ fluorescence around 336 nm is collected in the LIF detection zone. Detection of the metastable NH radicals in this way is almost background-free as straylight from the laser beam is completely blocked by the optical filter. For the excitation, a 4 mm diameter laser beam with a pulse energy of typically 30 mJ in a 0.04 cm^{-1} bandwidth is used. Under these conditions the spin-forbidden transition is still not saturated, as will be discussed later. Absolute frequency calibration of the excitation laser is achieved by passing a reflection of the laser beam through an iodine absorption cell. The reported frequencies are corrected for systematic errors in the iodine reference atlas [208, 209]. Measurements are performed for both ^{14}NH and ^{15}NH ; the latter is produced from $^{15}\text{NH}_3$ (Campro Scientific; ^{15}N purity better than 99 %).

The observed $A^3\Pi \leftarrow a^1\Delta$ excitation spectrum for ^{14}NH in the $17000\text{--}17200\text{ cm}^{-1}$ region is shown in Figure 8.4. The spectral lines are assigned by using the molecular constants for the $a^1\Delta$ and the $A^3\Pi$ states given in the literature [198, 201, 202]. The labelling of the lines is performed according to standard spectroscopic nomenclature. Using the Hund's case (a) description, the three F_i manifolds in the inverted $A^3\Pi$ state are labelled F_1 , F_2 and F_3 for $\Omega = 2$, $\Omega = 1$ and $\Omega = 0$, respectively. This gives rise to 9 branches in the $A^3\Pi_{\Omega}, J' \leftarrow a^1\Delta, J''$ transition which are denoted as $\Delta J_i(J'')$. The Q_1 , R_1 , P_2 , Q_2 and the P_3 branch of the $v = 0 \leftarrow v = 0$ band are contained in the measured frequency range. Due to the Λ -doublet splitting in both electronic states, all lines in principle appear as doublets. The Λ -doublet splitting in the $a^1\Delta$ state is very small [198], and can be neglected in this study. The splitting of the lines as observed in the spectrum therefore directly reflects the Λ -doublet splitting in the $A^3\Pi$ -state. The magnitude of this splitting strongly depends on the Ω -character in the wavefunction of the specific rotational level involved.

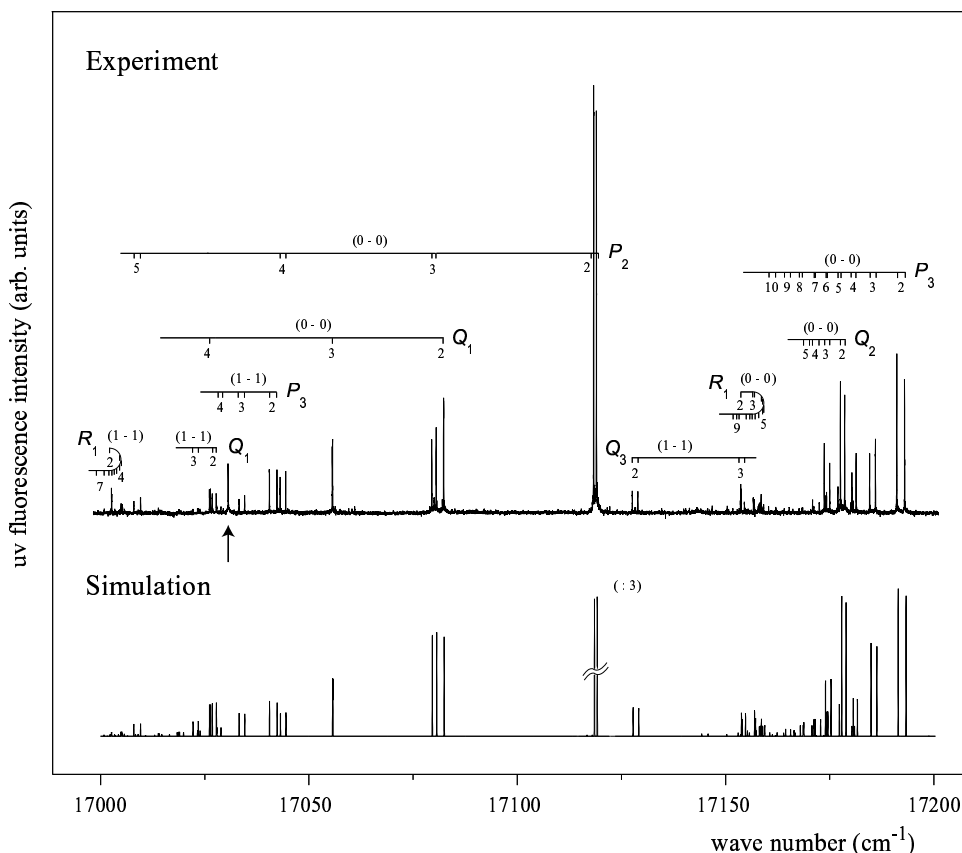


Figure 8.4: Observed $A^3\Pi, v = 0, 1 \leftarrow a^1\Delta, v = 0, 1$ excitation spectrum of ^{14}NH together with the line assignment. The simulated spectrum, based on the spin-orbit coupling between the $A^3\Pi$ and the $c^1\Pi$ states, is shown underneath. In the simulated spectrum, the intensity of the strong $P_2(2)$ line is reduced by a factor of 3. The line indicated with an arrow is due to metastable He atoms present in the beam.

The spin-forbidden transition can gain intensity from the mixing of singlet character into the $A^3\Pi$ wavefunction. The latter can in principle occur via spin-orbit mixing of the $A^3\Pi$ state with the $a^1\Delta$, $b^1\Sigma^+$, or $c^1\Pi$ state. Only the $a^1\Delta$ and the $c^1\Pi$ state can contribute to the $A^3\Pi \leftarrow a^1\Delta$ transition intensity as the $b^1\Sigma^+ \leftarrow a^1\Delta$ transition is not electric dipole allowed. Since the spin-orbit coupling only connects levels with the same Ω quantum number, the $c^1\Pi$ state and the $a^1\Delta$ state only couple to the $\Omega = 1$ and to the $\Omega = 2$ components of the wavefunctions in the $A^3\Pi$ state, respectively. From the low $a^1\Delta \rightarrow X^3\Sigma^-$ spontaneous emission rate [199] the triplet character in the $a^1\Delta$ state is known to be low, and the $A^3\Pi - a^1\Delta$ coupling can be expected to be small. Therefore, the $A^3\Pi \leftarrow a^1\Delta$ excitation spectrum is simulated by taking exclusively the $A^3\Pi - c^1\Pi$ coupling into account. This simulated spectrum is shown underneath the observed spectrum in Figure 8.4.

For the simulation of the relative intensities of the spectral lines, the degree of $\Omega = 1$ character in the wavefunction of the various rotational levels in the $A^3\Pi$ -state has to be calculated. Since the ratio of the spin-orbit coupling constant to the rotational constant in the $A^3\Pi$ -state is relatively small, this state rapidly approaches Hund's case (b) for higher rotational quantum numbers. Even for low values of J there is a large degree of Ω -mixing, and a significant fraction of $\Omega = 1$ character is present in

the wavefunction of all rotational levels. The relative intensity of a $A^3\Pi_\Omega, J', e/f \leftarrow a^1\Delta, J'', e/f$ transition is simulated by multiplying the amount of $\Omega = 1$ character in the wavefunction of the upper level with the Hönl-London factor of the corresponding dipole allowed $c^1\Pi, J' \leftarrow a^1\Delta, J''$ transition and with the population in the lower level. For the latter, the population distribution as deduced from the experiments described in section 8.3.2 is used.

As indicated in Figure 8.4, a significant population in the $v = 1$ -level of the $a^1\Delta$ -state is present. The $v = 1 \leftarrow v = 1$ band of the spin-forbidden transition is shifted some 150 cm^{-1} to the red, but several branches of this hot band appear in this same spectral region. The line observed at 17030.59 cm^{-1} (indicated with an arrow) is not reproduced in the simulated spectrum. This line appears at the same frequency in the spectra of both ^{14}NH and ^{15}NH and can be assigned to the $\text{He}(5^3D \leftarrow 2^3S)$ two-photon transition, that is expected at exactly this frequency [210]. The long-lived metastable $\text{He}(2^3S)$ atoms are produced in the discharge source, and their spectral signature serves as an additional absolute frequency marker in our spectrum.

The correspondence between the observed and simulated spectrum is excellent, confirming that the $A^3\Pi \leftarrow a^1\Delta$ transition indeed mainly gains intensity due to $A^3\Pi - c^1\Pi$ spin-orbit coupling. Within the experimental accuracy no evidence for a $A^3\Pi - a^1\Delta$ coupling is found.

The measured and calculated line positions are given in Table 8.1 for both ^{14}NH and ^{15}NH for levels up to $J'' = 4$. The rotational constants for ^{15}NH are deduced from those of ^{14}NH using the isotope scaling laws. For each isotope and for both vibrational bands the $A^3\Pi - a^1\Delta$ singlet-triplet splitting is adjusted such that the calculated frequency of the most intense line, indicated in Table 8.1, coincides with the observed line position. The overall agreement is excellent and apart from the singlet-triplet splitting for both isotopomers no adjustment of the spectroscopic constants is needed to fit the observed line positions.

As mentioned above, the measurements shown in Figure 8.4 are taken under conditions away from saturation. In order to investigate the optical pumping efficiency from the $a^1\Delta$ state to the $X^3\Sigma^-$ ground state, experiments on the $A^3\Pi \leftarrow a^1\Delta$ transition have been performed with a narrow-band pulsed laser system with a superior spectral brightness. In this laser the output of a frequency stabilized single mode ring dye laser (Spectra Physics 380) is amplified in a three stage pulsed dye amplifier (Lambda Physik LPD 3000) pumped by a frequency-doubled injection seeded Nd:YAG pump laser (Spectra Physics GCR 190-50). Up to 80 mJ of 584 nm radiation is produced in a 5 ns duration pulse, with a Fourier transform limited bandwidth of approximately 90 MHz. In view of the limited tunability of this laser system only the $A^3\Pi_1, v = 0, J = 1, e/f \leftarrow a^1\Delta, v = 0, J = 2, e/f$ transitions, the two strong components of the $P_2(2)$ doublet (see Figure 8.4), are measured. The intrinsic shape of these lines is recorded using a pulse energy of 1 mJ in a 4 mm diameter beam, avoiding saturation broadening. The measured line profiles are shown for ^{14}NH in Figure 8.5, and indicate unresolved hyperfine structure. Due to the nuclear spin of both the N and the H nucleus, the $a^1\Delta, J = 2, e/f$ and $A^3\Pi_1, J = 1, e/f$ Λ -doublet components are split into 6 (4) and 5 (4) hyperfine levels for ^{14}NH (^{15}NH), respectively. The hyperfine structure on the $A^3\Pi, v = 0 \leftarrow X^3\Sigma^-, v = 0$ transition and on the $c^1\Pi, v = 0 \leftarrow a^1\Delta, v = 0$ transition has been resolved and analyzed earlier [198, 211]. Unfortunately, there are some mistakes in the formalism used in that analysis, which complicates the interpretation of the hyperfine interaction parameters presented in

Table 8.1: Observed and simulated line positions (vacuum cm^{-1}) of the $A^3\Pi, v = 0, 1 \leftarrow a^1\Delta, v = 0, 1$ transition for ^{14}NH and ^{15}NH . The experimental error in the measured values is 0.03 cm^{-1} , unless stated otherwise. The deviation between measured and calculated values (observed – calculated) is given in parenthesis. The lines that are used to determine the $A^3\Pi - a^1\Delta$ singlet-triplet splitting are indicated.

$^1\Delta, J, e/f$	line	^{14}NH				^{15}NH			
		$v = 0 \leftarrow v = 0$		$v = 1 \leftarrow v = 1$		$v = 0 \leftarrow v = 0$		$v = 1 \leftarrow v = 1$	
2, e	$Q_1(2)$	17082.01	(0.02)			17082.31	(0.01)		
	$R_1(2)$	17153.70	(-0.01)	17002.20	(0.01)	17153.75	(0.03)	17002.68	(0.00)
	$P_2(2)$	17117.993(2)	(fi xed)			17118.315(10)	(fi xed)		
	$Q_2(2)$	17178.53	(-0.01)	17027.23	(-0.01)	17178.57	(-0.01)	17027.73	(-0.03)
	$P_3(2)$	17191.02	(0.01)	17039.98	(0.02)	17191.08	(0.02)	17040.49	(0.00)
	$Q_3(2)$			17128.81	(0.00)			17128.94	(0.02)
2, f	$Q_1(2)$	17082.01	(0.02)			17082.31	(-0.01)		
	$R_1(2)$	17153.63	(0.01)	17002.13	(0.02)	17153.63	(-0.01)	17002.59	(-0.01)
	$P_2(2)$	17118.675(10)	(0.014)			17118.987(2)	(0.006)		
	$Q_2(2)$	17177.49	(0.00)	17026.25	(-0.01)	17177.53	(0.00)	17026.76	(-0.02)
	$P_3(2)$	17192.90	(0.01)	17041.78	(fi xed)	17192.96	(0.01)	17042.31	(fi xed)
	$Q_3(2)$			17127.49	(0.03)			17127.60	(0.03)
3, e	$Q_1(3)$	17055.13	(0.00)			17055.58	(0.00)		
	$R_1(3)$	17156.87	(-0.01)	17004.62	(0.00)	17156.90	(0.00)	17005.09	(-0.03)
	$P_2(3)$	17078.99	(0.00)			17079.47	(0.00)		
	$Q_2(3)$	17174.95	(0.02)	17022.91	(0.01)	17174.97	(-0.01)	17023.42	(0.00)
	$P_3(3)$	17184.52	(0.01)	17032.70	(0.03)	17184.56	(0.00)	17033.21	(0.00)
	$Q_3(3)$			17154.52	(0.00)			17154.50	(0.00)
3, f	$Q_1(3)$	17055.21	(0.00)			17055.66	(-0.01)		
	$R_1(3)$	17156.62	(-0.02)	17004.40	(0.01)	17156.64	(-0.02)	17004.90	(0.01)
	$P_2(3)$	17080.05	(0.00)			17080.52	(0.00)		
	$Q_2(3)$	17173.59	(-0.01)	17021.67	(0.02)	17173.65	(0.01)	17022.16	(-0.01)
	$P_3(3)$	17185.91	(0.02)	17034.01	(-0.01)	17185.95	(0.00)	17034.55	(-0.01)
	$Q_3(3)$			17153.56	(0.01)			17153.53	(0.00)
4, e	$Q_1(4)$	17025.49	(-0.01)			17026.09	(-0.02)		
	$R_1(4)$	17158.46	(-0.02)	17005.19	(0.01)	17158.51	(0.01)	17005.72	(0.01)
	$P_2(4)$	17042.45	(-0.01)			17043.07	(-0.02)		
	$Q_2(4)$	17172.42	(-0.01)			17172.46	(-0.02)		
	$P_3(4)$	17180.25	(0.01)	17027.34	(-0.01)	17180.31	(0.01)	17027.88	(-0.01)
	$Q_3(4)$			17180.76	(0.01)			17180.02	(0.03)
4, f	$Q_1(4)$	17025.72	(-0.02)			17026.34	(-0.01)		
	$R_1(4)$	17157.98	(-0.02)	17004.77	(0.02)	17158.02	(0.00)	17005.27	(0.01)
	$P_2(4)$	17043.79	(0.00)			17044.41	(-0.02)		
	$Q_2(4)$	17170.80	(-0.01)			17170.86	(0.00)		
	$P_3(4)$	17181.22	(-0.01)	17028.31	(-0.01)	17181.30	(0.01)	17028.85	(-0.01)
	$Q_3(4)$			17180.16	(0.02)			17180.02	(0.03)

that work *. We therefore re-analyzed the original data of Ubachs *et al.* [198, 211] from which we

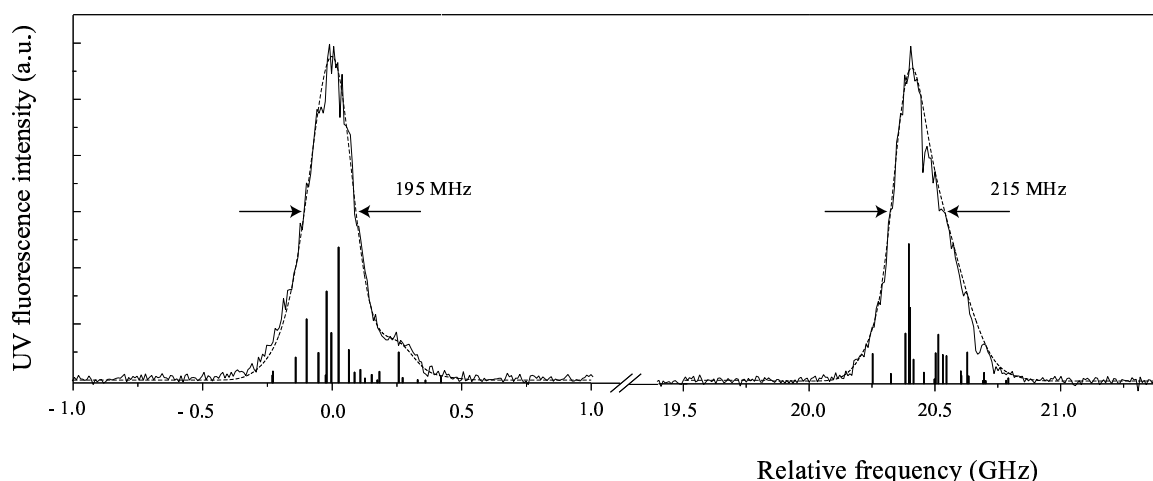
*The given matrix elements contain no errors, but are inconsistent with the given energies of the hyperfine levels.

Table 8.2: Hyperfine parameters of the NH radical in the vibrational ground state for different electronic states (in MHz).

Parameter	$X^3\Sigma^-$	$A^3\Pi$	$a^1\Delta$	$c^1\Pi$
a_N	-	93.4	109.8	105.8
b_N	19.7	157.5	-	-
c_N	-66.0	11.3	-	-
d_N	-	-66.2	-	-
eQq_1	-4.1	5.3	-6.2	11.1
eQq_2	-	-10.8	-	-13.3
a_H	-	68.9	69.9	59.7
b_H	-66.0	303.4	-	-
c_H	91.3	97.4	-	-
d_H	-	-26.2	-	-

calculated the expected hyperfine structure on the $P_2(2)$ line of the spin-forbidden transition. The hyperfine parameters for the $X^3\Sigma^-$, the $A^3\Pi$, the $a^1\Delta$ and the $c^1\Pi$ states that were obtained from this re-analysis are given in Table 8.2. Unfortunately, the original experimental spectrum was not available anymore, and only the published transition frequencies were used in the re-analysis. The hyperfine parameters in Table 8.2 are therefore given without error bars. The transitions between the various hyperfine levels are indicated in Figure 8.5 as a stick spectrum. The dashed curve is a convolution of the calculated spectrum with the spectral profile of the laser; for the latter a Gaussian distribution with a full width at half maximum of 90 MHz is assumed. There is an excellent match between the observed and expected line profiles. Equally good agreement is obtained for ^{15}NH (data not shown), when the re-analyzed hyperfine constants for ^{14}NH are isotopically scaled to ^{15}NH .

The absolute line frequencies for the two components of the $P_2(2)$ line as determined in these high

**Figure 8.5:** The $A^3\Pi \leftarrow a^1\Delta, P_2(2)$ transitions for ^{14}NH , measured with a 90 MHz bandwidth pulsed dye laser system. The calculated transitions between the various hyperfine levels are given as a stick spectrum. The dashed curve is the convolution of the stick spectrum with the spectral profile of the laser.

resolution measurements, calibrated against the simultaneously measured iodine absorption spectrum,

are incorporated in Table 8.1. The tabulated experimental errors are deduced from the accuracy of the frequencies and the number of the individual iodine lines [208] that are used as frequency markers. The frequency of the $P_2(2)$ component that is most accurately measured in our experiments can be used to accurately determine the singlet-triplet splitting in NH. Together with the absolute frequencies of transitions in the $A^3\Pi, v = 0 \leftarrow X^3\Sigma^-, v = 0$ band [201], this yields a splitting between the lowest ro-vibrational level in the $X^3\Sigma^-$ state and the lowest ro-vibrational level in the $a^1\Delta$ state for ^{14}NH of $12688.622 \pm 0.004 \text{ cm}^{-1}$. From a direct measurement of the $a^1\Delta, v = 0, J = 2 \rightarrow X^3\Sigma^-, v = 0, N = 0, J = 1$ transition, this singlet-triplet splitting has previously been reported to be $12687.8 \pm 0.1 \text{ cm}^{-1}$ [199]. The inaccurate frequency calibration method used in those experiments probably explains the discrepancy with the value determined in our measurements.

8.3.4 The strength of the $A^3\Pi \leftarrow a^1\Delta$ transition

By increasing the pulse energy of the narrow-band pulsed dye laser system, the $P_2(2)$ line of the spin-forbidden transition can be saturated; with 10 mJ in a 4 mm diameter beam saturation effects are already observed. This leads to an order of magnitude estimate for the peak absorption cross-section for this transition of 10^{-18} cm^2 , corresponding to a value of the Einstein A -coefficient of order unity, and a transition dipole moment of about 5×10^{-4} atomic units. The transition dipole moment for the $A^3\Pi \leftarrow a^1\Delta$ transition can also be calculated, taking exclusively the $^1\Pi - ^3\Pi$ coupling into account. The description of this coupling for the $A^3\Pi \leftarrow a^1\Delta$ transition in NH is similar to the description of the $a^3\Pi \leftarrow X^1\Sigma^+$ transition in CO, for which James calculated the $^1\Pi - ^3\Pi$ mixing to experimental accuracy. In analogy to this analysis [212], the transition moment $\mu_{0,0}$ of the $A^3\Pi(v' = 0) \leftarrow a^1\Delta(v = 0)$ transition in NH is given by

$$\begin{aligned} \mu_{0,0} = & \sum_{v'''} \frac{\langle A^3\Pi, v' = 0 | \mathcal{H} | c^1\Pi, v'''\rangle}{E(A^3\Pi, v' = 0) - E(c^1\Pi, v''')} \\ & \times \langle c^1\Pi, v'''\rangle \mu(r) | a^1\Delta, v = 0 \rangle \end{aligned} \quad (8.1)$$

where \mathcal{H} represents the spin-orbit interaction, and $\mu(r)$ the transition dipole moment function for the $c^1\Pi \leftarrow a^1\Delta$ electric dipole allowed transition. The sum extends over all vibrational levels v''' in the $c^1\Pi$ state, but is dominated by the contribution from the $v''' = 0$ level. Using the potential energy functions and $\mu(r)$ from literature [205, 213], we obtain $\mu_{0,0} \geq 4.4 \cdot 10^{-4}$ atomic units (a.u.). The rotational transition probability to a $(J', e/f)$ level in one of the $A^3\Pi_{\Omega'}$ manifolds is calculated by multiplying $\mu_{0,0}$ by the amount of $\Omega' = 1$ character in the particular manifold and by the appropriate Hönl-London factor for the $c^1\Pi(J', e/f) \leftarrow a^1\Delta(J = 2, f)$ transition. For the $P_2(2)$ transition a transition dipole moment of $\geq 4 \times 10^{-4}$ atomic units is obtained, in good agreement with the experimental findings.

In the accumulation scheme discussed earlier, the $A^3\Pi \leftarrow a^1\Delta$ transition needs to be induced in the presence of a magnetic field. Due to the Zeeman effect in both the $a^1\Delta$ and $A^3\Pi$ states, the M -resolved transition probability needs to be taken into account. In particular, a transition from the $(J = 2, M = 2, f)$ level in the $a^1\Delta$ state to either the $(J' = 2, M' = 2, e)$ level in the $A^3\Pi_2$ manifold ($Q_1(2)$ line) or the $(J' = 1, M' = 1, f)$ level in the $A^3\Pi_1$ manifold ($P_2(2)$ line) is of interest. After the spontaneous decay process, 62% (when the $Q_1(2)$ transition is used) or 32% ($P_2(2)$) of the excited molecules reside in the $X^3\Sigma^-(v'' = 0, N'' = 0, J'' = 1, M'' = 1)$ rotational ground state. The

transition moments for these transitions are $\mu \geq 0.16 \cdot 10^{-4}$ a.u. and $\mu \geq 2.0 \cdot 10^{-4}$ a.u., respectively. In the discussion presented here, the hyperfine structure is neglected, and the transfer efficiencies are therefore the sum over all contributing hyperfine sub-levels.

Considering the relatively high power that is needed for the pump laser, it is remarked that no (dissociative) resonances are expected at the two-photon level, both for molecules residing in the $a^1\Delta(v=0)$ state [213] and for ground state molecules being already confined inside the trap. Also, problems related to rescattering of spontaneously emitted photons, observed in optically dense atomic clouds and providing a mechanism for loss and heating, are not likely to occur in dense clouds of NH, as the electronic transition strength is much weaker than transitions typically used to cool and trap alkali atoms. In the accumulation scheme, the NH radicals are optically pumped to their electronic ground state at a point where the molecules have come to a near standstill. The strength of the spin-forbidden transition in NH suggests that in this case it will even be possible to achieve efficient optical pumping from the metastable state to the electronic ground state using a cw laser system. This allows optical pumping from selected hyperfine levels, and enables the production of trapped molecules that occupy only a limited, and well-defined, number of hyperfine levels.

The $A^3\Pi \leftarrow a^1\Delta$ transition characterized here allows the complete background free detection of metastable NH radicals; although the use of a spin-forbidden transition for LIF detection of molecules is unconventional, it might actually be the most sensitive method to detect metastable NH radicals.

8.4 A slow pulsed molecular beam of NH ($a^1\Delta$) radicals

For the application of NH in Stark deceleration experiments, an intense pulsed beam of metastable NH radicals, with a low initial velocity, is required. Although many cell experiments with NH ($a^1\Delta$), using a variety of production schemes, have been carried out, only a few studies have been performed with metastable NH in a pulsed [214–217] or continuous [211, 218] molecular beam. In most of these experiments the NH radicals are produced by photo-dissociation of a precursor, or in an electrical discharge. Photodissociation of gaseous HN_3 at 266 nm has been used by many groups to produce NH ($a^1\Delta$) in a cell. In this system, the NH radicals are almost exclusively produced in the $a^1\Delta$ state, since the $\text{NH}(X^3\Sigma^-) + \text{N}_2$ channel is a spin forbidden process [219–221]. However, the low absorption cross section of approximately $7 \cdot 10^{-20}$ cm² of HN_3 at this wavelength [222, 223] requires high laser powers to efficiently produce NH ($a^1\Delta$). The absorption cross section is about 40 times higher when 193 nm UV pulses are used, but a significant population of the NH radicals is produced in the ground $X^3\Sigma^-$ state, by both one [200] and two photon [223] processes. Photodissociation of HNCN at 193 nm is known to yield NH ($a^1\Delta$) radicals with a high quantum yield as well [224, 225]. The higher absorption cross section of approximately $5 \cdot 10^{-18}$ cm² [226] for this system is more favorable. Alternatively, NH ($a^1\Delta$) can be produced by photolysis of NH_3 [227], or from ground state NH by inducing the forbidden $a^1\Delta \leftarrow X^3\Sigma^-$ transition around 790 nm [199].

In order to reduce the initial velocity of the molecular beam, either Argon, Krypton or Xenon needs to be co-expanded from the pulsed valve as a heavy inert carrier gas. Unfortunately, Xe is known to efficiently quench NH ($a^1\Delta$) radicals [228–230]. The mechanism that causes the fast quenching rate for Xe is at present unknown [218, 231]. The quenching rate for Kr is about three orders of magnitude smaller [232], sufficiently low to enable the use of Kr as a carrier gas in a pulsed

molecular beam. We here describe the successful production of an intense molecular beam of NH ($a^1\Delta$) radicals that is suited to be used in Stark deceleration experiments.

The experiments are performed in the molecular beam machine described in section 8.3.1. The NH ($a^1\Delta$) radical beam is produced by photo-dissociation of HN_3 by focussing the 80 mJ output of a Nd:YAG laser at 266 nm just in front of the nozzle orifice. No quartz capillary was used in these experiments. The HN_3 gas is produced on line by heating hydrazoic azide in excess of stearic acid to 95 °C and is co-expanded with Kr into vacuum through a pulsed supersonic valve (Jordan Inc.). As mentioned above, the formation of NH radicals in the electronic ground state $X^3\Sigma^-$ is spin-forbidden, and the radicals are exclusively produced in the metastable $a^1\Delta$ state. The population in the $a^1\Delta$ and the $X^3\Sigma^-$ states is detected 24 cm from the nozzle by inducing the $c^1\Pi, v = 0 \leftarrow a^1\Delta, v = 0$ transition around 326 nm and the $A^3\Pi, v = 0 \leftarrow X^3\Sigma^-, v = 0$ transition around 336 nm, respectively. The spectrum that is obtained is shown in Figure 8.6. The observed lines are labelled

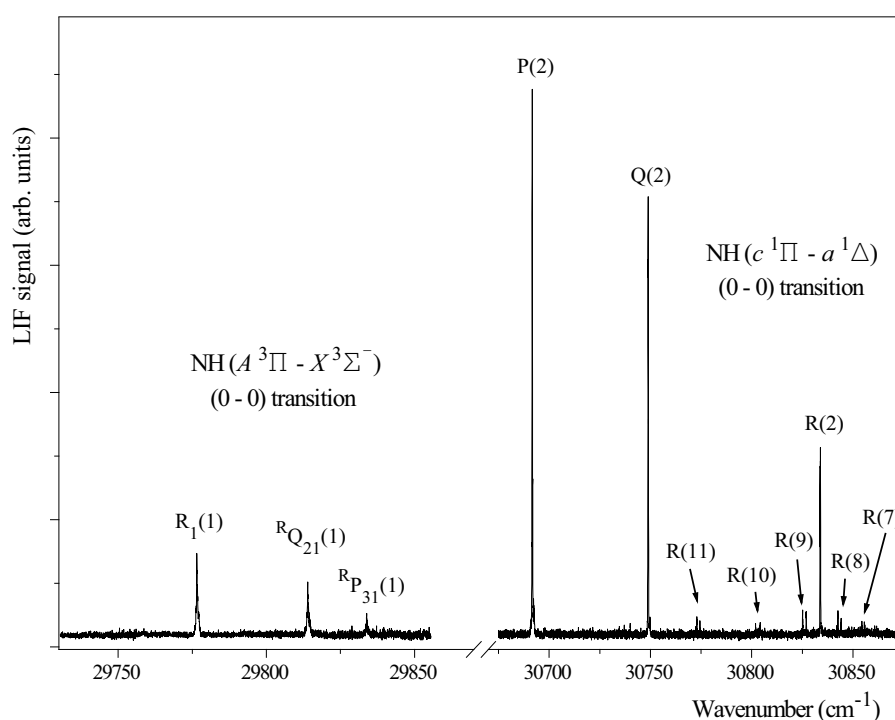


Figure 8.6: Laser fluorescence excitation spectrum of the $A^3\Pi, v = 0 \leftarrow X^3\Sigma^-, v = 0$ and the $c^1\Pi, v = 0 \leftarrow a^1\Delta, v = 0$ band for the molecular beam of NH. The lines are labelled using standard spectroscopic nomenclature.

using standard spectroscopic nomenclature. The majority of the NH radicals in the beam resides in the metastable $a^1\Delta$ electronic state. The small fraction of the population that is in the electronic ground state is believed to originate from electronic quenching of NH ($a^1\Delta$) by collisions with Kr, or by two-photon processes in the dissociation. In the $a^1\Delta$ state, the rotational level $J = 2$ is mostly populated, reflecting the efficient rotational cooling in the expansion region of the supersonic jet. A secondary maximum around $J = 9$ is found. A similar bimodal distribution has been observed before in a supersonic beam, if the NH ($a^1\Delta$) radicals were produced by photo-dissociation of HN_3 at 193 nm, using N_2 as a carrier gas [215]. The secondary maximum reflects the nascent rotational distribution of NH ($a^1\Delta$) upon photo-dissociation of HN_3 , and the low inelastic scattering cross sections for high

values of J .

The velocity distribution of the molecular beam critically depends on the time the dissociation laser is fired in the gas pulse that is emitted from the supersonic valve. This time, with respect to the trigger pulse that is applied to the valve, is indicated by T_{diss} . In Fig. 8.7, the TOF profiles of the beam of NH ($a^1\Delta$) are shown that are observed for different values of T_{diss} . The population in the $J = 2$ level is measured by inducing the $P_2(2)$ line of the $c^1\Pi \leftarrow a^1\Delta$ transition. The valve opens some 0.21 ms after the trigger pulse is applied. For low values of T_{diss} , the beam typically has a high mean velocity (>600 m/s), and a relatively large velocity spread. The beam velocity is much larger than can be expected for a room temperature expansion of Kr atoms. This reflects the 70°C temperature of the valve body during operation, and the high temperature of the gold hairpins of the valve opening mechanism, that support a peak current exceeding 4.0 kA when the valve opens. When the dissociation laser is fired 0.23 ms after the valve trigger pulse, the beam has a maximal peak intensity. The beam has a mean velocity of 575 m/s and a velocity spread (FWHM) of only 9%. For higher values of T_{diss} , the beam has a lower mean velocity and the inferior expansion conditions result in a lower peak intensity and a larger velocity spread. The decreasing beam velocity over the temporal profile of the gas pulse, is probably due to cooling of the nozzle by the gas that flows in between the hairpins.

Although difficult to quantify, the maximum peak intensity that has been reached with the current production scheme is about four times less than the typical peak intensity of the beam of OH radicals that is used in the experiments that are described in the previous chapters. Further optimization of the production scheme, or the use of a different dissociation laser or precursor molecule, may result in a higher beam intensity.

8.5 Deceleration of a molecular beam of NH ($a^1\Delta$) radicals

In this section, a preliminary experiment is discussed where a beam of NH ($a^1\Delta$, $J = 2$) radicals, described in section 8.4, is decelerated. The experiments are performed in the new generation molecular beam deceleration machine described in section 3.3 of chapter 3. The NH ($a^1\Delta$) radicals exiting the decelerator are state-selectively detected in the LIF detection zone. For this, the $P_2(2)$ line of the spin-forbidden $A^3\Pi, v = 0 \leftarrow a^1\Delta, v = 0$ transition around 584 nm is induced. The $A^3\Pi, v = 0 \rightarrow X^3\Sigma^-, v = 0$ fluorescence around 336 nm is imaged onto the photomultiplier (PMT). The transition is induced by the fundamental output of a pulsed dye laser system (Spectra physics, PDL3). Typically, an energy of 30 mJ in a 4 mm beam and a 5 ns pulse with a bandwidth of 0.04 cm^{-1} is used. This is not sufficient to saturate the transition. However, the detection of the NH radicals in this way is almost background-free as straylight from the laser is completely blocked by the optical filter in front of the PMT.

The decelerator is operated with a voltage difference of 40 kV between the electrodes in an electric field stage. For the first 102 stages of the decelerator, a time-sequence using a phase angle of 70° for a synchronous molecule with an initial velocity of 550 m/s ($E_{kin} = 190 \text{ cm}^{-1}$) is used. With these settings, the decelerator extracts about 1.2 cm^{-1} of kinetic energy from the synchronous molecule in every deceleration stage. NH radicals in the $M_J\Omega = -4$ component of the $a^1\Delta$, $J = 2$ state are decelerated to a final velocity of 330 m/s ($E_{kin} = 68 \text{ cm}^{-1}$). The decelerated molecules are guided to the detection area by operating the last 6 stages of the decelerator at a phase angle $\phi_0 = 0^\circ$, using a voltage difference of 24 kV between the electrodes. In Fig. 8.8 the time-of-flight (TOF) profile of

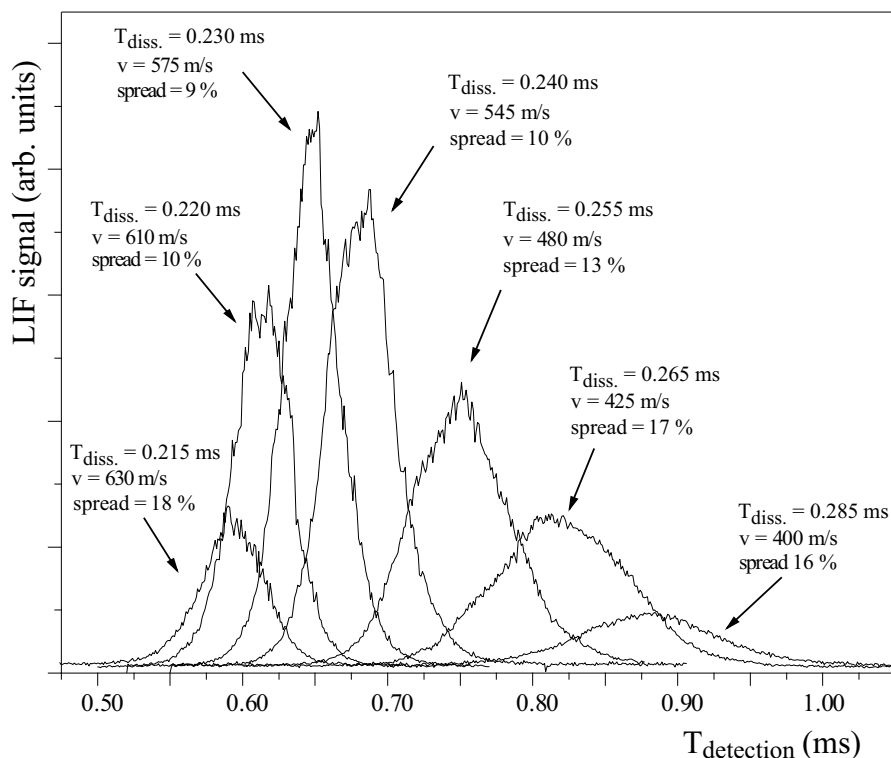


Figure 8.7: TOF profiles of the molecular beam of $NH(a^1\Delta, J = 2)$ radicals for different values of the timing T_{diss} of the dissociation laser with respect to the trigger pulse of the valve. For each profile, the mean velocity and velocity distribution of the beam is indicated.

the decelerated molecules is shown. The decelerated bunch of molecules arrives about 2.92 ms after production in the detection region. The arrival time distribution that results from a three dimensional trajectory simulation of the experiment is shown underneath the experimental data. The arrival time of the package of molecules is accurately reproduced by the simulations. The width of the distribution in the simulated TOF profile, however, is larger than in the experimental profile. This is probably the result of the spatial intensity distribution of the detection laser beam, that is assumed to be flat-topped in the calculations.

The poor signal-to-noise ratio of the preliminary experiment presented in Fig. 8.8 compared to the experiments that are presented in section 8.4, reflects the low beam intensity that was present when the molecular beam deceleration experiment was performed. In addition, the signal-to-noise ratio can be improved when a laser system with a superior optical brightness is used.

8.6 Conclusions

In this chapter a scheme is proposed to reload a magnetic trap with NH radicals in order to increase the phase-space density. After Stark deceleration in their metastable $a^1\Delta$ state, the NH radicals can be optically pumped via the spin-forbidden $A^3\Pi \leftarrow a^1\Delta$ transition to the $X^3\Sigma^-$ electronic ground state. Here, the radicals can be magnetically trapped. The laser-driven spontaneous decay process effectively switches off the electric-field interaction of the molecules enabling the accumulation of

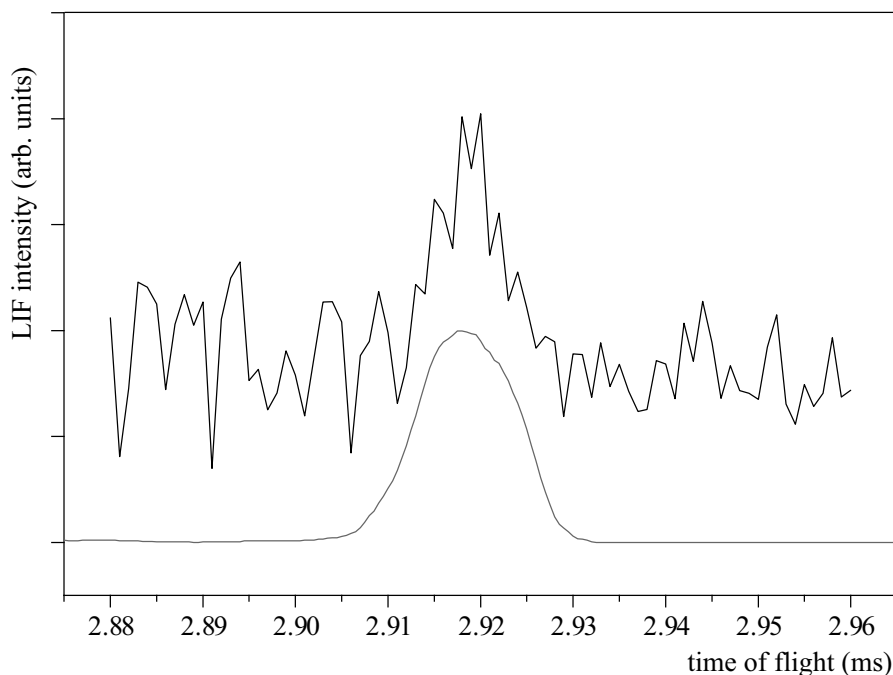


Figure 8.8: Observed TOF profile of decelerated NH ($a^1\Delta$, $J = 2$) radicals exiting the decelerator (upper curve). The package of molecules is decelerated from 550 m/s to 330 m/s. The TOF profile that results from a numerical simulation of the experiment is shown underneath the experimental profile.

several packages of molecules in the magnetic trap, and automatically fulfills the requirement of a unidirectional pathway to the ground state. The hitherto unobserved spin-forbidden $A^3\Pi \leftarrow a^1\Delta$ transition is found and characterized. The expected mechanism via which this transition gains intensity is verified, and the absolute transition probability is estimated from the experimental data. An intense slow pulsed molecular beam of metastable NH radicals, another prerequisite for the proposed accumulation scheme, is produced using Kr as a carrier gas. In a preliminary molecular beam deceleration experiment, part of this beam is decelerated from 550 m/s to 330 m/s, demonstrating the possibility of Stark deceleration (and ultimately the possibility of electrostatic trapping) of a beam of NH ($a^1\Delta$) radicals.

SUMMARY AND OUTLOOK

In this thesis a new generation Stark decelerator is described that is designed to capture and slow down a large fraction of a molecular beam pulse. Deceleration experiments are performed using a beam of OH radicals, a chemically highly relevant species. The Stark decelerator is extended with an electrostatic trap in which the selected part of the molecular beam can be brought to standstill, and stored up to seconds. The long interaction time afforded by the trap is exploited to directly measure the infrared radiative lifetime of the first vibrationally excited state of OH, that benchmarks the Einstein A -coefficients in the important Meinel system of OH.

The new generation Stark decelerator also allowed a detailed study of the phase-space evolution of a molecular beam in the decelerator. The large acceptance of the decelerator combined with a well characterized molecular beam result in time-of-flight profiles of molecules exiting the decelerator that contain previously unobserved features. Together with extensive numerical simulations of the trajectories of the molecules in the decelerator, these features reveal the complex 6 dimensional phase-space dynamics of the beam. These studies contribute significantly to the understanding of longitudinal phase stability in a Stark decelerator. The transverse focussing properties of a Stark decelerator, and the influence of the transverse motion of the molecules on longitudinal phase stability is studied in detail. The improved understanding of the molecular motion inside a Stark decelerator will, beyond doubt, contribute to the efficiency of future decelerators.

The produced cold packages of OH radicals are ideally suited to study cold (reactive) collisions between the trapped polar molecules, which is a very new and exciting field of physics. The density of $10^7 - 10^8$ OH radicals cm^{-3} that we have reached thus far, however, is not sufficient to observe these collisions in the trap. By improving the deceleration and trap-loading process, it is expected that about an order of magnitude can still be gained in density. If a more intense molecular beam can be produced, the density could be enhanced even further. Using state-of-the-art molecular beam techniques, densities exceeding 10^{10} molecules cm^{-3} should therefore be realistic. Once these densities are obtained, methods like evaporative cooling or sympathetic cooling could be applied to cool the trapped sample further down, and hence increase the phase-space density in the trap. These methods have not been demonstrated to work for molecules yet, and rely on the (presently unknown) elastic and inelastic collision cross sections. Another approach to increase the phase-space density in the trap is to accumulate several packages of molecules in the trap. In this thesis a novel scheme is presented that allows this trap re-loading for the NH radical. All prerequisites for the accumulation scheme have been experimentally demonstrated. Most notably, a beam of NH radicals in the metastable $a^1\Delta$ state has been produced, decelerated from 550 m/s to 330 m/s, and optically pumped to the $X^3\Sigma^-$ ground state.

Bibliography

- [1] G. Scoles, ed., *Atomic and molecular beam methods*, vol. 1 & 2 (Oxford University Press, New York, 1988 & 1992).
- [2] H. Stapelfeldt and T. Seideman, *Rev. Mod. Phys.* **75**, 543 (2003).
- [3] X. Yang and K. Liu, eds., *Modern Trends in Chemical Reaction Dynamics*, vol. 1 (World Scientific, Singapore, 2004).
- [4] H. Sato, *Chem. Rev.* **101**, 2687 (2001).
- [5] T. Rakitzis, A. van den Brom, and M. Janssen, *Science* **303**, 1852 (2004).
- [6] K. Liu, *Ann. Rev. Phys. Chem.* **52**, 139 (2001).
- [7] J. J. Lin, J. Zhou, W. Shiu, and K. Liu, *Science* **300**, 966 (2003).
- [8] H. L. Bethlem, G. Berden, and G. Meijer, *Phys. Rev. Lett.* **83**, 1558 (1999).
- [9] H. L. Bethlem, A. J. A. van Roij, R. T. Jongma, and G. Meijer, *Phys. Rev. Lett.* **88**, 133003 (2002).
- [10] F. M. H. Crompvoets, R. T. Jongma, H. L. Bethlem, A. J. A. van Roij, and G. Meijer, *Phys. Rev. Lett.* **89**, 093004 (2002).
- [11] H. L. Bethlem, G. Berden, F. M. H. Crompvoets, R. T. Jongma, A. J. A. van Roij, and G. Meijer, *Nature* **406**, 491 (2000).
- [12] J. van Veldhoven, H. L. Bethlem, and G. Meijer, *Phys. Rev. Lett.* **94**, 083001 (2005).
- [13] F. M. H. Crompvoets, H. L. Bethlem, R. T. Jongma, and G. Meijer, *Nature* **411**, 174 (2001).
- [14] H. L. Bethlem, F. M. H. Crompvoets, R. T. Jongma, S. Y. T. van de Meerakker, and G. Meijer, *Phys. Rev. A* **65**, 053416 (2002).
- [15] H. L. Bethlem and G. Meijer, *Int. Rev. Phys. Chem.* **22**, 73 (2003).
- [16] Special Issue on *Ultracold polar molecules*, *Eur. Phys. J. D* **31(2)** (2004).
- [17] R. Krems, *Int. Rev. Phys. Chem.* **24**, 99 (2005).
- [18] L. R. Hunter, *Science* **252**, 73 (1991).

- [19] J. J. Hudson, B. E. Sauer, M. R. Tarbutt, and E. A. Hinds, *Phys. Rev. Lett.* **89**, 023003 (2002).
- [20] D. Kawall, F. Bay, S. Bickman, Y. Jiang, and D. DeMille, *Phys. Rev. Lett.* **92**, 133007 (2004).
- [21] D. W. Rein, *J. Mol. Evol.* **4**, 15 (1974).
- [22] V. S. Letokhov, *Phys. Lett.* **53A**, 275 (1975).
- [23] J.-P. Uzan, *Rev. Mod. Phys.* **75**, 403 (2003).
- [24] S. Y. T. van de Meerakker, N. Vanhaecke, M. van der Loo, G. Groenenboom, and G. Meijer, *Phys. Rev. Lett.* **95**, 013003 (2005).
- [25] P. O. Wennberg *et al.*, *Science* **266**, 398 (1994).
- [26] M. E. Summers, R. R. Conway, D. E. Siskind, M. H. Stevens, D. Offermann, M. Riese, P. Preusse, D. F. Strobel, and J. M. Russell III, *Science* **277**, 1967 (1997).
- [27] P.O. Wennberg *et al.*, *Science* **279**, 49 (1998).
- [28] W. J. Wilson and A. H. Barrett, *Science* **161**, 778 (1968).
- [29] S. Chu, *Rev. Mod. Phys.* **70**, 685 (1998).
- [30] C. N. Cohen-Tannoudji, *Rev. Mod. Phys.* **70**, 707 (1998).
- [31] W. D. Phillips, *Rev. Mod. Phys.* **70**, 721 (1998).
- [32] M. H. Anderson, J. R. Ensher, M. R. Matthews, C. E. Wieman, and E. A. Cornell, *Science* **269**, 198 (1995).
- [33] M. Baranov, L. Dobrek, K. Goral, L. Santos, and M. Lewenstein, *Phys. Scr.* **T102**, 74 (2002).
- [34] L. Santos, G. V. Shlyapnikov, P. Zoller, and M. Lewenstein, *Phys. Rev. Lett.* **85**, 1791 (2000).
- [35] K. Goral, L. Santos, and M. Lewenstein, *Phys. Rev. Lett.* **88**, 170406 (2002).
- [36] D. DeMille, *Phys. Rev. Lett.* **88**, 067901 (2002).
- [37] D. Herschbach, *Rev. Mod. Phys.* **71**, S411 (1999).
- [38] N. Balakrishnan and A. Dalgarno, *Chem. Phys. Lett.* **341**, 652 (2001).
- [39] N. Balakrishnan, A. Dalgarno, and R. C. Forrey, *J. Chem. Phys.* **113**, 621 (2000).
- [40] J. M. Doyle, B. Friedrich, J. Kim, and D. Patterson, *Phys. Rev. A* **52**, R2515 (1995).
- [41] B. Friedrich, R. deCarvalho, J. Kim, D. Patterson, J. D. Weinstein, and J. M. Doyle, *J. Chem. Soc., Faraday. Trans.* **94**, 1783 (1998).
- [42] J. D. Weinstein, R. deCarvalho, T. Guillet, B. Friedrich, and J. M. Doyle, *Nature* **395**, 148 (1998).

- [43] G. Groenenboom, *private communications*.
- [44] D. Egorov, T. Lahaye, W. Schöllkopf, B. Friedrich, and J. M. Doyle, *Physical Review A* **66**, 043401 (2002).
- [45] D. Egorov, W. C. Campbell, B. Friedrich, S. Maxwell, E. Tsikata, L. D. van Buuren, and J. Doyle, *Eur. Phys. J. D* **31**, 307 (2004).
- [46] T. Takekoshi, B. M. Patterson, and R. J. Knize, *Phys. Rev. Lett.* **81**, 5105 (1998).
- [47] N. Vanhaecke, W. de Souza Melo, B. L. Tolra, D. Comparat, and P. Pillet, *Phys. Rev. Lett.* **89**, 063001 (2002).
- [48] A. J. Kerman, J. M. Sage, S. Sainis, T. Bergeman, and D. DeMille, *Phys. Rev. Lett.* **92**, 033004 (2004).
- [49] A. J. Kerman, J. M. Sage, S. Sainis, T. Bergeman, and D. DeMille, *Phys. Rev. Lett.* **92**, 153001 (2004).
- [50] C. Heimberger, J. Kleinert, M. Bhattacharya, and N. P. Bigelow, *Phys. Rev. A* **70**, 021402 (2004).
- [51] M. W. Mancini, G. D. Telles, A. R. L. Caires, V. S. Bagnato, and L. G. Marcassa, *Phys. Rev. Lett.* **92**, 133203 (2004).
- [52] D. Wang *et al.*, *Eur. Phys. J. D* **31**, 165 (2004).
- [53] J. M. Sage, S. Sainis, T. Bergeman, and D. DeMille, *Phys. Rev. Lett.* **94**, 203001 (2005).
- [54] M. Greiner, C. A. Regal, and D. S. Jin, *Nature* **426**, 537 (2003).
- [55] S. Jochim, M. Bartenstein, A. Altmeyer, G. Hendl, S. Riedl, C. Chin, J. Hecker-Denschlag, and R. Grimm, *Science* **302**, 2101 (2003).
- [56] M. W. Zwierlein, C. A. Stan, C. H. Schunck, S. M. F. Raupach, S. Gupta, Z. Hadzibabic, and W. Ketterle, *Phys. Rev. Lett.* **91**, 250401 (2003).
- [57] T. Bourdel, L. Khaykovich, J. Cubizolles, J. Zhang, F. Chevy, M. Teichmann, L. Tarruell, S. J. J. M. F. Kokkelmans, and C. Salomon, *Phys. Rev. Lett.* **93**, 050401 (2004).
- [58] C. A. Stan, M. W. Zwierlein, C. H. Schunck, S. M. F. Raupach, and W. Ketterle, *Phys. Rev. Lett.* **93**, 143001 (2004).
- [59] S. Inouye, J. Goldwin, M. L. Olsen, C. Ticknor, J. L. Bohn, and D. S. Jin, *Phys. Rev. Lett.* **93**, 183201 (2004).
- [60] M. S. Elioff, J. J. Valentini, and D. W. Chandler, *Science* **302**, 1940 (2003).
- [61] M. Gupta and D. Herschbach, *J. Phys. Chem. A* **103**, 10670 (1999).

- [62] S. A. Rangwala, T. Junglen, T. Rieger, P. W. H. Pinkse, and G. Rempe, *Phys. Rev. A* **67**, 043406 (2003).
- [63] T. Junglen, T. Rieger, P. W. H. Pinkse, and G. Rempe, *Phys. Rev. Lett.* **92**, 223001 (2004).
- [64] J. G. King, Proceedings of the 13th Annual Symposium on Frequency Control, Ashbury Park. U.S. Army Signal Research and Development Laboratory p. 603 (1959).
- [65] J. G. King and J. R. Zacharias, Quarterly Progress Report, Research Laboratory of Electronics, MIT 48, Jan. 15 (1958).
- [66] A. N. Oraevskii, Nauka, Moscow (1964).
- [67] V. S. Kazachok, *Sov. Phys. Tech. Phys.* **10**, 882 (1965).
- [68] R. Golub, Ph.D. thesis, Massachusetts Institute of Technology (1967).
- [69] D. Auerbach, E. E. A. Bromberg, and L. Wharton, *J. Chem. Phys.* **45**, 2160 (1966).
- [70] R. Wolfgang, *Sci. Am.* **219**, 44 (1968).
- [71] E. E. A. Bromberg, Ph.D. thesis, University of Chicago (1972).
- [72] H. L. Bethlem, G. Berden, A. J. A. van Roij, F. M. H. Crompvoets, and G. Meijer, *Phys. Rev. Lett.* **84**, 5744 (2000).
- [73] F. M. H. Crompvoets, H. L. Bethlem, J. Küpper, A. J. A. van Roij, and G. Meijer, *Phys. Rev. A* **69**, 063406 (2004).
- [74] J. van Veldhoven, J. Küpper, H. L. Bethlem, B. Sartakov, A. J. A. van Roij, and G. Meijer, *Eur. Phys. J. D* **31**, 337 (2004).
- [75] J. L. Bohn, *Phys. Rev. A* **63**, 052714 (2001).
- [76] S. A. Schulz, H. L. Bethlem, J. van Veldhoven, J. Küpper, H. Conrad, and G. Meijer, *Phys. Rev. Lett.* **93**, 020406 (2004).
- [77] M. R. Tarbutt, H. L. Bethlem, J. J. Hudson, V. L. Ryabov, V. A. Ryzhov, B. E. Sauer, G. Meijer, and E. A. Hinds, *Phys. Rev. Lett.* **92**, 173002 (2004).
- [78] J. R. Bochinski, E. R. Hudson, H. J. Lewandowski, G. Meijer, and J. Ye, *Phys. Rev. Lett.* **91**, 243001 (2003).
- [79] J. R. Bochinski, E. R. Hudson, H. J. Lewandowski, and J. Ye, *Phys. Rev. A* **70**, 043410 (2004).
- [80] C. Lisdat, *private communications* (2004).
- [81] Y. Yamakita, S. R. Procter, A. L. Goodgame, and T. P. Softley, *J. Chem. Phys.* **121**, 1419 (2004).
- [82] E. Vliegen, H. J. Wörner, T. P. Softley, and F. Merkt, *Phys. Rev. Lett.* **92**, 033005 (2004).

- [83] N. Vanhaecke, D. Comparat, and P. Pillet, *J. Phys. B: At. Mol. opt. Phys.* **38**, 409 (2005).
- [84] The work of J.R. Zacharias has never been published, but knowledge of the Zacharias fountain has been passed down in the oral tradition.
- [85] G. J. Dong, W. P. Lu, and P. F. Barker, *Phys. Rev. A* **69**, 013409 (2004).
- [86] P. F. Barker and M. N. Shneider, *Phys. Rev. A* **66**, 065402 (2002).
- [87] R. Fulton, A. I. Bishop, and P. F. Barker, *Phys. Rev. Lett.* **93**, 243004 (2004).
- [88] S. Y. T. van de Meerakker, P. H. M. Smeets, N. Vanhaecke, and G. Meijer, *Phys. Rev. Lett.* **94**, 23004 (2005).
- [89] M. Wardle and F. Yusef-Zadeh, *Science* **296**, 2350 (2002).
- [90] J. A. Miller and R. J. Kee, *Annu. Rev. Phys. Chem.* **41**, 345 (1990).
- [91] J. C. Whitehead, *Rep. Prog. Phys.* **59**, 993 (1996).
- [92] A. V. Avdeenkov and J. L. Bohn, *Phys. Rev. A* **66**, 052718 (2002).
- [93] A. V. Avdeenkov and J. L. Bohn, *Phys. Rev. Lett.* **90**, 043006 (2003).
- [94] A. V. Avdeenkov, D. C. A. Bortolotti, and J. L. Bohn, *Phys. Rev. A* **69**, 012710 (2004).
- [95] C. T. Ticknor and J. L. Bohn, *Phys. Rev. A* **71**, 022709 (2005).
- [96] A. V. Avdeenkov and J. L. Bohn, *Phys. Rev. A* **71**, 022706 (2005).
- [97] G. Herzberg, *The spectra and structure of simple free radicals* (Dover Publications Inc., New York, 1971).
- [98] R. N. Zare, *Angular momentum* (John Wiley & Sons, New York, NY, USA, 1987).
- [99] G. H. Dieke and H. M. Crosswhite, *J. Quant. Spectrosc. Radiat. Transf.* **2**, 97 (1962).
- [100] T. D. Hain, M. A. Weibel, K. M. Backstrand, and T. Curtiss, *J. Phys. Chem. A* **101**, 7674 (1997).
- [101] K. F. Freed, *J. Chem. Phys.* **45**, 4214 (1966).
- [102] G. C. Dousmanis, T. M. Sanders Jr., and C. H. Townes, *Phys. Rev.* **100**, 1735 (1955).
- [103] W. L. Meerts, *Chem. Phys. Lett.* **46**, 24 (1977).
- [104] P. Andresen and E. Rothe, *J. Chem. Phys.* **82**, 3634 (1985).
- [105] M. H. Alexander *et al.*, *J. Chem. Phys.* **89**, 1749 (1988).
- [106] J. J. ter Meulen, W. A. Majewski, W. L. Meerts, and A. Dymanus, *Chem. Phys. Lett.* **94**, 25 (1983).

- [107] J. J. ter Meulen, W. Ubachs, and A. Dymanus, *Chem. Phys. Lett.* **129**, 533 (1986).
- [108] M. Collard, P. Kerwin, and A. Hodgson, *Chem. Phys. Lett.* **179**, 422 (1991).
- [109] E. de Beer, M. P. Koopmans, C. A. de Lange, Y. Wang, and W. A. Chupka, *J. Chem. Phys.* **94**, 7634 (1991).
- [110] R. Forster, H. Hippler, K. Hoyer mann, G. Rohde, and L. B. Harding, *Chem. Phys. Lett.* **183**, 465 (1991).
- [111] C. McRaven, J. Alnis, B. Furneaux, and N. Shafer-Ray, *J. Phys. Chem. A* **107**, 7138 (2003).
- [112] J. J. ter Meulen and A. Dymanus, *Astrophys. J.* **172** (1972).
- [113] J. J. ter Meulen, W. L. Meerts, G. W. M. van Mierlo, and A. Dymanus, *Phys. Rev. Lett.* **36**, 1031 (1976).
- [114] M. Alagia, N. Balucani, P. Casavecchia, D. Stranges, and G. G. Volpi, *J. Chem. Phys.* **98**, 2459 (1993).
- [115] A. T. Droege and P. C. Engelking, *Chem. Phys. Lett.* **96**, 316 (1983).
- [116] T. D. Hain, M. A. Weibel, K. M. Backstrand, P. E. Pope, and T. Curtiss, *Chem. Phys. Lett.* **262**, 723 (1996).
- [117] M. C. van Beek and J. J. ter Meulen, *Chem. Phys. Lett.* **337**, 237 (2001).
- [118] D. T. Anderson, S. Davis, T. S. Zwier, and D. J. Nesbitt, *Chem. Phys. Lett.* **258**, 207 (1996).
- [119] H. J. Lewandowski, E. R. Hudson, J. R. Bochinski, and J. Ye, *Chem. Phys. Lett.* **395**, 53 (2004).
- [120] T. Bérces and S. Förgeteg, *Trans. Faraday Soc.* **66**, 633 (1970).
- [121] H. Johnston and R. Graham, *J. Phys. Chem.* **77**, 62 (1973).
- [122] H. Johnston, S. Chang, and G. Whitten, *J. Phys. Chem.* **78**, 1 (1974).
- [123] M. J. Krisch, M. C. Reid, L. R. McCunn, L. J. Butler, and J. Shu, *Chem. Phys. Lett.* **397**, 21 (2004).
- [124] A. A. Turnipseed, G. L. Vaghjiani, J. E. Thompson, and A. R. Ravishankara, *J. Chem. Phys.* **96**, 5887 (1992).
- [125] T. L. Myers, N. R. Forde, B. Hu, D. C. Kitchen, and L. J. Butler, *J. Chem. Phys.* **107**, 5361 (1997).
- [126] A. Schiffman, D. D. Nelson Jr., and D. J. Nesbitt, *J. Chem. Phys.* **98**, 6935 (1993).
- [127] C. L. Lin, H. K. Rohatgi, and W. B. De More, *Geophys. Res. Lett.* **5**, 113 (1978).
- [128] M. T. Berry, M. R. Brustein, and M. I. Lester, *Chem. Phys. Lett.* **153**, 17 (1988).

- [129] W. Gordy and R. L. Cook, *Microwave Molecular Spectra* (Wiley, New York, 1984), 3rd ed.
- [130] T. Hain, R. Moision, and T. Curtiss, *J. Chem. Phys.* **111**, 6797 (1999).
- [131] W. L. Meerts and A. Dymanus, *Chem. Phys. Lett.* **23**, 45 (1973).
- [132] K. I. Peterson, G. T. Fraser, and W. Klemperer, *Can. J. Phys.* **62**, 1502 (1984).
- [133] R. A. Frosch and H. M. Foley, *Phys. Rev.* **88**, 1337 (1952).
- [134] W. L. Meerts and A. Dymanus, *Can. J. Phys.* **53**, 2123 (1975).
- [135] S. Y. T. van de Meerakker, R. T. Jongma, H. L. Bethlem, and G. Meijer, *Phys. Rev. A* **64**, 041401(R) (2001).
- [136] S. Y. T. van de Meerakker, B. G. Sartakov, A. P. Mosk, R. T. Jongma, and G. Meijer, *Phys. Rev. A* **68**, 032508 (2003).
- [137] M. Weibel, T. Hain, and T. Curtiss, *J. Chem. Phys.* **108**, 3134 (1998).
- [138] M. Takezaki, H. Ohoyama, T. Kasai, and K. Kuwata, *Laser Chem.* **15**, 113 (1995).
- [139] M. Weibel, T. Hain, and T. Curtiss, *J. Vac. Sci. Technol. A* **15**, 2238 (1997).
- [140] D. Parker, H. Jalink, and S. Stolte, *J. Phys. Chem.* **91**, 5427 (1987).
- [141] P. W. Harland, W. P. Hu, C. Vallance, and P. R. Brooks, *Phys. Rev. A* **60**, 3138 (1999).
- [142] M. Drabbels, S. Stolte, and G. Meijer, *Chem. Phys. Lett.* **200**, 108 (1992).
- [143] R. T. Jongma, T. Rasing, and G. Meijer, *J. Chem. Phys.* **102**, 1925 (1995).
- [144] E. Jones and P. Brooks, *J. Chem. Phys.* **53**, 55 (1970).
- [145] N. van Hulst, J. ter Meulen, and A. Dymanus, *J. Chem. Phys.* **86**, 1407 (1987).
- [146] N. van Hulst, J. ter Meulen, and A. Dymanus, *J. Chem. Phys.* **86**, 4461 (1987).
- [147] N. van Hulst, J. ter Meulen, and A. Dymanus, *J. Chem. Phys.* **87**, 2750 (1987).
- [148] P. J. Dagdigian, B. E. Wilcomb, and M. H. Alexander, *J. Chem. Phys.* **71**, 1670 (1979).
- [149] J. C. Helmer, F. B. Jacobus, and P. A. Sturrock, *J. Appl. Phys.* **31**, 458 (1960).
- [150] S. Gandhi, Q. Xu, T. Curtiss, and R. Bernstein, *J. Phys. Chem.* **91**, 5437 (1987).
- [151] N. Butkovskaya, M. Larichev, I. Leipunskii, I. Morozov, and V. Tal'Rose, *Chem. Phys.* **12**, 267 (1976).
- [152] J. van Leuken, F. van Amerom, J. Bulthuis, J. Snijders, and S. Stolte, *J. Phys. Chem.* **99**, 15573 (1995).
- [153] H. Jalink, F. Harren, D. van den Ende, and S. Stolte, *Chem. Phys.* **108**, 391 (1986).

- [154] S. Gandhi and R. Bernstein, *J. Chem. Phys.* **87**, 6457 (1987).
- [155] K. Schreel, J. Schleipen, A. Eppink, and J. ter Meulen, *J. Chem. Phys.* **99**, 8713 (1993).
- [156] M. C. van Beek, G. Berden, H. L. Bethlem, and J. J. ter Meulen, *Phys. Rev. Lett.* **86**, 4001 (2001).
- [157] D. C. Radenović, A. J. A. van Roij, D. A. Chestakov, A. T. J. B. Eppink, J. J. ter Meulen, D. H. Parker, M. P. J. van der Loo, G. C. Groenenboom, M. E. Greenslade, and M. I. Lester, *J. Chem. Phys.* **119**, 9341 (2003).
- [158] T. Kasai, K. Ohashi, H. Ohoyama, and K. Kuwata, *Chem. Phys. Lett.* **127**, 581 (1986).
- [159] R. W. Anderson, *J. Phys. Chem. A* **101**, 7664 (1997).
- [160] R. V. Latham, *High voltage vacuum insulation: The physical basis*. (Academic Press, Inc., London, 1981).
- [161] D. R. Yarkony, *J. Chem. Phys.* **97**, 1838 (1992).
- [162] S. Y. Lee, *Accelerator physics* (World Scientific, Singapore, 1999).
- [163] B. Friedrich, *Eur. Phys. J. D* **31**, 313 (2004).
- [164] L. D. Landau and E. M. Lifshitz, *Mechanics* (Pergamon, Oxford, 1960).
- [165] M. Abramowitz and I. A. Stegun, *Handbook of Mathematical Functions* (Dover Publications, New York, 1970), 9th ed.
- [166] R. Alheit, X. Chu, M. Hofer, M. Holzki, G. Werth, and R. Blümel, *Phys. Rev. A* **56**, 4023 (1997).
- [167] M. Razvi, X. Chu, R. Alheit, G. Werth, and R. Blümel, *Phys. Rev. A* **58**, 34(R) (1998).
- [168] W. Paul and H. Steinwedel, *Zeitschrift für Naturforschung* **8A**, 448 (1953).
- [169] D. Zwillinger, *Handbook of differential equations* (Academic Press, 1997), 3rd ed.
- [170] E. R. Hudson, J. R. Bochinski, H. J. Lewandowski, B. C. Sawyer, and J. Ye, *Eur. Phys. J. D* **31**, 351 (2004).
- [171] M. Drabbels and A. M. Wodtke, *J. Chem. Phys.* **106**, 3024 (1997).
- [172] R. T. Jongma, G. Berden, T. Rasing, H. Zacharias, and G. Meijer, *Chem. Phys. Lett.* **273**, 147 (1997).
- [173] R. T. Jongma, G. Berden, and G. Meijer, *J. Chem. Phys.* **107**, 7034 (1997).
- [174] R. Schneider and G. Werth, *Z. Physik A* **293**, 103 (1979).
- [175] P. R. Huffman *et al.*, *Nature* **403**, 62 (2000).

- [176] A. B. Meinel, *Astrophys. J.* **111**, 555 (1950).
- [177] L. M. Kagan, M. J. Nicolls, M. C. Kelley, H. C. Carlson, V. V. Belikovich, N. V. Bakhmet'eva, G. P. Komrakov, T. S. Trondsen, and E. Donovan, *Phys. Rev. Lett.* **94**, 095004 (2005).
- [178] B. P. Bonev, M. J. Mumma, N. D. Russo, E. L. Gibb, M. A. DiSanti, and K. Magee-Sauer, *Astrophys. J.* **615**, 1048 (2004).
- [179] D. D. Nelson Jr., A. Schiffmann, D. J. Nesbitt, J. J. Orlando, and J. B. Burkholder, *J. Chem. Phys.* **93**, 7003 (1990).
- [180] R. S. Rothman *et al.*, *J. Quant. Spectrosc. Radiat. Transfer* **96**, 139 (2005).
- [181] D. H. Jaffer and I. W. M. Smith, *Faraday Discuss. Chem. Soc.* **67**, 212 (1979).
- [182] D. Yaron, K. Peterson, and W. Klemperer, *J. Chem. Phys.* **88**, 4702 (1988).
- [183] MOLPRO is a package of *ab initio* programs written by H.-J. Werner and P.J. Knowles, with contributions from J. Almlöf, R.D. Amos, A. Berning, D.L. Cooper, M.J.O. Deegan, A.J. Dobbyn, F. Eckert, S.T. Elbert, C. Hampel, R. Lindh, A.W. Lloyd, W. Meyer, N. Nickla, K. Peterson, R. Pitzer, A.J. Stone, P.R. Taylor, M.E. Mura, P. Pulay, M. Schütz, H. Stoll, and T. Thorsteinson.
- [184] F. Mélen, J. Sauval, N. Grevesse, C. B. Farmer, C. Servais, L. Delbouille, and G. Roland, *J. Mol. Spec.* **174**, 490 (1995).
- [185] S. R. Langhoff, C. W. Bauslicher Jr., and P. R. Taylor, *J. Chem. Phys.* **91**, 5953 (1989).
- [186] W. Ketterle and N. J. van Druten, *Adv. Atom. Mol. Opt. Phys.* **37**, 181 (1996).
- [187] B. DeMarco and D. Jin, *Science* **285**, 1703 (2004).
- [188] F. Schreck, G. Ferrari, K. Corwin, J. Cubizolles, L. Khaykovich, M. Mewes, and C. Salomon, *Phys. Rev. A* **64**, 011402 (2001).
- [189] M. Kajita, *Eur. Phys. J. D* **31**, 39 (2004).
- [190] M. Kajita, *Phys. Rev. A* **69**, 012709 (2004).
- [191] R. Krems and A. Dalgarno, *J. Chem. Phys.* **120**, 2296 (2004).
- [192] M. Di Rosa, *Eur. Phys. J. D* **31**, 395 (2004).
- [193] V. Vuletić and S. Chu, *Phys. Rev. Lett.* **84**, 3787 (2000).
- [194] P. Soldán and J. M. Hutson, *Phys. Rev. Lett.* **92**, 163202 (2004).
- [195] D. R. Yarkony, *J. Chem. Phys.* **91**, 4745 (1989).
- [196] P. W. Fairchild, G. P. Smith, D. R. Crosley, and J. B. Jeffries, *Chem. Phys. Lett.* **107**, 181 (1984).

- [197] W. Hack, *N-centered radicals* (John Wiley and Sons, 1998), chap. 13, pp. 413–466.
- [198] W. Ubachs, G. Meijer, J. J. ter Meulen, and A. Dymanus, *J. Mol. Spec.* **115**, 88 (1986).
- [199] J. L. Rinnenthal and K.-H. Gericke, *J. Mol. Spec.* **198**, 115 (1999).
- [200] R. D. Kenner, A. Kaes, R. K. Browarzik, and F. Stuhl, *J. Chem. Phys.* **91**, 1440 (1989).
- [201] C. R. Brazier, R. S. Ram, and P. F. Bernath, *J. Mol. Spec.* **120**, 381 (1986).
- [202] R. S. Ram and P. F. Bernath, *J. Opt. Soc. Am. B* **3**, 1170 (1986).
- [203] A. Gilles, J. Masanet, and C. Vermeil, *Chem. Phys. Lett.* **25**, 346 (1974).
- [204] R. D. Bower, M. T. Jacoby, and J. A. Blauer, *J. Chem. Phys.* **86**, 1954 (1987).
- [205] B. Bohn, F. Stuhl, G. Parlant, P. J. Dagdigian, and D. R. Yarkony, *J. Chem. Phys.* **96**, 5059 (1992).
- [206] G. Parlant, P. J. Dagdigian, and D. R. Yarkony, *J. Chem. Phys.* **94**, 2364 (1991).
- [207] W. Hack and T. Mill, *J. Phys. Chem.* **97**, 5599 (1993).
- [208] S. Gerstenkorn and P. Luc, *Atlas du Spectre d'Absorption de la Molecule d'Iode* (CNRS, Paris, 1978).
- [209] S. Gerstenkorn and P. Luc, *Rev. Phys. Appl.* **14**, 791 (1979).
- [210] W. Martin, *Phys. Rev. A* **36**, 3575 (1987).
- [211] W. Ubachs, J. J. ter Meulen, and A. Dymanus, *Can. J. Phys.* **62**, 1374 (1984).
- [212] T. James, *J. Chem. Phys.* **55**, 4118 (1971).
- [213] D. Patel-Misra, G. Parlant, D. G. Sauder, and D. R. Yarkony, *J. Chem. Phys.* **94**, 1913 (1991).
- [214] D. Patel-Misra and P. J. Dagdigian, *J. Chem. Phys.* **97**, 4871 (1992).
- [215] D. G. Sauder, D. Patel-Misra, and P. J. Dagdigian, *J. Chem. Phys.* **91**, 5316 (1989).
- [216] K.-H. Gericke, R. Theinl, and F. J. Comes, *J. Chem. Phys.* **92**, 6548 (1990).
- [217] R. W. Randall, C.-C. Chuang, and M. I. Lester, *Chem. Phys. Lett.* **200**, 113 (1992).
- [218] Y. Mo, C. Ottinger, and G. Shen, *J. Chem. Phys.* **111**, 4598 (1999).
- [219] J. R. McDonald, R. G. Miller, and A. P. Baronavski, *Chem. Phys. Lett.* **51**, 57 (1977).
- [220] H. H. Nelson and J. R. McDonald, *J. Chem. Phys.* **93**, 8777 (1990).
- [221] M. Hawley, A. P. Baronavski, and H. H. Nelson, *J. Chem. Phys.* **99**, 2638 (1993).
- [222] J. R. McDonald, J. W. Rabalais, and S. P. McGlynn, *J. Chem. Phys.* **52**, 1332 (1970).

- [223] F. Rohrer and F. Stuhl, *J. Chem. Phys.* **88**, 4788 (1988).
- [224] W. S. Drozdowski, A. P. Baronavski, and J. R. McDonald, *Chem. Phys. Lett.* **64**, 421 (1979).
- [225] T. Spiglanin, R. Perry, and D. Chandler, *J. Phys. Chem.* **90**, 6184 (1986).
- [226] H. Okabe, *J. Chem. Phys.* **53**, 3507 (1970).
- [227] R. D. Kenner, F. Rohrer, and F. Stuhl, *J. Chem. Phys.* **86**, 2036 (1987).
- [228] D. Patel-Misra and P. J. Dagdigan, *J. Chem. Phys.* **97**, 4871 (1992).
- [229] W. Hack and K. Rathmann, *J. Phys. Chem.* **96**, 47 (1992).
- [230] J. S. Adams and L. Pasternack, *J. Phys. Chem.* **95**, 2975 (1991).
- [231] P. J. Dagdigan, *Annu. Rev. Phys. Chem.* **48**, 95 (1997).
- [232] W. Hack and A. Wilms, *J. Phys. Chem.* **93**, 3540 (1989).

SAMENVATTING

In dit proefschrift wordt een methode beschreven om een bundel molekulen in de gasfase af te remmen en op te sluiten. Eenmaal opgesloten in de val hebben de molekulen een zeer lage temperatuur, slechts enkele duizendste graad boven het absolute nulpunt. Deze temperatuur is veel lager dan voorkomt op ook maar het koudste plekje in het heelal, en kan alleen maar bereikt worden met speciale technieken in een laboratorium. Het doel van deze experimenten is het gedrag van molekulen onder deze extreme omstandigheden te bestuderen. Maar waarom zijn deze "koude molekulen" voor ons dan zo interessant? Wat bedoelen we eigenlijk precies met temperatuur? Wat verwachten we te ontdekken als de molekulen koud worden, en hoe werkt precies de methode om de molekulen zo koud te krijgen?

Beweging en temperatuur

Temperatuur is niets anders dan een maat voor de snelheid van deeltjes. Nemen we als voorbeeld een gas, zoals de lucht om ons heen. In zo'n gas bewegen de molekulen waaruit het bestaat met een snelheid die past bij de temperatuur van het gas. Is het gas op kamertemperatuur, dan bewegen de molekulen met een snelheid van ongeveer 2000 km per uur. Daalt de temperatuur, dan daalt ook de snelheid van de molekulen. Maar dit betekent dus ook dat er een ondergrens voor temperatuur bestaat: de laagst mogelijke temperatuur is bereikt als de molekulen compleet stil staan en niet meer bewegen. Dit is het absolute nulpunt, en correspondeert met een temperatuur van 0 Kelvin (-273.15 °C).

Bij extreem lage temperaturen gedragen de molekulen zich heel anders dan bij kamertemperatuur. Als de temperatuur extreem wordt verlaagd, komen namelijk de kwantummechanische eigenschappen van de natuur naar boven. Welke bizarre consequenties dit kan hebben kan het best worden uitgelegd aan de hand van een voorbeeld. Laten we twee molekulen nemen en we sturen die op botsingskoers. Bij hoge temperaturen (bijv. kamertemperatuur) botsen de molekulen met elkaar alsof het biljartballen zijn. Het hele botsingsproces kan dan ook redelijk accuraat met behulp van de wetten van de klassieke mechanica beschreven worden. Niets is minder waar voor dezelfde botsing bij hele lage temperaturen. Bij deze temperaturen gedragen de molekulen zich niet meer als biljartballen, maar als golven. De kwantummechanica leert ons namelijk dat als de temperatuur laag genoeg wordt, het golfkarakter van de materie belangrijker wordt. En golven botsen nu eenmaal heel anders dan massieve biljartballen: golven kunnen elkaar lokaal versterken of uitdoven (interfereren). En zoals elke golf heeft ook een materie-golf een karakteristieke golflengte, en deze wordt groter naarmate de temperatuur lager wordt. Echt spannend wordt het als een groot aantal koude molekulen dicht op elkaar worden gebracht zodat de golflengte van de molekuul-golven groter wordt dan de afstand tussen de afzonderlijke molekulen. Het bestuderen van molekulen onder dit soort exotische omstandigheden is de belangrijkste motivatie methoden te ontwikkelen om molekulen zo dicht mogelijk tot 0 Kelvin af te koelen. Bij deze lage temperaturen bewegen de molekulen bijna niet meer en kunnen ze worden opgesloten in een val om ze goed te kunnen bestuderen. Er zijn echter ook nog andere, niet minder interessante toepassingen van koude molekulen.

Worden molekulen opgesloten in een val, dan krijg je ook nog iets anders kado, namelijk de mogelijkheid om een molekuul gedurende een erg lange tijd te bestuderen. Normaal gesproken bewegen molekulen heel snel, en heb je maar een hele kleine fractie van een seconde de tijd om het molekuul te bestuderen. Maar zitten de molekulen vast in de val, dan kan deze interactie-tijd oplopen tot vele seconden. En dit is van groot belang om met hoge nauwkeurigheid de eigenschappen van molekulen te kunnen achterhalen. Bovendien stelt het je in staat processen die erg langzaam verlopen "live" te volgen. In hoofdstuk 7 van dit proefschrift is een eerste toepassing hiervan beschreven. Door gebruik te maken van de lange tijd die de molekulen in de val doorbrengen is een belangrijke eigenschap van een molekuul, namelijk de levensduur van een aangeslagen toestand, met hoge precisie direct gemeten. Dit soort metingen waren voorheen alleen indirect, en vergezeld met een hoge onnauwkeurigheid, mogelijk.

De Stark-afremmer

Maar hoe krijgen we de molekulen nu in de val *? De methode die we in onze groep hebben ontwikkeld om de molekulen stil te zetten en op te sluiten heet Stark-afremming. De werking van de Stark-afremmer is schematisch weergegeven in Figuur 8.9. De afremmer bestaat uit kruislings opgehangen elektrodeparen. Als op een elektrodepaar een groot spanningsverschil wordt gezet, ontstaat een hoog elektrisch veld tussen de elektroden. De molekulen die in onze experimenten gebruikt worden, ondervinden een kleine kracht ten gevolge van dit veld. De interactie van het molekuul met het elektrische veld wordt het "Stark-effect" genoemd, vandaar de naam Stark-afremmer. Voor het molekuul is het effect van het aangelegde veld hetzelfde als dat van een berg, en het kost arbeid om tegen de berg op te bewegen. En juist dit laatste wordt gebruikt in de Stark-afremmer: door met behulp van de spanning op de elektroden een berg voor de molekulen te creëren, wordt het molekuul gedwongen tegen de berg omhoog te bewegen, en remt daarbij een beetje af. Deze effecten zijn echter enorm klein, en de snelheids-afname die zo bereikt kan worden is beperkt. Bovendien versnelt het molekuul weer als het de top van de berg heeft bereikt en weer naar beneden "rolt". Door echter de spanning tussen de elektroden juist op tijd uit te schakelen, kan voorkomen worden dat het molekuul gaat versnellen. Het molekuul schiet nu met de afgeremde snelheid door naar het volgende elektrodenpaar, dat precies op tijd weer onder spanning wordt gezet. Tussen elk paar remt het molekuul zo iets verder af, en kunnen de molekulen worden afgeremd tot elke gewenste snelheid. Een foto van de gebruikte Stark-afremmer is te zien in Figuur 8.10.

In onze groep was al eerder aangetoond dat op deze manier molekulen kunnen worden afgeremd, in eerste instantie door een bundel CO molekulen door een prototype afremmer te schieten. En met een bundel ND_3 molekulen was het zelfs mogelijk om de molekulen af te remmen tot stilstand, en ze vervolgens op te sluiten in een val. Het nadeel was alleen, dat deze prototype afremmer slechts in staat was een zeer klein deel van de molekuulbundel af te remmen. Teneinde de eigenschappen van de geproduceerde koude molekulen daadwerkelijk te kunnen onderzoeken, is het nodig een flink groter deel van de bundel af te kunnen remmen en op te kunnen sluiten. Hiervoor is een opgeschaalde versie van het bestaande prototype ontworpen en gebouwd. Deze nieuwe afremmer staat beschreven in dit

*Helaas werken de methoden om *atomen* te koelen niet voor molekulen. Daarvoor is de energiestructuur van molekulen te gecompliceerd.

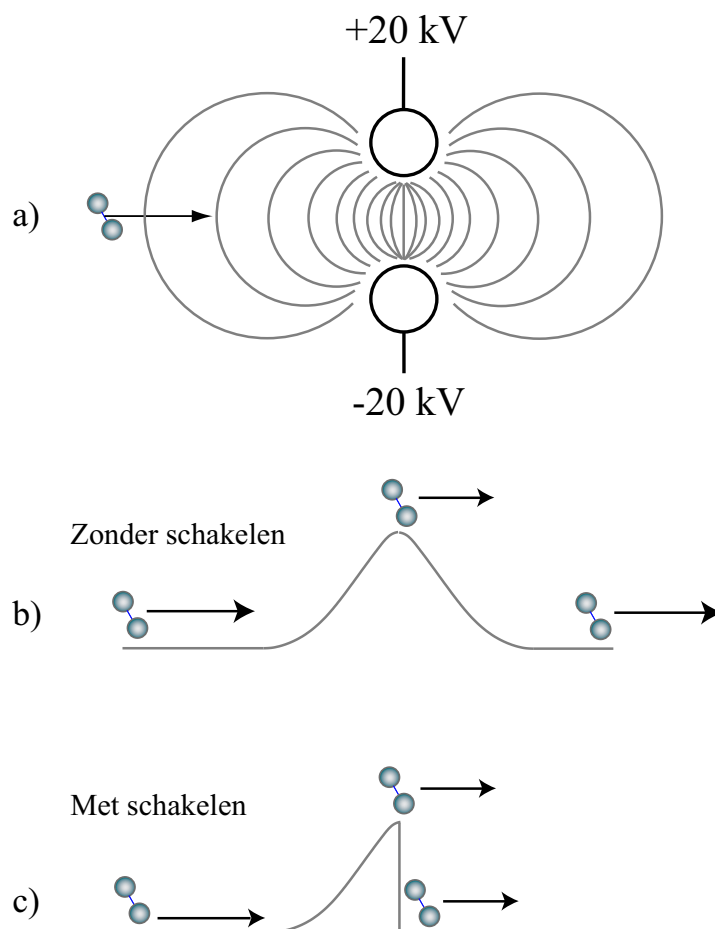


Figure 8.9: Schematische weergave van de werking van de Stark-afremmer. Tussen twee elektroden wordt een groot spanningsverschil gezet. Hierdoor ontstaat tussen de elektroden een hoog elektrisch veld (a). Voor de molekulen is dit veld een 'berg' (b). Als de molekulen nu tussen de elektroden door bewegen, lopen ze eerst tegen de berg op en remmen daardoor af. Zouden we niets doen, dan rollen ze daarna de berg af, en versnellen weer naar hun oorspronkelijke snelheid. Dit laatste wordt voorkomen door de hoogspanning op de juiste tijd snel uit te schakelen (c). De molekulen schieten nu met een iets lagere snelheid door naar het volgende elektrodepaar, dat ook weer precies op tijd onder hoogspanning wordt gezet.

proefschrift. Met deze afremmer is het inderdaad mogelijk gebleken een zeer veel groter deel van de bundel af te remmen dan voorheen mogelijk was. Deze afrem-experimenten zijn uitgevoerd met een bundel OH radicalen. Het OH radicaal is een chemisch zeer relevant molecuul, en speelt een grote rol in vele biologische, chemische, atmosferische en interstellaire processen, en staat daarom voor vele wetenschappers in het middelpunt van de belangstelling. De afrem-experimenten staan beschreven in hoofdstuk 3. Hier is ook een gedetailleerde beschrijving van het afremproces gegeven.

De opgeschaalde afremmer heeft ons ook in staat gesteld de beweging van de molekulen door de afremmer te bestuderen met ongeëvenaarde nauwkeurigheid. Subtiële details, voorheen nooit geobserveerd en/of begrepen, zijn aan het licht gekomen. Door deze metingen, en met behulp van uitgebreide numerieke simulaties, kon de theorie van de werking van een Stark-afremmer worden getest

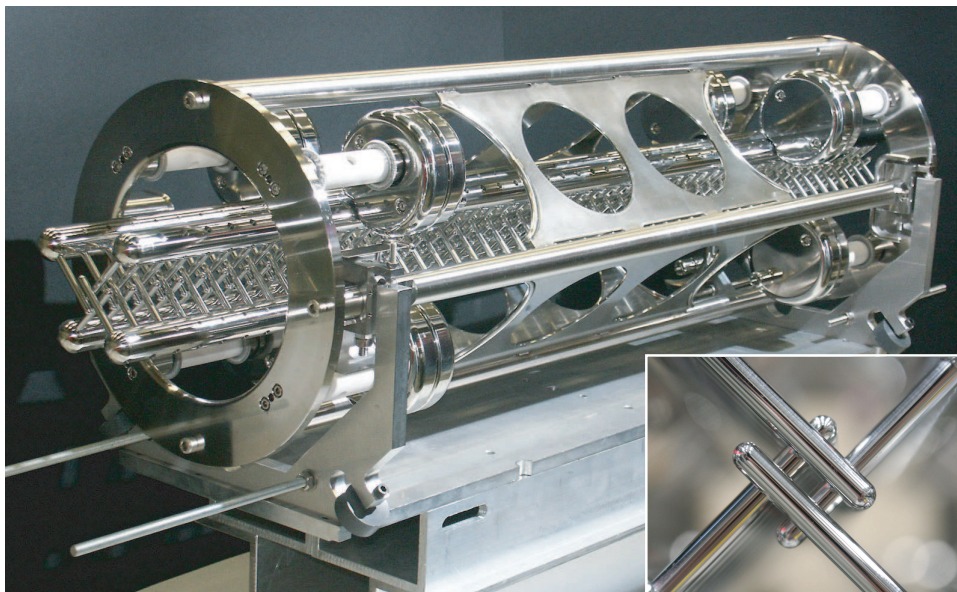


Figure 8.10: Foto van de Stark-afremmer. De afremmer bestaat uit 102 elektrode-paren, die elk 11 mm uit elkaar staan. De molekulare bundel beweegt door de $4 \times 4 \text{ mm}^2$ doorsnede, zoals is te zien in de inzet rechtsonder. Het spanningsverschil tussen tegenoverliggende elektroden bedraagt 40 kV.

en uitgebreid. Deze onderwerpen worden behandeld in de hoofdstukken 4 en 5. In hoofdstuk 4 wordt ingegaan op de voorwaartse beweging van de molekulen in de afremmer, en wordt een uitbreiding op het bestaande model voor fase-stabiliteit (de theorie die beschrijft waarom een afremmer eigenlijk kan werken) gegeven. In hoofdstuk 5 wordt de invloed van de zijwaartse beweging van de molekulen door de afremmer op fase-stabiliteit bestudeerd; een tot op heden nog onontgonnen gebied. Deze studies hebben ons begrip van de werking van een Stark-afremmer duidelijk vergroot.

De elektrostatische val

Nadat de bundel OH radicalen is afgeremd tot ongeveer 20 m/s, kunnen de molekulen worden stilgezet en opgeslagen in een val. De val bestaat uit 3 elektroden, die op hoogspanning kunnen worden gezet. De wijze waarop de afgeremde molekulen in de val kunnen worden geladen staat schematisch weergegeven in Figuur 8.11. Afhankelijk van de waarde van de hoogspanning op de elektroden, kan óf een laatste "berg" voor de molekulen worden gecreëerd, óf een "put" worden gemaakt. Als de langzame molekulen uit de afremmer komen, worden de elektroden van de val in de "berg"-configuratie geschakeld. De molekulen lopen tegen de berg omhoog, en remmen daarbij verder af. De molekulen zijn echter te langzaam om de top van de berg te bereiken, en komen ongeveer halverwege, in het midden van de val, tot stilstand. Op dit moment worden de elektroden van de val in de "put"-configuratie geschakeld. De inmiddels stilstaande molekulen kunnen nu niet meer uit de put ontsnappen, en zijn gevangen in de val. Deze experimenten zijn beschreven in hoofdstuk 6. In de val, waar de molekulen worden gedetecteerd met behulp van een laser en een fluorescentie detector, hebben de OH radicalen een temperatuur van ongeveer 50 mK.

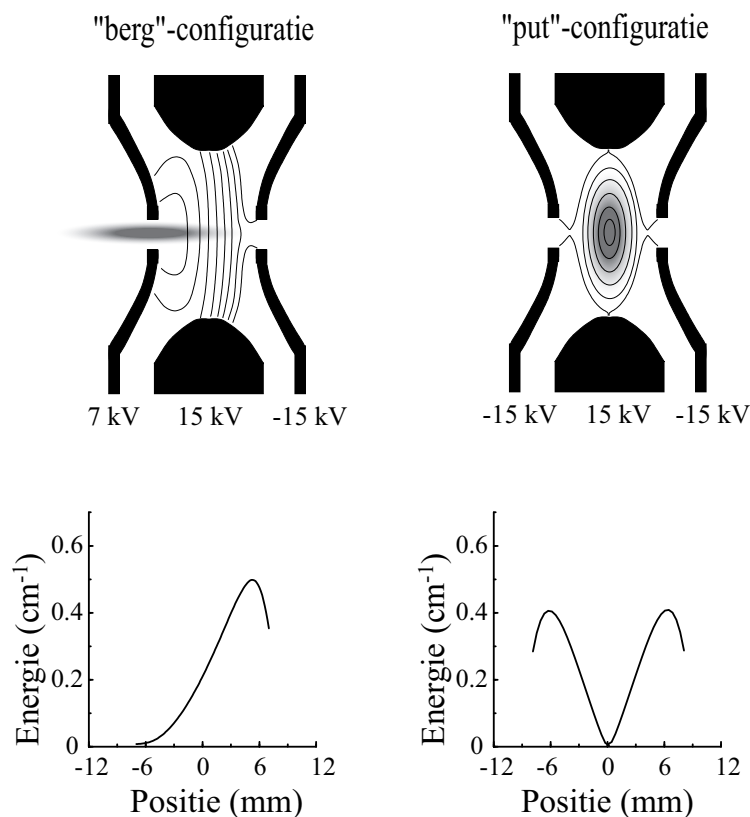


Figure 8.11: Schematische weergave van de laadprocedure van de electrostatische val. Afhankelijk van de spanning op de elektroden kan óf een laatste "berg" voor de molekulen worden gecreëerd (links), óf een "put" waarin de molekulen kunnen worden gevangen (rechts). Als de afgeremde molekulen de val binnenkomen, staat de val in de "berg"-configuratie. De molekulen lopen tegen de berg op, remmen af, en komen in het midden van de val tot stilstand. Op dit moment wordt de val in de "put"-configuratie geschakeld. De molekulen zitten nu gevangen in de put en kunnen niet meer ontsnappen.

Hoe verder?

Nu we in staat zijn een groot deel van een molekuulbundel af te remmen en op te sluiten, komen het bestuderen van de spannende en exotische eigenschappen van koude molekulen binnen handbereik. Een van de meest interessante processen die we willen bestuderen zijn botsingen tussen de molekulen in de val. De dichtheden (aantal molekulen per volume) die we tot op heden hebben bereikt zijn hiervoor echter nog te laag. Zijn de dichtheden in de val eenmaal hoog genoeg voor het plaatsvinden van botsingen, dan kan mogelijk ook de temperatuur in de val verder worden verlaagd. Dit kan bijvoorbeeld gebeuren door selectief de heetste molekulen uit de val te verwijderen ("verdampings koeling"), of door de molekulen veelvuldig te laten botsen met veel koudere atomen ("sympathetische koeling").

Eén van de belangrijkste taken die voor ons liggen is dus het bereiken van hogere dichtheden in de val. Met de huidige machine kan dit bijvoorbeeld gerealiseerd worden door de optimalisatie van de molekuulbundel, het afremproces, en met name het laadproces van de val. Maar de meest directe manier om meer molekulen in de val te krijgen is, nadat een pakketje molekulen in de val gevangen

is, de val te herladen met een nieuw pakketje molekulen. Helaas is dit echter fundamenteel onmogelijk met tijdsgeschakelde elektrische velden, zonder de al opgesloten molekulen óf te verliezen óf te verwarmen. Dit is ook duidelijk uit de in Figuur 8.11 gepresenteerde laadprocedure van de val: om een nieuw pakketje in de val te laden, moet de val weer in de "berg"-configuratie worden gezet, waardoor de al getrapte molekulen de "berg afrollen" en de val verlaten. In hoofdstuk 8 staat echter een methode beschreven die dit fundamentele probleem omzeilt door slim gebruik te maken van de energie-structuur van de molekulen. Het schema werkt specifiek voor het NH radicaal, en alle voorwaarden voor het realiseren van het herladen van de val zijn experimenteel gerealiseerd.

Met de in dit proefschrift beschreven machine verwachten we in de nabije toekomst de exotische eigenschappen van molekulen bij lage temperatuur te kunnen onderzoeken, en daarmee een zeer interessant nieuw vakgebied te kunnen ontsluiten.

CURRICULUM VITAE

Op 30 mei 1977 ben ik geboren te Eindhoven, als zoon van Jan van de Meerakker en Jo van den Boom, en als broer van Helga en Franca. De lagere school heb ik doorgebracht op basisschool "de Klepper" te Luyksgestel. In 1989 ben ik mijn middelbare school opleiding begonnen aan het "Hertog-Jancollege" in Valkenswaard. Na het *cum laude* behalen van mijn VWO diploma in 1995, ben ik natuurkunde gaan studeren aan de Katholieke Universiteit Nijmegen. Mijn afstudeerstage heb ik gedaan onder begeleiding van Michiel van Beek en Hans ter Meulen. Mijn onderzoek betrof populatie-inversie in de productie van OH in een moleculaire bundel, en de meting van differentiële doorsnedes voor inelastische botsingen tussen OH en Ar. In 2000 ben ik *cum laude* afgestudeerd in de experimentele natuurkunde.

In april 2000 ben ik begonnen met mijn promotie-onderzoek in de groep van Gerard Meijer aan het FOM Instituut voor Plasmafysica "Rijnhuizen" in Nieuwegein. Doel van het onderzoek was het ontwikkelen van een nieuwe moleculaire bundel machine waarmee het mogelijk is een bundel OH radicalen af te remmen en op te sluiten. De resultaten van dit onderzoek staan beschreven in dit proefschrift. Vanaf 1 december 2003 is het onderzoek uitgevoerd aan het Fritz-Haber-Instituut der Max-Planck-Gesellschaft te Berlijn, Duitsland.

Sinds april 2005 werk ik als groepsleider aan het Fritz-Haber-Instituut, en draag zorg voor een bestaande en een nieuwe onderzoekslijn en de begeleiding van verschillende promovendi en postdocs. Doel van het onderzoek is het bestuderen van botsingsprocessen tussen (ultra) koude moleculen.

LIST OF PUBLICATIONS

- *Accumulating NH radicals in a magnetic trap*
Sebastiaan Y.T. van de Meerakker, Rienk T. Jongma, Hendrick L. Bethlem, and Gerard Meijer
Phys. Rev. A **64**, 041401(R) (2001).
- *Deceleration and trapping of ammonia using time-varying electric fields*
Hendrick L. Bethlem, Floris M.H. Crompvoets, Rienk T. Jongma, Sebastiaan Y.T. van de Meerakker, and Gerard Meijer
Phys. Rev. A **65**, 053416 (2002).
- *Optical pumping of metastable NH radicals into the paramagnetic ground state*
Sebastiaan Y.T. van de Meerakker, Boris G. Sartakov, Allard P. Mosk, Rienk T. Jongma, and Gerard Meijer
Phys. Rev. A **68**, 032508 (2003).
- *Electrostatic trapping of OH radicals*
Sebastiaan Y.T. van de Meerakker, Paul H.M. Smeets, Nicolas Vanhaecke, Rienk T. Jongma, and Gerard Meijer
Phys. Rev. Lett. **94**, 23004 (2005).
- *Higher-order resonances in a Stark decelerator*
Sebastiaan Y.T. van de Meerakker, Nicolas Vanhaecke, Hendrick L. Bethlem, and Gerard Meijer
Phys. Rev. A **71**, 053409 (2005).
- *Direct measurement of the radiative lifetime of vibrationally excited OH radicals*
Sebastiaan Y.T. van de Meerakker, Nicolas Vanhaecke, Mark P.J. van der Loo, Gerrit C. Groenenboom, and Gerard Meijer
Phys. Rev. Lett. **95**, 013003 (2005).
- *Transverse stability in a Stark decelerator*
Sebastiaan Y.T. van de Meerakker, Nicolas Vanhaecke, Hendrick L. Bethlem, and Gerard Meijer
Submitted to Phys. Rev. A
- *Stark deceleration and trapping of OH radicals*
Sebastiaan Y.T. van de Meerakker, Nicolas Vanhaecke, and Gerard Meijer
Ann. Rev. of Phys. Chem. **57** (2006) (*in press*).